Supervisors: Dr Rachael Elder and Prof Raymond Allen

The University Of Sheffield.

High Temperature Co-electrolysis of Carbon dioxide and Steam in a Solid Oxide Cell for Synthesis Gas Production

---

By

Kayode Omojola, MEng (Hons)

Submitted for the degree of Doctor of Philosophy (PhD)

Department of Chemical and Biological Engineering

March 2015

Abstract

The utilisation of CO_2 as a feedstock in the production of valuable products such as synthetic fuel is a promising pathway for mitigating its atmospheric concentration. A review of the high temperature co-electrolysis of CO_2 and H_2O in a solid oxide cell for syngas production has identified that further understanding of the co-electrolysis reaction mechanism is one of three key areas of development.

In this work, a co-electrolysis test facility was designed, developed and commissioned. Additionally, the performance of a NextCell^{TM} electrolyte supported cell was investigated for CO_2 electrolysis and CO_2/H_2O co-electrolysis with an aim to gain a better understanding of the reaction mechanism.

During CO_2 electrolysis, an increase in cell area specific resistance was observed with increasing CO_2 concentration. In addition, AC impedance spectra measurements showed a significant increase in polarisation resistance at the fuel electrode with increasing CO_2/CO ratio. Short term durability studies carried out at -0.5 A/cm^2, 850^{o}C and fuel electrode compositions of 50% CO_2, 25% CO and 25% N_2 showed a sharp increase in cell voltage corresponding to a passivation rate of 120 mV/h in the first 5 hours of operation. This increase in cell voltage was caused by the adsorption of impurities to the Ni surface prompting partial blockage of the active Ni sites.

During CO_2/H_2O co-electrolysis, the exhaust gas compositions measured at open circuit voltage were ±2 mol % of the thermodynamic equilibrium compositions. AC impedance spectra measurements showed a slight increase in polarisation resistance at the fuel electrode with increasing CO_2/H_2O concentration. Direct current measurements showed a 21% increase in cell performance during CO_2/H_2O co-electrolysis compared to CO_2 electrolysis. Furthermore, co-electrolysis durability studies carried out at -0.5 A/cm^2 showed a significantly lower degradation rate of 1.3 mV/h over 44 hours of operation compared to CO_2 electrolysis.

Acknowledgements

This thesis is dedicated to my parents Dr Moses and Mrs Martina Omojola. Without your love, support and encouragement throughout my life, I would never have made it this far. To my siblings Toyin, Kunle and Yemisi, your advice and continuous encouragement has made this all possible.

Sincere thanks go to my supervisor, Dr Rachael Elder, who gave me the opportunity to work closely with her. Her support, guidance as well as pain-staking effort in proof reading the drafts, are greatly appreciated. A special thanks to Prof. Raymond Allen, Dr Denis Cumming and Prof. Derek Sinclair for their technical advice and discussions that helped shape this project. Thanks, also to the brilliant technical staff, Oz McFarlane, Mark McIntosh, Usman Younis, Keith Penny, Mark Jones, Dave Wengraf, Andy Patrick, Steven Blackburn, Stuart Richards, Adrian Lumby, Andrew Mould, Dan Jackson and Richard Stacey for the support and training provided.

To all my friends, thank you for your understanding and encouragement in my many moments of crisis. Your friendship makes my life a wonderful experience.

I would also like to thank EPSRC, 4CU and Dr Moses and Mrs Martina Omojola for financially supporting this project.

Finally thank you, Lord, for always being there for me

Table of Contents

Abstract.....III

Acknowledgements.....IV

List of Tables.....IX

List of Figures.....XII

List of Abbreviations.....XVIII

Chapter 1: Introduction

1.1 Background 2

1.1.1 Carbon dioxide Utilisation 3

1.2 High Temperature Co-electrolysis of Steam and Carbon dioxide in a SOE 4

1.2.1 Solid Oxide Electrolysis Cells 5

1.2.2 Introduction to High Temperature CO_2/H_2O Co-electrolysis 6

1.2.3 Operating Principle of SOECs under CO_2/H_2O conditions 8

1.3 Operation and Electrolysis efficiency of SOECs 10

1.3.1 Open Circuit Voltage and Nernst Potential 10

1.3.2 Electrolysis Efficiency 11

1.4 Economics and Performance of SOEs under H_2O/CO_2 conditions 13

1.5 Aims of this Work 16

1.6 Layout of Thesis 17

Chapter 2: High Temperature Co-electrolysis of CO_2 and H_2O in SOEs - A Review

2.1 Polarisation Losses and SOEC Performance 19

2.1.1 Ohmic Loss 19

2.1.2 Activation Polarisation 20

2.1.3 Concentration Polarisation 21

2.2 Electrochemical Methods for SOEC Evaluation 21

2.2.1 Current density (*i*) – voltage (V) curves 21

2.2.2 Electrochemical Impedance Spectroscopy 22

2.3 High Temperature Electrolysis of Carbon dioxide in a SOC 30

2.4 High Temperature Co-electrolysis of CO_2 and H_2O in a SOC - Reaction Mechanisms for Syngas Production 31

2.4.1 Co-electrolysis Electrochemical Model for Syngas Production 32

2.4.2 Experimental Investigation 35
2.5 Properties, Materials and Characteristics of SOECs 38
2.5.1 Electrolyte 39
2.5.2 Requirements of Electrode Materials 42
2.6 Experimental Investigations of High Temperature Co-electrolysis of CO_2 and H_2O 46
2.6.1 Electrochemical Performance 46
2.6.2 Degradation of SOCs under electrolysis operations 47

Chapter 3: Experimental Design, Methods and Commissioning

3.1 Experimental test facility 56
3.2 In-house cell rig design 58
3.2.1 Material selection 58
3.2.2 Solid oxide cell sealing 58
3.2.3 Electrochemical measurements 60
3.2.4 In-house cell rig conclusions 61
3.3 Cell rig – ProboStat™ 61
3.3.1 Cell rig damage 64
3.4 Experimental Button cell Testing 65
3.4.1 Solid Oxide Cells 65
3.5 Steam Production 67
3.5.1 Experimental setup 67
3.5.2 Effect of varying the water bath temperatures and carrier gas flow rate 69
3.5.3 Condensation of Steam downstream of the Water bath 72
3.6 Electrochemical testing 74
3.7 Gas Chromatography 76
3.7.1 Gas Chromatograph – Method development 76
3.7.2 Gas Chromatograph Calibration 78
3.8 Cathode and Electrolyte Supported Solid Oxide Electrolysis Cells 79
3.8.1 Experimental setup and procedure 80
3.8.2 Results and Discussion - Electrolyte Supported SOEC 80
3.8.3 Results and Discussion - Cathode Supported SOEC 82
3.8.4 Cathode Supported SOEC with Platinum ink 83
3.9 Identification of Electrochemical Processes in Impedance Spectra - Experimental 86
3.9.1 Experimental 86
3.9.2 Oxygen Electrode 87

3.9.3 Fuel Electrode 89
3.9.4 Equivalent Circuit Model and Data Analysis 92

Chapter 4: High Temperature Electrolysis of CO_2 in a Solid Oxide Cell

4.1 Introduction 94
4.2 Electrolysis of Carbon dioxide 94
4.2.1 Introduction 94
4.2.2 Initial Cell Characterisation 95
4.2.3 Open Circuit Voltage 96
4.2.4 DC and AC Characterisation 98
4.2.5 Poisoning and Regeneration of NiO electrode during Electrolysis of Carbon dioxide .. 103
4.3 Electrochemical Performance of SOCs operating at varying Flow rates and Current densities during CO_2 electrolysis 109
4.3.1 Experimental 109
4.3.2 Current Efficiency and Gas Conversion 109
4.4 Durability of the SOCs during High Temperature Electrolysis of Carbon Dioxide 112
4.4.1 Experimental 112
4.4.2 Effect on Cell Voltage 112
4.4.3 AC characterisation – Effect on Impedance Spectra 116

Chapter 5: High Temperature Co-electrolysis of CO_2/H_2O in a Solid Oxide Cell

5.1 Introduction 121
5.2 Co-electrolysis of H_2O and CO_2 121
5.2.1 Experimental set-up 121
5.2.2 Initial Cell Characterisation 123
5.2.3 Equilibrium of the rWGSR 125
5.3 Electrochemical Measurements 131
5.3.1 DC Characterisation 131
5.3.2 Area Specific Resistance during CO_2/H_2O co-electrolysis 134
5.3.3 AC Characterisation 136
5.4 Durability of SOCs during High Temperature Co-electrolysis of Carbon dioxide and Steam 138
5.4.1 Experimental 138
5.4.2 Cell Voltage and AC Characterisation 139
5.5 Current Efficiency and Syngas Production at varying Current Densities 143

Chapter 6: Conclusions and Future Work

6.1 Conclusion 148

6.2 Future Work 152

6.2.1 Eliminating Issues of Steam Condensation 153

6.2.2 Sulphur Poisoning 153

6.2.3 Optimisation of the Electrode Supported Cells 154

6.2.4 Detailed Electrochemical Characterisation of Electrode supported cells 155

Chapter 7: References 156

Chapter 8: Appendices 164

List of Tables

Table 1–1: Assumptions for cost estimate (Graves et al. 2010).....14

Table 1–2: Status of SOEC capabilities and base case economic estimation.....15

Table 2–1: Comparison of cold gas compositions to the fuel electrode, measured gas compositions and the calculated thermodynamic equilibrium composition (Ebbesen et al. 2012).....38

Table 2–2: Approximate ionic conductivities for electrolyte materials (Wincewicz and Cooper 2005).....40

Table 2–3: OCV of different materials for steam electrolysis at 800^{o}C (Kim-Lohsoontorn et al. 2011).....41

Table 2–4: Initial SOEC performance from high temperature co-electrolysis of CO_2 and H_2O.....46

Table 3–1: Description of the components in cell rig assembly.....62

Table 3–2: Electrolyte supported SOEC.....66

Table 3–3: Electrode supported SOEC.....66

Table 3–4: Individual gas retention times at 30^{o}C and split ratio of 20:1 through a Plot Q column.....76

Table 3–5: Retention time of gasses under the developed method.....78

Table 3–6: Retention times of the various calibrated compounds.....79

Table 3–7: Measured OCV of an electrolyte supported cell at 850^{o}C.....80

Table 3–8: Measured OCV of a cathode supported solid oxide cell at 850^{o}C.....82

Table 3–9: Experimental OCV of a cathode supported solid oxide cell at 850^{o}C under a new experimental set-up.....85

Table 4–1: Operating conditions for CO_2 electrolysis.....95

Table 4–2: Ohmic and polarisation resistances under NiO reducing conditions, obtained using equivalent circuit model from experimental Nyquist plot.....96

Table 4–3: Open circuit voltage of CO_2/CO mixture at varying temperatures.....98

Table 4–4: Ohmic and polarisation resistances during CO_2 electrolysis, obtained using equivalent circuit model from experimental Nyquist plot.....101

Table 4–5: Operating conditions for the electrolysis of CO_2 in a SOC.....109

Table 4–6: Operating conditions, cell voltage and passivation during the CO_2 electrolysis durability tests (first and second measurement) 113
Table 4–7: Ohmic and polarisation resistances during durability studies for CO_2 electrolysis (first measurement), obtained using equivalent circuit model from experimental Nyquist plot 117
Table 4–8: Ohmic and polarisation resistances during durability studies for CO_2 electrolysis (second measurement), obtained using equivalent circuit model from experimental Nyquist plot 118
Table 5–1: Fuel electrode operating conditions for H_2O/CO_2 co-electrolysis process 122
Table 5–2: Measured OCV of electrolyte supported cells at 850^oC under NiO reducing conditions.....123
Table 5–3: Ohmic and polarisation resistances of both cells under NiO reducing conditions, obtained using equivalent circuit model from experimental Nyquist plot 124
Table 5–4: Thermodynamic equilibrium and exhaust gas composition at 850^oC using the electrolyte supported cell 126
Table 5–5: Thermodynamic equilibrium and exhaust gas composition at 850^oC using the electrode supported cell (without Pt ink added to the fuel electrode) 127
Table 5–6: Thermodynamic equilibrium and exhaust gas composition at 850^oC using the electrode supported cell (with Pt ink added to the fuel electrode) 127
Table 5–7: Measured current densities of similar CO_2 and CO_2/H_2O compositions at 1.46 V and 850^oC cell temperature 132
Table 5–8: Measured ASR of equivalent CO_2 and CO_2/H_2O mixtures at -0.1A/cm^2.....135
Table 5–9: Ohmic and polarisation resistances during CO_2/H_2O co-electrolysis, obtained using equivalent circuit model from experimental Nyquist plot.....137
Table 5–10: Operating conditions, cell voltage and degradation during the CO_2/H_2O co-electrolysis durability tests 139
Table 5–11: Ohmic and polarisation resistances during durability studies for CO_2/H_2O co-electrolysis, obtained using equivalent circuit model from experimental Nyquist plot 141
Table 5–12: Exhaust gas compositions measured at open circuit voltage and -0.5 A/cm^2 when operating at 850^oC and inlet gas compositions of 50% CO_2 – 25% H_2 – 25% N_2 at 20 ml/min.....143
Table 5–13: Current efficiency of syngas produced at varying current densities 144

Table 5–14: Predicted and measured exhaust gas compositions at OCV and -0.25 A/cm^2 when operating at 850^{o}C and inlet gas compositions of 50% CO_2, 25% H_2 & 25% N_2 at 20 ml/min.....145

List of Figures

Figure 1–1: Global annual average temperatures measured over land and oceans indicating how the earth has warmed over the past 200 years (NOAA 2013) 2

Figure 1–2: Schematic diagram showing the production of fuel via high temperature co-reduction of CO_2 and H_2O in a SOE 4

Figure 1–3: Thermodynamics of water electrolysis 7

Figure 1–4: Thermodynamics of carbon dioxide electrolysis 8

Figure 1–5: Schematic diagram showing the principle of operation of SOEC 8

Figure 1–6: Diagram of active and inactive TPB sites in the cathode/electrolyte region [Acknowledgement: Dr Denis Cumming] 9

Figure 1–7: Schematic diagram of the proposed CO_2-recycled synthetic fuel production (Graves et al. 2010) 14

Figure 1–8: Estimate of synthetic fuel costs versus electricity price (Graves et al. 2010) 15

Figure 2–1: Current density vs voltage plot indicating the different overpotentials 20

Figure 2–2: Electrochemical Impedance Spectra measured at OCV and 850^oC of fuel electrode compositions 50% CO_2, 25% CO and 25% Ar (Green) and 50%CO_2, 25% H_2 and 25% Ar (Red) with pure oxygen flowing across the oxygen electrode (Ebbesen et al. 2012) 25

Figure 2–3: a) Illustration of basic equivalent circuits for an electrochemical system with one time constant showing a resistor (R1) in series with a parallel connection of a capacitor (C1) and resistor (R2). b) Nyquist plot of a one-time constant model simulated over the frequency range 10 kHz-0.01 Hz (R1 = 0.45 Ω, R2 = 0.4 Ω and C1 = 0.1 F). c) Bode plot of a one-time constant simulated over the same conditions above. 27

Figure 2–4: a) Illustration of basic equivalent circuits for an electrochemical system with one time constant showing a resistor (R1) in series with a parallel connection of a constant phase element (CPE1) and resistor (R2). b) Nyquist plot of a one-time constant model simulated over the frequency range 10 kHz-0.01 Hz (R1 = 0.45 Ω, R2 = 0.4 Ω, CPE1-T = 0.1 F and CPE1-P (α) = 0.85). c) Bode plot of a one-time constant simulated over the same conditions above 28

Figure 2–5: Working mechanisms of SOEC for co-electrolysis of H_2O and CO_2 (Ni 2011) 32

Figure 2–6: Effect of temperature on co-electrolysis of H_2O and CO_2. Figure A and B shows H_2 and CO fluxes at 873 and 1073 K respectively (Ni 2011) 33

Figure 2–7: Effect of varying cathode inlet gas compositions on co-electrolysis of H_2O and CO_2. Figure A shows H_2 and CO fluxes at case 2 49.7% H_2O, 0.3% H_2, 25% CO_2, 25% CO while Figure B shows H_2 and CO fluxes for case 3 at 25% H_2O, 25% H_2, 49.7% CO_2, 0.3% CO (Ni 2011) 34

Figure 2–8: Effect of temperature on co-electrolysis of H_2O and CO_2. Figure A and B show H_2 and CO fluxes at 1.0 and 1.3 V respectively (Ni 2011) 35

Figure 2–9: AC characterisation operated at 750 and 850^oC at varying CO_2, H_2O, CO_2/H_2O mixtures (Ebbesen et al. 2012) 36

Figure 2–10: DC characterisation operated at 750 and 850^oC at varying CO_2, H_2O, CO_2/H_2O mixtures (Ebbesen et al. 2012) 37

Figure 2–11: Durability test showing cell voltage at Ni-YSZ electrode during co-electrolysis (-0.25 A/cm^2, 45% H_2O-45% CO_2-10% H_2) operation before inlet gasses were cleaned (Ebbesen et al. 2010) 48

Figure 2–12: Durability test showing cell voltage at Ni-YSZ electrode during co-electrolysis (-0.25 A/cm^2, 45% H_2O-45% CO_2-10% H_2) operation after inlet gasses were cleaned (Ebbesen et al. 2010) 49

Figure 2–13: Thermodynamics of CO_2 electrolysis for carbon monoxide and carbon production 51

Figure 2–14: I-V curve recorded at 70% steam concentration and at 895^oC (Laguna-Bercero et al. 2011) 53

Figure 2–15: (a) represents the original cell, b) origin of degradation, c) cracking of the YSZ electrolyte and d) delamination of the electrode from the electrolyte (Laguna-Bercero et al. 2011) 54

Figure 3–1: Schematic diagram of the experimental setup for the production of syngas via the high temperature co-electrolysis of carbon dioxide and steam 56

Figure 3–2: Picture of high temperature electrolysis test facility 57

Figure 3–3: Schematics showing the 1.5 m heated stainless steel tube as a spiral tube 57

Figure 3–4: Front view design of the in-house cell rig design with dimensions in mm. 59

Figure 3–5: Expanded view of metal caps attached to the inlet and outlet tubes of the fuel electrode 60

Figure 3–6: Description of the key parts of the base unit (NorECs 2014) 61

Figure 3–7: Primary components of the cell rig 62

Figure 3–8: Schematic diagram showing the flow of gasses in and out of the cell rig 63
Figure 3–9: Procedure of cell loading during rig set-up 63
Figure 3–10: Picture of the corroded cell rig.....65
Figure 3–11: A) SEM image of the electrolyte supported cell and B) Top and bottom view of the electrolyte supported cell.....66
Figure 3–12: A) SEM image of the electrode supported cell and B) Top and bottom view of the cell.....67
Figure 3–13: Schematic diagram showing the process of steam production and measurement.....68
Figure 3–14: Steam content measured at varying water bath temperature between 30 – 75^{o}C when operating at a heat traced line temperature of 84^{o}C 69
Figure 3–15: Steam spikes observed water bath temperature of 75^{o}C, heat traced line at 84^{o}C when operating at a carrier gas flow rate of 50 ml/min 70
Figure 3–16: Steam content measured at varying water bath temperature between 30 – 75^{o}C when operating at a heat traced line temperature of 120^{o}C 71
Figure 3–17: Stability of the steam produced with and without the use of a heater.....72
Figure 3–18: Schematics of the heater sandwiched between 2 copper sheets.....73
Figure 3–19: Nyquist plot of oxygen and air measured at OCV, 850^{o}C and fuel electrode compositions 2% H_2O, 49% H_2 and 49% N_2 with pure oxygen flowed to the oxygen electrode when using an electrolyte supported cell.....75
Figure 3–20: Chromatogram showing the retention times of overlapped H_2 and O_2 peaks through a HP-PLOT Q column 77
Figure 3–21: Chromatogram showing the retention times of separated H_2 and O_2 peaks through a PLOT Q and molecular sieve column 77
Figure 3–22: Ohmic resistance of electrode and electrolyte supported SOCs operating at 850^{o}C and fuel electrode compositions 2% H_2O, 49% H_2 and 49% N_2 with synthetic air flowed to the oxygen electrode.....81
Figure 3–23: Ohmic resistance of electrode supported SOCs operating at 850^{o}C and fuel electrode compositions 2% H_2O, 49% H_2 and 49% N_2 with synthetic air flowed to the oxygen electrode 84
Figure 3–24: Nyquist plot of oxygen and air measured at OCV while operating at a temperature of 850^{o}C with cathode compositions of 70% N_2, 28% H_2 and ~2% H_2O 87

Figure 3–25: Difference plot of changes in impedance spectra at the oxygen electrode due to gas variations as described in Figure 3–24 88
Figure 3–26: Nyquist plot of 4.5 and 8.5% H_2O measured at OCV while operating at a temperature of 850^oC with oxygen electrode kept constant at 100% O_2 89
Figure 3–27: Difference plot of changes in impedance spectra at the fuel electrode due to gas variations as described in Figure 3–26 90
Figure 3–28: Illustration of the equivalent circuit model. A resistor (R1) in series with two parallel connection of constant phase elements (CPE1 and CPE2) and resistors (R2 and R3) 92
Figure 4–1: AC impedance spectra recorded at OCV under NiO reducing conditions 95
Figure 4–2: Bar chart showing the theoretical and measured OCV for CO_2 fuel electrode compositions shown in Table 4–1 97
Figure 4–3: DC characterisation measurement at 850^oC under different CO_2 partial pressures 99
Figure 4–4: Area specific resistance with increasing CO_2 partial pressure 100
Figure 4–5: AC impedance spectra recorded at OCV under different CO_2 partial pressures 100
Figure 4–6: Polarisation resistance across the oxygen and fuel electrode at varying CO_2 compositions 102
Figure 4–7: Open circuit voltage against time at 850^oC with 15% CO_2, 60% H_2 and 25% N_2 supplied to the fuel electrode using the aged cell 105
Figure 4–8: Open circuit voltage against time at 850^oC with 15% CO_2, 60% H_2 and 25% N_2 supplied to the fuel electrode using a fresh cell 105
Figure 4–9: Thermodynamic analysis of the Boudouard reaction as a function of temperature operating at 70% CO_2, 5% CO and 25% N_2 flowed to the fuel electrode 106
Figure 4–10: Thermodynamic analysis of the Boudouard reaction as a function of temperature operating at 15% CO_2, 60% CO and 25% N_2 flowed to the fuel electrode 107
Figure 4–11: Current efficiency when operating at a current density of -0.5 A/cm^2 110
Figure 4–12: Current efficiency when operating at a current density of -0.61 A/cm^2 110
Figure 4–13: Gas conversion of carbon monoxide produced at -0.5 and -0.61 A/cm^2 111
Figure 4–14: Cell voltage measured during CO_2 electrolysis with 50% CO_2 – 25% CO – 25% N_2 supplied to the fuel electrode, synthetic air supplied to the oxygen electrode at an operating temperature of 850^oC and a current density of -0.5 A/cm^2 113

Figure 4–15: Thermodynamic analysis of the Boudouard reaction as a function of temperature operating at 50% CO_2, 25% CO and 25% N_2 flowed to the fuel electrode.....115
Figure 4–16: AC impedance spectra recorded at 850^oC before and after durability study at -0.5 A/cm^2 (first measurement).....116
Figure 4–17: AC impedance spectra recorded at 850^oC before and after durability study at -0.5 A/cm^2 (second measurement).....117
Figure 5–1: AC impedance spectra recorded at OCV, 850^oC, fuel electrode gas compositions of 49% N_2, 49% H_2 and ~2% H_2O and synthetic air to the oxygen electrode 123
Figure 5–2: Schematic diagram showing a mass balance around the cell rig during the high temperature CO_2/H_2O co-electrolysis process 125
Figure 5–3: Open circuit voltage measured of varying CO_2/H_2O compositions at 850^oC when using an electrolyte supported cell 129
Figure 5–4: Open circuit voltage measured of varying CO_2/H_2O compositions at 850^oC when using an electrode supported cell 129
Figure 5–5: Open circuit voltage measured of varying CO_2/H_2O compositions at 850^oC when using an electrode supported cell with platinum paste added to the fuel electrode.....130
Figure 5–6: DC characterisation measurement at 850^oC under varying mixtures of CO_2/H_2 132
Figure 5–7: DC characterisation measurement at 850^oC and 50% CO_2, 25% H_2 and 25% N_2 (4b3) when using a new and aged cell.....133
Figure 5–8: Simultaneous DC measurements at 850^oC and fuel electrode compositions of 50% CO_2, 25% H_2 and 25% N_2 (4b3) when using a new cell.....134
Figure 5–9: Area specific resistance with increasing CO_2/H_2O compositions 135
Figure 5–10: AC impedance measurement recorded at OCV under different CO_2/H_2 compositions.....136
Figure 5–11: Polarisation resistance at the fuel electrode during CO_2 electrolysis and CO_2/H_2O co-electrolysis between 0.65 and 0.1 Hz 138
Figure 5–12: Cell voltage measured during CO_2/H_2O co-electrolysis at -0.5 A/cm^2 and 850^oC 139
Figure 5–13: AC impedance spectra at 850^oC before and after durability study at -0.5 A/cm^2 141

Figure 5–14: Graph showing the mol. composition of syngas produced at OCV, -0.25, -0.4 and -0.5 A/cm^2 144

List of Abbreviations

AC	Alternating current
ADIS	Analysis of difference in impedance spectra
ASR	Area specific resistance
CCS	Carbon capture and storage
CDU	Carbon dioxide utilisation
DC	Direct current
EIS	Electrochemical impedance spectroscopy
EDX	Energy-dispersive X-ray spectroscopy
FTS	Fischer-Tropsch synthesis
GC	Gas Chromatograph
GDC	Gadolinium doped ceria
GHG	Greenhouse gas
IS	Impedance spectra
i-V	Polarisation curve
LSM	Lanthanum Strontium Manganate
MIEC	Mixed ionic and electronic conductor
NiO	Nickel oxide
OCV	Open circuit voltage
R_{ohm}	Ohmic resistance
R_P	Polarisation resistance
R_T	Total resistance
rWGSR	Reverse water gas shift reaction
SEM	Scanning electron microscope
SOC	Solid oxide cell
SOE	Solid oxide electrolyser
SOEC	Solid oxide electrolysis cell
SOFC	Solid oxide fuel cell
TPB	Triple phase boundary
YSZ	Yttria stabilised zirconia
Z	Impedance
Z”	Imaginary part of the impedance
Z’	Real part of the impedance

Chapter 1

1. Introduction

The combustion of fossil fuels produces carbon dioxide, a greenhouse gas (GHG), generally believed to be the major cause of climate change. Recent investigations have sought to recycle and utilise this greenhouse gas to produce valuable products – carbon dioxide utilisation (CDU). The high temperature co-reduction of CO_2 and H_2O in a solid oxide electrolyser (SOE) is a promising and efficient pathway towards CO_2 utilisation. Synthesis gas (syngas), primarily consisting of hydrogen and carbon monoxide, is produced during this process. This fuel gas mixture is extremely valuable as it can be converted into liquid fuel via chemical reactions, such as Fischer-Tropsch Synthesis (FTS). This work concentrates on characterisation of the co-reduction of CO_2 and H_2O in a Solid Oxide Electrolysis Cell (SOEC), with a view to improving the process.

1.1 Background

Carbon dioxide (CO_2), a greenhouse gas, is produced mainly from the combustion of fossil fuels and is considered to be a major cause of climate change (IPCC 2007). Fossil fuels are widely available and their use currently represents approximately 85% of total world energy (IEA 2013). With new reserves continuously being discovered, and the price of renewable energy being substantially higher in comparison, it has been predicted that fossil fuels will continue to provide 80 - 85% of the world energy consumption at least until 2030 (Plasseraud 2010).

Monitoring of CO_2 levels has been ongoing since the industrial revolution when the atmospheric concentration was measured to be around 280 ppm (Butler and Montzka 2013; IPCC 2007; NRC. 2010). Today, this value is significantly higher at ~400 ppm due to man-made CO_2, largely arising from fossil fuel consumption (NOAA 2014). The most recent report from the Intergovernmental Panel on Climate Change (IPCC) presents further evidence of this occurrence (IPCC 2013). The report concludes that 'scientists are 95% certain that humans are the dominant cause of global warming since the 1950s'. Figure 1–1 shows the increase in global surface temperatures and the rise in atmospheric CO_2 concentration over the last 200 years (NOAA 2013).

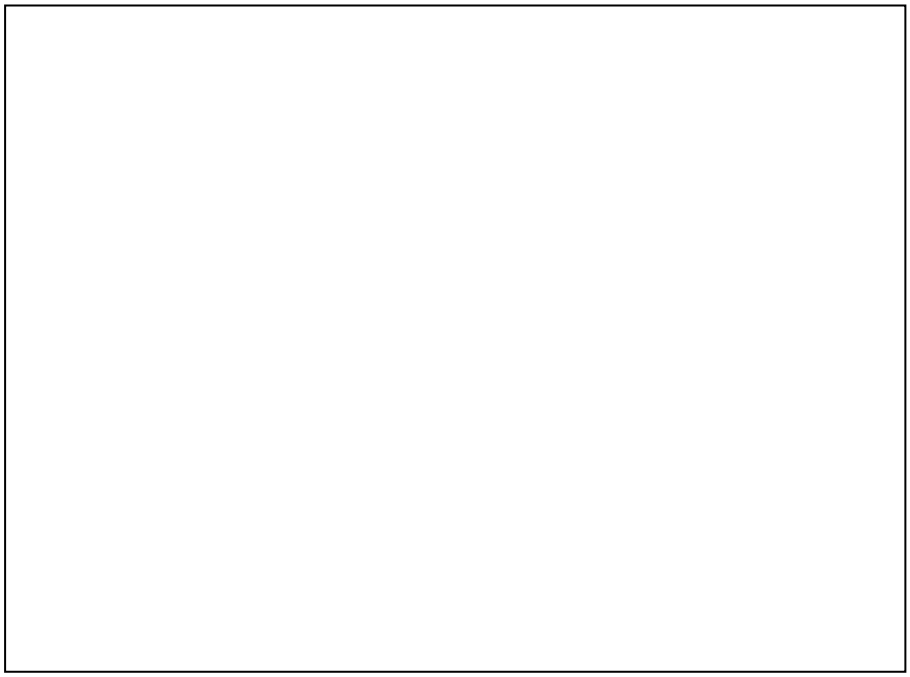

Figure 1–1: Global annual average temperatures measured over land and oceans indicating how the earth has warmed over the past 200 years (NOAA 2013)

As a result of this environmental issue, significant research into the use of low carbon energy options such as wind (Åžahin 2004; Jay 2011), biofuel (Demibras 2009; Lin et al. 2011), solar (Mekhilef et al. 2011), hydropower (Huber 2004), geothermal (Chamorro et al. 2012), nuclear energy (Forsberg 2009) and carbon capture and storage (CCS) (Leung et al. 2014) have been conducted. Amongst these low carbon options, fossil fuels coupled with CCS is currently the only technology with the potential to significantly reduce greenhouse emissions while allowing energy needs to be met securely and affordably in developed countries such as UK, USA etc. (Davey 2012). Some of the current issues with CCS includes high investment costs and variable operating costs particularly regarding transportation, storage uncertainty and safety concerns (International Energy Agency 2010; Pires et al. 2011; Rai et al. 2010; Styring et al. 2011).

However, because of the potential of this technology to significantly reduce GHG emissions and the substantially higher renewable energy prices, there is a significant investment within this area with an aim to improve plant efficiency and reduce overall costs. The UK, for example, is heavily relying on the successful implementation of this technology in order to achieve its emission targets of 80% GHG reduction below base levels of year 1990 by 2050. This is evidenced in its £1 billion investment in the “White rose” and “Peterhead” carbon capture and storage projects (DECC 2014).

1.1.1 Carbon dioxide Utilisation

Carbon dioxide utilisation (CDU) is an emerging pathway to reduce CO_2 emissions. CDU involves recycling the captured gas and converting this “negative feedstock” into a valuable chemical. The conversion of CO_2 into valuable chemicals is a mature process which has been on-going for many years (Graves et al. 2010). However the large scale utilisation of carbon dioxide as a chemical feedstock is currently limited to a few processes (synthesis of urea, salicylic acid, and polycarbonates). Quadrelli et al. (2011) reviews some potential industrial applications available for recycling CO_2 and also presents some major R&D technical challenges towards achieving a valuable end product. Although the majority of these investigations are still at a research level, their long term potential is promising.

Graves et al. (2010) review a number of processes that have been previously investigated in converting CO_2 to hydrocarbon fuel. A few of these processes, with the availability of H_2,

directly produce hydrocarbons for example catalytic hydrogenation of CO_2 to produce methanol. However, in most cases, a two-step process is employed with syngas produced initially, followed by FTS to convert the syngas to longer chain hydrocarbons.

The production of syngas will not be sustainably viable in principle if hydrogen is produced from fossil fuel sources. Therefore, a cleaner hydrogen production source (such as electrolysis of water from renewable or nuclear energy) is needed to produce syngas with a lower carbon footprint. The process of syngas production described in this thesis involves the high temperature co-reduction of CO_2 and H_2O in a SOC. Desired H_2/CO ratios in syngas vary from ~ 1.4 to 2.1 to provide a useful feed for FTS (Kim et al. 2009).

1.2 High Temperature Co-electrolysis of Steam and Carbon dioxide in a SOE

The high temperature co-reduction of CO_2 and H_2O in a SOE has the potential to produce an overall carbon neutral synthetic fuel if nuclear or renewable sources are used (heat & electricity) as shown in Figure 1–2.

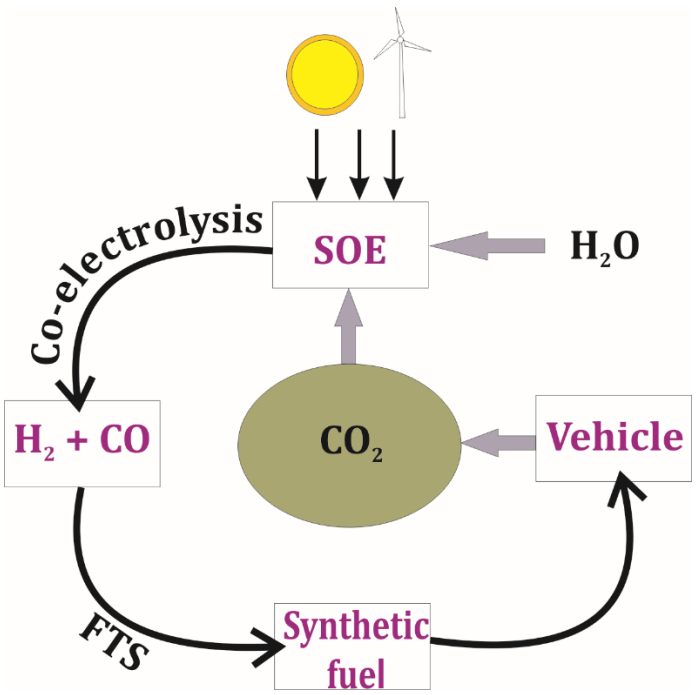

Figure 1–2: Schematic diagram showing the production of fuel via high temperature co-reduction of CO_2 and H_2O in a SOE

1.2.1 Solid Oxide Electrolysis Cells

A solid oxide cell (SOC) is made up of an oxygen-ion conducting electrolyte sandwiched between two electrodes (cathode and anode). They operate at high temperatures (750 – 1000^{o}C) to ensure oxygen ions are effectively transported from one electrode to the other. A SOEC is an electrochemical device that converts electric and thermal energy into chemical energy stored in a fuel. The operating principle of a SOEC works in a reverse mode to a solid oxide fuel cell (SOFC).

The history of SOCs dates back to early 1900 when a German physical chemist, Walther Nernst, developed a high temperature electrolyte material ZrO_2 (zirconium oxide) with 15% Y_2O_3 (yttrium oxide). This formed the basis for both solid oxide fuel and electrolysis cell operation with ZrO_2 evolving to be the most commonly used electrolyte material. In the late 1960s, electrolysis of H_2O, CO_2 and H_2O/CO_2 mixtures in SOCs was first demonstrated by NASA for purpose of O_2 production for life supports and propulsion in submarines and spacecraft (Elikan and Morris 1969; Elikan et al. 1972; Weissbart and Smart 1967). However, it wasn't until the early 1980's when a great deal of attention was brought to this research area (Donitz et al. 1980). During this period, Dönitz and Erdle (1985) reported the first SOEC results within the HOT Elly project from Dornier System GmbH using electrolyte supported tubular SOECs. When operating at a current density of -0.3 A/cm^2, Dönitz and Erdle (1985) reported a faraday efficiency (See Section 1.3.2.1) of 100% at 1.07 V.

The use of SOCs for electrolysis investigations has focused predominantly on water reduction for hydrogen production and in recent years there has been a huge advancement in this research area (Jensen et al. 2007a; Laguna-Bercero 2012; Ni et al. 2008; Ursua et al. 2012). More recent investigations have also shown the feasibility of SOEs to effectively simultaneously reduce CO_2 and H_2O (Ebbesen et al. 2010; Ebbesen et al. 2009; Ebbesen et al. 2011; Ebbesen et al. 2012; Graves et al. 2011; Graves et al. 2010; Jensen et al. 2010; Kim-Lohsoontorn and Bae 2010; Kim-Lohsoontorn et al. 2011; O'Brien et al. 2009; Stoots et al. 2007; Zhan et al. 2009). The electrochemical reduction of CO_2 in SOEs has also been explored by other authors (Ebbesen et al. 2012; Ebbesen and Mogensen 2009; Zhan et al. 2009; Zhan and Zhao 2010).

1.2.2 Introduction to High Temperature CO_2/H_2O Co-electrolysis

The total cell reaction during the high temperature co-electrolysis of CO_2 and H_2O is given in Equation 1.

$$CO_2 + H_2O \xrightarrow[Electricity]{Heat} CO + H_2 + O_2 \quad (1)$$

The three reactions that take place during high temperature co-electrolysis of CO_2 and H_2O in a SOEC are steam electrolysis, carbon dioxide electrolysis and the reverse water gas shift reaction (rWGSR) as shown in Equations 2, 3 & 4 respectively. The proportions of each reaction in the contribution to H_2/CO production depend on the cell materials, cell morphology, operating temperature, inlet gas compositions and operating voltages. The reverse water gas shift reaction is a heterogeneous catalytic reaction which is catalysed by metal catalysts (such as nickel which is commonly found in fuel side electrodes of a SOEC). The rWGSR is a kinetically fast equilibrium reaction at high temperatures.

$$H_2O \rightarrow H_2 + \frac{1}{2}O_2 \qquad \Delta H_{298K} = 286\ \mathrm{kJ/mol} \quad (2)$$

$$CO_2 \rightarrow CO + \frac{1}{2}O_2 \qquad \Delta H_{298K} = 283\ \mathrm{kJ/mol} \quad (3)$$

$$H_2 + CO_2 \rightleftharpoons H_2O + CO \qquad \Delta H_{298K} = +41\ \mathrm{kJ/mol} \quad (4)$$

It was previously suggested by Stoots et al. (2008) that steam electrolysis and the rWGSR were the only reactions which took place within this process; the hydrogen produced from steam electrolysis was thought to reduce CO_2 to CO via the rWGSR when operating at 850°C. The rWGSR is favoured at high temperatures above 816°C. More recent investigations by Ni (2011) and Ebbesen et al. (2012) have argued that all three reactions occur during co-electrolysis. The H_2O/CO_2 co-electrolysis reaction mechanism is still not yet fully understood and it is the aim of this work to further understanding of this process. Section 2.4 gives a detailed review of current understanding of the co-electrolysis reaction mechanism.

Thermodynamics

The total energy required for a reaction at constant temperature and pressure is determined by the process enthalpy change (ΔH). The minimum electrical energy supply required for the electrolysis process is equal to the change in the Gibbs free energy (ΔG):

$$\Delta G = \Delta H - T\Delta S \quad 5$$

where TΔS represents the thermal energy supply, T is the operating temperature and ΔS is the entropy change.

Figure 1–3 and Figure 1–4 show the energy demand for water and carbon dioxide electrolysis respectively against temperature. The energy demands were calculated using the thermodynamic properties from process simulation software HSC Chemistry 5.11 and Equation 5. As previously indicated, SOECs operate between 700 – 1000°C. One of the key advantages of operating at higher temperatures as shown in Figure 1–3 and Figure 1–4 is that the required electrical energy (ΔG) considerably decreases with an increase in temperature.

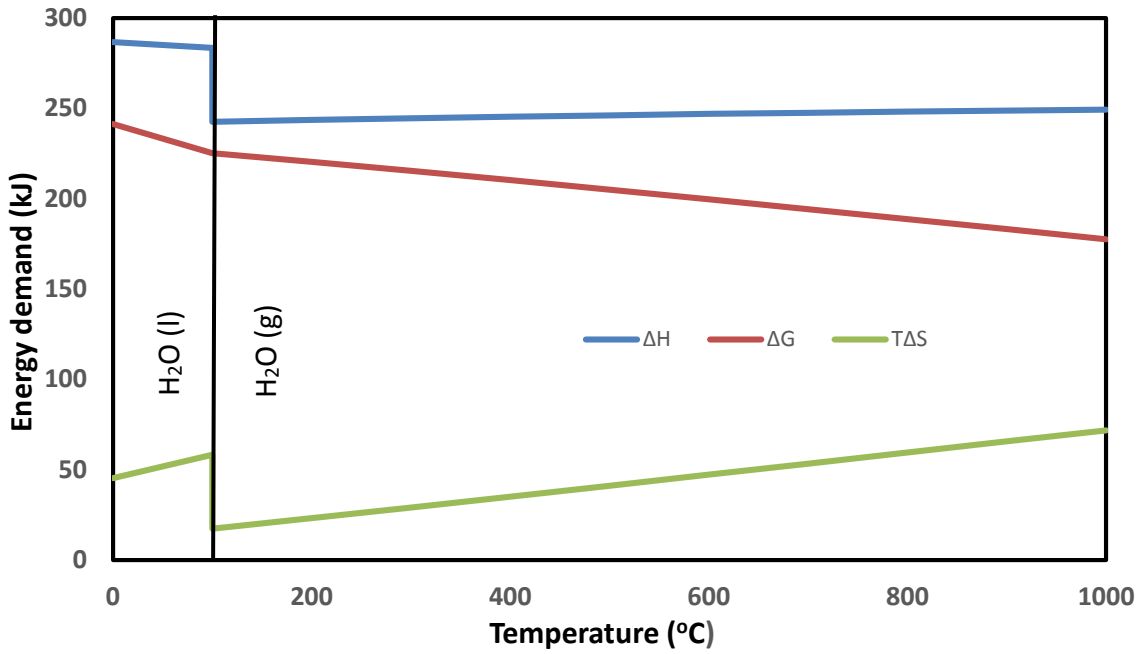

Figure 1–3: Thermodynamics of water electrolysis

Where ΔH, ΔG and TΔS are the total, electrical and thermal energy demand

The enthalpy of the reaction for water splitting as shown in Figure 1–3 sharply drops at 100°C due to the phase change from water to steam.

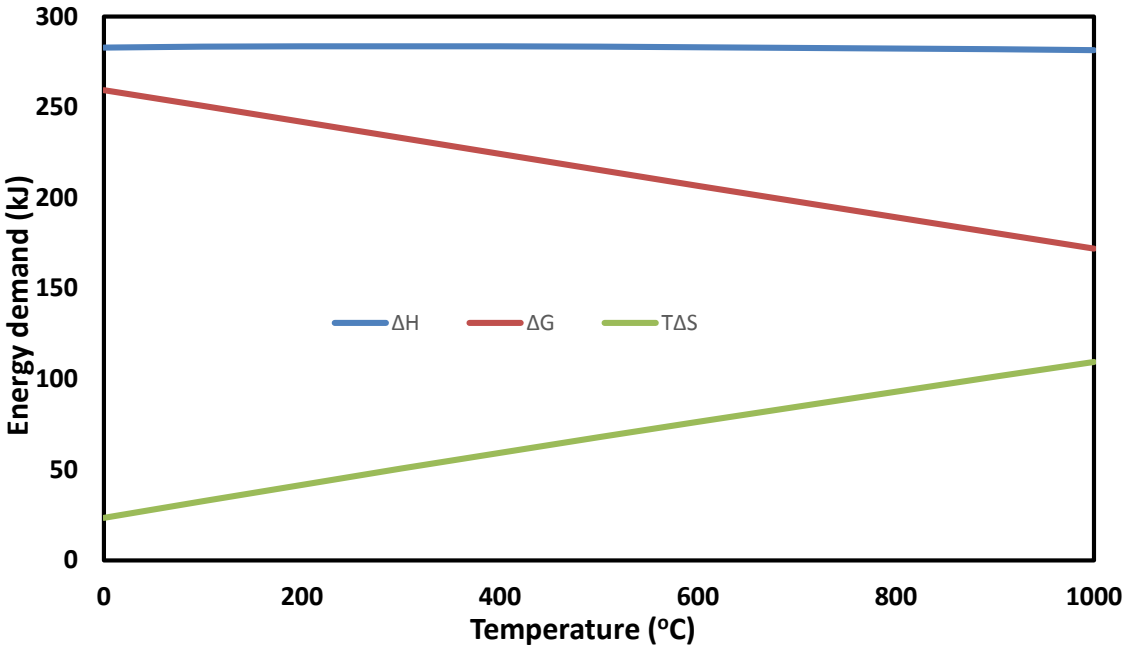

Figure 1–4: Thermodynamics of carbon dioxide electrolysis

1.2.3 Operating Principle of SOECs under CO_2/H_2O conditions

The principle of operation of a SOEC operating under reducing CO_2/H_2O conditions as shown in Figure 1–5 is described below.

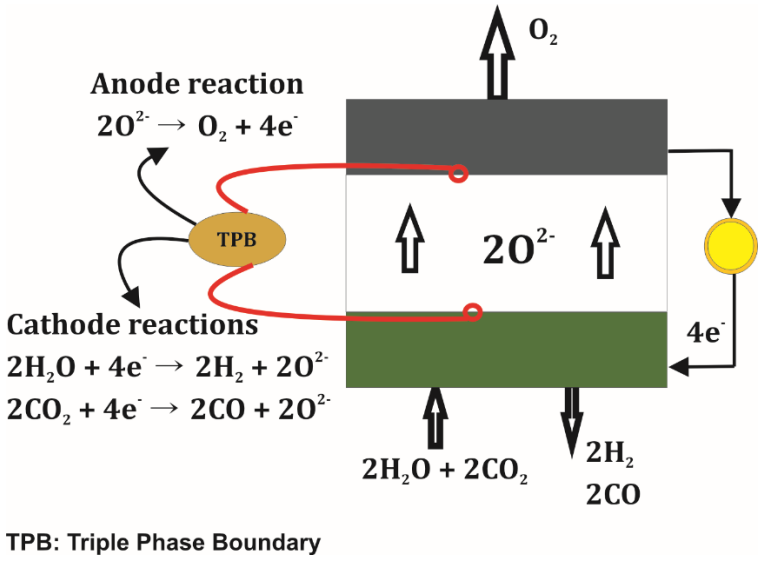

Figure 1–5: Schematic diagram showing the principle of operation of SOEC

- The triple phase boundary (TPB) is the region where the gas, electrode and electrolyte meet. It consists of active and inactive sites as shown in Figure 1–6 with the electrochemical reactions occurring at the active TPB.
- The feed gasses flow through the porous cathode and to the TPB of the cathode-electrolyte region. The cold inlet gas compositions differ from the hot inlet equilibrium gas compositions at the fuel electrode in the presence of a metal catalyst as a result of the rWGSR/WGSR equilibrium.
- Thermal energy, in addition to the electrical energy supplied is then used to split the gasses at the active TPB sites. The electrolysis products and the unreacted feed gasses then flow outwards through the cathode.
- Oxide ions produced from the dissociation process are transported through the electrolyte to the TPB of the anode/electrolyte layer. At the anode TPB, oxide ions recombine, forming oxygen gas which flows outwards through the anode.

Figure 1–6 is an illustration of the TPB at the fuel electrode of a SOEC. In this diagram, Nickel-yttria stabilised zirconia (Ni-YSZ) is the chosen cathode material and used to describe the important features within the cell. Ni-YSZ is used in this illustration because it is the most commonly used cathode material in SOEC applications, with YSZ used as the electrolyte and LSM-YSZ (Lanthanum Strontium Manganite) as the oxygen electrode.

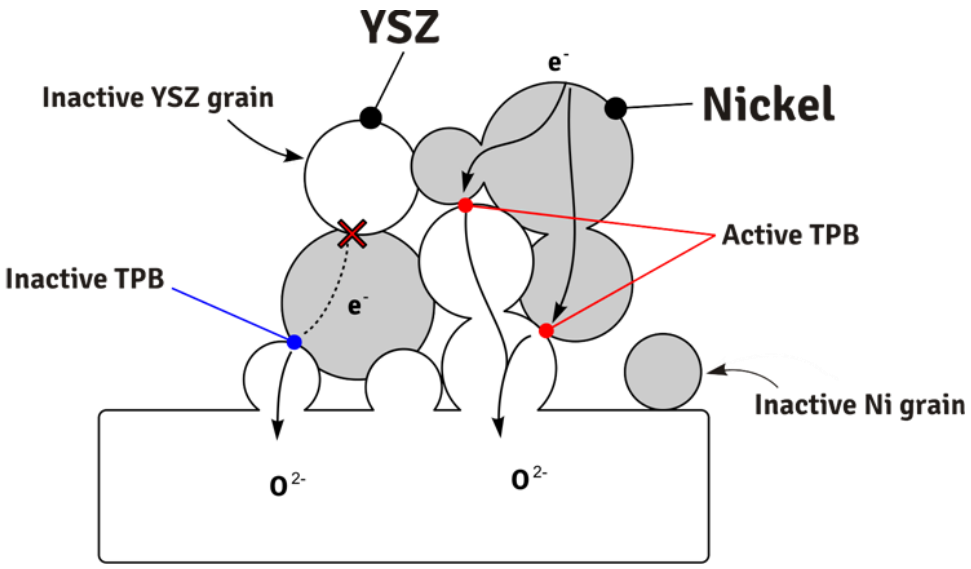

Figure 1–6: Diagram of active and inactive TPB sites in the cathode/electrolyte region [Acknowledgement: Dr Denis Cumming]

It is generally thought that the electrochemical reactions occur closest to the electrolyte (i.e. the active TPB sites are located approximately 10 µm from the electrolyte into the electrode) (Brown et al. 2000; Gorte and Vohs 2003; McIntosh and Gorte 2004). An increase in the reaction sites (i.e. active TPB length) is an important part of developing this technology as this further promotes the electron transfer reaction which in turn increases the performance of the SOC.

1.3 Operation and Electrolysis efficiency of SOECs

1.3.1 Open Circuit Voltage and Nernst Potential

The open circuit voltage (OCV) is the voltage when there is no flow of current across the cell. This voltage can be measured or calculated using the equilibrium Nernst Equation for the electrochemical reaction. As seen in Equation 6, the Nernst potential is calculated using the partial pressure of the chemical species at the cathode and partial pressure of oxygen at the anode and is also dependent on the operating temperature of the cell. In this study, the ΔG values as a function of temperature were calculated using the thermodynamic properties from process simulation HSC Chemistry 5.11.

$$\boldsymbol{E} = \frac{\Delta G_{H_2O}(T)}{2F} + \frac{RT}{4F} ln\left(\frac{P_{H2}^2 \, x \, P_{O2}}{P_{H2O}^2}\right)$$

$$= \frac{\Delta G_{CO_2}(T)}{2F} + \frac{RT}{4F} ln\left(\frac{P_{CO}^2 \, x \, P_{O2}}{P_{CO2}^2}\right) \qquad 6$$

Where E = Nernst potential, R = Gas rate constant (8.314 J/K mol), T = Temperature (K) and F = Faraday's constant (C/mol)

Note: During CO_2/H_2O co-reduction using a NiO fuel electrode, the chemical species at the fuel electrode used in calculating the Nernst potential is the hot equilibrium inlet compositions and not the cold inlet gas compositions. This is due to the equilibrium reaction which occurs in the bulk of the fuel electrode before electrolytic co-reduction of H_2O and/or CO_2.

The partial pressures at the hot equilibrium inlet compositions need to be taken into account when calculating the co-electrolysis Nernst potential. McKellar et al. (2010) at the Idaho National Laboratory (INL) fully describe a chemical equilibrium model in determining the hot inlet compositions at the cathode surface. Once the equilibrium compositions are

determined, the Nernst potential can be calculated from either the steam or CO_2 parameters in Equation 6.

The Nernst potential and the measured OCV are identical under ideal conditions. However, as a general rule, a measured OCV more than 3 mV below the Nernst potential for a predominantly ionic electrolyte material such as YSZ indicates leakages around the cell. Gaseous partial pressure differences (indicating a leak) are the most likely reason for a much higher change in the difference between the experimental and theoretical value. Issues associated with electronic current leakages are typical in electrolyte materials with mixed ionic and electronic conductivity for example ceria based materials such as gadolinium doped ceria (GDC). These electrolyte materials usually have an OCV much lower than the corresponding Nernst potential under reducing conditions due to their higher electronic conducting properties arising from the partial reduction of Ce^{4+} to Ce^{3+}at reducing atmospheres. A typical example can be seen in an investigation carried out by Kim-Lohsoontorn et al. (2011) under compositions 50% H_2O and 50% H_2 operating at 850°C. Kim-Lohsoontorn et al. (2011) found the OCV of cells with the following materials Ni-GDC/YSZ/LSM-YSZ, Ni-GDC/GDC/LSM-YSZ and Ni-GDC/YSZ/GDC/LSM-YSZ to be 0.88, 0.68 and 0.80 V respectively. In the third case of a bi-layered electrolyte (Ni-GDC/YSZ/GDC/LSM-YSZ) an OCV of 0.80 V was achieved as the YSZ layer was added in-between the Ni-YSZ electrode and the GDC electrolyte to block off any electronic short circuit in the cell.

1.3.2 Electrolysis Efficiency

1.3.2.1 Faraday Efficiency

For H_2O electrolysis, the H_2 production rate in an ideal electrolysis cell is directly proportional to the quantity of electric charge through the cell according to Faraday's law. The Faraday efficiency (η_F), also known as the current efficiency, is the ratio of the real electric charge consumed to the theoretical electric charge required for the production of a given amount of H_2. The H_2 production rate in ml/min can be expressed as

$$Q\ (ml/min)_{H_2\ Prod} = \frac{I}{zF} \times 60 \times \frac{10^6}{\rho_M} \qquad 7$$

Where Q is H_2 production rate (ml/min), I is the total cell current, z is the number of electron moles and ρ_M is the standard state molar density in mol/m^3

Equation 7 can also be applied in the case of CO_2 electrolysis for CO production. However, in the case of the high temperature CO_2/H_2O co-electrolysis in a SOEC, determining the faradaic efficiency for the amount of H_2 and CO produced is more complicated. This is because the co-electrolysis reaction mechanism is still not yet fully understood and therefore it is difficult to quantify the electric charge from the total applied current supplied for individual CO_2 and H_2O splitting.

1.3.2.2 Electrical Conversion Efficiency

Electrical conversion efficiency is defined as the ratio of the thermoneutral voltage (V_{tn}) to the operating voltage as seen in Equation 8.

$$\eta_{ef} = \frac{V_{tn}}{V} \quad 8$$

Where V is the cell voltage and η_{ef} is the electrical conversion efficiency

The thermoneutral voltage, described in Equation 9, is defined as the potential at which the generated Joule heat in the electrolysis cell and the heat consumption for the electrolysis reaction are equal:

$$V_{tn} = \frac{\Delta H_f}{zF} \quad 9$$

where ΔH_f is the total energy demand for the electrolysis reaction

At the typical SOEC operating temperature of ~850^{o}C, the co-electrolysis thermoneutral voltage is 1.346 V (between the V_{tn} of steam and carbon dioxide at 1.288 and 1.462 V respectively). The thermoneutral voltages of steam and carbon dioxide are calculated using Equation 9 and the data presented in Figure 1–3 and Figure 1–4. Operating above the thermoneutral voltage would result in theoretical electrical efficiencies below 100% and vice versa if operated below this point. Most solid oxide electrolysers operate above the thermoneutral voltage to accommodate any heat losses. In addition, higher current densities can be obtained and therefore increased syngas production rates. This is particularly interesting in cases where excess energy from sources such as wind farms and solar power are available.

1.4 Economics and Performance of SOEs under H_2O/CO_2 conditions

The commercial feasibility of a SOE to produce syngas competitively for liquid fuel production has been shown to be highly dependent on the resistance of the cell and the cost of electricity. To maximise efficiency and minimise capital costs, it is vital that operating cells are designed to produce the least possible resistance at start up (i.e. low initial stack area specific resistance) and stay unchanged over long periods of operation (i.e. low degradation rate). The area specific resistance (ASR) represents the net effect of all loss mechanisms in the cell.

Advanced manufacturing processes, improved design and selection of better suited materials all play an important role in the makeup of a cell with low resistance (Badwall 2001; Laguna-Bercero 2012; Minh 2004; Sun and Stimming 2007). Furthermore, cells have to be managed and optimised such that they are not adversely affected by their operating conditions (temperature, gas flow conditions, operating voltage) over long periods of operation. Stability of SOECs is discussed in Section 2.6.

To assess the economic performance of the process shown in Figure 1–7, the cost of petrol from conventional fossil fuel sources was compared to the cost when synthetic petrol is produced through the combination of the high temperature co-reduction of steam and carbon dioxide in a SOE (for syngas production) and FTS (to convert the syngas into synthetic fuel) (Graves et al. 2010). Using the schematic flow diagram in Figure 1–7 and information stated in

Table 1–1 and Table 1–2; Graves et al. (2010) calculated the cost of fuel produced relative to various electricity prices and advanced electrolyser operating conditions. These two factors were found to be critical in determining the commercial feasibility of this process as shown in Figure 1–8. An energy balance for the process shown in Figure 1–7 was carried out and energy requirements were used to estimate the costs of various processes shown in Table 1–1.

.

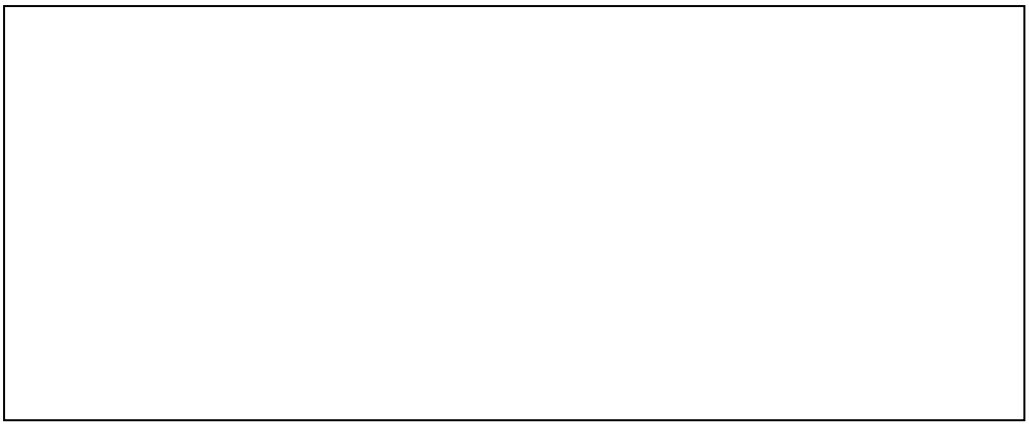

Figure 1–7: Schematic diagram of the proposed CO_2-recycled synthetic fuel production (Graves et al. 2010)

Where HX represents heat exchanger, Q_{th} is the thermal energy and Q_{el} is the electrical energy

Table 1–1: Assumptions for cost estimate (Graves et al. 2010)

Cost of CO_2 capture	\$30/tCO_2. Broken down as 0.32 kWh/kg CO_2 electricity costs and \$15/tCO_2 capital based cost
Cost of H_2O	\$1 m^{-3}
Cost of fuel synthesis	\$1.50/Gj Fischer-Tropsch petrol or diesel from syngas
Cost of dissociation	
Operating temperature	850^oC
Electrolysis cell stack	\$2000 m^{-2} investment including financing
Stack life	5 years
Balance of system	\$5000 m^{-2} investment including financing
Balance of system life	20 years
Initial current density	-0.50 A/cm^2
Initial stack ASR	0.30 Ω cm^2
Average degradation rate	0.006 mΩ cm^2/h
Capacity factor	100% = 1 – intermittency
Operation and Maintenance	\$ 0.5/Gj fuel

Note: The assumptions made on processes such as the degradation rate, cost of fuel synthesis, etc. were based on the state of art electrolyser and FTS performances at best.

Table 1–2: Status of SOEC capabilities and base case economic estimation

	Current density (A/cm^2)	**Initial ASR ($\Omega\ cm^2$)**	**Degradation ($m\Omega\ cm^2/h$)**	**Ref**
Economic estimation for Fig. 7c & 7d	-2	0.30	~0.018	(Graves et al. 2010)
Current state of the art technology	-0.75	0.58	No degradation observed	(Ebbesen et al. 2011)
Degradation issue and future consideration	> -1		Delamination of oxygen electrode from electrolyte over 10mins. of operation (Long term stability of SOEs still a major issue, particularly anode degradation at high current densities.)	(Laguna-Bercero et al. 2011)

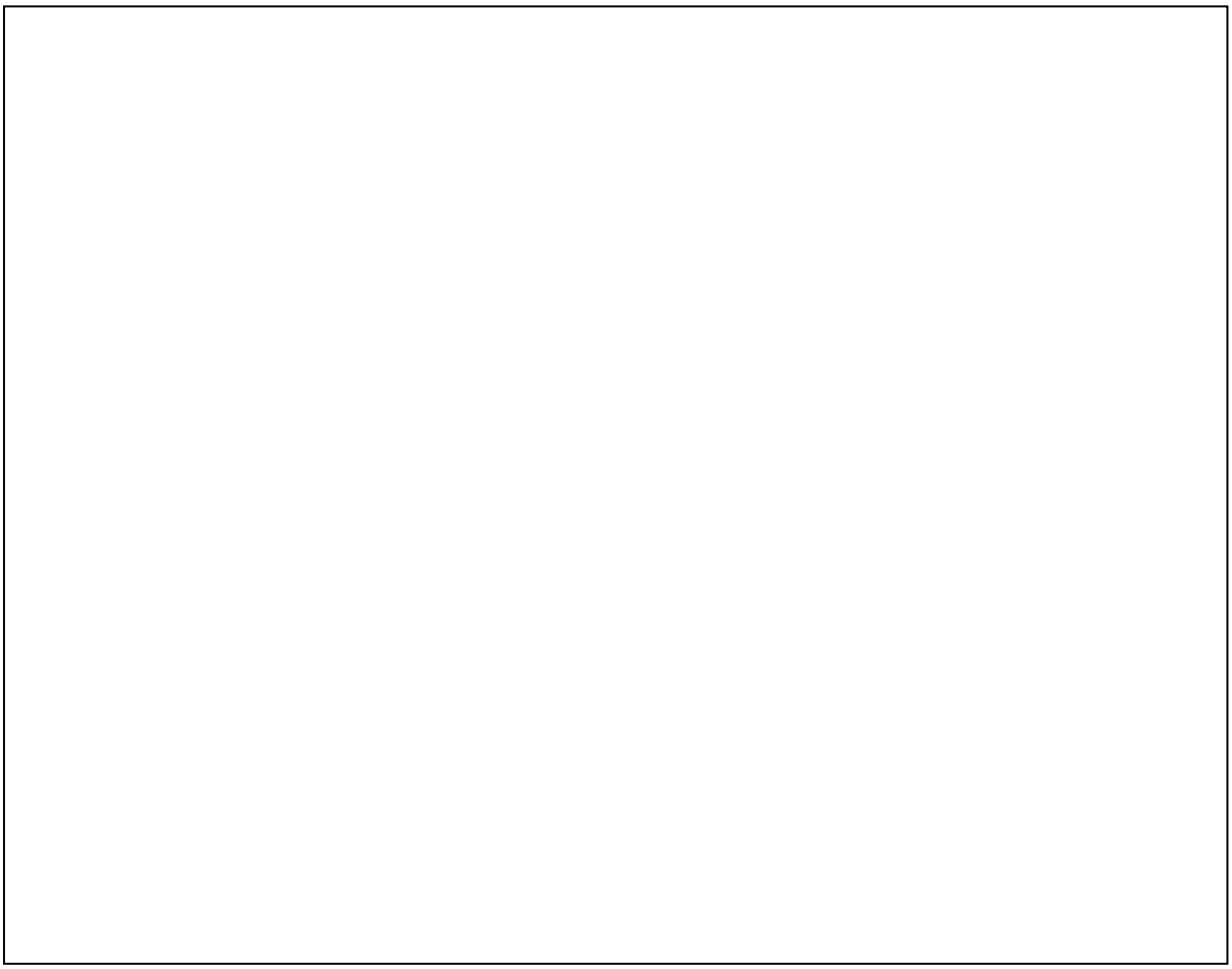

Figure 1–8: Estimate of synthetic fuel costs versus electricity price (Graves et al. 2010)

Figure 1–8a shows that using the information presented in Table 1–1, synthetic fuel can be produced at a price close to the then wholesale gasoline price ($2/gal) if electricity costs $0.02/kWh. However, the average wholesale price of electricity is around 4 – 5 U.S. cents/kWh. Figure 1–8b shows an instance when the cell is driven solely by solar energy i.e. the sensitivity of intermittent operation to electrolysers. In this case, it has been assumed that production can only be carried out 20% of the time. To therefore accommodate for this decrease, an increase in capacity costs by a factor of 5 is needed. Figure 1–8c shows a scenario of constant operation if the electrolysis stack is assumed to operate at the optimum conditions shown in Table 1–2. From this data, it has been shown that an increase in fuel prices to $3/gal, for example, would significantly improve the commercial competitiveness of this technology.

The production of synthetic fuels would be commercially competitive if cell stacks could be run at -2 A/cm^2, the approximate full current density attainable at 1.45 V (~93% electrical conversion efficiency), with a degradation rate of ~0.018 mΩ cm^2/h. However, a huge technological advancement is still needed particularly in eliminating the issues of cell failure at high current density discussed in Section 2.6.2.2.

1.5 Aims of this Work

The main aims of this PhD project are to:

- Analyse and compare the electrochemical performances of CO_2 electrolysis and co-electrolysis of H_2O/CO_2 by measuring the cell resistances through AC and DC characterisation, with a view to improving the co-electrolysis process. These electrochemical measurements are useful in determining the processes that contribute to the resistances during cell operation.
- Investigate the co-electrolysis reaction mechanisms. This is carried out by comparing the amount of hydrogen and carbon monoxide produced at varying current densities using gas chromatography with an aim to understand the effect of the co-electrolysis reactions on the amount of syngas produced.

1.6 Layout of Thesis

Chapter 2 reviews current understanding into the co-electrolysis reaction mechanism, development of SOE materials and degradation of electrolysers at low and high current densities. In Chapter 3, the experimental methods and design of the test facility are described, while chapter 4 discusses the performance of an electrolyser operating under varying compositions of CO_2. Chapter 5 discusses the performance of the electrolyser under CO_2/H_2O compositions and compares with that for CO_2 electrolysis discussed in Chapter 4. Furthermore, the durability of the electrolyser is investigated over short periods during CO_2/H_2O co-electrolysis at a current density of -0.5 A/cm^2 and compared with that CO_2 electrolysis. Chapter 6 discusses the overall thesis conclusions drawn from each chapter and future work for this research while Chapter 7 details the references cited.

Chapter 2

2. Status of the High Temperature Co-electrolysis of Steam and Carbon dioxide in SOEs

This Chapter provides a detailed review into the state-of-art of the high temperature co-reduction of CO_2 & H_2O in SOEs. It covers the recent developments into understanding the co-electrolysis reaction mechanisms. Furthermore, the need for materials specific to co-electrolysis purposes is highlighted. The challenges that arise, and potential solutions in achieving a highly durable SOEC with little /no degradation at low and high current densities (≥-0.75 A/cm^2) are also discussed.

2.1 Polarisation Losses and SOEC Performance

When a direct current is supplied to a SOEC, electric charge flows through the cathode to the TPB where a reduction process occurs. As a result of the applied current, the cell voltage increases with respect to the open circuit voltage (V_{OCV}). This increase is known as an overvoltage. Overvoltage, also known as Polarisation, arises as a result of cell resistance from defects in the microstructure of the cell, imperfections in materials, cell design, and the applied current.

The cell potential (V_{cell}), is a function of the parameters that affect SOEC performance and can be expressed as;

$$\mathrm{V}_{cell} = \mathrm{V}_{ocv} + \eta_{ohm} + \eta_{act} + \eta_{con} \quad 10$$

Where V_{ocv} is the open circuit voltage; the total polarisation comprises of $\eta_{ohm,}$ (the ohmic losses), $\eta_{act,}$ (the activation polarisation) and $\eta_{con,}$ (concentration polarisation). These polarisations are briefly described below.

2.1.1 Ohmic Loss

The ohmic loss of a cell, $\eta_{\mathrm{ohm},}$ is caused by contact resistance of all cell layers i.e. electrodes, current collectors and interconnections, electronic resistance in the electrodes and ionic resistance of the electrolyte. The increase in voltage mainly originates from resistive losses in the electrolyte because the ionic resistivity of the electrolyte is much greater than the electronic resistance in the electrodes. Temperature, cell configuration, electrolyte thickness and microstructure all play an important role in decreasing the ohmic loss of a cell. Electrode supported cells are therefore generally preferable in SOC operation over electrolyte supported cells due to their thinner electrolyte thus leading to lower ohmic resistance. Ohmic loss is directly proportional to the applied current through the system as seen in Equation 11;

$$V_{ohm} = i \times r = \frac{I}{A} \times r \quad 11$$

Where I is the current (A), A is the active electrode area (cm^2), i is the current density (A/cm^2) and r is the area specific cell resistance ($\Omega\ cm^2$).

The cell resistance is usually defined as a function of the active electrode area, known as the area specific resistance (ASR). The ASR represents the net effect of all loss mechanism in the cell, indicating the performance over the full polarisation range. However, as explained by Mogensen and Hendriksen (2003), 'the concept of ASR is not standardised' and it is therefore important to always specify the conditions for the value quoted. The ASR can be calculated from the linear region of a measured *i*-V curve using Equation 12.

$$ASR = \frac{V_{cell} - V_{ocv}}{i} \qquad 12$$

2.1.2 Activation Polarisation

Activation polarisation, $\eta_{act,}$ is also known as charge transfer polarisation and occurs mainly at the electrodes of the cell. For any reaction to occur, an external energy is required to overcome the activation energy barrier of the reaction. The overvoltage in this case arises as a result of resistance of the slow kinetics in the charge transfer reactions at the electrode/electrolyte interfaces. The presence of a catalyst in the electrode/electrolyte region is vital in reducing the activation energy. Activation polarisation is dominant at low current densities as shown in Figure 2–1.

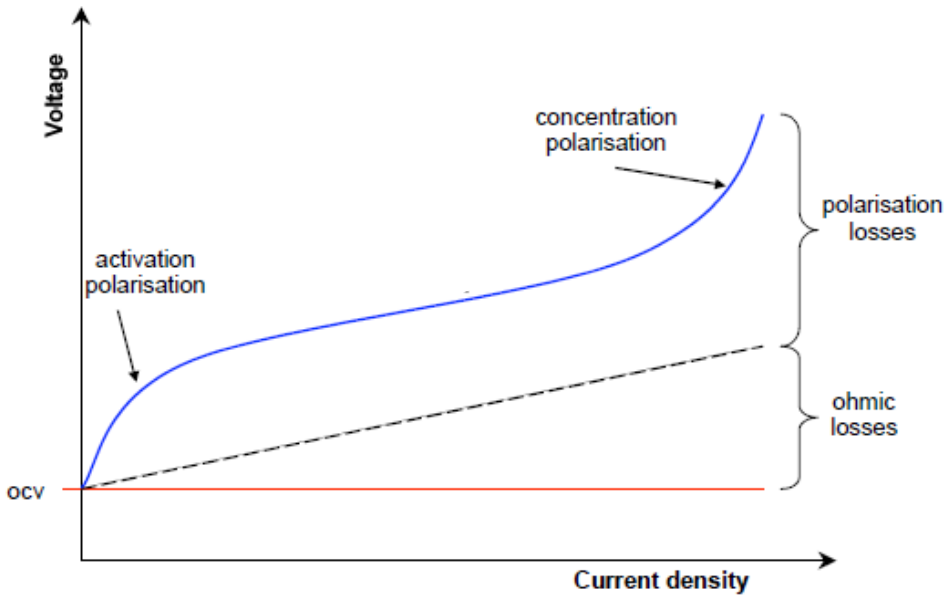

Figure 2–1: Current density vs voltage plot indicating the different overpotentials

2.1.3 Concentration Polarisation

The effect of concentration polarisation $\eta_{con,}$ can be due to gas diffusion and gas utilisation/conversion. Concentration polarisation due to gas diffusion occurs when the product species do not move fast enough through the porous electrode. The effect of gas diffusion can be seen at the oxygen and fuel electrode of an SOEC. On the other hand, concentration polarisation due to gas conversion occurs only at the fuel electrode of an electrolysis cell. Conversion polarisation reflects the change in composition at the active electrode in comparison with that at the bulk of the fuel electrode during electrolysis.

Concentration polarisation is a function of the diffusivity of the gas species, the electrode microstructure, the partial pressure of the gas and the current density. As the current density increases, the effect of concentration polarisation becomes more evident as there are insufficient reactants moving to the electrode surface. Thus, the flow rate of the reactant for the electrochemical reactions should increase with an increase in current density. Activation and concentration polarisation have a non-linear response on the *i*-V plot of Figure 2–1.

2.2 Electrochemical Methods for SOEC Evaluation

2.2.1 Current density (*i*) – voltage (V) curves

DC (direct current) and AC (alternating current) techniques often are used to characterise SOECs. During SOEC evaluation, DC characterisation is usually performed by recording current density (*i*) – voltage (V) curves as shown in Figure 2–1. The *i*-V plot characterises the electrochemical behaviour of a cell at set operating conditions (temperature and gas compositions) and this graphical illustration typically reflects the type of processes (i.e. charge transfer reactions and gas utilisation at low and high current densities respectively) that are occurring within the cell under operation. As previously indicated, the ASR can also be calculated from the *i*-V curve using Equation 12.

2.2.2 Electrochemical Impedance Spectroscopy

2.2.2.1 Introduction

Electrochemical Impedance Spectroscopy (EIS) is a tool often used in characterising cell changes and understanding the electrochemical behaviour of the cell. This technique has previously led to increased understanding of SOCs for fuel cell operation (Barford et al. 2007; Jensen et al. 2007b).

2.2.2.2Theory

Resistances across an electrochemical cell depends on a number of processes. These processes can include gas movement of reactants/products, charge-transfer reactions at the TPB, gas conversion and electronic and ionic conduction of the electrodes and electrolyte respectively. As these processes often have different time constants and proceed on different time scales, applying AC impedance can provide detailed information about them and their contribution to the overall resistance. Since AC can be generated at various frequencies, it offers a means to probe these processes with different time constants (Yuan et al. 2010).

AC impedance is usually obtained by applying a small AC potential onto a DC voltage and then measuring the current through the cell. The magnitude of the applied AC potential is small enough (~10mV) that it does not affect the steady-state of the system, and a nearly linear AC current response to a sinusoidal potential is achieved.

As described by Qi (2008), when a sinusoidal AC voltage, $\dot{E}=E\sin(\omega t)$, is applied to a pure resistor (R) as $\dot{E}_R$, the corresponding current,

$$\dot{I}= \dot{E}_R/R = (\dot{E}_R\sin(\omega t))/R \quad (13)$$

is in phase with $\dot{E}_R$. Both $\dot{E}$ and $\dot{I}$ are vectors rotating at an angular frequency of ω. When $\dot{E}$ is applied to a capacitor (C) as $\dot{E}_C$, the corresponding current,

$$\dot{I}= C(d\dot{E}_C/dt) = \omega C\dot{E}_C\cos\omega t = \dot{E}_C\sin(\omega t + \pi/2)/X_C \quad (14)$$

is $\pi/2$ ahead of $\dot{E}_C$. Here, $X_C = 1/(\omega C)$, and is called the capacitive resistance, which is a counterpart to the Ohmic resistance. If we plot vectors $\dot{E}$ and $\dot{I}$ in a complex plane, and assign the positive segment of the abscissa to $\dot{I}$, then $\dot{E}_R$ and $\dot{E}_C$ will have 0 and $\pi/2$ angles

with $\dot{I}$, respectively. $\dot{E}_C$ falls on the ordinate and can be assigned as imaginary in a complex notation by using $j = (-1)^{1/2}$. The $\dot{E}_C = -jX_C\dot{I}$, where j means $\dot{E}_C$ *is* $\pi/2$ degrees apart from İ, and the minus sign means that the voltage lags behind the current.

When $\dot{E}$ is applied to a resistor R and a capacitor C that are connected in series,

$$\dot{E} = \dot{E}_R + \dot{E}_C = \dot{I}(R - jX_C) = \dot{I}\dot{Z} \quad (15)$$

where $\dot{E}$ and $\dot{I}$ has a phase angle between 0 and π/2 with İ being ahead of Ė. Vector

$$\dot{Z} = R - jX_C \quad (16)$$

is the impedance. In a complex plane notation, R and X_C are plotted along the abscissa and the ordinate, and are typically referred to as “real” and “imaginary” axis respectively. They are often expressed as Z’ and Z” respectively as shown in Figure 2–2.

If two processes have similar time constants it is very difficult to identify the individual contributions using this technique. However, it has been shown that careful design of experiments in which conditions are systematically varied can still yield a great deal of information on the processes involved (Jensen et al. 2007b; Primdahl and Mogensen 1998). The frequency response of the AC signal may vary from 1 MHz or higher to 1 mHz or lower.

During EIS, cell characterisation can be obtained with the cell operating at open circuit condition or at a higher cell voltage. For a detailed understanding of the processes occurring within the cell and their resistances, characterisation at both conditions (OCV and higher voltages) is important. This is because, for example, if a SOEC is operating at higher cell voltages, mass transport resistance is more dominant and the effect of charge-transfer kinetics could be subdued within the corresponding impedance spectra. When operating at OCV it becomes difficult to quantify the resistances contributing to mass transport processes (Orazem and Tribollet 2008). Therefore, a combination of cell characterisation at both conditions is vital in quantitatively understanding the contribution of all processes to cell resistance.

Nyquist and Bode plots are commonly used to illustrate an impedance spectrum. A Nyquist plot (complex-plane diagram) is displayed for the experimental data set of points (Z’ and Z”) measured at different frequencies, with each point representing the real and imaginary parts of the impedance at a particular frequency. The real impedance (Z’) on the x-axis and

the imaginary impedance (Z") on the y-axis in a complex plane are plotted against each other and examples of this plot can be seen in Figure 2–3b and Figure 2–4b. A Bode plot is an alternative representation of the impedance showing the frequency response of the system. As shown in Figure 2–3c and Figure 2–4c, there are two types of Bode diagrams. One describes the frequency dependence of the modulus (log ω against log $|Z|$ plotted on the primary axis of both figures) and the other describes the frequency dependence of the phase (log ω against θ plotted on the secondary axis of both figures).

The Nyquist plot of an impedance spectrum is more illustrative than a Bode plot and enables quick and easy identification of ohmic and polarisation resistances as well as inductance effects. Figure 2–2 shows two impedance spectra on the same plot for CO_2 electrolysis and CO_2/H_2O co-electrolysis. The cell processes identified in this plot include:

- Ohmic resistance (R_{ohm}), also known as serial resistance, which is the real part resistance taken at the intercept of the x-axis
- Total cell resistance (R_T), which is the final value of the real part resistance
- Polarisation resistance (R_P), which is taken as the difference between the ohmic and total cell resistance (R_T).

$$R_T = R_{ohm} + R_p \quad (17)$$

- Inductance (L), which is often observed at high frequencies, is seen in Figure 2–2 below zero on the imaginary Z" axis.

Inductance has a negative effect on the accurate measurement of the ohmic and polarisation resistances. In Figure 2–2, the effect of inductance would lead to an artificially high ohmic resistance. Although it is primarily observed at high frequencies, it has been shown that inductance can also influence the middle and low frequencies leading to errors in the polarisation resistance (Raikova et al. 2009). Inductance primarily occurs due to wiring and the cables connected to the electrochemical interface. Implementing an error correction procedure is therefore important in increasing the reliability of the electrochemical impedance results. Further details on techniques for error correction due to cable inductance can be found in literature (Stoynov and Vladikova 2009). Furthermore short wires are helpful for minimising the inductance effects as described by (Qi 2008).

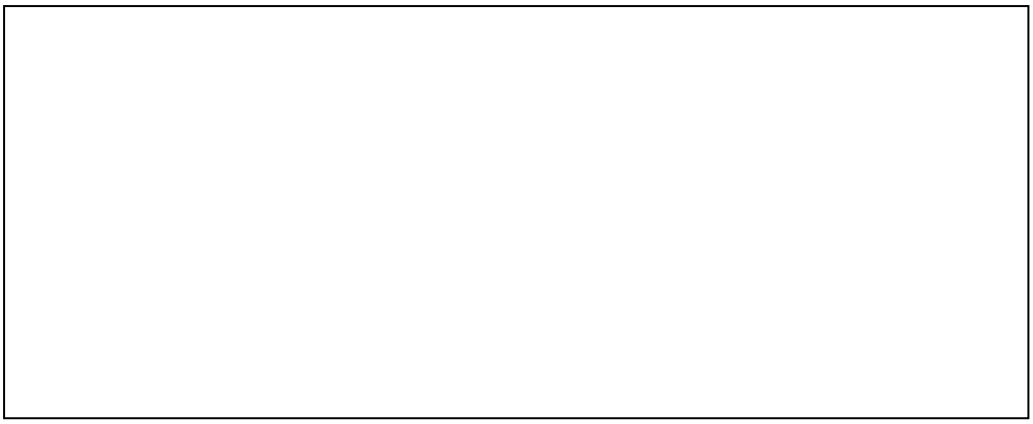

Figure 2–2: Electrochemical Impedance Spectra measured at OCV and 850^oC of fuel electrode compositions 50% CO_2, 25% CO and 25% Ar (Green) and 50%CO_2, 25% H_2 and 25% Ar (Red) with pure oxygen flowing across the oxygen electrode (Ebbesen et al. 2012).

2.2.2.3 Electrochemical Circuit Elements

EIS data are commonly analysed by fitting to an equivalent circuit model (comprising of a combination of resistors, capacitors, inductors, etc). This is because the response of a reaction process to an AC perturbation is similar to that of a combination of resistors and capacitors, as well as a few specific electrochemical elements (such as Warburg diffusion elements and constant phase elements) (Macdonald 1992; Yuan et al. 2010). Resistors are involved in the reaction process since electronic and ionic resistances will be encountered when the electrons move through the electrodes and ions through the electrolyte. Capacitors are involved as a result of charge accumulation which occurs at the electrode-electrolyte interface during the reaction process. The combination of resistors and capacitors can therefore be used to simulate a reaction process (charge transfer, mass transport, etc).

The most commonly used circuit elements used in equivalent circuit models include resistance (R), capacitance (C), inductance (L), constant phase elements (CPE), Warburg diffusion element (Ws), Gerischer element (GE), etc. Figure 2–3 is an example of an impedance spectrum of an electrochemical system with one time constant. Figure 2–3a shows the basic equivalent circuit. In this figure, a resistor (R1) in series with a parallel connection of a capacitor (C1) and resistor (R2) is described. Figure 2–3b and c are the simulated Nyquist diagram, and bode plot respectively. The series resistance R1 (ohmic resistance) represents the electric resistance, which comprises of ionic resistance of the

electrolyte, electronic resistance of the electrodes and contact resistances. R2 (polarisation resistance) represents the resistance between the ohmic and total cell resistance. C1 is the double layer capacitance associated with the electrode-electrolyte interfaces.

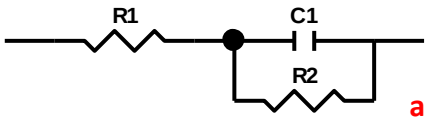

a

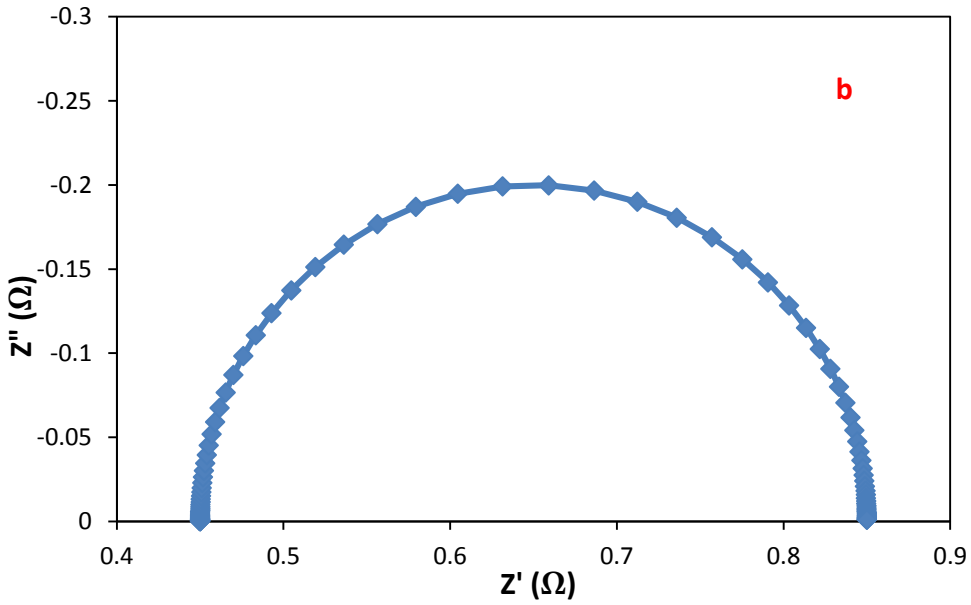

b

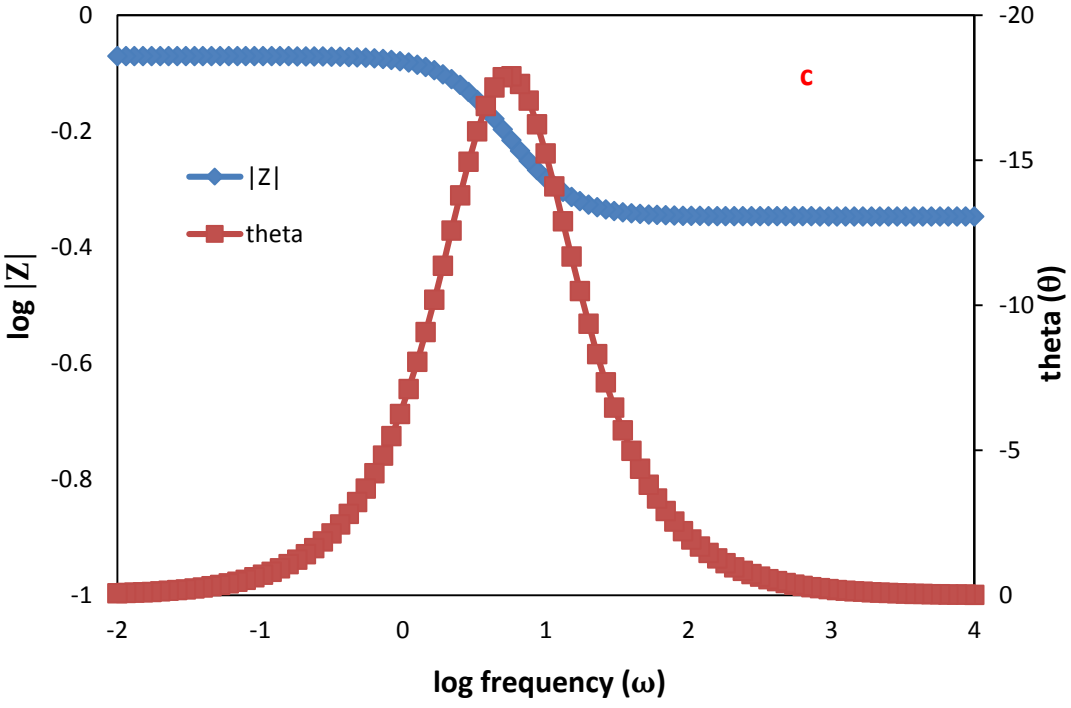

c

Figure 2–3: a) Illustration of basic equivalent circuits for an electrochemical system with one time constant showing a resistor (R1) in series with a parallel connection of a capacitor (C1) and resistor (R2). b) Nyquist plot of a one-time constant model simulated over the frequency range 10 kHz-0.01 Hz (R1 = 0.45 Ω, R2 = 0.4 Ω and C1 = 0.1 F). c) Bode plot of a one-time constant simulated over the same conditions above.

The shape of a model's impedance spectrum is controlled by the style of electrical elements in the model and the interconnections between them (series or parallel combination). The size of each feature in the spectrum is controlled by the circuit elements' parameters. Zview, for example, is a numerical analysis tool commonly used to fit the spectra, and this tool gives the best values for the equivalent circuit parameters. The major shortcomings of an equivalent circuit approach are that an impedance pattern obtained experimentally can be presented by more than one equivalent circuit. So to setup a suitable equivalent circuit model, an understanding of the underlying processes is needed and a fundamental understanding of the behaviour of the cell elements.

Figure 2–4a shows an equivalent circuit of a resistor (R1) in series with a parallel connection of a constant phase element (CPE1) and resistor (R2). Figure 2–4b and c are the simulated Nyquist and bode plot respectively. The only difference between Figure 2–4 and Figure 2–3 is that the capacitor has been replaced with a CPE. The constant phase element is a non-intuitive circuit element commonly used to represent real systems in which the arc of the semi-circle is depressed. In reality, the double layer of an electrochemical reaction does not behave like a pure capacitor. For example, for SOC, a depressed semi-circle will be expected due to its electrode porosity, electrode inhomogeneity and surface roughness, variability in thickness and conductivity of surface coating, uneven current distribution, differences in reaction rates at the TPB (Nechache et al. 2014). As a result, a constant phase element (CPE) is used instead of the capacitor to compensate for the distribution of the system. In this study, a simple equivalent circuit model consisting of resistors and constant phase elements has been applied as shown in Section 3.9.4.

A CPE's resistance is given by

$$\boldsymbol{X_{CPE}} = \mathbf{1}/(\boldsymbol{\omega C})^{\boldsymbol{\alpha}} \tag{18}$$

where α, called the phase parameter, is less than 1. The CPE represents C, R, and L respectively for α value 1, 0 and -1. For α = 0.5, it gives the Warburg impedance.

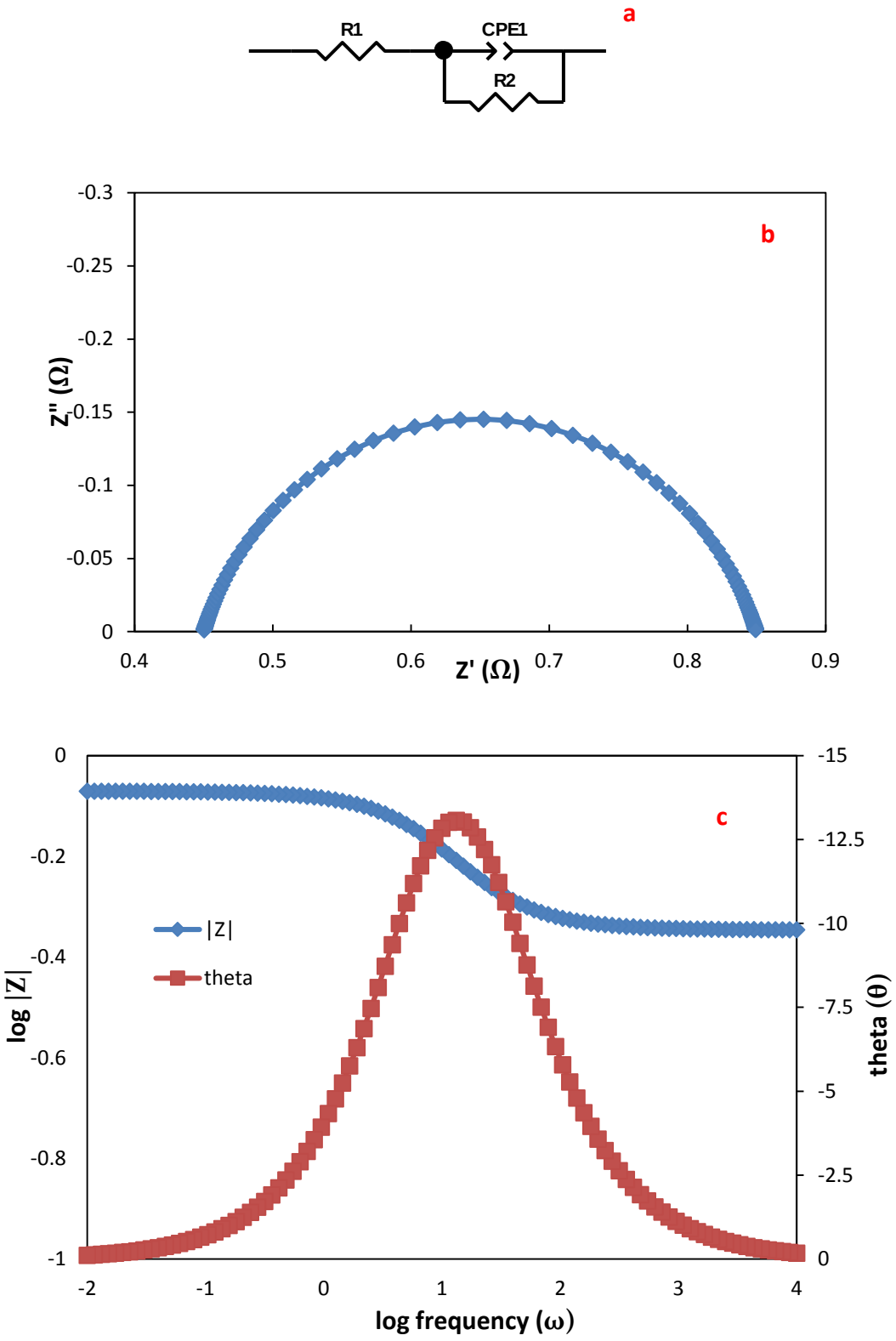

Figure 2–4: a) Illustration of basic equivalent circuits for an electrochemical system with one time constant showing a resistor (R1) in series with a parallel connection of a constant phase

element (CPE1) and resistor (R2). b) Nyquist plot of a one-time constant model simulated over the frequency range 10 kHz-0.01 Hz (R1 = 0.45 Ω, R2 = 0.4 Ω, CPE1-T = 0.1 F and CPE1-P (α) = 0.85). c) Bode plot of a one-time constant simulated over the same conditions above

As previously described, the series resistance R1 represents the electric resistance, which comprises of ionic resistance of the electrolyte, electronic resistance of the electrodes and contact resistances. R2 represents the resistance between the ohmic and total cell resistance.

Note: For the high frequency arc (CPE1), the fitted CPE-P values in all data presented in this thesis varied from 0.63 to 0.75 while that for the low frequency arc varied from between 0.7 to 0.95.

Warburg diffusion element (Ws) is generally used to describe a diffusion limited process. As previously indicated, the Warburg element is also a specialised element with a phase value of 0.5 (See Equation 18). In a situation, for example, where a process is also influenced by diffusion to and from the electrode (charge transfer for example), the Warburg impedance will be seen in the impedance plot. The real and imaginary axis of a spectrum of the Warburg impedance forms a straight line with a slope of 45^{o}C with the abscissa. Further details on the Warburg element is described elsewhere (Lvovich 2012)

2.3 High Temperature Electrolysis of Carbon dioxide in a SOC

High temperature electrolysis of carbon dioxide in a SOC has been less frequently investigated compared to H_2O electrolysis and H_2O/CO_2 co-electrolysis. Although SOCs were initially optimised for H_2O/H_2 investigations, the oxygen ionic conductivity of the electrolyte enables the electrolysis of carbon dioxide for CO production. The potential of a SOEC to reduce CO_2 to CO has been explored in a number of studies (Ebbesen et al. 2012; Ebbesen and Mogensen 2009; Elikan et al. 1972; Kim-Lohsoontorn and Bae 2010; Kim-Lohsoontorn et al. 2010; Zhan and Zhao 2010). In the late 1960s, electrolysis of CO_2 in SOECs was first demonstrated by NASA for purpose of O_2 production for life supports and propulsion in submarines and spacecraft (Elikan et al. 1972).

Ebbesen and Mogensen (2009) tested planar Ni/YSZ supported cells of 5 cm x 5 cm with an active electrode area of 4 cm x 4 cm under varying gas compositions of CO_2 and CO mixtures at 850^{o}C. ASRs (calculated from *i*-V curves at -0.25 A/cm^2 using Equation 12) of 0.36 Ω cm^2 and 0.37 Ω cm^2 were calculated for 50% CO_2/50% CO and 70% CO_2/30% CO respectively when operating in electrolysis mode. On the other hand, ASRs of 0.30 Ω cm^2 and of 0.31 Ω cm^2 were calculated for 50% CO_2/50% CO and 70% CO_2/30% CO respectively, when operating in fuel cell mode, indicating a higher activity for oxidation of CO than reduction for the cells employed. Using the same planar Ni/YSZ supported cell, an ASR of 0.24 Ω cm^2 was calculated for 50% H_2O/50% H_2 during steam electrolysis indicating a significantly higher performance of the electrolyser under H_2O/H_2 conditions.

Kim-Lohsoontorn and Bae (2010) also tested fuel electrode Ni-GDC button cells with an active electrode layer of 0.785 cm^2 at 800^{o}C under varying compositions of CO_2/CO mixtures. The polarisation resistance (from the impedance plot) was found to increase with an increase in CO_2 content (i.e. 70% CO_2/30% CO > 50% CO_2/50% CO) and a significant increase in polarisation resistance was observed when operating at 100% CO_2 to the fuel electrode. Zhan et al. (2009) explains that the higher polarisation resistance observed in a cell with a higher CO_2 content in a CO_2/CO mixture is due to the lower diffusivity of the higher molecular weight CO_2 through the porous cathode. The use of pressurised CO_2 gasses

during SOEC operation could aid in the reduction of polarisation resistance due to mass transport limitations.

SOC degradation during CO_2 electrolysis has been investigated over long periods of operation (over 500 hours).The mechanism of cell degradation during CO_2 electrolysis is similar to that of CO_2/H_2O co-electrolysis discussed in Section 2.6.2.1. Furthermore, issues relating to formation and deposition of carbon, from the reduction of CO, on the active sites of the TPB are also discussed in Section 2.6.2.2.

2.4 High Temperature Co-electrolysis of CO_2 and H_2O in a SOC - Reaction Mechanisms for Syngas Production

The relative contribution of the electrochemical and chemical reactions to syngas production in an SOEC is a highly debated topic. There is debate as to whether CO is produced from CO_2 electrolysis, the rWGSR or both.

Stoots et al. (2008) suggested that steam electrolysis and the rWGSR were the only reactions which took place within this process; the hydrogen produced from steam electrolysis is thought to be used to reduce CO_2 to CO via the rWGSR. Stoots et al. (2008) proposed this reaction mechanism having observed a similar ASR for H_2O electrolysis and H_2O/CO_2 co-electrolysis. Furthermore, the ASR for CO_2 electrolysis was observed to be significantly higher than H_2O electrolysis and H_2O/CO_2 co-electrolysis. Ebbesen et al. (2009) also suggested that “part of (possibly most of) the CO produced results from the rWGSR” because rWGSR equilibrium favours the chemical reaction at 850^oC.

Recent investigations by Ni (2011) and Ebbesen et al. (2012) described in Section 2.4.1 and 2.4.2 respectively have argued otherwise, that CO is produced both from the rWGSR and the electrochemical reaction during the high temperature co-electrolysis of carbon dioxide and steam in a SOC.

2.4.1 Co-electrolysis Electrochemical Model for Syngas Production

Ni (2011) developed an electrochemical model to quantify the contribution of the rWGSR to CO production by comparing the fluxes of CO at the cathode-electrolyte interface (where the electrochemical reactions predominantly occur) and at the cathode surface (where the chemical reaction occurs).

The Dusty-Gas Model (DGM) (Ni 2011) was employed to determine the transport of the gas species through the porous cathode (which relates to the rate of the rWGSR and the rate of the electrochemical reactions). At the cathode-electrolyte interface, the flux caused by the electrochemical reactions was related to the current densities. The difference therefore in fluxes at the cathode surface and the cathode-electrolyte interface was assumed to be caused by the rWGSR. The working mechanisms proposed for the high temperature co-electrolysis of CO_2 and H_2O can be seen in Figure 2–5. In this study, the electrochemical reactions were assumed to occur at the electrode/electrolyte interface while the chemical reaction occurs across the full depth of the fuel electrode.

Figure 2–5: Working mechanisms of SOEC for co-electrolysis of H_2O and CO_2 (Ni 2011)

2.4.1.1 Effect of temperature

In determining the effect of temperature on the co-electrolysis reactions, Ni (2011) varied the operating temperature between 873 K and 1073 K while operating at 1.3 V and a cathode inlet composition of 49.7% H_2O, 25% CO_2, 25% H_2, 0.3% CO.

As shown in Figure 2–6A, the study found larger CO flux at the cathode surface (S) than the cathode-electrolyte (E) interface at 873 K indicating the rWGSR was contributing to CO production. CO_2 electrolysis was calculated to contribute to CO production by 75% while the rWGSR contributed 25%. This implies that CO is indeed also produced from the electrochemical reaction. At a higher temperature of 1073 K however, CO was consumed by the water gas shift reaction (WGSR). At a higher temperature, it can also be observed that electrochemical reduction of CO_2 occurs owing to the larger CO flux at the cathode electrolyte interface, as seen in Figure 2–6B.

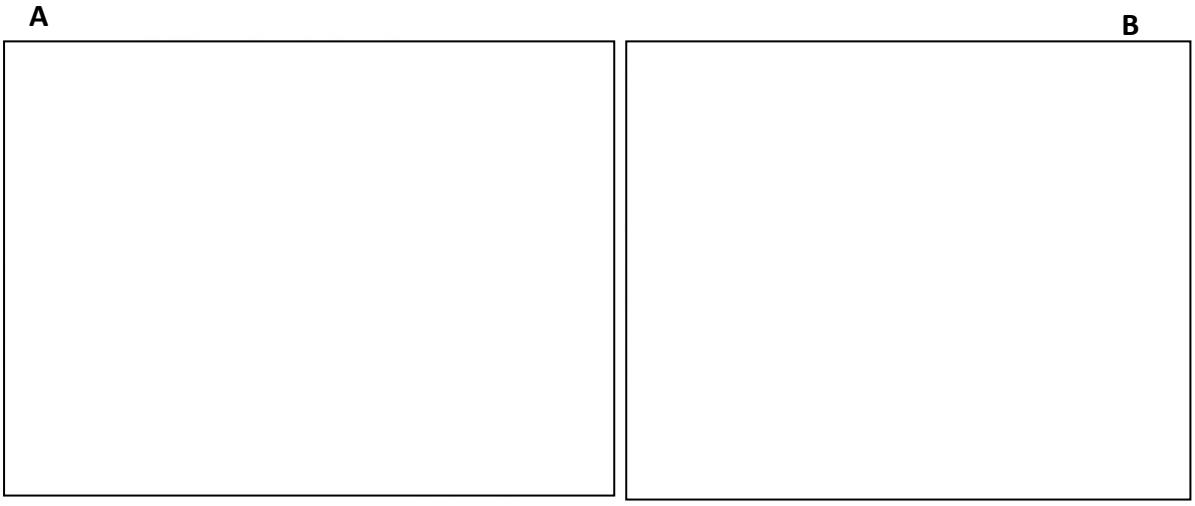

Figure 2–6: Effect of temperature on co-electrolysis of H_2O and CO_2. Figure A and B shows H_2 and CO fluxes at 873 and 1073 K respectively (Ni 2011)

2.4.1.2 Effect of gas composition at cathode surface

The gas compositions were varied (case 1: 49.7% H_2O, 25% H_2, 25% CO_2, 0.3% CO, case 2: 49.7% H_2O, 0.3% H_2, 25% CO_2, 25% CO and case 3: 25% H_2O, 25% H_2, 49.7% CO_2, 0.3% CO) while comparing the fluxes of CO and H_2 at the cathode surface and cathode-electrolyte interface. In all cases, the operating temperature and voltage was 1073 K and 1.3 V respectively.

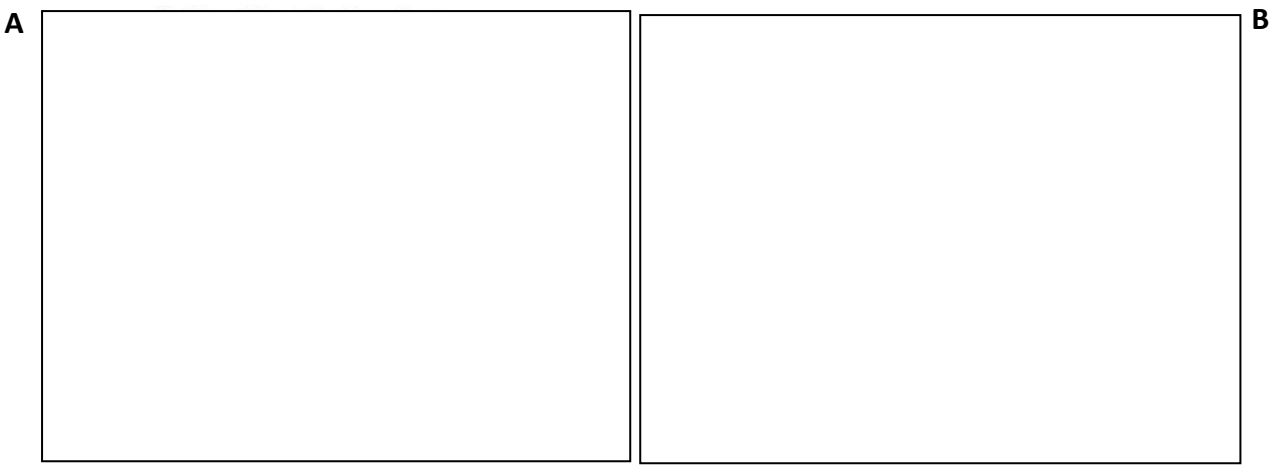

Figure 2–7: Effect of varying cathode inlet gas compositions on co-electrolysis of H_2O and CO_2. Figure A shows H_2 and CO fluxes at case 2 49.7% H_2O, 0.3% H_2, 25% CO_2, 25% CO while Figure B shows H_2 and CO fluxes for case 3 at 25% H_2O, 25% H_2, 49.7% CO_2, 0.3% CO (Ni 2011)

In case 2 shown in Figure 2–7A, the CO flux increased from negative value at the cathode-electrolyte interface (CO production from electrolysis) to positive value at the cathode surface (CO consumption via the WGSR). For case 3 shown in Figure 2–7B, the flux of CO was considerably higher at the cathode surface than the cathode-electrolyte interface due to the high rate of rWGSR inside the cathode.

2.4.1.3 Effect of operating potential

The fluxes of CO and H_2 at the cathode surface and cathode-electrolyte interface were compared while varying the operating potential between 1.0 V and 1.4 V at 1073 K with an inlet gas composition of 49.7% H_2O, 25% CO_2, 25% H_2, 0.3% CO.

At 1.0 V, the CO flux at the cathode surface was about 3 times higher than the flux at the cathode-electrolyte interface indicating the significant contribution of the rWGSR to CO production (shown in Figure 2–8A). At a higher potential of 1.4 V, the flux of CO at the cathode surface, shown in Figure 2–8B, was smaller than that at the cathode-electrolyte interface indicating CO was being consumed. This is further observed in the higher flux of H_2 at the cathode surface indicating CO was being consumed at higher operating voltages.

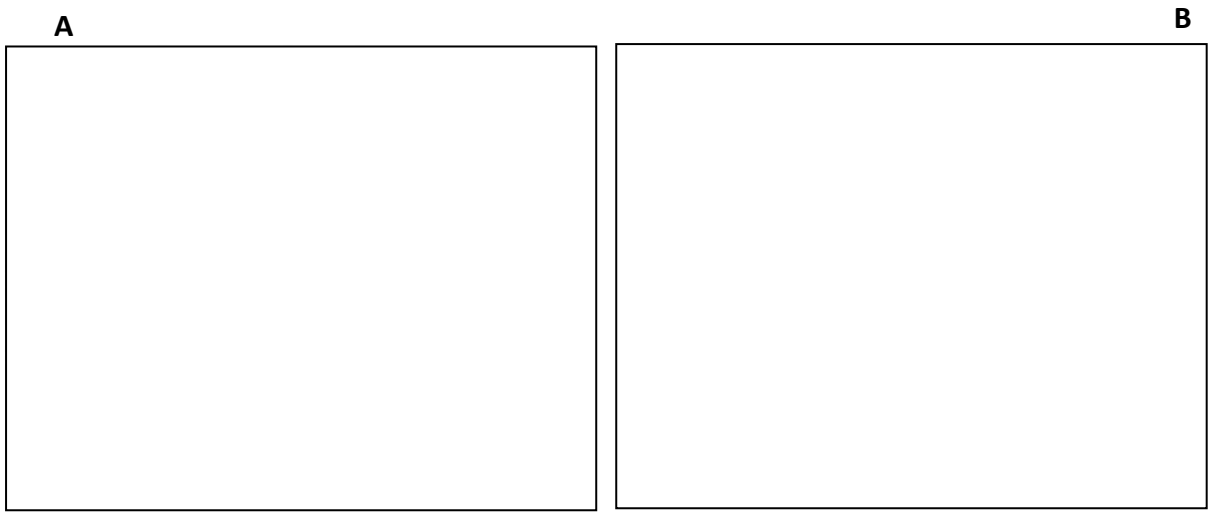

Figure 2–8: Effect of temperature on co-electrolysis of H_2O and CO_2. Figure A and B show H_2 and CO fluxes at 1.0 and 1.3 V respectively (Ni 2011)

The results shown in this model agree well with the experimental data from Zhan et al. (2009). These electrochemical model findings contradict the understanding that CO is produced solely from the rWGSR. The model shows that both electrochemical and chemical reactions occur during the high temperature co-electrolysis of carbon dioxide and steam in a SOEC. The amount of CO produced is also shown to be highly dependent on the operating temperature, inlet gas composition and applied voltages.

2.4.2 Experimental Investigation

The reaction mechanisms for the electrochemical co-reduction of H_2O and CO_2 in SOECs were briefly investigated in a study by Ebbesen et al. (2012). The ASRs of all three mixtures (H_2O-H_2, CO_2-CO and H_2O-CO_2-H_2-CO) were compared. A Ni-YSZ supported solid oxide cell (Ni-YSZ/YSZ/LSM-YSZ) was operated at 750 and 850^oC with a CO_2/H_2O feed and pure oxygen sweep gas at the oxygen electrode side. The measured ASR (calculated from Figure 2–10 at -0.16 A/cm^2) for CO_2 electrolysis was slightly higher than that for H_2O and H_2O/CO_2 co-electrolysis. Other studies have also shown this trend of a higher ASR for CO_2 electrolysis than H_2O and co-electrolysis (Ebbesen et al. 2009; Kim-Lohsoontorn and Bae 2010; Kim-Lohsoontorn et al. 2011; Stoots et al. 2008; Yue and Irvine 2012; Zhan et al. 2009). Ebbesen et al. (2012) explains that "if only steam electrolysis would occur, and CO_2 would be inert in the chemical reaction, then the observed ASR would be identical to the ASR for steam electrolysis". Furthermore, the co-electrolysis polarisation resistance which specifically reflects the electrochemical activity within the cell was found from Figure 2–9 to be

between that for individual CO_2 and H_2O electrolysis. Ebbesen et al. (2012) concludes therefore that both CO_2 and H_2O electrolysis would be active in the electrochemical reactions.

The base comparison of the fuel electrode compositions of CO_2, H_2O and H_2O/CO_2 co-electrolysis is very important (Ebbesen et al. 2012). The equilibrium compositions of CO_2 and H_2O in the co-electrolysis process were equal to cold inlet compositions during individual steam and carbon dioxide electrolysis. The CO_2 electrolysis carried out by Zhan et al. (2009) for example was performed under cold inlet gas compositions of 75% CO_2 and 25% H_2 at 800^oC while using a fuel electrode supported cell (Ni-YSZ/YSZ/LSCF-GDC). Operating under these conditions would result in the presence of the rWGSR and therefore the anticipated CO_2 electrolysis reaction is actually a co-electrolysis process consisting of electrochemical and chemical reactions. Furthermore, the 56% H_2O and 19% CO_2 equilibrium composition were different to the inlet feed of H_2O electrolysis which had a 50% H_2O content.

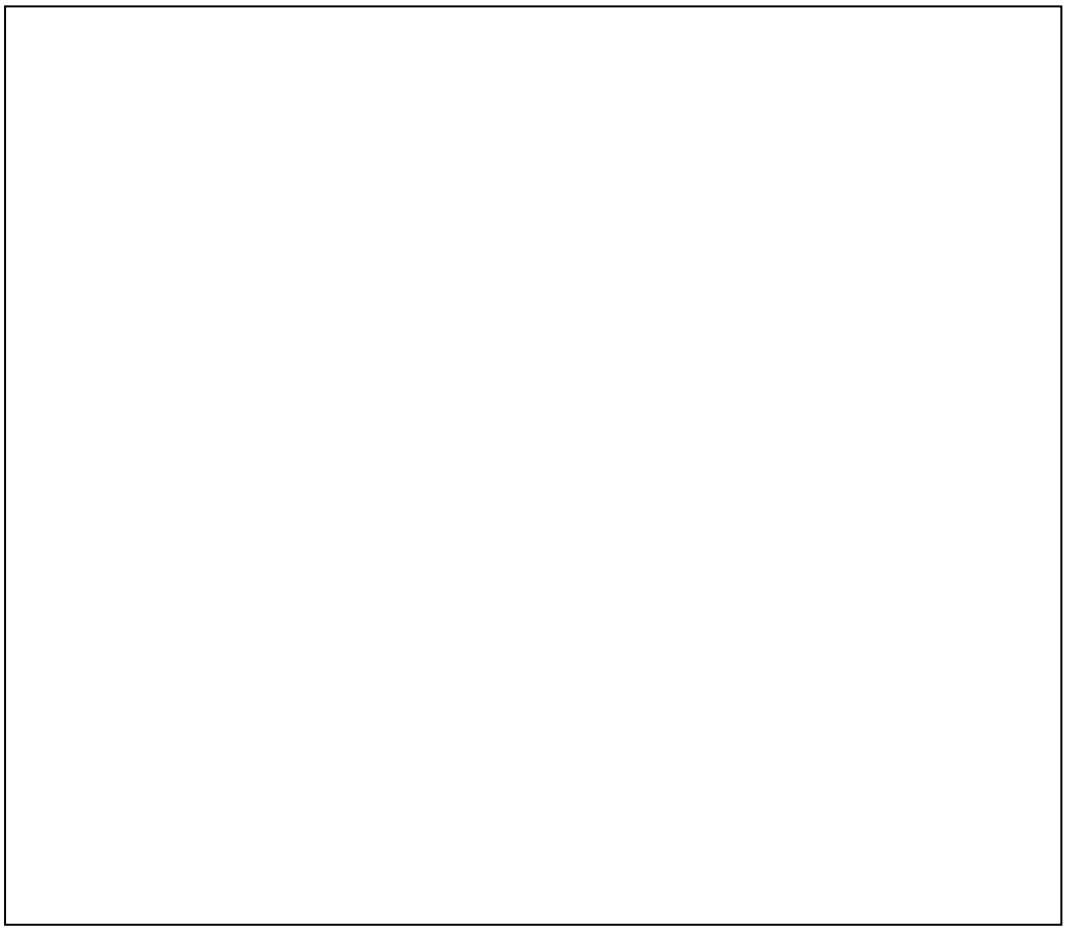

Figure 2–9: AC characterisation operated at 750 and 850^oC at varying CO_2, H_2O, CO_2/H_2O mixtures (Ebbesen et al. 2012)

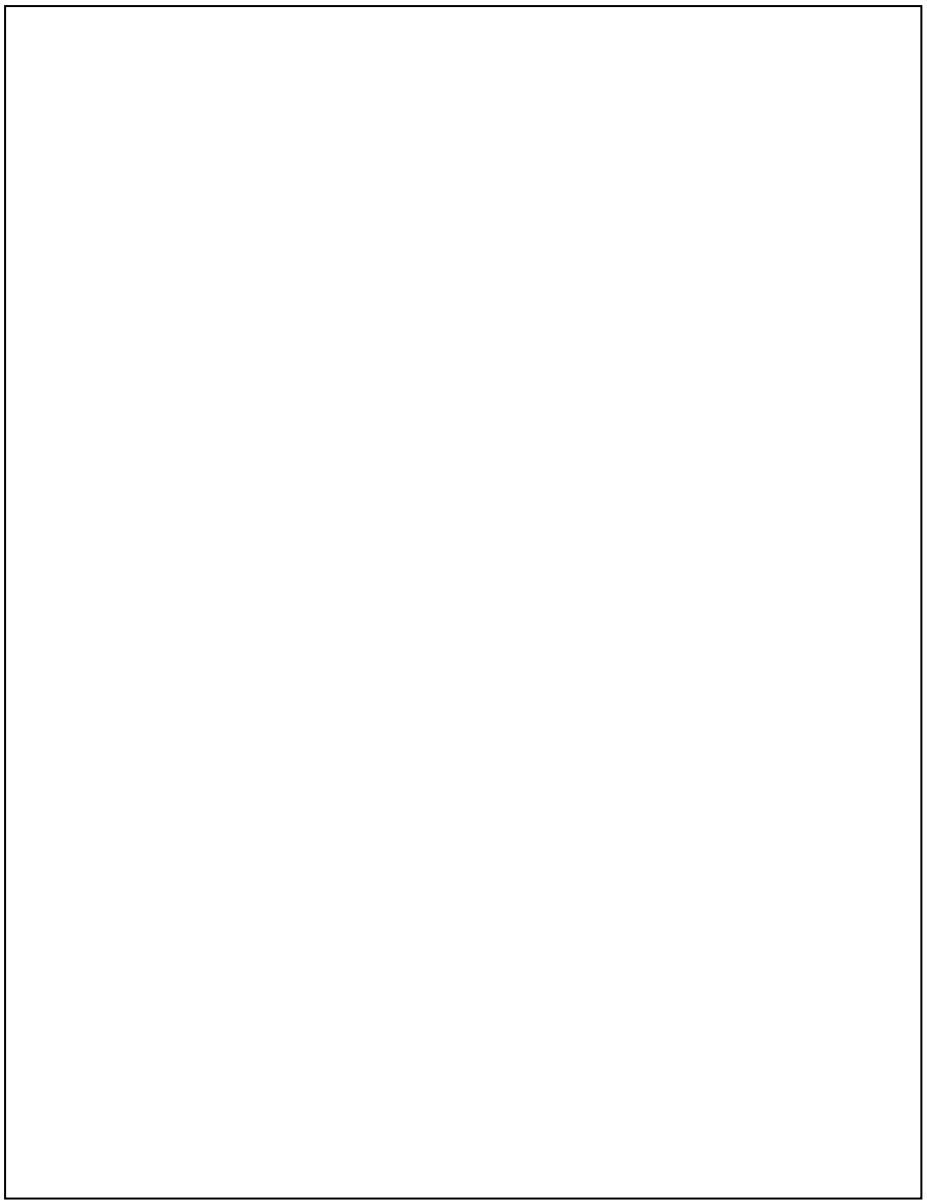

Figure 2–10: DC characterisation operated at 750 and 850^oC at varying CO_2, H_2O, CO_2/H_2O mixtures (Ebbesen et al. 2012)

2.4.2.1 Effect of temperature and Ni catalyst in the fuel electrode

Ebbesen et al. (2012) found the measured gas composition of the co-electrolysis mixture at OCV to be close to the thermodynamic equilibrium composition indicating the equilibrium of the WGS/rWGSR was reached within the cell as shown in Table 2–1. This was achieved with nickel present in the fuel electrode of the cathode supported cell. The effect of varying the operating temperatures can also be seen in the measured gas composition shown in Table 2–1. At a lower temperature of 750^oC, the effect of the water gas shift reaction is seen due to the slight increase in CO_2 and H_2 mixtures compared to that at 850^oC.

Table 2–1: Comparison of cold gas compositions to the fuel electrode, measured gas compositions and the calculated thermodynamic equilibrium composition (Ebbesen et al. 2012)

Temp.	Gas composition to the Ni-YSZ electrode	Measured gas composition	Thermodynamic equilibrium composition
850°C	25% CO_2 – 25% H_2O – 25% CO – 25% Ar	34% CO_2 – 16% H_2O – 16% CO – 8% H_2 – 25% Ar	33% CO_2 – 17% H_2O – 17% CO – 8% H_2 – 25% Ar
750°C	25% CO_2 – 25% H_2O – 25% CO – 25% Ar	35% CO_2 – 15% H_2O – 16% CO – 9% H_2 – 25% Ar	34% CO_2 – 16% H_2O – 16% CO – 9% H_2 – 25% Ar

To summarise, the electrochemical performance of the SOC operating under steam electrolysis has been observed to be slightly higher than CO_2/H_2O co-electrolysis and significantly higher than CO_2 electrolysis. The co-electrolysis polarisation resistance which specifically reflects the electrochemical activity within the cell has been found to be between that for individual CO_2 and H_2O electrolysis indicating steam and carbon dioxide electrolysis reactions are active in the production of H_2 and CO respectively. Based on the experimental and mathematical model findings, it can be said that the proportion of syngas produced will ultimately depend on temperature, inlet gas compositions and applied voltage with all three reactions contributing to H_2 and CO production.

2.5 Properties, Materials and Characteristics of SOECs

The majority of investigations into the high temperature electrolysis of CO_2 and H_2O in SOECs have focused on the development of novel SOEC materials and optimisation of conventional materials under varying operating conditions. Solid oxide electrolysis investigations have benefited greatly from the advancement in fuel cell technology particularly with regards to material selection for enhanced SOC performance (Goodenough and Huang 2007; Minh 2004; Sun and Stimming 2007).

There is, however, differences in operating conditions such as the high steam content environment in the bulk of the fuel electrode which can accelerate the agglomeration of Ni particles present in the fuel electrode (see Section 2.5.2.1) (Eguchi et al. 1996; Eguchi et al. 1995; Tanasini et al. 2009). Furthermore, high oxygen partial pressure at the

electrolyte/oxygen electrode interface is observed at high current densities, leading to the degradation of the oxygen electrode (see Section 2.5.2.2) (Chen and Jiang 2011; Kim-Lohsoontorn et al. 2010; Knibbe et al. 2010; Laguna-Bercero et al. 2011; Virkar 2010). Consequently, there is a great interest in the optimisation of conventional materials and development of new SOE materials.

2.5.1 Electrolyte

The electrolyte must have a high ionic conductivity at the operating temperature. Yttria-stabilised zirconia (YSZ) is the most commonly used electrolyte material and is typically composed of 8 mol % Y_2O_3 doped in ZrO_2. YSZ is predominantly used for this application due to its high ionic conductivity (see Table 2–2), mechanical strength and chemical stability with most electrodes at elevated temperatures. In addition, the electrolyte material also has to be compatible with the thermal expansion coefficient of both electrodes as well as being gas tight (Wincewicz and Cooper 2005).

Pure zirconia on its own shows polymorphism i.e. it undergoes a phase change from monoclinic at room temperature to tetragonal at around 1170^oC and cubic phase at 2370^oC. The change in state upon cooling causes a volume expansion which induces stress onto the material causing it to ultimately crack. By substituting Zr^{4+} with Y^{3+}, the structure stabilises at tetragonal and cubic phases at low temperatures and, as a result of the lower valence cation, oxygen vacancies are introduced in order to maintain charge neutrality in the lattice thus increasing the ionic conductivity of the material (Yokokawa and Horita 2003)

Scandia stabilised zirconia (ScSZ) is an electrolyte material with a higher ionic conductivity than YSZ (see Table 2–2) leading to the possibility for operation at lower temperatures. One problem associated with the use of scandium is that it is only found in trace amounts and has a low world production rate resulting in prices per kilogram almost 15 times that of yttrium (metal-pages.com 2015). In addition, its use is mostly limited due to its polyphase system resulting in an unstable ionic conductivity over long periods of operation at high temperatures (~700 – 1000^oC) (Badwal et al. 2000; Ciacchi and Badwal 1991). Recent investigations have sought to stabilise the conductivity and crystal phase of this material (Miller et al. 2013; Spirin et al. 2012; Yamaji et al. 2013). In a recent study conducted by Spirin et al. (2012), 10 and 11 mol % Sc_2O_3-ZrO_2 were doped with yttria. At low sintering

temperatures of 1010 – 1300°C, stabilisation of the cubic-fluorite phase was achieved for Y-doped ScSZ composites. In addition, high and stable conductivity was obtained during extended annealing at 850°C for 2700 hours for Y-doped ScSZ composites sintered below 1100°C. Further investigations are still ongoing to achieve stability for even longer periods of operations.

Table 2–2: Approximate ionic conductivities for electrolyte materials (Wincewicz and Cooper 2005)

	Operating temperature = 800°C				
Electrolyte material	YSZ	ScSZ	GDC	YDC	*LSGM
Ionic conductivity (S cm^{-1})	0.02	0.1	0.158	0.0355	0.158

*LSGM is Lanthanum Strontium Gallate Magnesite

Gadolinium doped ceria (GDC) and Samarium doped ceria (SDC) are a family of ceria based electrolytes with a higher ionic conductivity than the conventional YSZ thus leading to the possibility of operation at lower temperatures as shown in Table 2–2. In addition, they have been shown to be more compatible with higher performing anode materials such as lanthanum strontium cobalt ferrite (LSCF); (YSZ and LSCF are not chemically compatible due to the formation of a resistive layer(Lee et al. 2009)). Ceria (CeO_2) exhibits high electronic conductivity and by substituting with dopant (gadolinium or samarium), oxygen vacancies are created within the material without introducing further electric charge carriers. There is, however, a number of drawbacks to the use of ceria electrolytes in electrolysis operation. In a material investigation study, Eguchi et al. (1996) concluded that “bare ceria electrolyte cannot be used as the electrolyte for SOEC investigation”. This is because at high voltages, partial reduction of Ce^{4+} to Ce^{3+} occurs which in turn decreases the ionic transport number of the material. This reduction induces electronic conductivity onto the material which effectively partially short circuits the cell. It is the electronic current leakage through the electrolyte which causes a drop in open circuit voltage and leads to a loss in cell efficiency. As a result of this electronic conductivity, ceria based electrolytes are generally referred to as mixed ionic and electronic conducting (MIEC) material. Furthermore, the reduction of ceria has been shown to be thermally activated (effect increases at ~700°C and above) and this process could induce mechanical stress onto the material thus leading to cracking (Kim-Lohsoontorn and Bae 2010; Leah et al. 2011).

To offset the possibility of electronic leakages, Kim-Lohsoontorn et al. (2011) investigated the performance of a bi-layered YSZ/GDC electrolyte during co-electrolysis operation. The electronic properties of ceria based material reduced the cell OCV when operating at 800^oC and H_2O/H_2 = 50/50 are given in Table 2–3.

Table 2–3: OCV of different materials for steam electrolysis at 800^oC (Kim-Lohsoontorn et al. 2011)

	Ni-GDC/GDC/LSM-YSZ	Ni-GDC/YSZ/LSM-YSZ	Ni-GDC/YSZ/GDC/LSM-YSZ
OCV (V)	0.68	0.88	0.80

The YSZ layer was added to block off the electronic short circuit in the cell however Kim-Lohsoontorn et al. (2011) suggested it might not have been dense enough hence there was a lower OCV in the YSZ/GDC than the YSZ electrolyte. The electrolyte had large thickness of ~1.5 mm and further work is still needed to optimise the cells. The results showed that the bi-layered YSZ/GDC electrolyte cell exhibited significantly higher performance when compared to the cell using YSZ or GDC electrolyte during electrolysis operation. Unlike YSZ electrolytes which exhibit a lower performance in SOEC mode than SOFC operation, the ASR of the bi-layered electrolyte was higher in SOEC mode than SOFC. Durability tests at operating conditions of 800^oC, 60 mA cm^{-2} and H_2O/H_2 = 50/50 on the bi-layered electrolyte however showed decay in performance over a 93 h period (Kim-Lohsoontorn et al. 2011). Further investigations are still needed to understand the decay mechanism of this material.

Other high performing SOE electrolyte materials, particularly at intermediate temperatures, include a family of perovskites based on $LaGaO_3$ doped at both A- & B- sites such as LSGM (with Sr doped on the A- site and Mg doped at the B- site) (Mizutani et al. 1994; Steele 2000). At intermediate temperatures, LSGM has been shown to have a higher ionic conductivity than YSZ as shown in Table 2–2. At a 1000^oC, it was observed by Yan et al. (2002) to have a similar ionic conductivity to YSZ. Several problems have been reported with the use of LSGM. They include difficulty in manufacture of thin electrolytes, high costs of materials (Yamamoto 2000) and a lower long term mechanical stability compared to YSZ (Yan et al. 2002).

2.5.2 Requirements of Electrode Materials

Key requirements of the electrode materials and their effect on SOC operation are:

- Sufficient porosity to allow for the inlet and outward flow of species
- Chemical stability and thermal compatibility with other contacting materials (electrolyte and interconnect),
- Inert to the reacting gas species
- Matching thermal expansion coefficient to other contacting materials
- Chemical stability of fuel and oxygen side electrodes in reducing and oxidising atmospheres respectively.

2.5.2.1 Fuel Electrode: SOE Cathode

The electrolyser cathode is usually a composite ceramic and metallic (cermet) material made up of Ni as the metallic material and a ceramic electrolyte, usually YSZ or GDC. The ceramic cathode is important to limit the nickel agglomeration at high temperatures; increase the active length and to match the thermal expansion coefficient to that of the ceramic electrolyte. Ni is usually added in the form of NiO and then subsequently reduced to metallic Ni during experimental start-up. Other promising cathode materials include perovskite structured materials such as lanthanum strontium chromium manganate (LSCrM) and lanthanum strontium titanate (LST), all used combined with an electrolyte (Jin et al. 2011; Li et al. 2012). These perovskites structured electrodes are promising over Ni based electrodes because they do not require a reducing gas to achieve performance (Badwall 2001).

Ni-YSZ is the most commonly used cathode material for electrolysis operation and most investigations have focused on improving its performance (i.e. increasing the length of the active TPB). The use of a metal catalyst such as Nickel in the electrode might be advantageous in improving the kinetics for syngas production. It has been shown that the equilibrium of the rWGSR is easily reached when using Ni-YSZ cathode supported cells (Ebbesen et al. 2012). There are a number of disadvantages with the use of Ni in the fuel electrode. It has been shown that high steam environment accelerates the agglomeration of Ni particles (Tanasini et al. 2009), consequently leading to a change in the electrode microstructure and a decrease in the length of the TPB (Sehested 2006). Eguchi et al. (1995)

also reported that the polarisation of the Ni electrode became large as the operating pO_2 approached that of the Ni-NiO system. Eguchi et al. (1996) proposed the formation of a less active layer arising from the oxidation of Ni particles under high steam content environment, consequently suggesting that the use of a precious metal may be preferable under a high steam environment.

Kim-Lohsoontorn and Bae (2010) studied the electrochemical performance of Ni-YSZ, Ni-GDC and Ni/Ru-GDC (Ru = ruthenium) cathodes over a range of temperatures and inlet gas compositions (H_2O, CO_2 and CO_2/H_2O). They observed a higher performance of the Ni-GDC and Ni/Ru-GDC electrodes over the Ni-YSZ electrode during electrolysis operation. (Kim-Lohsoontorn and Bae 2010) suggested the higher performance of the ceria based electrode was as a result of the oxygen storage capacity of GDC which helped to supress the oxidation of the Ni surface. However, as the steam to H_2 ratio increased (H_2O/H_2 ratio = 50/50 to 90/10), they observed a slight decrease in the overpotential of the Ni-YSZ electrode; however a significant increase in overpotential was observed for the ceria based electrodes when these steam compositions were increased. The sensitivity of the GDC conductivity to pO_2 was attributed to the significant increase in overpotential.

As an alternative to metal catalysts such as Ni which requires a continuous flow of reducing gas (such as H_2) to avoid Ni oxidation, the use of perovskite structured electrode materials has gained significant interest (Lee et al. 2010; Li et al. 2012; Yang and Irvine 2008; Yue and Irvine 2012). Yang and Irvine (2008) first proposed the use of LSCrM/GDC as a cathode for electrolysis, although their study only focused on low steam concentrations (3 vol. % H_2O). Yang and Irvine (2008) observed a better performance for the LSCrM/GDC over Ni-YSZ electrodes in atmospheres with low hydrogen content. However, the LSCM/GDC cathode showed a much larger resistance at lower voltages (I.0 V) and this effect was attributed to the reduction of the perovskite-structured LSCrM phase. Yang and Irvine (2008) noted that further work was still needed to improve the electrode microstructure and current collection as well as to explore the partitioning of processes related to the conditioning of electrodes. Furthermore, chemical changes associated with the reduction of the LSCrM/GDC perovskite phase were observed.

Li et al. (2012) investigated the use of perovskite $La_{0.2}Sr_{0.8}TiO_{3+\delta}$ (LST) composite cathode as an alternative to the conventional Ni-YSZ under CO_2/H_2O conditions. The reduction of the

LST cathode was the main process at low applied voltages whereas electrolysis operations were prominent at high voltages. Further investigations are still needed to eliminate reduction of this material and improve its performance.

2.5.2.2 Oxygen Electrode: SOE Anode

The electrolyser anode is usually composed of YSZ and a perovskite, most commonly LSM with the perovskite serving a purpose to provide electronic activity. Although LSM is a poor ionic conductor, it is typically used with doped zirconia due to its compatibility with the electrolyte material. Other promising anode materials due to their mixed ionic and electronic conductivity include barium strontium cobalt ferrite (BSCF), lanthanum strontium cobalt ferrite (LSCF), lanthanum strontium copper ferrite (LSCuF), lanthanum strontium ferrite (LSF) and barium cobalt ferrite niobium (BCFN) (Bo et al. 2008; Liu et al. 2012; Simner et al. 2003; Yamaura et al. 2005; Yang et al. 2011).

In recent years, mixed ionic and electronic conductivity electrodes (MIECs) have been widely investigated for fuel cell operation due to their ability to extend the reaction sites beyond the conventional idea of the TPB. This implies that the electrochemical reaction zone of MIECs is not confined to the TPB at the electrode – electrolyte region and therefore electrochemical reaction can occur over the depth of the electrode. Various studies have shown an increased electrochemical area with these materials over conventional anode materials, leading to a lower activation polarisation across this electrode and therefore higher electrochemical performance (DiGiuseppe and Sun 2011; Wang et al. 1999; Yokokawa and Horita 2003)

In an electrode material study, Kim-Lohsoontorn and Bae (2010) observed higher performances in LSCF and LSF electrodes than LSM-YSZ electrodes both under fuel and electrolysis cell operations. The higher activity of LSCF during fuel cell operation is due to its ability to increase the reaction zone beyond the TPB due to its mixed ionic and electronic conductive characteristic. The activity of all electrode materials was higher in fuel cell operation than electrolysis; however LSM-YSZ displayed a more symmetrical behaviour in both modes of operation. Similar observations were also seen in a previous study by Marina et al. (2007) where a depletion of oxygen vacancy concentration when changing from SOFC

to SOEC mode in MIEC electrodes (LSCF and LSCuF) was thought to be the reason for lower performances during electrolysis operation.

Kim-Lohsoontorn et al. (2010) compared the performances of the conventional LSM-YSZ with BSCF oxygen electrodes under electrolysis operation. Over a range of operating conditions, they found the BSCF oxygen electrodes (Ni-YSZ/YSZ/BSCF) showed a higher performance than LSM-YSZ based cells. However over a 20 h operational period, at 0.3 A cm^{-2}, 850^oC, H_20/H_2 70/30 ratio, they found a higher decay in performance for the BSCF cell over the composite LSM-YSZ. The EIS measurements showed a significant increase in polarisation resistance arcs and a shift in the purely ohmic resistance. Further investigations are still ongoing in determining the causes of these resistances.

To summarise, there is a huge focus currently on the optimisation of conventional materials as well as the development of novel materials particularly perovskite structured materials for the oxygen electrode. For the electrolyte, YSZ is still seen as the most durable electrolyte material for SOC investigations. The use of bi-layered YSZ/GDC electrolytes have been shown to be promising in increasing the ionic conductivity of the electrolyte and allowing for the use of higher performing MIEC oxygen electrodes. For co-electrolysis investigations, the use of Ni-YSZ over emerging perovskite fuel electrodes could be advantageous because of the increased gas conversion in the chemical reaction during H_2O/CO_2 co-electrolysis. At the oxygen electrode, MIEC electrodes are being thoroughly investigated because of their increased active site length which extends across the full length of the electrode.

2.6 Experimental Investigations of High Temperature Co-electrolysis of CO_2 and H_2O

2.6.1 Electrochemical Performance

The majority of co-electrolysis experiments have focused on improving the performance of conventional SOCs (Ni-YSZ/YSZ/LSM-YSZ). Table 2–4 summarises some key recent results from the high temperature co-electrolysis of CO_2 and H_2O.

Table 2–4: Initial SOEC performance from high temperature co-electrolysis of CO_2 and H_2O

Cell materials, compositions and specifications	Area specific inlet gas flow rate ($m^3/h\ m^2$)	Temp. (°C)	Gas composition at the fuel electrode	Total Initial ASR ($\Omega\ cm^2$)	Current density (A/cm^2)	Initial voltage at current density (mV)	Ref
Single cell planar Ni-YSZ electrode supports (Ni-YSZ/YSZ/LSM-YSZ) with cell active area of 4 x 4 cm	15.5	850	Cathode: 45% H_2O, 45% CO_2 & 10% H_2 Anode: 100% O_2	** 0.33	-0.25	920	(Ebbesen et al. 2010)
Multi cell stack planar Ni-YSZ electrode supports (Ni-YSZ/YSZ/LSM-YSZ) with active electrode area of 9.6 x 9.6cm. Stacks were composed of 10 RU* containing cell and interconnects	3.9	850	Cathode: 45% H_2O, 45% CO_2 & 10% H_2 Anode: 100% O_2	Ave. RU = **0.58	-0.2	~920	(Ebbesen et al. 2011)
Ni-YSZ electrode supports (Ni-YSZ/YSZ/LSCF-GDC) with cell active area, 0.5~2.4cm^2	20 ~ 12.5	800	Cathode: 50% H_20, 25% CO_2 & 25% H_2 Anode: Air	*** 0.22	~-0.2	~920	(Zhan et al. 2009)

*Where RU represents the repeating unit in the stack. ** The ASR (0.58 $\Omega\ cm^2$) was calculated from the *i*-V curve. ***The ASR (0.22 $\Omega\ cm^2$) was taken as the total cell resistance obtained from the impedance spectra and not calculated from the polarisation curve

Co-electrolysis of CO_2/H_2O using SOC stacks is vital for achieving large scale syngas production. The performance of the co-electrolysis stack was compared with previous identical single cell as shown in Table 2–4 under similar operating conditions. However, the area-specific inlet gas flow rate which directly relates to the gas conversion polarisation resistance was lower in stack operation (3.9 $m^3/h\ m^2$) than the single cells (15.5 $m^3/h\ m^2$). In the case of multi stack testing, impedance measurements for each repeating unit showed the effects of ohmic and polarisation resistances. The increase in ohmic resistance was observed to originate mainly from cell contact resistance to the interconnect plates while the polarisation resistance originated from an increased gas conversion due to the lower gas flow rates used. In two separate studies carried out under the same operating conditions of 50% H_20 – 50% H_2 at 850^oC and Ni-YSZ fuel electrode, a lower gas conversion resistance was also recorded when operating at a higher flow rate. A gas conversion resistance of 0.05 Ω cm^2 (Ebbesen et al. 2010) was recorded at an area specific inlet gas flow rate of 15.5 $m^3/h\ m^2$ and 0.13 Ω cm^2 (Ebbesen et al. 2011) at 4.9 $m^3/h\ m^2$.

The information given in comparing single cell and stack operation highlights important aspects associated with large scale testing.

2.6.2 Degradation of SOCs under electrolysis operations

Degradation of SOCs during electrolysis investigations can be classified into low current density (<-0.75 A/cm^2) and high current density degradation (>-0.75 A/cm^2) (Ebbesen et al. 2010; Schiller et al. 2009). It has been argued by Ebbesen et al. (2010) that degradation at low current densities is largely attributed to the adsorption of impurities in the feed at the TPB. On the other hand, the effect of cell operation at high current density has predominantly led to degradation and delamination of the oxygen electrode from the electrolyte. Oxygen electrode degradation occurs due to the high oxygen partial pressures at the oxygen electrode/electrolyte interface (Chen and Jiang 2011; Kim-Lohsoontorn et al. 2010; Knibbe et al. 2010; Laguna-Bercero et al. 2011; Virkar 2010).

The majority of the investigations into the degradation of SOCs during electrolysis operations have focused primarily on the use of H_2O/H_2 mixtures. Advancement in the development of this technology (i.e. eliminating all issues of cell degradation) for steam electrolysis would directly benefit CO_2 electrolysis and CO_2/H_2O co-electrolysis operations.

This is because the key issue of cell degradation while operating at high current densities is not a consequence of the chemical feedstock flowed to the fuel electrode but a failure in cell components (i.e. material and microstructure).

2.6.2.1 Degradation mechanism and durability of SOECs at low current density operation

Degradation of SOECs at low current density has been studied over long periods (~1300 hours) of operation. Zhan et al. (2009) tested an electrode supported Ni-YSZ/YSZ/LSM-YSZ, LSM cell under co-electrolysis conditions of 25% H_2, 25% CO_2 and 50% H_2O mixture at 800^oC and current density of -1.05 A/cm^2. A passivation rate of 0.26 mV/h was observed over 100 hours of operation. The slight degradation observed was attributed to a number of possible processes; possible Ni migration in the Ni-YSZ electrodes as a result of the high steam content environment, instability of the LSM air electrodes on YSZ electrolyte and air electrode delamination from the electrolyte.

The co-electrolysis investigation by Ebbesen et al. (2010) operating at 850^oC, -0.25 A/cm^2, 45% H_2O-45% CO_2-10% H_2 and an initial short term cell voltage of 920 mV attributed the effect of operation at low current densities to the presence of impurities in the gas stream. After 50h of operation, they observed a passivation rate of 0.377 mV/h as seen in Figure 2–11. This rate further altered (mostly degradation rather than activation) with time and the last 50 h of operation showed a long term degradation of 0.003 mV/h.

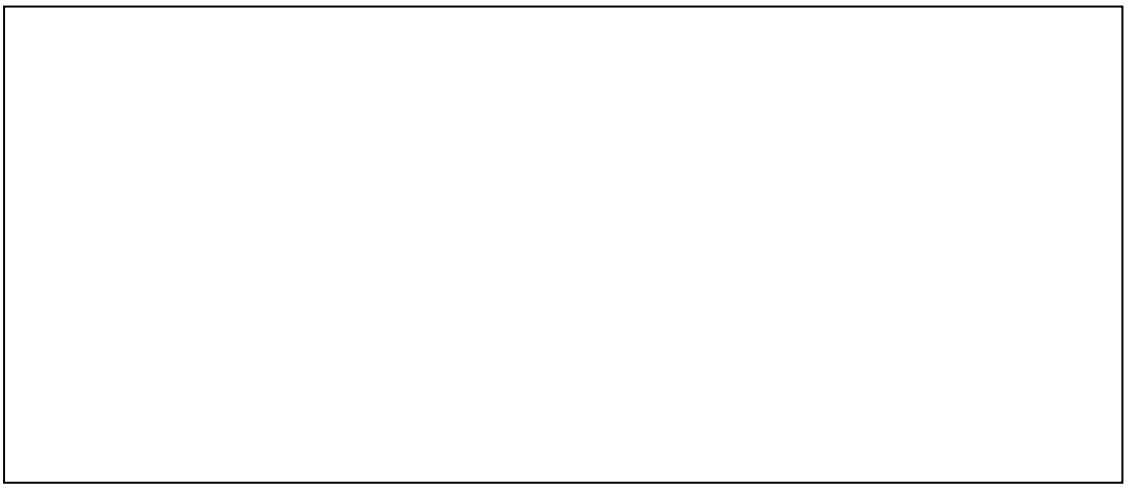

Figure 2–11: Durability test showing cell voltage at Ni-YSZ electrode during co-electrolysis (-0.25 A/cm^2, 45% H_2O-45% CO_2-10% H_2) operation before inlet gasses were cleaned (Ebbesen et al. 2010)

The in-plane voltage shown on the right hand y-axis of Figure 2–11 represents how evenly the direct current is distributed on the metal foil that serves as a current conductor to the cell. Although not entirely shown in Figure 2–11, Ebbesen et al. (2010) observed a slight increase in the cell voltage when the in-plane voltage remained fairly stable towards the end of the operation. Further impedance analysis of the cell showed no change in ohmic resistance whereas polarisation resistance increased indicating the cause of cell degradation. Gas shift analysis of both electrodes showed a significant change in the fuel electrode of the cell whereas only minor changes occurred at the oxygen electrode.

After the inlet gasses had been cleaned to remove any impurities, it was found that both co-electrolysis cells ($A_{H_2O-CO_2}$ and $B_{H_2O-CO_2}$) as shown in Figure 2–12 remained fairly stable with no degradation. During the first 150 hours, the cell voltage of AH_2O-CO_2 increased from 912 mV to 917 and remained stable for 600 h of operation.

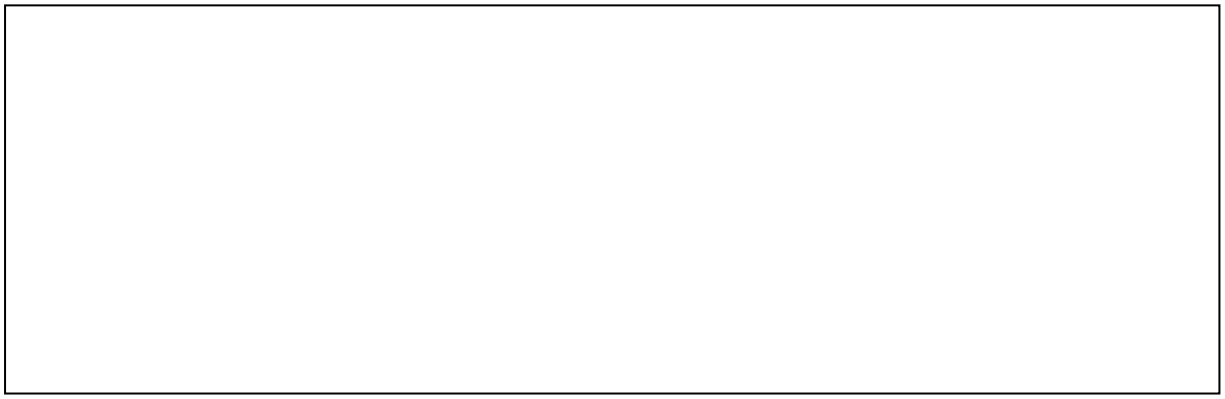

Figure 2–12: Durability test showing cell voltage at Ni-YSZ electrode during co-electrolysis (-0.25 A/cm^2, 45% H_2O-45% CO_2-10% H_2) operation after inlet gasses were cleaned (Ebbesen et al. 2010)

Cell A and B shown in Figure 2–12 are similar cells operating under the same co-electrolysis conditions, however cell A has air supplied to the oxygen electrode while oxygen was supplied to the oxygen electrode of cell B.

Degradation mechanism

From Figure 2–11, an uneven distribution of current was thought to be the reason for the cell passivation. This uneven distribution occurred as a result of the presence of impurities on active sites at the TPB causing partial blockage. Degradation due to poisoning of the Ni in

SOCs under CO_2/CO mixtures has been widely reported in literature particularly during the oxidation of carbon monoxide in fuel cell operation (Cheng et al. 2006; Cheng et al. 2007; Dong et al. 2006; Ebbesen et al. 2010; Ebbesen and Mogensen 2009; Haga et al. 2008; Lussier et al. 2008; Matsuzaki and Yasuda 2000; Rasmussen and Hagen 2009; Sasaki et al. 2006; Zha et al. 2007). This type of catalyst poisoning is typically due to the presence of impurities (typically sulphur compounds such as H_2S) in the Ni electrode with the sulphur compound being adsorbed on the surface of the active Ni sites. It was shown by Oliphant et al. (1978) that poisoning of the Ni catalyst is likely caused by chemisorption of sulphur on the Ni surface.

$$H_2S\ (gas) + Ni\ (solid) \rightleftharpoons Ni\text{-}S\ (surface) + H_2 \qquad 19$$

Zha et al. (2007) explains that the degree of Ni fuel electrode degradation caused by sulphur poisoning is highly dependent on the concentration of H_2S present in the electrode. In another study, nickel sulphides (Ni_3S_2) were observed in the Ni-YSZ electrode which is thought to also contribute to the electrode degradation (Dong et al. 2006). Thermodynamic analysis however suggests that Ni_3S_2 will decompose to metallic nickel and H_2S when operating at temperatures above ~700^oC and partial pressure of H_2S/H_2 is below ~10^{-3} (Cheng et al. 2006).

Ebbesen et al. (2010) argued that as the sulphur impurities accumulated within a certain active site; an increase in voltage difference occurred. As impurities continued to accumulate over more active sites, the cell voltage continued to increase while the in-plane voltage reached its peak point and decayed afterwards. Ebbesen and Mogensen (2009) also observed a similar trend when investigating the durability of SOECs under CO_2 operation. By cleaning the inlet gasses, the initial in-plane voltage decreased to less than 0.1 mV and was seen to be stable for long periods of operation. These results have been further confirmed by Ebbesen et al. (2011) when investigating the performance of a multi SOC stack under CO_2/H_2O co-electrolysis conditions. No degradation was observed at the cathode at current densities up to at least -0.75 A/cm^2 when the inlet gasses had been cleaned.

2.6.2.2 Degradation mechanism and durability of SOECs under high current density operation

Degradation of solid oxide electrolysis cells at high current density (> -0.75 A/cm^2) is one of the greatest concerns for electrolysis operations. For this technology to be commercially competitive, as explained in Chapter 1, the electrolysis cells ought to be durable (with little/no degradation) over long periods of operation. Short-term degradation (~10 minutes) is a frequent occurrence at high current densities. Recent experimental and modelling studies have shown that the effect of high current density operation in SOECs is mainly attributed to the degradation of the oxygen electrode.

It is also important to note that at high cell voltages and according to thermodynamics, electrolysis of dry CO_2 will lead to the formation of carbon, deposited at the fuel electrode and electrode/electrolyte layer of the SOC. This is because the reduction of CO_2 to C (via the reduction of CO) occurs at only a slightly higher potential than the reduction of CO_2 to CO as shown in Figure 2–13. However, carbon formation via electrolytic reduction of CO will only occur above CO_2 reactant conversion rate of 99%.

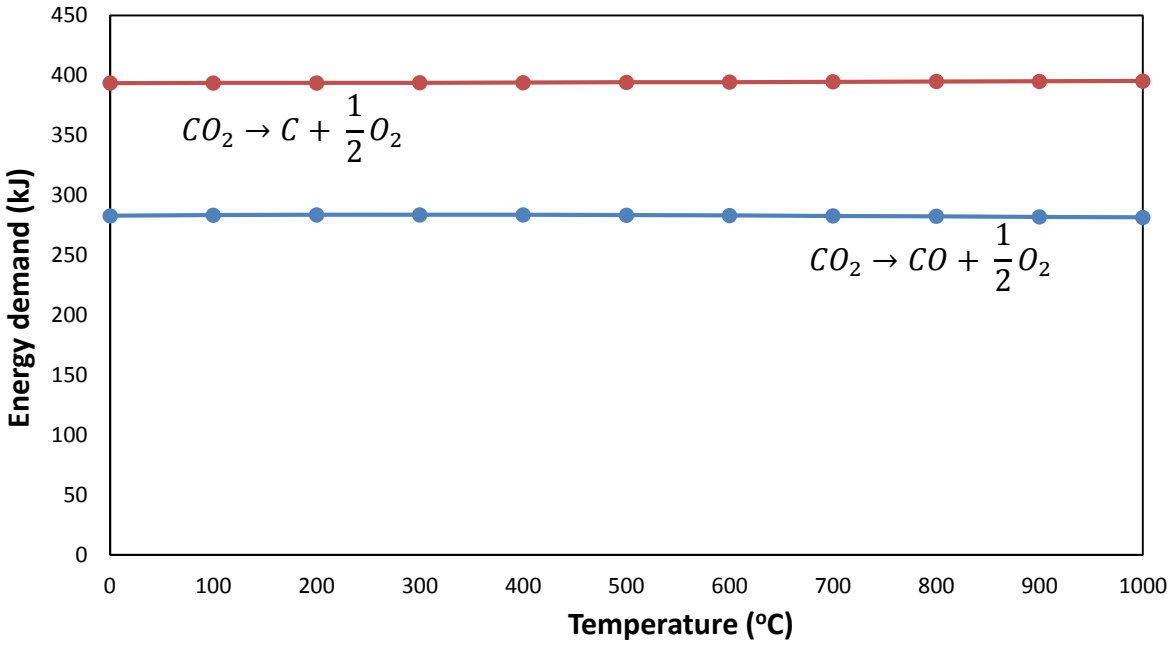

Figure 2–13: Thermodynamics of CO_2 electrolysis for carbon monoxide and carbon production

The formation of carbon is also favoured by the presence of nickel in the fuel electrode which acts as a catalyst for the Boudouard reaction shown in Equation 20. However, the equilibrium reaction favours the reverse reaction under realistic concentrations and SOEC operating temperatures of 850^oC.

$$2CO \rightleftharpoons CO_2 + C \qquad 20$$

The formation of carbon in the active Ni-YSZ electrode is a challenge as this may reduce active TPB sites therefore leading to reduced activity. Recent investigations by (Tao et al. 2014) have observed the formation of carbon in the active Ni-YSZ electrode during co-electrolysis of H_2O and CO_2. This was observed when operating in low porosity Ni-YSZ based SOC at -2.0 and -2.25 A/cm^2, with fuel electrode compositions of 45% CO_2 - 45% H_2O - 10% H_2 and a reactant conversion of 67%. Carbon formation was not observed when operating with cells of high porosity. Tao et al. (2014) ascribes the observed carbon formation to a change in gas composition due to diffusion limitations within the Ni-YSZ support and the active Ni-YSZ electrode.

An investigation by Laguna-Bercero et al. (2011) into SOEC electrolyte degradation at high voltages of operation linked the effect of high current densities to ohmic resistance during steam electrolysis operation. Operating at 895^oC using 70% steam, Ni-YSZ electrode supported cell at current densities above -1.75 A/cm^2, Laguna-Bercero et al. (2011) observed a huge change in potential difference after 10 minutes of operation as shown in Figure 2–14. EIS measurements further showed a 63% increase in ohmic resistance (from 0.23 Ωcm^2 measured before electrolysis operation to 0.37 Ω cm^2 after the test) whereas the polarisation contributions remained almost unchanged (0.31-0.32 Ω cm^2).

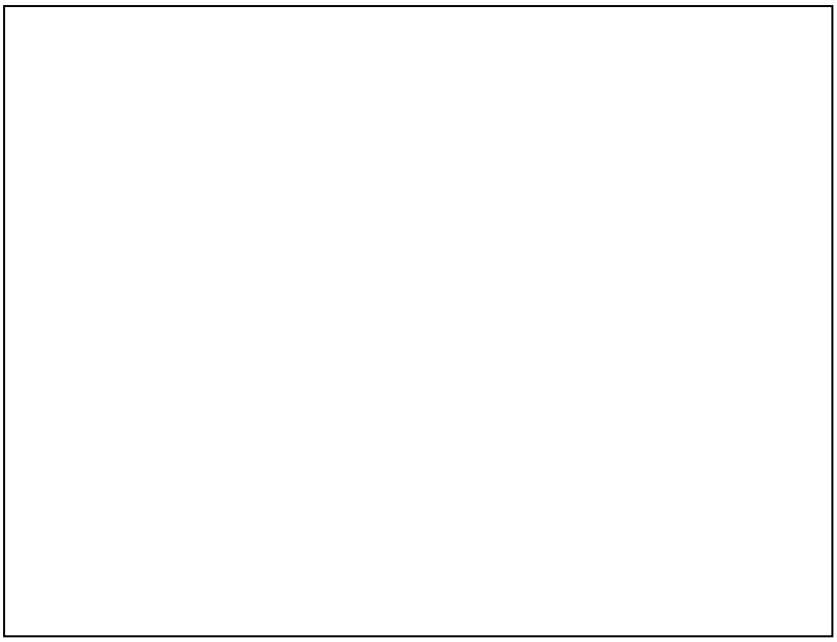

Figure 2–14: I-V curve recorded at 70% steam concentration and at 895^{o}C (Laguna-Bercero et al. 2011)

In addition, further microstructural studies showed that the main damage is observed at the electrode/electrolyte interface at the oxygen electrode. Figure 2–15 shows the effects of a SOEC when operated at high current densities. The scanning electron microscope (SEM) image shows the formation of voids at the grain boundaries of the YSZ electrolyte which leads to the generation of cracks in the electrolyte. The delamination of the oxygen electrode from the electrolyte is thought to be caused by the high rate of oxygen released into the interface layer.

Knibbe et al. (2010) also investigated the effect of high current densities (>-1 A/cm^2) on SOECs. They found ohmic polarisation to be the only cause of degradation. Microstructural analysis in this study further supports the evidence of the effect of high current densities with the formation of voids at the grain boundaries of the YSZ in the region adjacent to the oxygen electrode, even generating larger cracks in the electrolyte. Similar degradation observations have also been reported by other authors (Graves et al. 2011; Knibbe et al. 2010; Laguna-Bercero et al. 2011; Virkar 2010). An electrochemical model by Virkar (2010) predicted this phenomenon of delamination at high current densities. The model showed that under certain conditions, high pressures can develop in the electrolyte/electrode interface at the anode, thus leading to oxygen electrode delamination. Virkar (2010) findings suggested that “an oxygen ion conductor of the highest possible ionic transport

number for example YSZ, may be more prone to degradation and thus is not the desired material as an electrolyte". The presence of electronic conduction in the electrolyte material was suggested to be a potential solution as it could lower the tendency for the formation of high internal pressures. In another study, Chen et al. (2010) showed that the addition of GDC nanoparticles effectively inhibited the delamination of the oxygen electrode from the YSZ electrolyte layer.

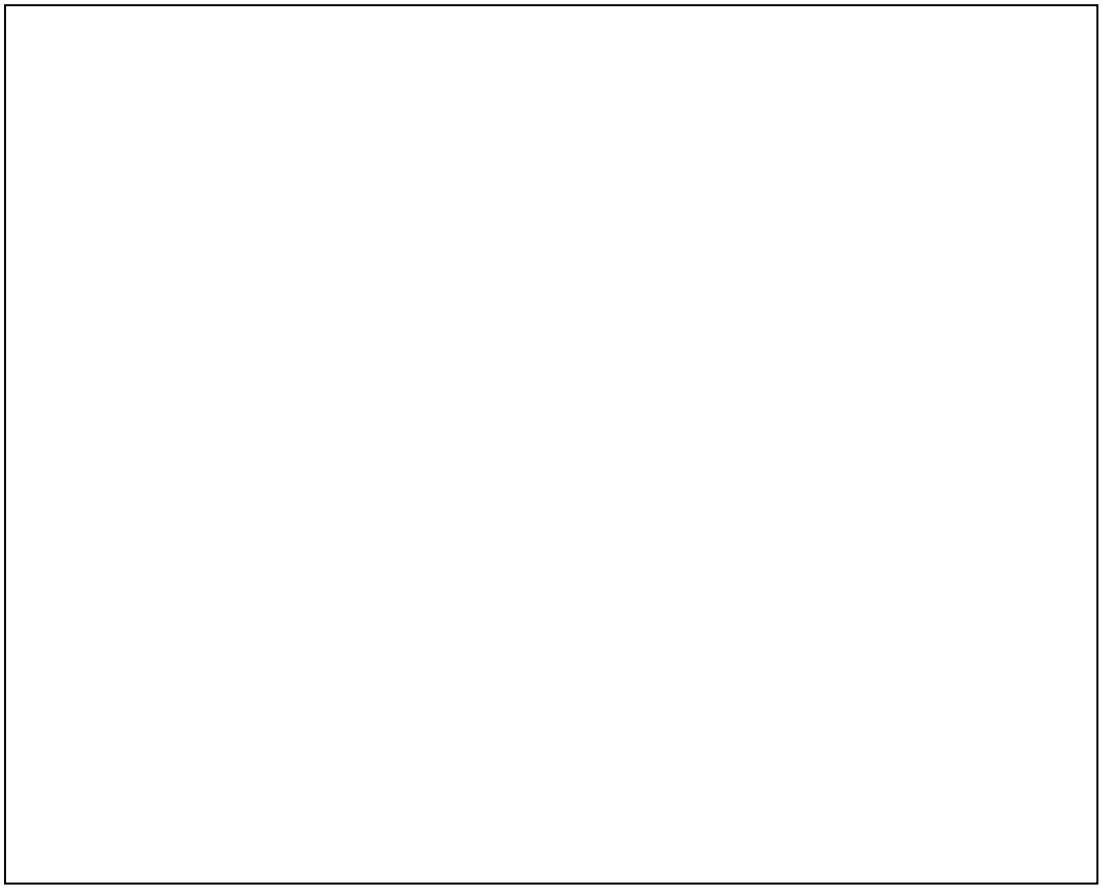

Figure 2–15: (a) represents the original cell, b) origin of degradation, c) cracking of the YSZ electrolyte and d) delamination of the electrode from the electrolyte (Laguna-Bercero et al. 2011)

To summarise, it was shown in Chapter 1 that high current density operation is critical in the advancement of this technology for commercialisation. The studies reviewed in this chapter conclude that operation at high current density is a major challenge due to short term cell failure arising from delamination of the oxygen electrode from the electrolyte. Optimisation of current materials and development of newer materials is needed to eliminate these issues.

Chapter 3

3. Experimental Design, Methods and Commissioning

This chapter details the experimental setup and procedures used in this research. There was no experimental facility available at the start of this research therefore all equipment and instruments were purchased new or designed and constructed in-house.

3.1 Experimental test facility

Figure 3–1 and Figure 3–2 respectively show a schematic flow diagram and picture of the co-electrolysis test setup. Steam and carbon dioxide electrolysis were also carried out using this apparatus. The key experimental components include gas cylinders, mass flow controllers (MFC), temperature controllers, rope heaters, water bath, steam sensor, cell rig, high temperature furnace and a solid oxide cell (SOC).

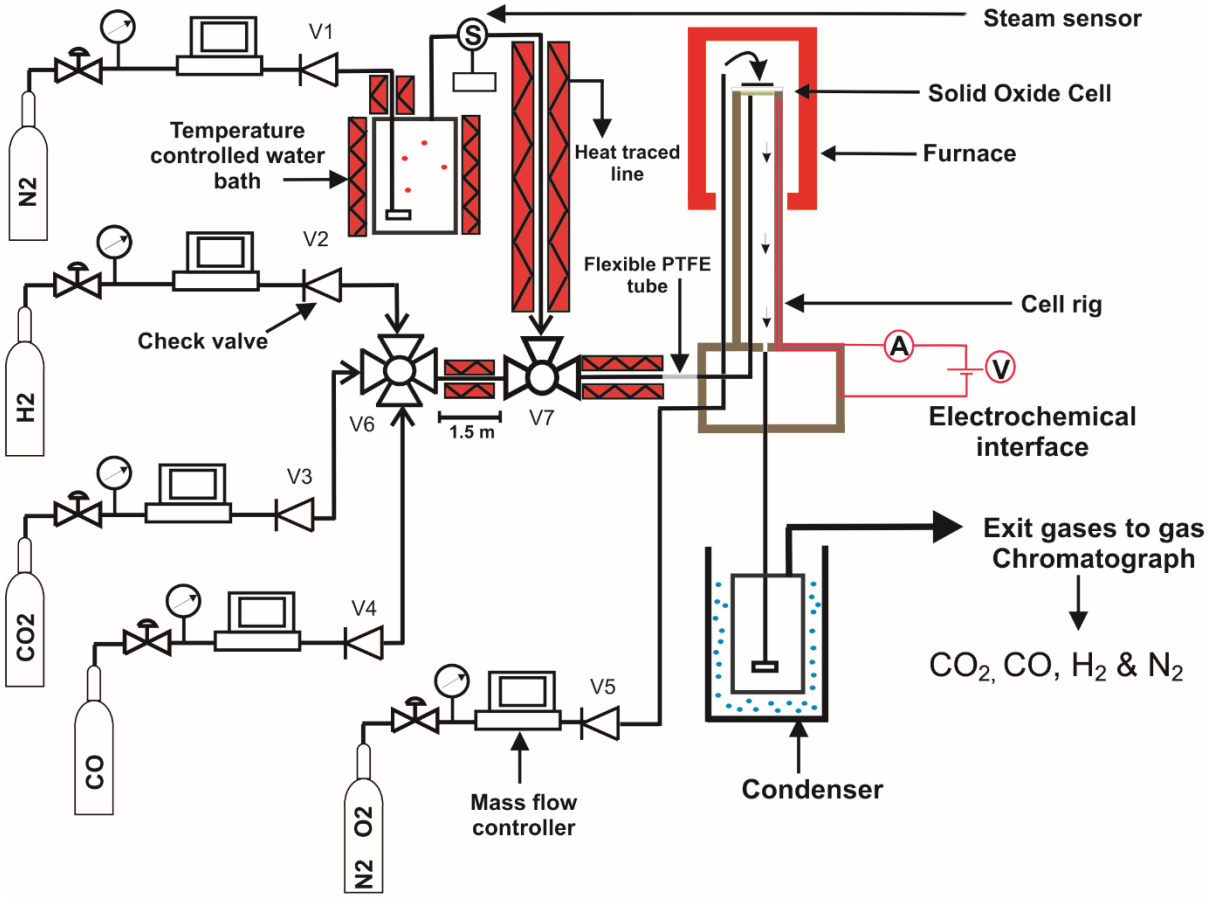

Figure 3–1: Schematic diagram of the experimental setup for the production of syngas via the high temperature co-electrolysis of carbon dioxide and steam

To minimise the presence of impurities in the SOC, gasses (80% N_2, 20% O_2: Research grade, BOC; N_2: Research grade, BOC; CO_2: Research grade, BOC; H_2: Research grade, BOC and CO: Research grade, BOC) with 99.999 % purity were used with an exit pressure of 1 bar. In addition, a gas filter is fitted prior to each MFC to prevent a build-up of particles in the flow equipment, thus avoiding damage. The flow rates of the gasses were controlled by precise mass flow controllers (red-y) each with a full scale accuracy of ±1.5 %. The check valves (V1

to V5) indicated in Figure 3–1 are important in order to avoid reverse flow of gasses to the MFCs which could result in the damage of the mass flow equipment. The steam content was controlled by varying the temperature of water in the water bath with nitrogen used as a carrier gas.

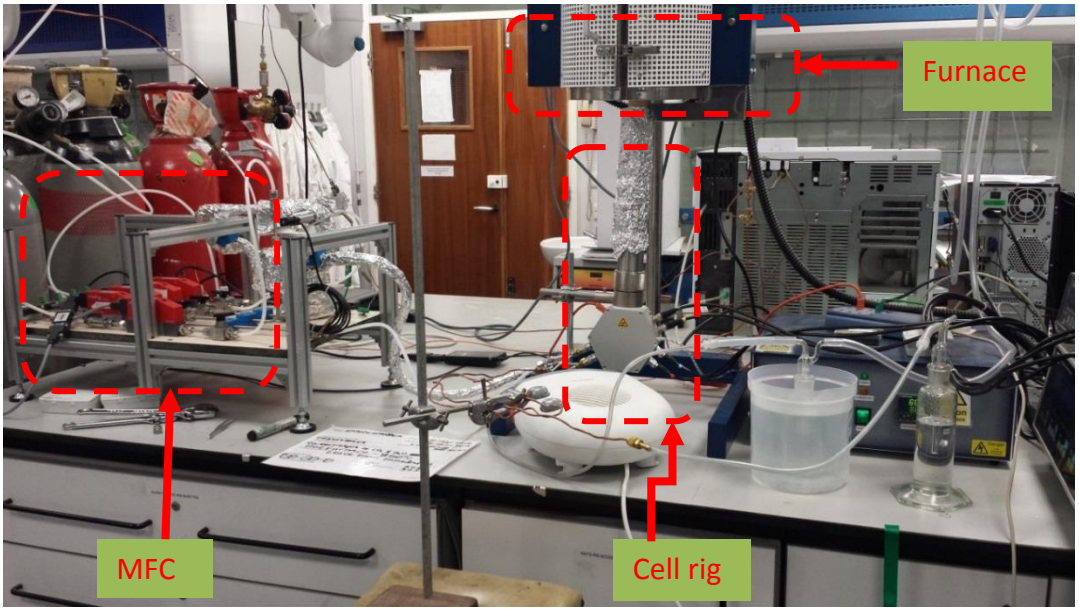

Figure 3–2: Picture of high temperature electrolysis test facility

The connecting gas line between valves 6 and 7, as shown in Figure 3–1, is about 1.5 m long (as a spiral tube shown in Figure 3–3) and heated to 120°C to ensure the cold gasses (exiting the cylinders) do not condense the steam/N_2 mixture. Downstream of the water bath, all gas lines are heat traced (120°C) to avoid any steam condensation before entering the cell rig located in the furnace. The gas lines within the base unit of the cell rig are also heated to 120°C.

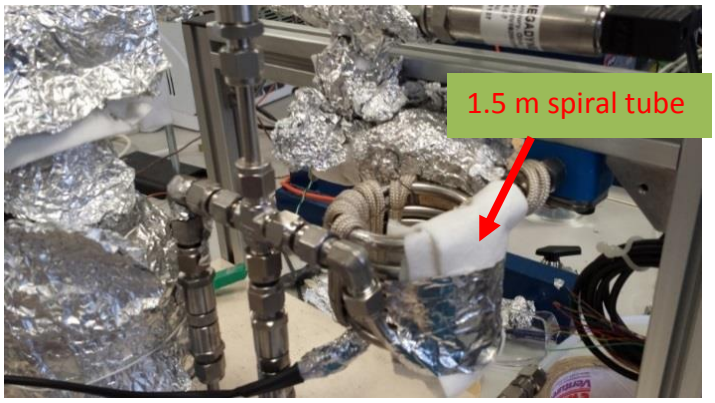

Figure 3–3: Schematics showing the 1.5 m heated stainless steel tube as a spiral tube

The high temperature furnace is a vertical split tube furnace (Elite Thermal Systems Ltd) with a height of 300 mm and an inner diameter of 38 mm. The electrolysis products and unreacted gases exiting the cell rig pass through a condenser to remove any steam content before analysis in a gas chromatograph (GC). This is done to avoid damaging the GC as reaction of water with the polymer in the stationary phase typically leads to the degradation of the stationary phase (Kuhn 2002). Other issues regarding the presence of water in the GC include quenching of the flames within the flame ionisation detector (Kuhn 2002). Exiting the GC, the co-electrolysis products are directed to a fume cupboard to remove the hazardous exhaust gasses.

3.2 In-house cell rig design

At the initial stage of this project, an in-house button cell rig was designed and partially constructed prior to the acquisition of the ProboStat^{TM} (cell rig used during this research). Due to time constraints and mechanical issues associated with sealing around the cell to avoid gas leakages, the in-house cell rig project could not be fully completed. The design of the in-house button cell rig and recommended solutions to the sealing issue is discussed in this Section. In the design and development of this cell rig, two crucial factors were identified. They include appropriate material selection to avoid any long term failure and solid oxide cell sealing to avoid any gas leakage.

3.2.1 Material selection

Due to its high operating temperature and the possibility of corrosion arising from steam use at the fuel electrode over long periods of operation, the selected material must retain its strength and be resistant to corrosion at elevated temperatures. Therefore, the selected material for use at the fuel electrode was Inconel alloy 625. Inconel is a family of nickel-chromium super alloy commonly used in high temperature environments or/and in cases of potential corrosion issues. At the oxygen electrode, stainless steel was used due to its relatively low cost and ability to also withstand temperatures of up to 950^{o}C.

3.2.2 Solid oxide cell sealing

As shown in Figure 3–4, the inlet and outlet tubes for both electrodes were sized differently. At the inlet, the gasses from the fuel and oxygen electrode sides were sized to have a 3 mm OD diameter tube while at the outlet, the gasses from the fuel and oxygen electrode side

were designed to have a 5 mm OD diameter tube. The outlet tubes were sized larger than the inlet tubes in order to minimise back pressure on the cell. The most important aspect of this design focused on ensuring any form of gas leakage in the rig is avoided, therefore good sealing is important. As shown in Figure 3–4, a spring loaded sealing assembly was employed. In order to understand this method of sealing, the purposes of the metal cap and holding zirconia tubes are explained.

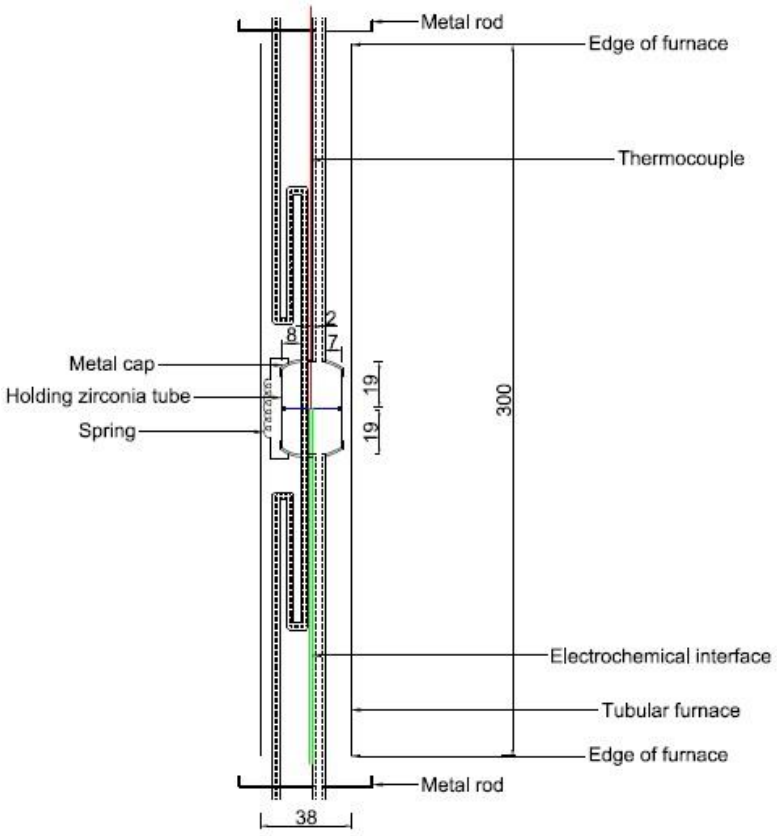

Figure 3–4: Front view design of the in-house cell rig design with dimensions in mm.

The metal caps were made out of stainless steel and are important to provide support to the inlet and outlet tubes of both electrodes. In addition, they act as a platform for the springs. During construction, these caps were joined to the holding zirconia tubes at the fuel and oxygen electrode sides. Zirconia was the chosen material for the holding tubes due to its ability to retain its strength at elevated temperatures and because it is resistant to corrosion. The holding tubes are also important to provide support to the inlet tubes at the fuel and oxygen electrode Section.

The mesh, cell and seal were sized to fit into the inner space between the zirconia holding tube at the fuel and oxygen electrode. Mica, a compression seal, was selected as the preferred sealing material. Unlike other sealing materials such as glass which require a high temperature (up to 950^{o}C) heating profile to form its seal, mica is generally known to be as effective at low (room temperature) and high temperatures. Furthermore, the use of Mica would significantly reduce the start-up time which is usually at least 14 hours when a glass seal is employed. The attached spring shown in Figure 3–4 is situated in the middle of the furnace and is vital in holding the cell mesh and seal. This compression is important for two reasons; to avoid gas leakages at either electrode sides and to aid electrical contact between the mesh and the cell.

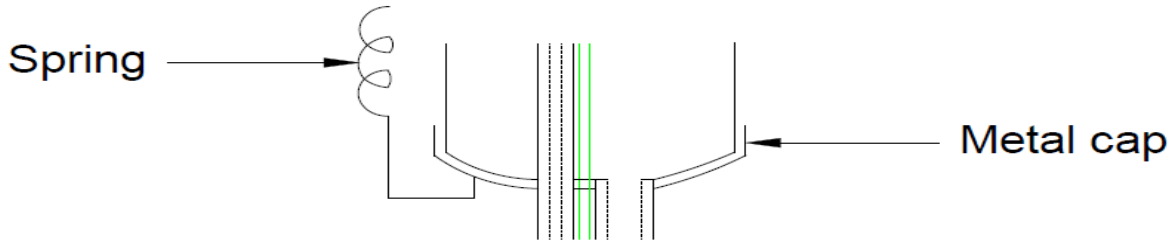

Figure 3–5: Expanded view of metal caps attached to the inlet and outlet tubes of the fuel electrode

3.2.3 Electrochemical measurements

Electrochemical measurements are important in characterising the cells under operating conditions. As seen in Figure 3–5, one of the platinum wires is used as a current lead and the other as a voltage. In addition, a thermocouple is located next to the cell for continuous measurement of the cell temperature. An electrical current collector (Ni and Ag mesh at the fuel and oxygen electrode respectively) were designed to be used in the transfer of electrons across the cell. In a study conducted by Yoon et al. (2007) at 800^{o}C, a higher contact resistance was observed when operating using a platinum mesh instead of silver. It was proposed that because the melting temperature of Ag (961^{o}C) was significantly lower than Pt (1772^{o}C), Ag is expected to be softer than Pt at 800^{o}C, leading to a higher interfacial area between the contact electrode and the Ag current collector. As a result, the contact resistance is lowered. Based on the above findings, the rig was designed for use with Ag mesh and operated to a maximum temperature of 850^{o}C.

The details of the instruments expected to be used as well as the electrical measurements such as scan rate in acquiring polarisation curves, electrode type measurements, impedance amplitude, frequency ranges, etc are given in Section 3.6.

3.2.4 In-house cell rig conclusions

The key challenge with this design, as later discovered, was associated with the durability of the springs at high temperature. At 850^{o}C, the springs lost their strength over a short period of operation. As such, this weakness could lead to gas leakages during operation. The main solution proposed to this problem involved the use of extension springs made out of either Inconel or hastelloy, a nickel based alloy able to withstand temperatures of up to 1100^{o}C with extremely stable performances.

3.3 Cell rig – ProboStat™

The cell rig (ProboStat™) used during this study was purchased from Norwegian Electro Ceramics AS (NorECs). Figure 3–6 explains the constituents of the ProboStat™ base unit. The different accessories used are shown in Figure 3–7 and discussed in Table 3–1. In addition, a schematic of the inwards and outwards flow of gasses to the cell rig is shown in Figure 3–8.

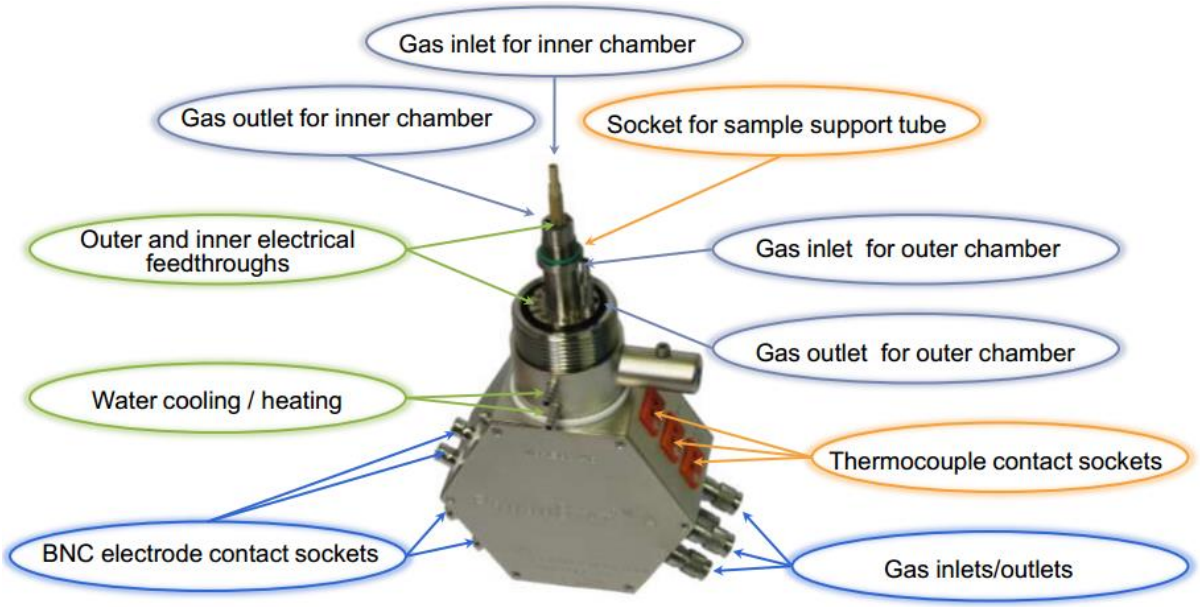

Figure 3–6: Description of the key parts of the base unit (NorECs 2014)

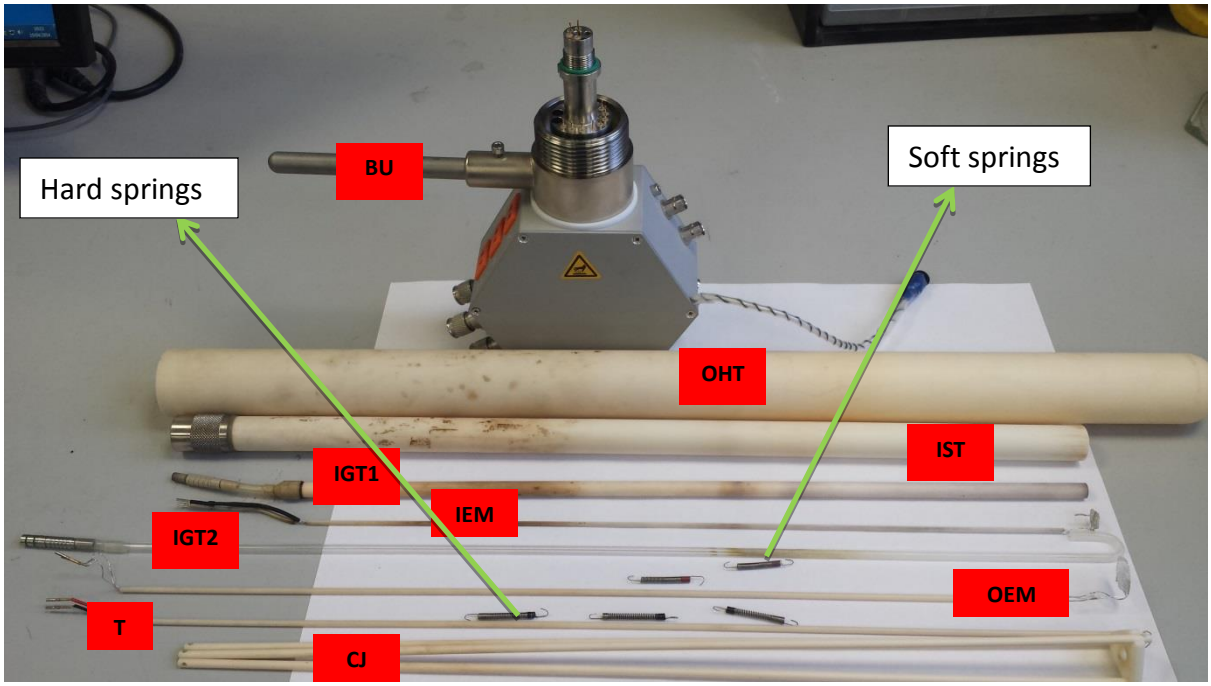

Figure 3–7: Primary components of the cell rig

Table 3–1: Description of the components in cell rig assembly

Initials	Description	Purpose
BU	Base unit of the cell rig	See Figure 3**–6**
IGT1	Inner gas tube for the inner chamber	This tube connects the inlet gasses to the fuel electrode of the SOEC
IEM	Inner electrical mesh	The IEM is used as a current collector on one electrode side
IST	Inlet support tube	This tube is used to support the cell and the seal.
OEM	Outer electrical mesh	The IEM is used as a current collector on the other electrode
T	Thermocouple	Connected to the electrical feed through and used to continuously monitor the cell temperature
CJ	Compression jig	This is used with the springs attached to impose pressure onto the cell and seal thereby minimising gas leakages
IGT2	Inner gas tube for the outer chamber	Made out of glass, this tube connects the sweep gasses to the oxygen electrode of the SOEC
OHT	Outer holding tube	This holding tube is used to prevent the loss of sweep gasses to the surrounding environment

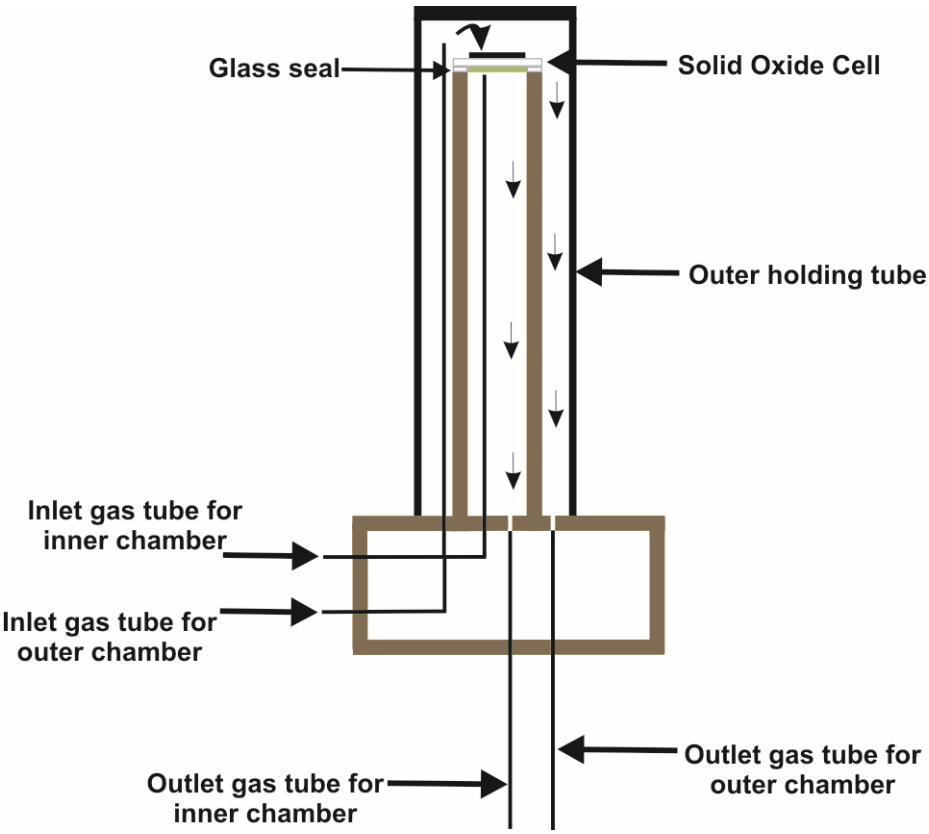

Figure 3–8: Schematic diagram showing the flow of gasses in and out of the cell rig

The soft springs shown in Figure 3–7 were used for the majority of the cell investigations. The stiffer springs (hard springs) were later found to be more efficient in reducing gas leakages and consequently employed in later studies.

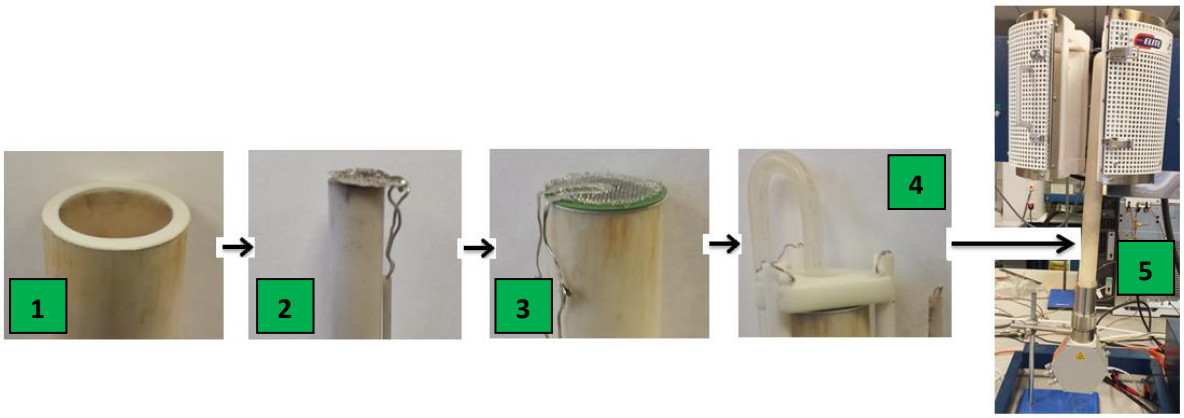

Figure 3–9: Procedure of cell loading during rig set-up

Figure 3–9 shows the procedure of cell loading during the rig set-up. The steps are:

1. A glass seal (Kerafol) is initially mounted onto the inlet support tube, which is held in place using an adhesive
2. The inner gas tube for inner chamber and inner electrical platinum mesh are then connected to the base unit
3. With the glass seal firmly held on the inlet support tube, the cell and outer electrical platinum mesh are then placed on top of the tube. The glass seal is a high temperature sealing material sourced from Kerafol and its firing schedule is described in Section 3.6 (Kerafol 2014).

   Mica, a compression seal was also tested. Initial investigations showed an OCV of 46 mV below the measured potential when using a glass seal at the same operating conditions, indicating larger gas leakages with mica. Mica was therefore not used in experiments.

4. The thermocouple and the inner glass tube for outer chamber are then connected to the base unit.
5. Finally, the outer holding tube is then mounted before the cell rig is placed in the furnace

3.3.1 Cell rig damage

During initial investigations and shortly after the acquisition of the rig, the current and voltage feedthroughs were observed to have significantly corroded under steam electrolysis operation as shown in Figure 3–10. The damage is thought to have occurred as a result of an electrochemical reaction of the feedthroughs with water acting as an electrolyte. The presence of H_2O is thought to have originated from a slight leak of H_2 around the cell burning in oxygen within the hot-zone of the furnace. It is important to note that no stray currents were observed as the electrical cell rig measurements showed no signs of electrical short circuit across anywhere on base unit of the cell rig.

The base unit and the electrochemical interface were replaced with a newer model changing from a Solatron 1286 to a 1287 electrochemical interface instrument. No further electrical damages were observed after the changes had been made although small amounts of water were still frequently seen upon dismantling of the cell rig.

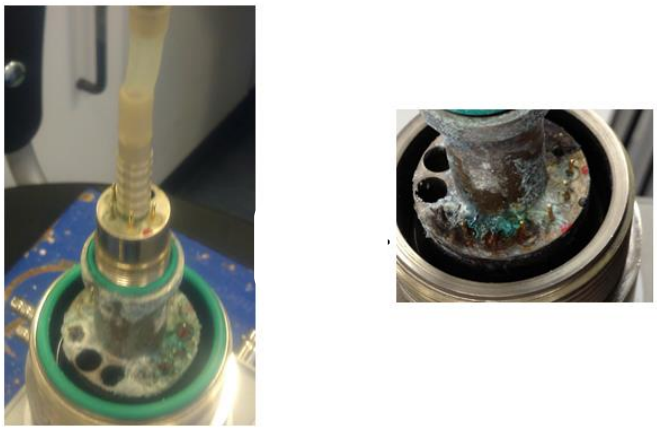

Figure 3–10: Picture of the corroded cell rig

3.4 Experimental Button cell Testing

3.4.1 Solid Oxide Cells

The SOCs used throughout this research were sourced from an external supplier fuelcellmaterials (FuelCellMaterials 2013). Both electrolyte and electrode supported cells are tested. Scanning electroscope microscopy (SEM) was used to confirm the components of the cells.

3.4.1.1 NextCell™ Electrolyte Supported SOEC

The NextCell™ electrolyte supported SOEC is made up of NiO-GDC/NiO-YSZ as the fuel electrode, LSM/LSM-GDC as the oxygen electrode and a Hionic™ electrolyte support. The "Hionic™ substrate is more than four times stronger than conventional fully stabilised YSZ - 8 (8 mole% yttria stabilised zirconia) electrolyte with ionic conductivity comparable to ScSZ – 10 (10 mole % scandia stabilised zirconia)" (FuelCellMaterials 2013). Table 3–2 shows the various properties (diameter and thickness) of the cell. Figure 3–11 is a SEM image of the electrolyte supported cell confirming the relative thickness of each region. The porosity of the electrodes in this cell is about 20-35%.

Table 3–2: Electrolyte supported SOEC

	Anode	Cathode	Electrolyte
Material	LSM/LSM-GDC	NiO-GDC/ NiO-YSZ	Hionic^{TM} electrolyte support
Diameter (mm)	12.5	12.5	20
Thickness (µm)	50	50	130 - 170

The active cell area for the electrolyte supported cell is 1.227 cm^2

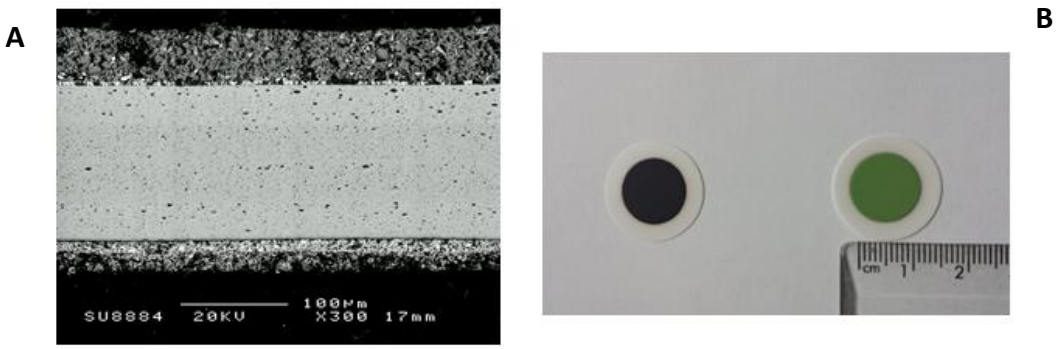

Figure 3–11: A) SEM image of the electrolyte supported cell and B) Top and bottom view of the electrolyte supported cell

3.4.1.2 NiO Electrode Supported SOEC

The electrode supported SOEC is made up of NiO-YSZ support as the fuel electrode, LSM-GDC as the oxygen electrode and 8-mol YSZ as the electrolyte. Table 3–3 shows the material compositions and dimensions (diameter and thickness) of the cell. SEM analysis was also carried out on an electrode supported cell as shown in Figure 3–12. The porosity of electrodes in this cell is about 40-50%.

Table 3–3: Electrode supported SOEC

	Anode	Cathode	Electrolyte
Material	LSM-GDC	NiO-YSZ	YSZ-8
Diameter (mm)	12.5	20	20
Thickness (µm)	50	220-260	6-10

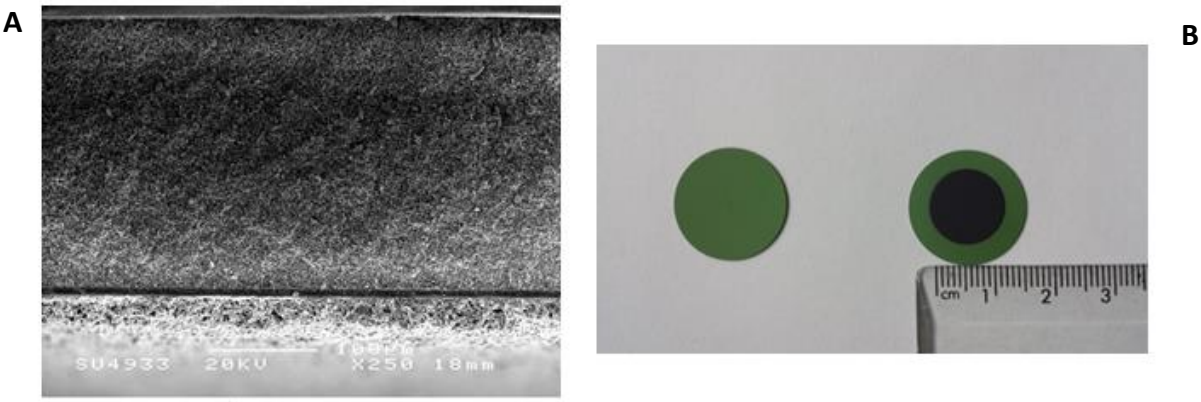

Figure 3–12: A) SEM image of the electrode supported cell and B) Top and bottom view of the cell

3.5 Steam Production

Reliable and accurate steam production is essential for experimental work on CO_2/H_2O co-electrolysis; however, it is also difficult due to issues with precise temperature control and condensation. The reaction between H_2 and O_2 over a catalyst bed is a process employed at the Risø research facility at the Technical University of Denmark. In this process, continuous monitoring of furnace temperature is important due to the exothermic nature of the reaction (Ebbesen et al. 2012).

In the work carried out by Kim-Lohsoontorn et al. (2010), steam was produced by supplying a known quantity of water through a liquid pump onto a heated sand bath. The produced steam is then mixed with a carrier gas which is vital for controlling steam ratio in the gas compositions. In this project, steam is produced via the use of a temperature controlled heated water bath and a carrier gas (N_2). This method of steam production is similar to that employed at the Idaho National Laboratory.

3.5.1 Experimental setup

Figure 3–13 shows the temperature controlled water bath and humidity sensor employed for steam production and measurement. The heated water bath is a 500 ml gas wash bottle (Duran) wrapped with a heat tape and insulated using fibre glass insulation and aluminium foil. A filter with pore size 100 – 160 µm is fitted to the diffuser in the water bath and this is vital in order to increase the efficiency of gas absorption in the water bath. Duran (2014) has previously shown that the efficiency of gasses absorbed in liquids can increase up to a factor

of four when a filter plate is employed. De-ionised water was used in the water bath to avoid the presence of any impurities. The water bath temperature is measured with a K-type thermocouple and controlled with a proportional-integral-derivative (PID) temperature controller (Chemical and Biological Engineering - Electronics workshop, University of Sheffield) to adjust the set point temperature (SP).

The control and performance of the employed PID controller is very important during steam production. Using the first generation controllers, an excess supply of power was frequently observed when the set-point temperature was increased, thus leading to a temperature overshoot. This temperature overshoot was due to the large set-point range for the PID temperature controller (-200 to 200^{o}C); resulting to an increased start up time of ~90 minutes. Using the second generation controllers in which the set-point range for the PID temperature controller was adjusted closer to the project operating conditions (-10 to 100^{o}C), the process temperature became equal to the set point temperature after ~15 minutes

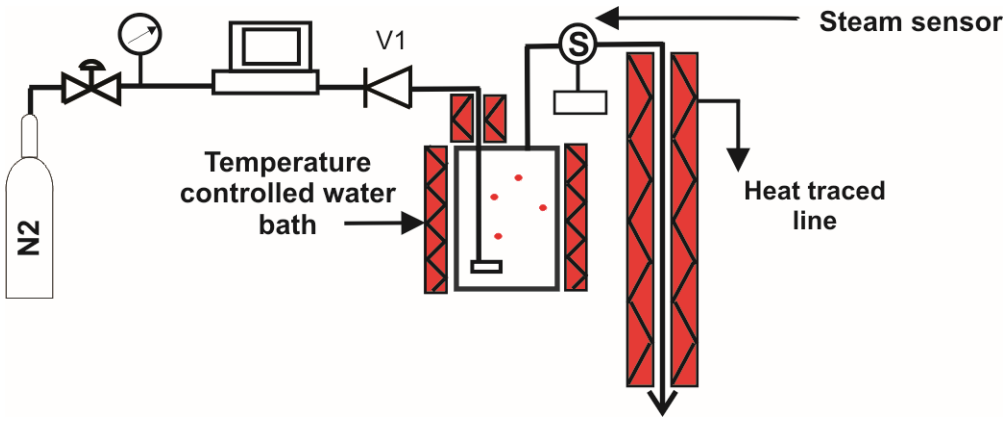

Figure 3–13: Schematic diagram showing the process of steam production and measurement

Using the set-up shown in Figure 3–13, the produced steam/N_2 mixture was measured over a range of water bath temperatures. A steam sensor (Viasala HMT 338 humidity and temperature transmitter) mounted downstream of the water bath was used to monitor the steam content exiting the water bath. The sensor is a thin film water-active polymer sandwiched between two electrodes and it measures the relative humidity (RH) of the gas. The sensor works by absorbing and releasing moisture which changes the dielectric properties of the polymer and changes the capacitance. The capacitance is directly related

to the relative humidity (RH). With the measured RH value, the vapour pressure and other steam parameters are then calculated.

Note: The steam sensor used in this research did not have a data logger. As a result, the output data were collected manually from the visual display of the instrument.

3.5.2 Effect of varying the water bath temperatures and carrier gas flow rate

Initially, all gas lines downstream of the water bath were heat traced to 84 ±1°C. The test rig was calibrated for varying flow rates of N_2 (10 and 50 ml/min) and water bath temperatures (30 – 75°C) to determine the steam content within the mixture as show in Figure 3–14. During measurement, the steam/N_2 mixture was continuously recorded for 3 hours after the process temperature had reached its set point temperature and the steam produced in all cases was observed to be stable within the error range shown in Figure 3–14.

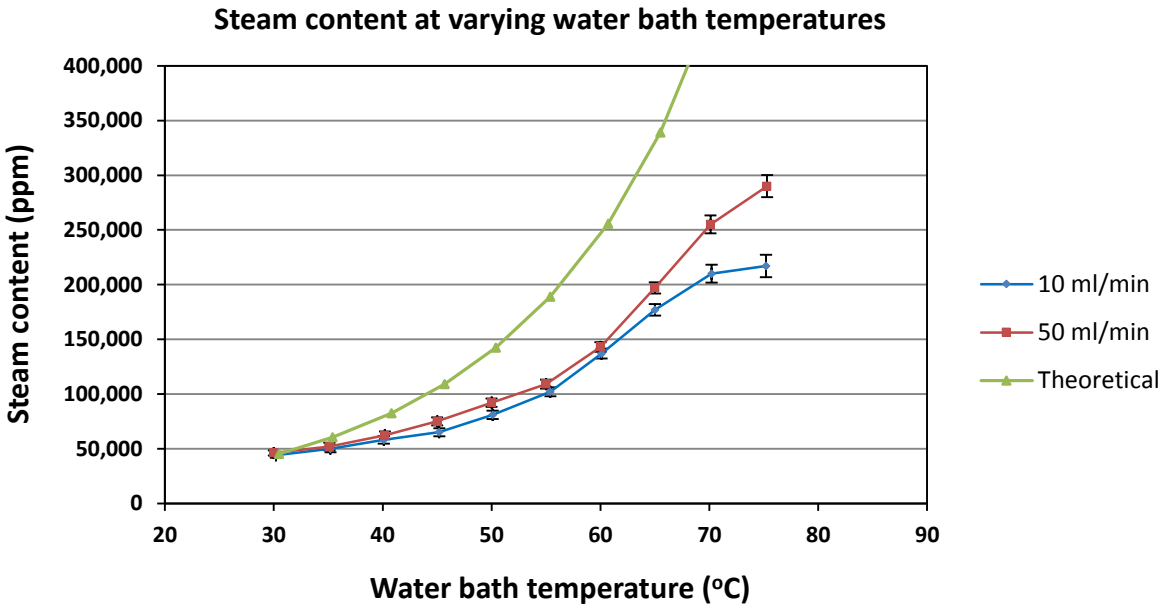

Figure 3–14: Steam content measured at varying water bath temperature between 30 – 75°C when operating at a heat traced line temperature of 84°C

The error in the measured values originates from two key sources;

- 1% measured relative humidity accuracy of the instrument, equivalent to ~±360 ppm and ~±5200 ppm at 30 and 75°C water bath temperatures respectively.

- Random error caused by fluctuations in the measured value over the period of operation. This error is equivalent to about 2000 ppm at 30°C and 5000 ppm at 75°C.

The theoretical data given in Figure 3–14 assumes 100% saturation of N_2 in the water bath (i.e. water bath temperature equal to the dew point temperature) and was calculated from humidity parameters using the Viasala humidity calculator (Vaisala 2014). An increasing difference of experimental and theoretical values with increasing water bath temperature indicates either a possibility of condensation before measurement or difficulty in saturation of the carrier gas. From Figure 3–14, it has been shown that the steam content increases with an increase in water bath temperature. This is expected due to a more rapid movement of the water molecules with increasing supply of heat thereby causing an increased separation of the hydrogen bonds that holds the molecules. At water bath temperatures above 75°C, the measured steam content at 50 ml/min of N_2 became increasingly unstable leading to the formation of water spikes as shown in Figure 3–15. This instability is thought to be caused by the formation of tiny water droplets close to the sensor as the dew point temperature became closer to the temperature of the heat traced line.

The dew point temperature when operating at 84°C process line temperature and 75°C water bath temperature is 58°C and 63°C for 10 and 50 ml/min respectively.

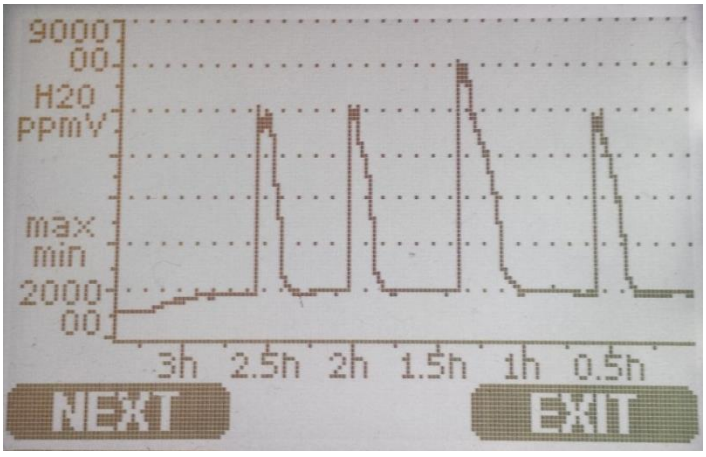

Figure 3–15: Steam spikes observed water bath temperature of 75°C, heat traced line at 84°C when operating at a carrier gas flow rate of 50 ml/min

The heat traced lines were heated to 120 ±1°C and the steam content was measured for 10 ml/min of carrier gas and varying water bath temperatures (30 – 85°C). As expected and

shown in Figure 3–16, the steam content increased with increasing water bath temperatures. Furthermore, at water bath temperatures above 75°C, the increased steam content was observed to be stable. This enhanced performance confirms the previous hypothesis that the unstable steam content at higher water bath temperatures was mainly caused by the lower heat traced line temperature which therefore resulted in condensation.

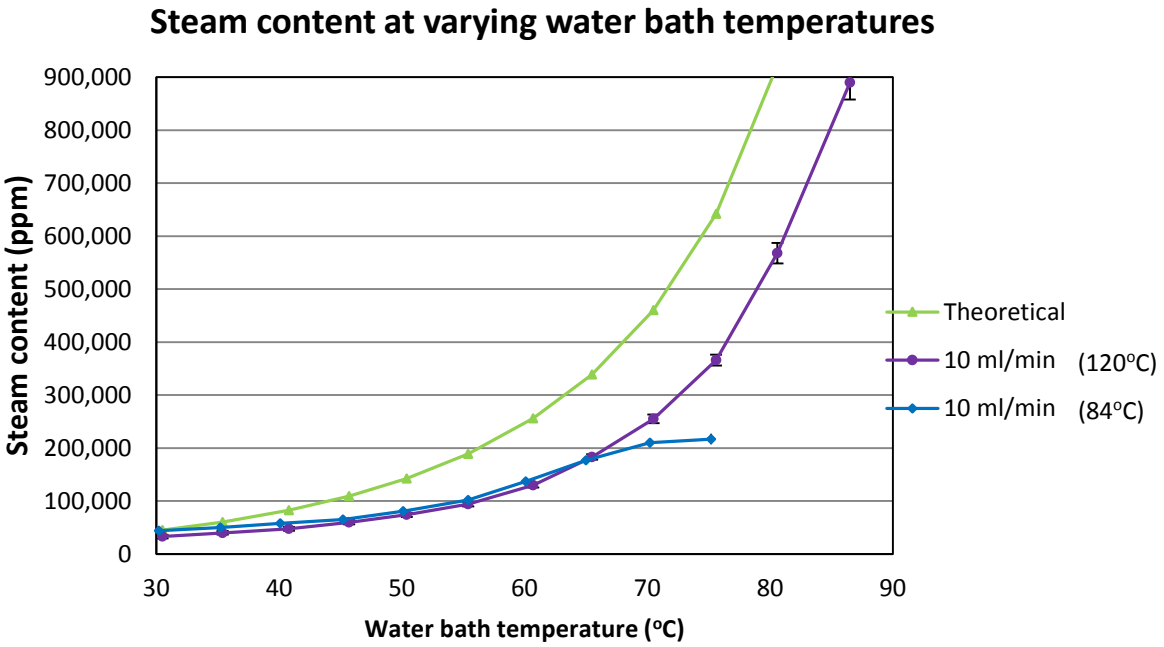

Figure 3–16: Steam content measured at varying water bath temperature between 30 – 75°C when operating at a heat traced line temperature of 120°C

As shown in Figure 3–14, the steam content increases with an increase in carrier gas flow. This result is in direct contrast with literature sources (Duran 2014; Namies´nik 1984) which shows that a test gas concentration is closer to the saturation when a bubbler system works with a low flow rate. This is because the residence time of the gas in the liquid is longer. In this study as shown in Figure 3–14, the concentration of steam at 50 ml/min is closer to saturation than at 10 ml/min. One possible explanation is that condensation continuously occurs at varying degrees along the process line. As a result, a higher flow gas is therefore expected to condense at a much slower rate.

3.5.3 Condensation of Steam downstream of the Water bath

Downstream of the steam sensor, two key regions of condensation were identified. They include the flexible PTFE tube Section and the region between the base unit of the cell rig and the furnace.

A fan heater is now used to heat the flexible PTFE tube in order to eliminate any condensation. The use of the PTFE tube instead of a heated stainless steel pipe is important to avoid any electrical short circuit from the rope heater on the gas line to the base unit of the cell rig. In addition, the flexibility of the PTFE tube is crucial in gas connection due to the orientation of the base unit upon loading to the furnace.

A simple experiment was carried out to understand the effect of condensation in this region. While operating at a gas line and water bath temperatures of 135°C and 70°C respectively, N_2 was flowed through the water bath at 10 ml/min. The N_2/steam mixture was measured downstream of the initial steam sensor with and without the use of the heater at the PTFE Section. Figure 3–17 is a graph of steam content against time of operation with and without the use of a fan heater. The steam spikes seen in Figure 3–17 are very similar to that shown in Figure 3–15 and are thought to originate from sudden flashes of water droplets which condensed at the cold PTFE tube region.

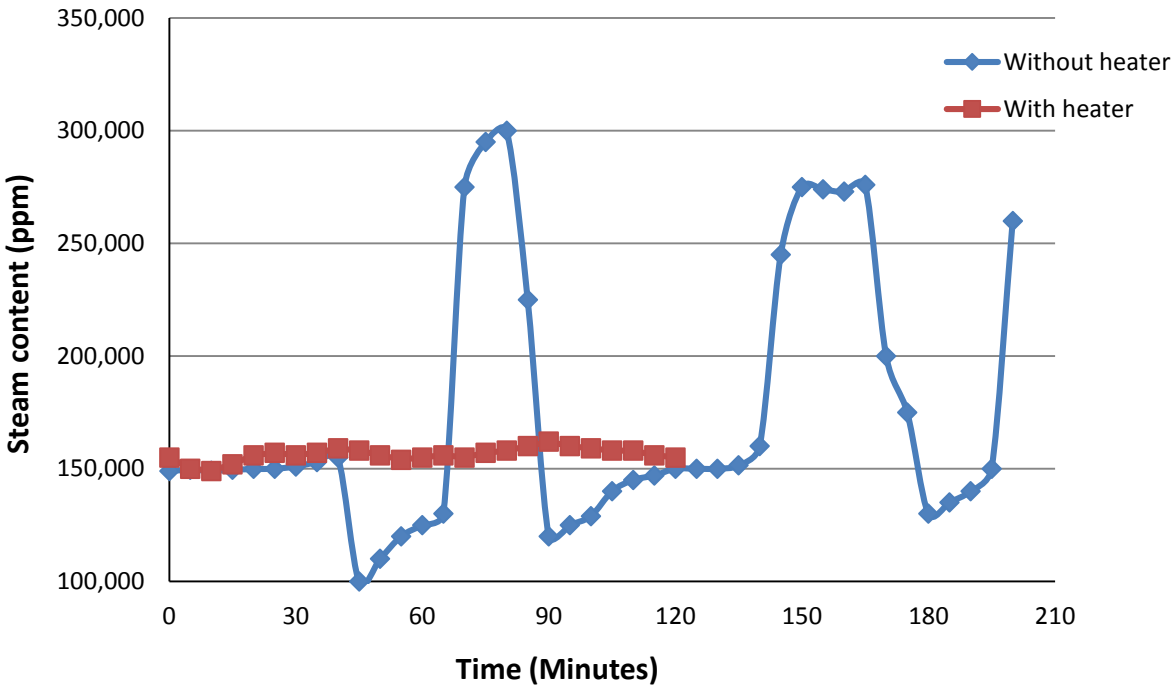

Figure 3–17: Stability of the steam produced with and without the use of a heater

Condensed water was frequently observed in the inlet support tube between the bottom of the furnace and the base unit due to the short furnace length. With the outer tube temperature of the cold spot area measured to be ~ 40°C (lower than the dew point temperature while operating at high steam content), it was therefore concluded that a large portion of the steam previously directed towards the fuel electrode was likely to have condensed in this region.

To eliminate this issue of condensation, a copper heated insulation system as shown in Figure 3–18 was developed. The insulation consists of a rope heater sandwiched between two thin copper sheets. For use, the heated sheets are wrapped around the holding tube between the base unit and the furnace while operating at 200°C. It is expected that at this temperature, the heater will supply enough power to the inlet gas tube for the inner chamber. The layout of the rope heater across the copper sheet was designed such that the heat will be evenly distributed across the length of the copper sheet in order to avoid cracking of the alumina tube.

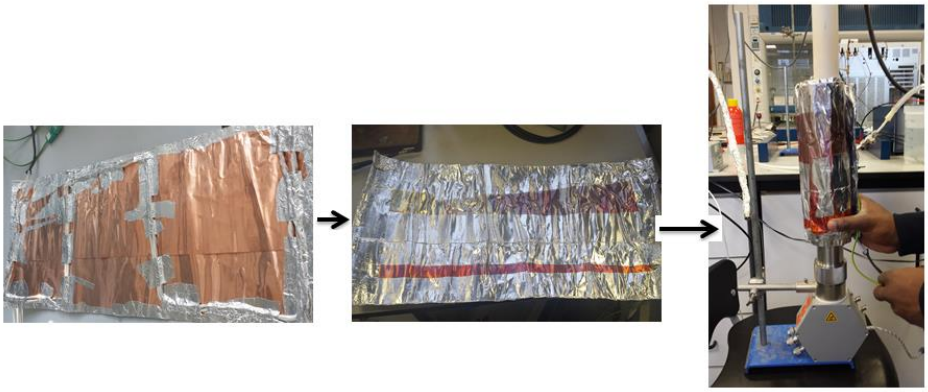

Figure 3–18: Schematics of the heater sandwiched between 2 copper sheets

To summarise, it has been shown that the use of a carrier gas and a bubbler coupled with a temperature controller is a feasible process for stable steam production up to 900,000 ppm. However, further work is still needed to optimise this system; 1) Optimisation of gas-liquid contact to increase saturation of N_2 in the water bath. 2) All issues of condensation downstream of the water bath ought to be eliminated and a monitoring system should be developed such that the steam content can be continuously and accurately accounted for. Potential solutions to this problem are discussed in detail in Chapter 6.

3.6 Electrochemical testing

Cells are tested at temperatures between 750 - 950^{o}C. At the beginning of each test, the cell is sealed using a glass seal to avoid any gas leakages around the cell. The firing conditions for the sealing process, recommended by the manufacturers, are described below:

- At a ramp rate of 2^{o}C/min, the furnace is steadily heated from room temperature to 500^{o}C and left for 2hours.
- The furnace temperature is then increased to 950^{o}C at 2^{o}C/min and then left for 2 hours to ensure the glass is completely melted. At this point, a ceramic seal is formed indicating the strength of the seal.
- Finally, the furnace temperature is reduced to the cell's operating temperature at a ramp rate of -2^{o}C/min and left for at least 2 hours.

The total time required to form a seal based on the heat profile indicated is ~15 hours.

Upon completion of the sealing process, reduction of the NiO in the fuel electrode commences. Reduction of NiO to metallic Ni is carried out by introducing H_2 to the fuel electrode and this is important in order to induce electronic conductivity. In addition, H_2 provides a continual reducing atmosphere. During reduction, H_2, N_2 and H_2O at flow rates of 10, 10 and ~0.36 ml/min respectively are flowed towards the fuel electrode. The cell is then left to reduce for a total of 8 hours with 10 ml/min of synthetic air flowed to the anode.

During the reduction process, an OCV measurement is recorded. This is important to determine the degree of partial pressure and/or electronic leakages around the cell as it can be compared with the theoretical Nernst potential as discussed in Section 1.3.1. Afterwards, the reduced cell is then characterised by AC impedance spectroscopy to determine its initial ohmic and polarisation resistances. An example of this characterisation under reducing conditions can be seen in the Nyquist plot shown in Figure 3–19. The instrument used during electrochemical testing includes a Solatron 1286 electrochemical interface and a Solatron 1250 frequency response analyser. The frequency range for the impedance measurement was between 60 kHz – 0.1 Hz and an amplitude signal of 10 mV was applied in all cases. Upon completion of NiO reduction as well as initial AC impedance measurements, various electrochemical measurements can then be taken under different operation conditions.

Note: Two-electrode measurements were used in obtaining all impedance spectra presented in this thesis. Practically this implies that a working (WE)/reference (RE1) probe and counter (CE)/reference (RE2) are connected to either electrodes. This was done in order to measure the resistance of the whole cell.

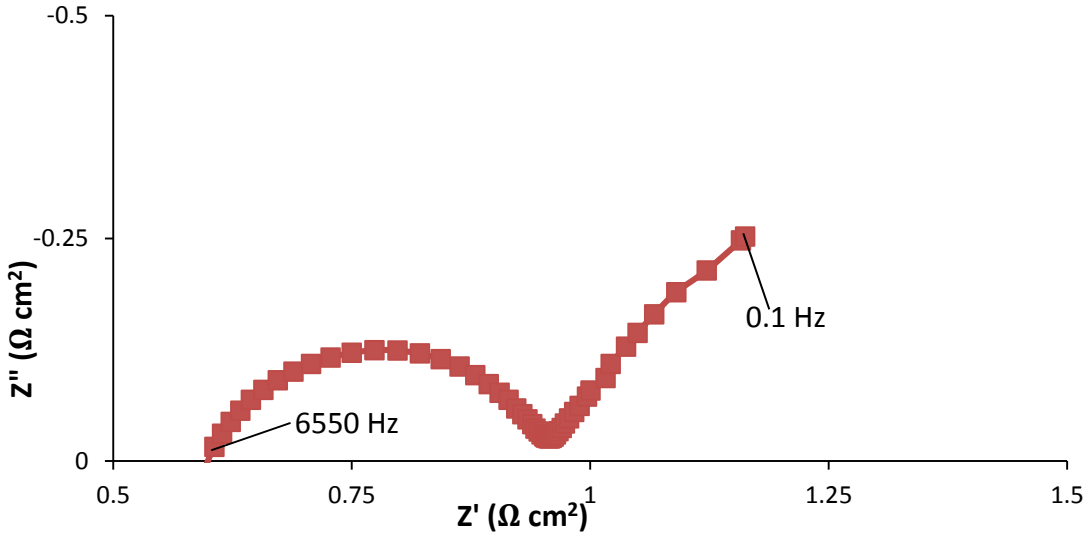

Figure 3–19: Nyquist plot of oxygen and air measured at OCV, 850°C and fuel electrode compositions 2% H_2O, 49% H_2 and 49% N_2 with pure oxygen flowed to the oxygen electrode when using an electrolyte supported cell

During any experimental investigation, for example CO_2 electrolysis, the procedure for measurement is as follows;

- Following the sealing process, NiO reduction for 8 hours occurs with the OCV being continuously monitored during this period
- AC impedance spectroscopy is then carried out under NiO reducing conditions to determine the initial performance of the cell
- The $N_2/CO_2/CO$ mixtures are flowed to the fuel electrode and the OCV is continuously monitored. During this period, the exhaust gas compositions are also measured using a GC. In all cases, the OCV is measured for about 2 hours
- DC characterisation (10 minutes) which involves recording *i*-V curves (at a scan rate of 5 mA/second) and finally AC impedance measurements (10 minutes) at OCV are carried out

3.7 Gas Chromatography

Gas chromatography is used to identify and analyse the molar compositions of the co-electrolysis products. A gas chromatograph (GC) consists of a mobile and a stationary phase with a detector located immediately after the column for identification of the compounds. The GC used in this research is an Agilent 7820A system with a thermal conductivity and flame Ionisation detector (FID). The FID was not used as no hydrocarbons were predicted to be detected during this research. Nitrogen was used as the carrier gas while the stationary phase was made up of two HP-PLOT Q columns connected in series and a Molecular sieve column located after the second HP-PLOT Q column and just before the detector. Following the separation process in the stationary phases, the column effluent passes through the thermal conductivity detector (TCD) where an electrical signal is produced.

The gasses to be analysed include CO_2, H_2, CO and O_2. The HP-PLOT Q column is effective in separating H_2, CO_2 and CO however doesn't separate H_2 and O_2 mixture. As a result, the molecular sieve column is employed in order to separate H_2 and O_2.

3.7.1 Gas Chromatograph – Method development

The information below details the development process in achieving a suitable method capable of separating the gasses to be analysed.

- All investigations were carried out at an oven temperature of 30^{o}C with all three columns located within the oven.
- To begin the method development, the molecular sieve column was initially isolated and individual gasses shown in Table 3–4 were passed through the GC to identify their retention times.

Table 3–4: Individual gas retention times at 30^{o}C and split ratio of 20:1 through a Plot Q column

Gas	CO_2	H_2	O_2	CO
Retention time (min)	4.6	3.4	3.6	3.0

- As seen from Table 3–4, the retention time for H_2 and O_2 was very close. Furthermore, the peaks for both gasses overlapped when samples containing O_2 and H_2 were run as shown in Figure 3–20.

Figure 3–20: Chromatogram showing the retention times of overlapped H_2 and O_2 peaks through a HP-PLOT Q column

- At this stage, a molecular sieve column was introduced as this column is well known to separate permanent gasses
- Individual samples of both H_2 and O_2 were then run through the system with the molecular sieve column in use and the peaks were effectively separated with retention times of 4.46 and 4.85 minutes respectively

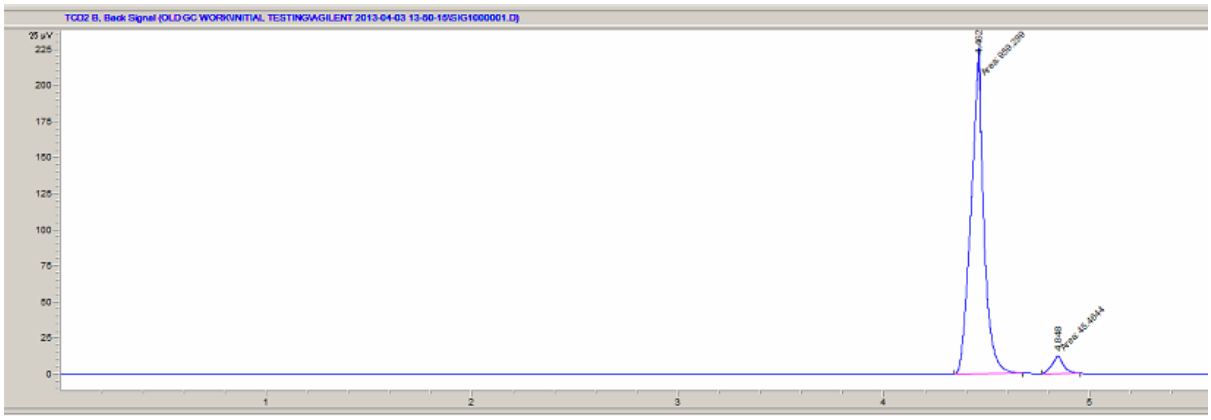

Figure 3–21: Chromatogram showing the retention times of separated H_2 and O_2 peaks through a PLOT Q and molecular sieve column

- The final method had to be created such that the molecular sieve column was isolated when CO_2 was moving from the HP-PLOT Q column to the detector. This is because the diffusion of CO_2 is restricted within the molecular sieve column.

- The final method was constructed such that;
  - ❖ Between 0 - 3.8 minutes when the HP-PLOT Q and molecular sieve columns are in use, it is expected that H_2, O_2 and CO will be in the molecular sieve column.
  - ❖ After 3.8 minutes, the molecular sieve column becomes isolated and holds up H_2, O_2 and CO products. Because the valve on the molecular sieve column is temporarily shut down, CO_2 then goes straight to the detector having exited the plot Q columns
  - ❖ At 5 minutes run time, the molecular column is then switched back on after which H_2, O_2 and CO then separate

Table 3–5: Retention time of gasses under the developed method

	Carbon dioxide	Hydrogen	Oxygen	Carbon monoxide
Retention time (minutes)	4.3	5.7	6.1	11.3

3.7.2 Gas Chromatograph Calibration

Having completed the method development process, the GC was then calibrated for CO_2, H_2 and CO. To carry out this process, the rig setup shown in Figure 3–1 was employed with the water bath and cell rig isolated i.e. the gasses from the MFCs was flowed directly to the GC. Each of the gasses to be analysed were calibrated at four different points 10, 25, 50 and 75% (the range of molar composition estimated from electrolysis operation). To minimise the error of the calibration data, each point was ran 7 times and the data closest to the average of the last 4 readings was used in generating a calibration curve.

From the above compositions, a calibration curve of the amount against the area underneath each curve was produced with a linear graph seen as expected. The correlation coefficient was greater than 0.99 for all gasses (0.99963 for CO_2, 0.99721 for H_2 and 0.99985 for CO). Despite a high correlation coefficient, a maximum error of ~±1% was calculated. This arises from uncertainties in the integration of the area under the curve, poor detector response at low concentrations (indicated by its response factor relative to higher concentrations as shown in Table 3–6) and the accuracy reading of the MFCs.

Table 3–6: Retention times of the various calibrated compounds

Retention time (minutes)	Compound	Amount (%)	Area	Response factor
4.309	Carbon dioxide	10	53.953	0.18531
		25	117.280	0.21316
		50	234.500	0.21322
		75	341.630	0.21953
5.697	Hydrogen	10	325.550	0.030718
		25	601.270	0.041579
		50	1096.100	0.045616
		75	1573.800	0.047655
11.409	Carbon monoxide	10	3.295	3.035
		25	7.957	3.142
		50	16.076	3.110
		75	24.668	3.040

Over the duration in which the GC was operated, calibration of the instrument was carried out every 6 months to check for any deviation from the initial calibration of the instrument.

3.8 Cathode and Electrolyte Supported Solid Oxide Electrolysis Cells

Prior to the CO_2 electrolysis and CO_2/H_2O co-electrolysis investigations discussed in Chapters 4 and 5 respectively, three electrolyte and cathode supported SOECs were characterised under $N_2/H_2/H_2O$ mixtures. The aim of the study was to evaluate the gas leakages across the cell and the initial performance of the cell under operation. As a result, the operating cell to be used in the CO_2 and CO_2/H_2O co-electrolysis study can be determined.

- The measured OCV is vital in determining the performance of the sealing material as an experimental OCV more than 3 mV below the theoretical maximum Nernst potential typically indicates gas leakages across the cell. The measured and theoretical potentials under NiO reducing conditions are given in Table 3–7 and Table 3–8.

- The initial performance is determined by analysing the degree of variation in the ohmic resistance arising from contact resistance of the electrodes and platinum current collectors over short periods of operation (~50 hours). A solid connection between the electrodes and current collector is important as without this, DC characterisation results will be poor and potentially useless.

Figure 3–22 is a graph of ohmic resistances plotted against time of operation using the electrolyte and cathode supported SOEC.

3.8.1 Experimental setup and procedure

The test set-up and operation of the different SOCs investigated was described in detail in Section 3.1. In each case, the cells were operated at under NiO reducing conditions described in Chapter 3 at 850^{o}C with a 49% N_2, 49% H_2 and ~2% H_2O flowed to the fuel electrode and synthetic air flowed to the oxygen electrode. Following the reduction of the metal oxide where the OCV was measured simultaneously, an impedance spectrum was recorded to determine the initial cell performance. Afterwards, DC and AC impedance measurements were carried out at varying compositions of N_2, H_2 and H_2O.

3.8.2 Results and Discussion - Electrolyte Supported SOEC

Table 3–7 shows the measured and theoretical open circuit potentials for all 3 electrolyte supported cells under NiO reducing conditions. Comparing the experimental and theoretical values shown, the equivalent voltage leakages are calculated to be around 18 mV. These measured OCV values are comparable to similar information given in literature. For example under NiO reducing conditions, Ebbesen et al. (2012) measured an OCV value 27 mV below the Nernst potential while operating at 1000^{o}C with 4% H_2O – 96% H_2 to the fuel electrode and pure oxygen to the oxygen electrode using a Ni-YSZ/YSZ/LSM-YSZ cathode supported cell.

Table 3–7: Measured OCV of an electrolyte supported cell at 850^{o}C

Cold inlet gas composition (%)			Theoretical Nernst Potential (mV)	Experimental OCV (mV)		
N_2	H_2	H_2O		Cell 1	Cell 2	Cell 3
49.1	49.1	1.8 (±0.2)	1086 (±3)	1068 (±4)	1060 (±4)	1062 (±4)

Note that the error of the steam composition arises from variation in its measurement as discussed in Section 3.5. In addition, the theoretical Nernst potential was calculated using Equation 6 and the operating conditions stated in Table 3–7.

The error in the measured OCV value originates from three sources within the test facility;

- 1.5% accuracy of the reading range for the MFC, equivalent to ±1 mV. This voltage is calculated using the Nernst Equation for gas compositions with the error range.
- The Solatron electrochemical interface instrument has an error equivalent to a maximum of ±3 mV. This is evident from the fluctuations in the instruments reading arising predominantly from an unstable flow of steam at the fuel electrode.

Although not shown in this Section, the measured OCV at the conditions described in Table 3–7 increased to 1075 (±4mV) when stiffer springs were employed in the compression jig. This increase in OCV indicates lower gas leakages across the fuel electrode.

Figure 3–22 is a graph of ohmic resistance taken from the impedance spectrum and plotted against time of operation at varying $N_2/H_2/H_2O$ compositions for three set of electrode and electrolyte supported cells. The electrolyte supported cells are represented as cells 1, 2 & 3. In each case, the ohmic resistance was initially measured 8 hours after 49% N_2, 49% H_2 and ~2% H_2O was flowed to the fuel electrode for NiO reduction to metallic Ni.

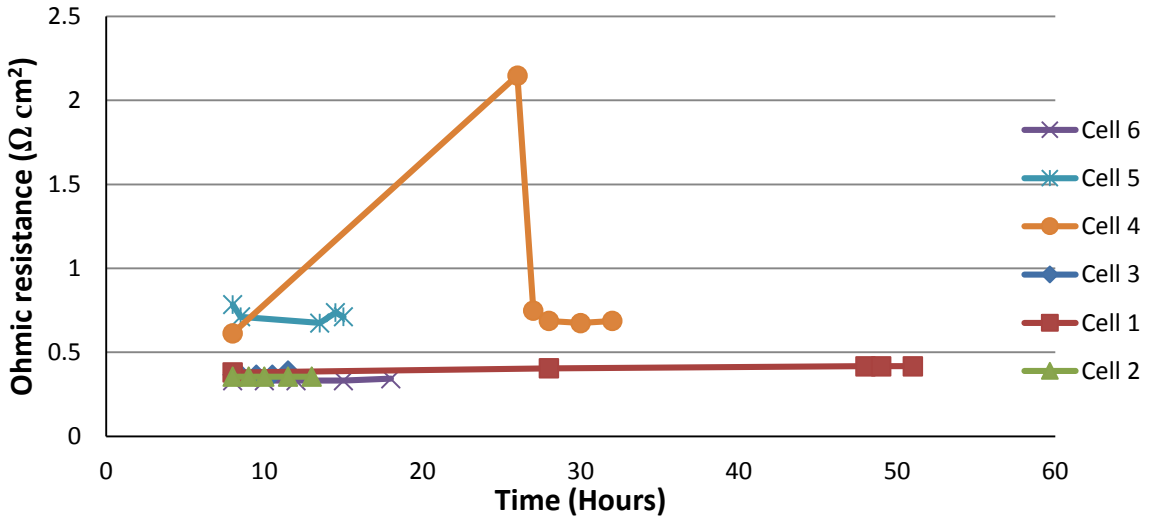

Figure 3–22: Ohmic resistance of electrode and electrolyte supported SOCs operating at 850°C and fuel electrode compositions 2% H_2O, 49% H_2 and 49% N_2 with synthetic air flowed to the oxygen electrode.

Note: Cells 1, 2, and 3 are electrolyte supported cells while cells 4, 5 and 6 are electrode supported cells.

The initial measured ohmic resistance varied marginally between all three cells from 0.38, 0.37 and 0.36 Ω cm^2 in cells 1, 2 and 3 respectively. The consistency of the initial results indicates an approximate optimum value of the ionic resistance of the electrolyte. As shown in Figure 3–22, cell 1 was operated for about 50 hours. During this period, the ohmic resistance increased from 0.38 Ω cm^2 at the 8th hour of reduction to 0.42 Ω cm^2 after 50 hours. This slight increase in ohmic resistance with time is as a result of poorer contact of electrode and current collector mesh. For cells 2 and 3 where investigations were carried out over ~15 hours, the ohmic resistance remained constant.

3.8.3 Results and Discussion - Cathode Supported SOEC

Table 3–8 shows that the measured OCV is ~42 mV below the calculated potential for cells 5 and 6 while for cell 4 the measured OCV was 59 mV below the calculated potential. This large difference indicates an increased amount of gas leakage.

Table 3–8: Measured OCV of a cathode supported solid oxide cell at 850°C

Inlet gas composition (%)			Theoretical Nernst Potential (mV)	Experimental OCV (mV)		
N_2	H_2	H_2O		Cell 4	Cell 5	Cell 6
49.1	49.1	1.8 (±0.2)	1086 (±3)	1027 (±4)	1044 (±4)	1044 (±4)

Note: The theoretical Nernst potential given above was calculated using Equation 6 and the operating conditions stated in Table 3–8.

The reason for a lower gas leakage with the electrolyte supported cells is because the O-ring glass seal fills the unoccupied electrode area around the fuel electrode/electrolyte region leading to an overall flat cell and seal surface. The pressure exerted onto the cell and seal from the springs then allows for a solid contact, and the overall flat surface significantly reduces the possibility of any gas leakages. In the case of the 'flat-surfaced' NiO-GDC electrode supported cells, the gas leakages are related to an imbalance at the fuel electrode of the cell upon loading with the glass seal. This imbalance leads to increased gas leakages at the fuel electrode.

Figure 3–22 is a graph of ohmic resistance taken from the of the impedance spectrum and plotted against time of operation. The ohmic resistance was initially measured 8 hours after NiO reduction began when operating with the cathode supported cell. The initial ohmic resistances in this case varied considerably for all three cells from 0.33, 0.79 and 0.61 Ωcm^2 in cells 4, 5 and 6 indicating a large contact resistance between the electrodes and current collector. Although the ohmic resistance in cell 6 increased slightly over 18 hours of operation, the resistances in cells 4 and 5 measured over 15 and 33 hours respectively varied considerably over time. The degree of variation indicates insufficient contact between the electrodes and the Pt current collector.

To summarise, initial investigations showed that the electrolyte supported cells were more consistent, reproducible and relatively durable over short periods of operation. The measured OCV of the electrolyte supported cells was seen to be closer to the maximum theoretical value indicating lower gas leakages compared to the electrode supported cell. Based on this evidence which shows lower gas leakages and relatively consistent and reproducible ohmic resistance, the majority of the investigations shown in this thesis was carried out using electrolyte supported SOCs. The degrees of variation in these cells were observed to be much lower than the electrode supported cells. Furthermore, DC characterisation measurements showed discontinuity of the *i*-V plot when operating from fuel to electrolysis mode using the electrode supported cells.

3.8.4 Cathode Supported SOEC with Platinum ink

3.8.4.1 Experimental

To decrease the ohmic resistance seen with the electrode supported cells, Pt ink was added over the fuel electrode side of the cell. Platinum has been shown to be an excellent current collector and extremely effective during high temperature operations. For cell 7, the Pt was screen printed onto the NiO fuel electrode, dried at 200^oC for 30 minutes and sintered in-situ during the glass sealing process described in Section 3.6. For cells 8 and 9, platinum ink was painted onto the NiO fuel electrode using a paint brush. Pure Pt was used in cell 8 while a Pt/acetone mixture was used in cell 9. Following this operation, the cell was then left to dry in an oven at 200^oC for 30 minutes. Finally, the sample was then sintered in a furnace at

900°C for 2 hours to evaporate all organic solvents. The test set-up and operation of the three different SOCs investigated are similar to those described in Section 3.1.

3.8.4.2 Results and Discussion

Figure 3–23 is a graph of ohmic resistance against time of a cathode supported solid oxide cell with Pt ink added on its fuel electrode. Cell 7 shows a continuous increase in the ohmic resistance with time. The reason for this rise in ohmic resistance is unknown; however, a significant improvement can be seen in cells 8 and 9. The investigations for cells 2 and 3 were carried out after all electrolyte supported cell studies had been conducted. It should be noted that Pt of varying compositions with acetone was mixed with cell 9 (~2:1 Pt to acetone ratio) whereas pure platinum was used with cell 8. Hence, the ohmic resistance decreased from 0.25 to 0.21 Ω cm^2. With the effective use of Pt paste, the ohmic resistance decreased significantly by ~ 40% from cathode supported cell without Pt. Furthermore, data collected over 50 hours of operation upon varying compositions of CO_2/CO and CO_2/H_2 showed the cells to be durable with no increase in the ohmic resistance.

Despite the improved contact between the fuel electrode and current collector, the use of pure Pt led to partial blockage of the pores in the fuel electrode needed for gas transport. This is a critical problem that needs to be avoided, or at least minimised and further details on these processes can be found in Section 5.2.3.1

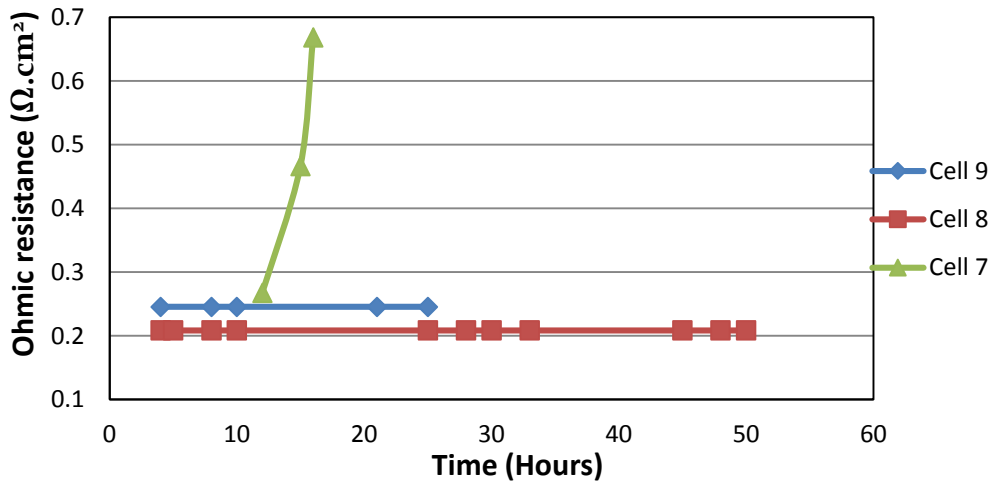

Figure 3–23: Ohmic resistance of electrode supported SOCs operating at 850°C and fuel electrode compositions 2% H_2O, 49% H_2 and 49% N_2 with synthetic air flowed to the oxygen electrode

Cell 7 is an electrode supported cell with Pt ink screen printed onto the fuel electrode. Cells 8 and 9 are electrode supported cells with Pt ink painted onto the NiO fuel electrode using a paint brush.

In addition, as shown in Table 3–9, the experimental OCV increased to 1055 (±4mV) from 1044 mV when stiffer springs were employed in the compression jig indicating lower H_2 leakages across the cell. The increased applied pressure as a result of the stiffer springs increases cell/seal and tube contact thus leading to lower gas leakages across the fuel electrode.

Table 3–9: Experimental OCV of a cathode supported solid oxide cell at 850°C under a new experimental set-up

Inlet gas composition (%)			Theoretical Nernst Potential (mV)	Experimental OCV (mV)	
N_2	H_2	H_2O		Cell 8	Cell 9
49.1	49.1	1.8 (±0.2)	1086 (±3)	1050 (±4)	1055 (±4)

Note: The theoretical Nernst potential stated above was calculated using Equation 6 and the operating conditions given in Table 3–9.

To summarise, the cell rig set-up involving the use of stiffer springs helped to reduce the H_2 leakages across the fuel electrode. Addition of the Pt paste to the fuel electrode led to a lower ohmic resistance. However, the use of Pt resulted into the partial blockage of the fuel electrode. It is important to note that the optimisation processes (improved electrode/mesh contact, lower ohmic resistance and lower gas leakages) described in this Section were carried out after the majority of the electrolyte supported cell investigations had been conducted. Therefore, limited results are presented using the more promising electrode supported cells.

3.9 Identification of Electrochemical Processes in Impedance Spectra - Experimental

The cause of resistances across the electrodes of electrochemical cells depends on a number of operating processes. These processes can include gas movement of reactants/products, charge-transfer reactions at the TPB, gas conversion, electronic and ionic conduction of the electrodes and electrolyte respectively, etc. The resistances that arise from these processes can be related to information shown in the impedance spectra. Section 2.2.2 describes the theory of EIS and details how equivalent circuit models are vital in analysing and modelling impedance spectra.

Several mathematical techniques have been proposed to assist in the identification of electrochemical processes in impedance spectra (Schichlein et al. 2002; Vladikova et al. 2005). The method used in this thesis for separation of process impedance contributions was proposed by Jensen et al. (2007b) and further details on the theory of this process can be found in literature (Jensen et al. 2007b). This mechanism of identification of electrochemical processes in impedance spectra is based on the change that occurs in impedance spectrum when an operational parameter is changed. It is known as analysis of the difference in impedance spectra (ADIS). ADIS enables identification of the impedance contribution from the cathode and anode by recording an impedance spectrum before and after a parameter is changed. The difference therefore between the two spectra with respect to frequency, $\frac{\partial Z\prime(f)}{\partial \ln(f)}$, assuming the real part of the spectra which can be plotted against frequency. This plot can help provide some information about the type of processes involved.

3.9.1 Experimental

In this investigation, the arc (high or low frequency) dominated by both the anode and cathode processes was determined by varying the gas compositions to the fuel and oxygen electrode while recording an impedance spectrum before and after the change using a fresh electrolyte supported cell. The AC impedance characterisation, carried out at OCV and a cell temperature of 850^{o}C was recorded using an electrolyte supported cell and the difference in the spectrum before and after the change is plotted against $\ln f$. The gasses to the oxygen

electrode were varied between air and pure oxygen. Varying compositions of H_2O/H_2 mixtures were flowed to the fuel electrode.

3.9.2 Oxygen Electrode

To understand the contribution of the electrolyser anode processes to the impedance plot, the sweep gasses were switched between oxygen and synthetic air at a flow rate of 5 ml/min while keeping the cathode composition constant at 70% N_2, 28% H_2 and ~2% H_2O at 71.4 ml/min. The AC impedance characterisation, seen in Figure 3–24, was measured at OCV while operating at a temperature of 850°C with oxygen and air interchanged at the oxygen electrode.

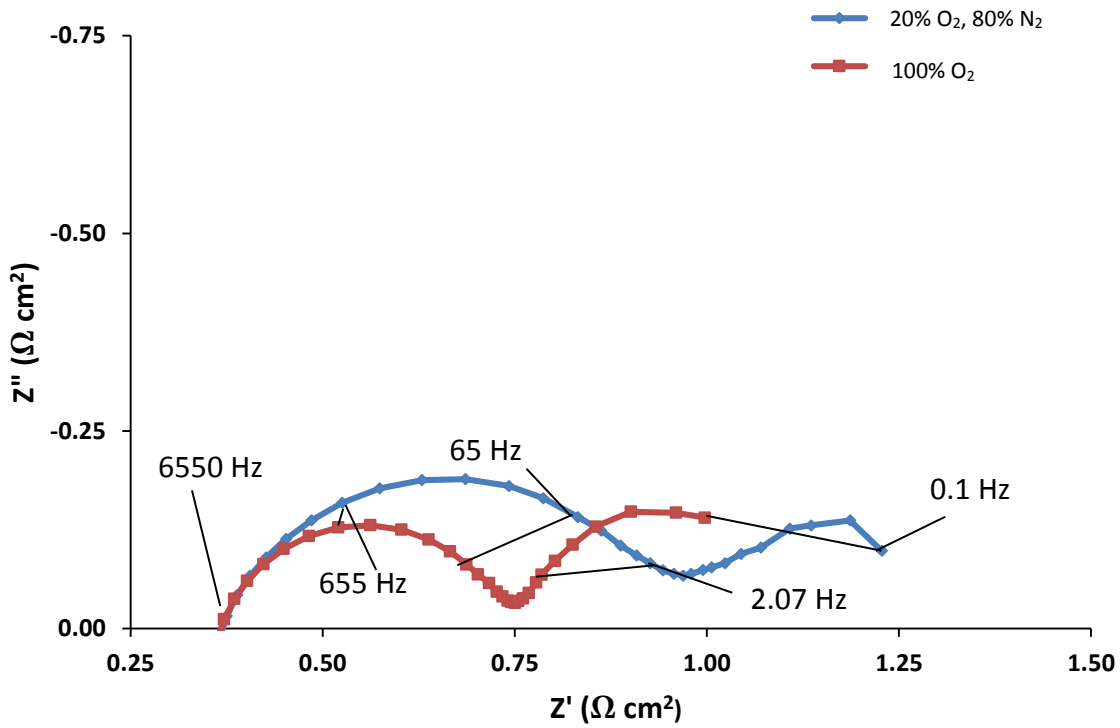

Figure 3–24: Nyquist plot of oxygen and air measured at OCV while operating at a temperature of 850°C with cathode compositions of 70% N_2, 28% H_2 and ~2% H_2O

Using the data shown in Figure 3–24, the difference in impedance spectrum at the oxygen electrode was obtained by subtracting the real part of the spectra between oxygen and synthetic air as shown in Equation 21.

$$\Delta_{O_2\ electrode\ gas\ shift} = \frac{\partial\, Z'(f)_{LSM-GDC}}{\partial\, \ln(f)} = \frac{\partial\, Z\prime(f)_{20\%\,O_2,\ 80\%\,N_2}}{\partial\, \ln(f)} - \frac{\partial\, Z\prime(f)_{100\%\,O_2}}{\partial\, \ln(f)} \qquad 21$$

The difference in the spectra between the contributions of oxygen and air is plotted against $\ln f$. The resulting difference plot as shown in Figure 3–25 enables identification of the frequency arc and region, primarily associated with the oxygen electrode.

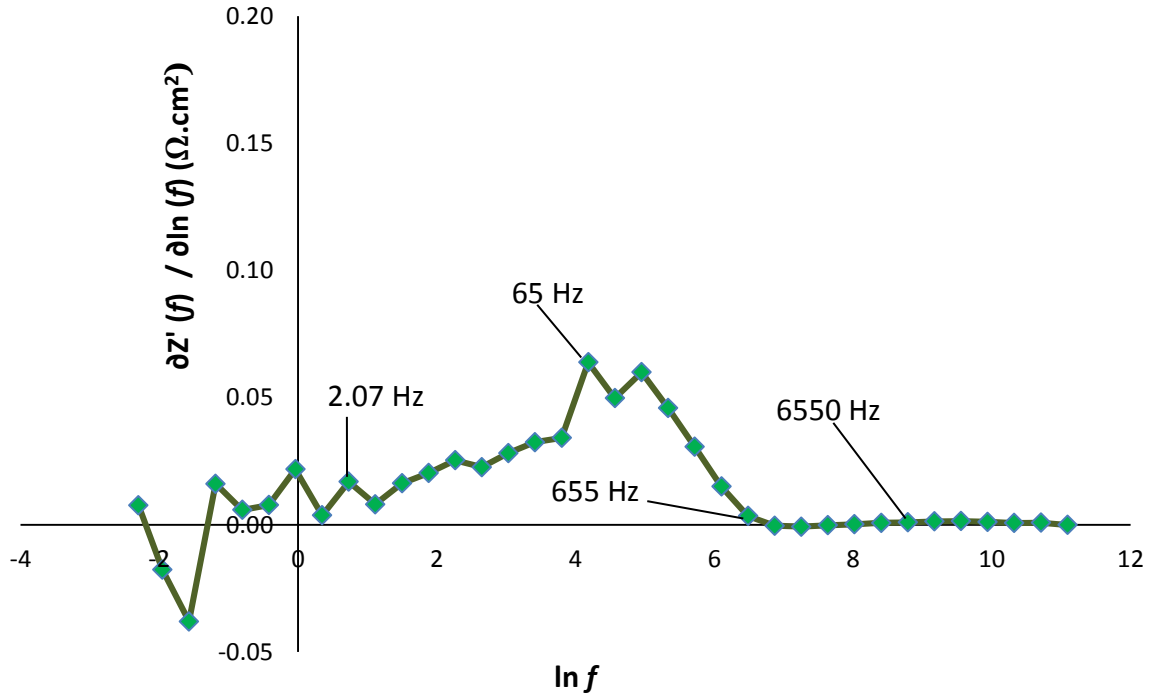

Figure 3–25: Difference plot of changes in impedance spectra at the oxygen electrode due to gas variations as described in Figure 3–24

From Figure 3–24, it can be seen that the higher frequency arc corresponds to processes occurring at the oxygen electrode. In addition, the difference plot of Figure 3–25 shows that the region between 655 and 2.07 Hz correlate to processes that are most likely to occur at the oxygen electrode. At 2.07 Hz, a noisy and unstable region is seen beyond this point and therefore it is difficult to determine any small changes associated with the oxygen electrode at lower frequencies. As shown in Figure 3–25, this region remains consistently unstable and does not decrease with time.

In addition to mass transport limitations relating to the diffusion of the gasses in and out of the electrode, there are a number of other processes that may well contribute to resistances at the oxygen electrode of the SOEC. These processes as described by Jensen et al. (2007b) and Barford et al. (2007) include “oxygen-intermediate transport in the LSM/YSZ structure near the electrode-electrolyte interface, the dissociative adsorption/desorption of oxygen and transfer of species across the triple phase boundary”. Further work is still

needed in ascribing these electrochemical processes to specific frequency ranges and ultimately resistances within the SOEC.

3.9.3 Fuel Electrode

The gas shift analysis carried out for the fuel electrode is similar to that carried out for the oxygen electrode. In this case, the sweep gas of 5 ml/min of oxygen was kept constant. At the fuel electrode, the compositions were switched between 71.5% N_2, 24% H_2 and ~4.5% H_2O at 70 ml/min and 71.5% N_2, 20% H_2 and ~8.5% H_2O at 70 ml/min. It is important to note that the above compositions are cold inlet compositions from the mass flow controllers and not compositions at the fuel electrode. The two can differ during steam electrolysis due to condensation of some of the steam in the region between the base unit of the cell rig and the furnace as discussed in Section 3.5.3.

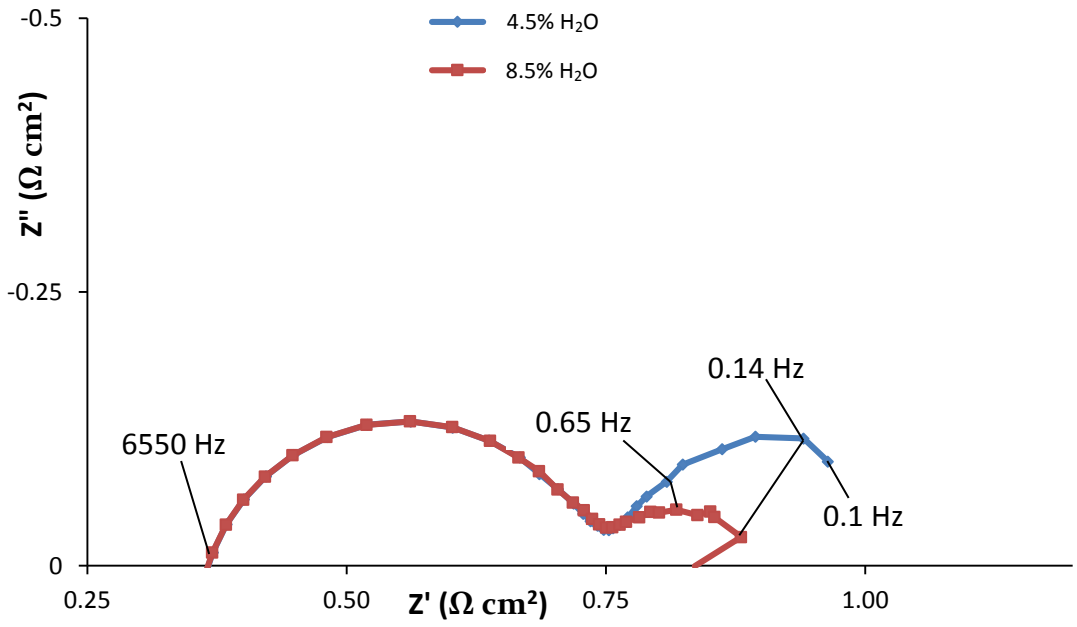

Figure 3–26: Nyquist plot of 4.5 and 8.5% H_2O measured at OCV while operating at a temperature of 850°C with oxygen electrode kept constant at 100% O_2

The data at 0.1 Hz of 8.5% H_2O is not shown in Figure 3–26. This inconsistent data point is caused due to the noise observed at the lowest frequency point.

Using the data from Figure 3–26, the difference in impedance spectrum at the fuel electrode was obtained by subtracting the real part of the spectra between the varying H_2O/H_2 compositions as shown in Equation 22.

$$\Delta_{O_2\ electrode\ gas\ shift} = \frac{\partial\, Z\prime(f)_{NiO-GDC}}{\partial \ln(f)} = \frac{\partial\, Z\prime(f)_{70\%\ N_2,\ 20\%\ H_2,\ 8.5\%\ H_2O}}{\partial \ln(f)} - \frac{\partial\, Z\prime(f)_{70\%\ N_2,\ 24\%\ H_2,\ 4.5\%\ H_2O}}{\partial \ln(f)} \qquad 22$$

The difference in impedance spectra was plotted against $\ln f$ as seen in Figure 3–27.

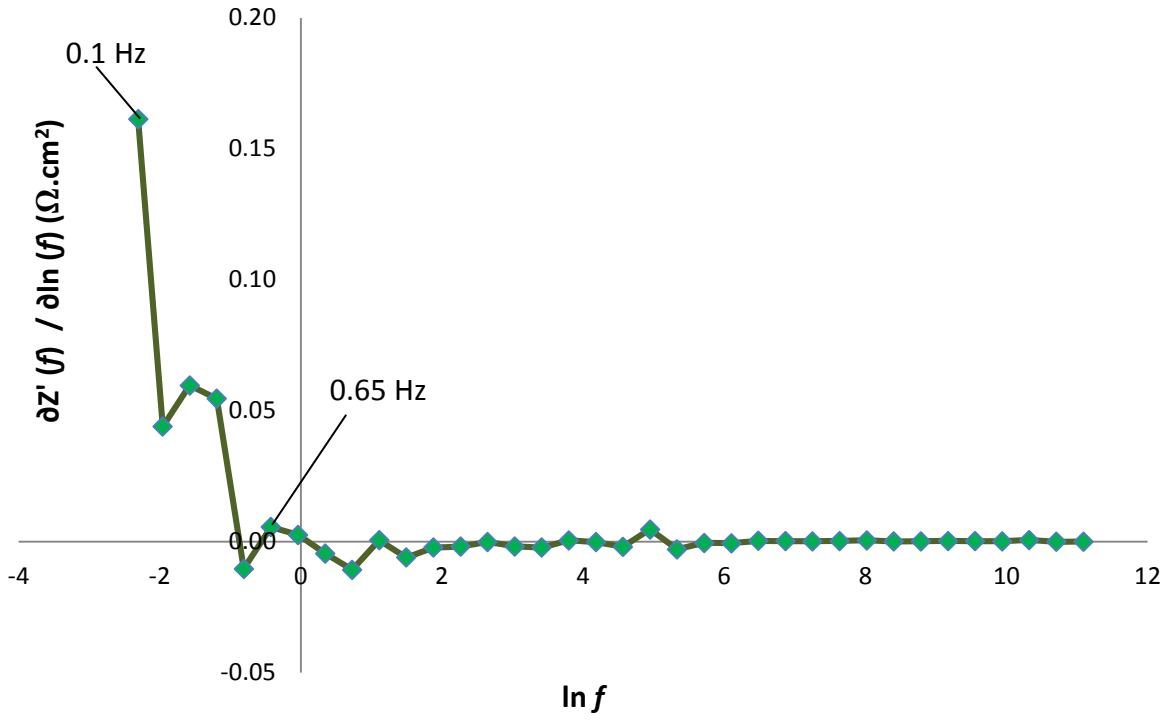

Figure 3–27: Difference plot of changes in impedance spectra at the fuel electrode due to gas variations as described in Figure 3–26

Analysis of this region shows a distinct difference in the impedance data before and after the change in gas compositions. The changes in impedance spectra are seen to occur predominantly at the lower frequency arc between 0.65 and 0.1 Hz. The processes associated with the fuel electrode that could contribute to cell resistance as described by Barford et al. (2007) include gas diffusion, gas conversion and gas-solid reaction. Further characterisation work is still needed to understand the contribution of these electrochemical processes and assign their characteristic frequencies to the impedance spectra.

The results of the ADIS analysis suggesting that the high and low frequency arcs are primarily associated with the oxygen and fuel electrode respectively have been applied for CO_2/CO and CO_2/H_2O mixtures discussed in Chapters 4 and 5.

It is important to note, as described in Section 2.2.2, that electrode processes on the impedance spectra contributing to the cell resistance could overlap. Hence, a detailed cell characterisation is vital in order to ascribe all processes to the impedance spectra.

From the impedance spectra presented in this thesis, noise is only observed at low frequencies (~0.4 to 0.1 Hz) when steam is present at the fuel electrode. Although it is not currently known as to why this happens, it could be speculated that the uneven introduction of steam at the surface of the fuel electrode can cause slight variations in cell temperature. According to the Nernst equation, the OCV would vary in such instances as it is highly sensitive to changes in cell temperature. It is therefore possible that the slight and continuous changes in OCV during EIS could have played a role in the noise observed at the lower frequency arc of the spectra.

To summarise, it has been shown that the processes between 655 to 2.07 Hz (high frequency arc) and 0.65 to 0.1 Hz (low frequency arc) are primarily associated with the oxygen and fuel electrodes respectively. Understanding primarily what arcs are associated to individual regions within the cell is important in this thesis as this enables identification of cell resistances contributing to the fuel and oxygen electrode during CO_2 electrolysis and co-electrolysis of CO_2 and H_2O.

3.9.4 Equivalent Circuit Model and Data Analysis

In Chapters 4 and 5 of this thesis, a resistor (R1) in series with two parallel connections of CPE (CPE1 and CPE2) and resistor (R2 and R3) are fitted to the high and low frequency impedance arcs presented in order to estimate the total polarisation resistance. In each section, a table is followed by the impedance spectra detailing the following; Ohmic resistance, polarisation resistance at the high and low frequency arcs, total polarisation resistance and total cell resistance obtained from the equivalent circuit model. Furthermore, the full impedance spectra (graphical illustration) obtained experimentally including the inductance effects, and equivalent circuit model data are presented in Appendices A-1 to A16.

Arc fitting, simulation and data analysis have been carried out using circuit elements within the impedance software ZView.

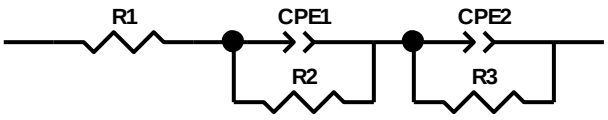

Figure 3–28: Illustration of the equivalent circuit model. A resistor (R1) in series with two parallel connection of constant phase elements (CPE1 and CPE2) and resistors (R2 and R3)

where R1 represents the ohmic resistance, R2 represents the resistance of the higher frequency arc (oxygen electrode) and R3 represents the resistance of the lower frequency arc associated with the fuel electrode.

The combination of the constant phase element CPE1 and R2 is modelled for the processes occurring at the high frequency arc (primarily the oxygen electrode) while the combination of CPE2 and R3 has been modelled for the processes occurring at the low frequency arc (primarily the fuel electrode).

Chapter 4

4. High Temperature Electrolysis of Carbon dioxide in a Solid Oxide Cell

This chapter discusses the performance of an electrolysis cell operating under varying CO_2/CO compositions. A durability study at -0.5 A/cm^2, 850^{o}C and fuel electrode compositions of 50% CO_2, 25% CO and 25% N_2 was carried out. The performance of the cell under varying compositions of CO_2 is compared to similar CO_2/H_2O co-electrolysis investigations discussed in Chapter 5.

4.1 Introduction

During CO_2 electrolysis, H_2 is sometimes used as a reducing gas as shown in investigations carried out by Zhan and Zhao (2010) and Zhan et al. (2009). The use of H_2 during CO_2 electrolysis when using a NiO fuel electrode inevitably leads to the formation of steam as a result of the rWGSR. The presence of steam at the fuel electrode during CO_2 electrolysis therefore alters the "true performance" of the electrolyser under operation as co-electrolysis will occur.

This study was carried out with an aim to understand the effect of carbon mixtures (CO_2/CO) on the electrolyser and determine the electrochemical performance of the cells under CO_2 electrolysis. CO is therefore used as a reducing gas and not H_2. Furthermore, in line with the initial aims of this thesis, the results will be compared with CO_2/H_2O co-electrolysis data to gain further understanding into the co-electrolysis reaction mechanisms. All of the work discussed in this Chapter was carried out using electrolyte supported SOCs described in Chapter 3 with AC and DC characterisation and GC analysis.

4.2 Electrolysis of Carbon dioxide

4.2.1 Introduction

Using a fresh NiO-GDC/Hionic^{TM}/LSM-GDC electrolyte supported cell, CO_2/CO mixtures shown in Table 4–1 were varied to investigate their effect on SOEC operation at 850^{o}C. In each case, synthetic air was flowed to the oxygen electrode at a flow rate of 10 ml/min. Reproducibility and consistency of results is crucial in a research environment and thus all investigations presented in this Chapter were repeated.

Table 4–1: Operating conditions for CO_2 electrolysis

Fuel electrode flow rate = 20 ml/min			
Fuel electrode compositions (mol %)			
Exp. No	CO	CO_2	N_2
4c1	60	15	25
4c2	50	25	25
4c3	25	50	25
4c4	15	60	25
4c5	5	70	25

Note: The above experiments were performed in the order shown (i.e. 4c1, 4c2, 4c3, etc.)

4.2.2 Initial Cell Characterisation

It is important that each operating cell displays a similar initial performance (i.e. similar OCV, ohmic and polarisation resistances) for base comparison of the CO_2/H_2O co-electrolysis process discussed in Chapter 5. Therefore, prior to the CO_2 electrolysis investigations, each cell was characterised by AC impedance spectroscopy under NiO reducing conditions of $N_2/H_2/H_2O$ mixtures. The AC impedance measurement can be seen in Figure 4–1. The measured OCV under NiO reducing conditions of 49% N_2, 49% H_2 and ~2% H_2O at 850°C was determined to be 1065 ±4mV. The breakdown of the impedance contributions from each of the two electrodes can be seen in Table 4–2.

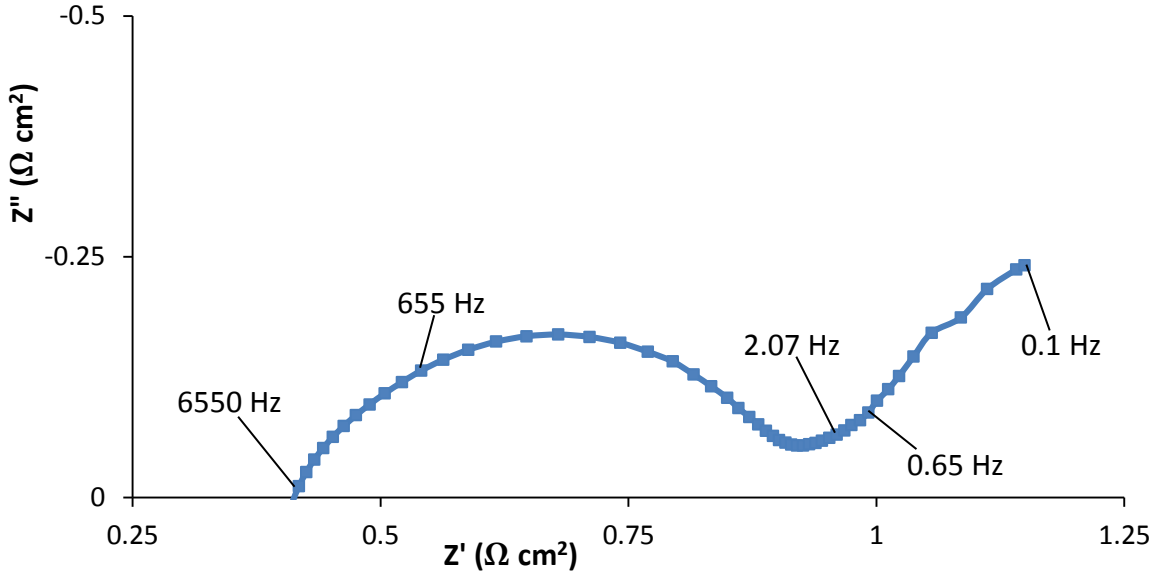

Figure 4–1: AC impedance spectra recorded at OCV under NiO reducing conditions

Table 4–2: Ohmic and polarisation resistances under NiO reducing conditions, obtained using equivalent circuit model from experimental Nyquist plot

	Cell $_{CO2elec}$
Ohmic resistance ($\Omega.cm^2$) - R1	0.41
Oxygen electrode polarisation resistance ($\Omega.cm^2$) - R2	0.53
Fuel electrode polarisation resistance ($\Omega.cm^2$) – R3	1.02
Total polarisation resistance ($\Omega.cm^2$)	1.55
Total cell resistance ($\Omega.cm^2$)	1.96

The full impedance spectra for the data in the Table 4–2 and Figure 4–1 is shown in Appendix A-1.

4.2.3 Open Circuit Voltage

4.2.3.1 Varying oxygen partial pressure to the fuel electrode

Figure 4–2 shows the measured and theoretical OCV values at 850°C with the compositions shown in Table 4–1. The theoretical GC voltage is the calculated Nernst potential based on the exhaust composition of the cell rig, analysed by the gas chromatograph. The theoretical potentials shown in Figure 4–2 were calculated using the Nernst Equation (Equation 6) and the operating conditions given in Table 4–1. The measured OCV in all cases was between 3 - 6 ±2 mV below the theoretical value. Using the GC data, the measured OCV in all cases was between 3 - 9 ±2 mV below the theoretical value (from the GC compositions). The theoretical potentials calculated using the GC compositions also have an error of ±1 mV originating from uncertainties in the integration of the area under the curve and poor detector response at low concentrations as discussed in Section 3.7.2.

Overall, the difference between the theoretical and measured potentials indicates very little leakages across the cell. This information indicates a high effectiveness for the operating system employed in cell sealing to avoid any gas leakages.

Error Analysis

- The Solatron electrochemical interface instrument used when monitoring the OCV during CO_2 electrolysis showed an error equivalent to ±1 mV.
- 1.5% reading accuracy of the MFC equivalent to ±1 mV.

The measured OCV shown in Figure 4–2 are comparable to those given in literature. While operating at 850°C with 50% CO_2 – 25% CO – 25% Ar to the fuel electrode and pure oxygen to the oxygen electrode and using a Ni-YSZ/YSZ/LSM-YSZ cathode supported cell, Ebbesen et al. (2012) measured an OCV value 15 mV below the theoretical value. Within the same research group, Ebbesen and Mogensen (2009), measured OCV between 1 – 4 mV below the theoretical value for various CO_2/CO mixtures when using a Ni-YSZ supported cell and operating at 850°C. In another CO_2 electrolysis investigation, when operating using Ni-YSZ electrode supports (Ni-YSZ/YSZ/LSCF-GDC) at an operating temperature of 800°C, Zhan et al. (2009) observed OCV within 70 mV of the predicted values.

In this study, the very small differences between the Nernst potential and the OCV indicate that the cell sealed satisfactorily.

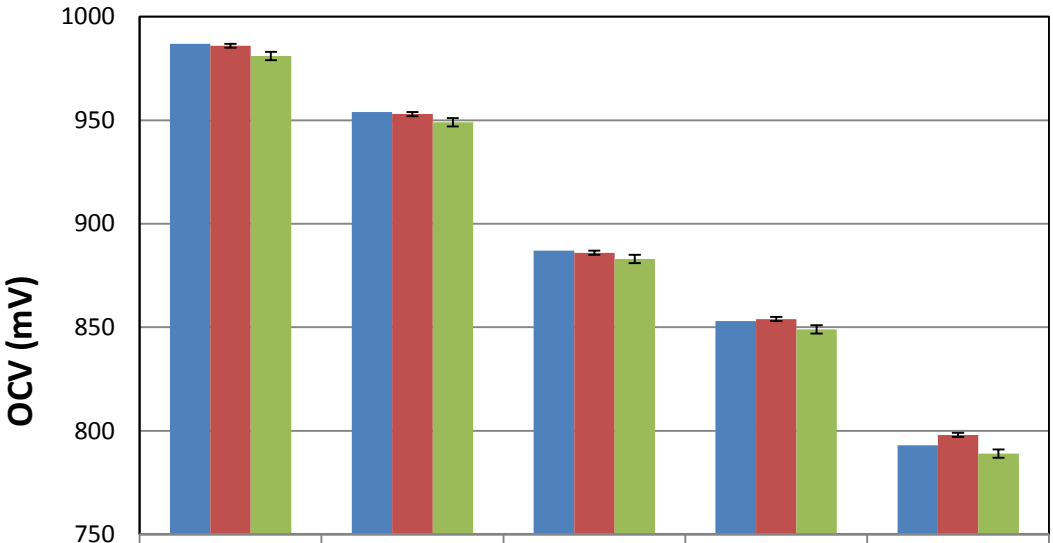

	4c1	4c2	4c3	4c4	4c5
Theoretical OCV	987	954	887	853	793
GC theoretical OCV	986	953	886	854	798
Experimental OCV	981	949	883	849	789

Figure 4–2: Bar chart showing the theoretical and measured OCV for CO_2 fuel electrode compositions shown in Table 4–1

Figure 4–2 shows a decrease in OCV with increasing CO_2 compositions at 850°C. A decrease in OCV is expected as described by the Nernst Equation.

4.2.3.2 Varying operating temperature

The OCV was measured at 750 and 850°C with 50% CO_2 – 25% CO – 25% N_2 to the fuel electrode and pure oxygen to the oxygen electrode. Operating with pure oxygen to the oxygen electrode enables a direct comparison with information in literature as seen in Table 4–3. According to the Nernst Equation, the OCV is expected to decrease with an increase in cell temperature because the Gibbs free energy which represents the electrical demand decreases with an increase in temperature. As shown in Table 4–3, the OCV decreases with an increase in temperature.

Table 4–3: Open circuit voltage of CO_2/CO mixture at varying temperatures

Oxygen electrode composition = Pure oxygen					
	Fuel electrode compositions			Theoretical OCV (mV)	Experimental OCV (mV)
Temperature (°C)	CO	CO_2	N_2		
750	25	50	25	973	968 ±1 (958*)
850	25	50	25	925	922 ±1 (910*)

*The values given in bracket are taken from a study carried out by Ebbesen et al. (2012) at the compositions given above while using a Ni-YSZ supported cell (Ni-YSZ/YSZ/LSM-YSZ).

4.2.4 DC and AC Characterisation

The initial performance of the cell was measured by recording *i*-V curves at the varying fuel electrode compositions and the results of the initial DC characterisation measurements are shown in Figure 4–3. The *i*-V curves shown were recorded at 850°C with synthetic air flowed to the oxygen electrode. From Figure 4–3, it can be seen that the current density values at a given voltage generally increases with increasing CO_2 concentration. At higher feed concentrations (50%, 60% and 70% CO_2); a plateau in the current density can be seen above ~1.2 V indicating a maximum loss in activation polarisation across the fuel electrode.

The ASR of the mixtures was calculated from the *i*-V plot as the line from the OCV to the cell voltage measured at a current density of -0.1 A/cm^2 as shown in Equation 23.

$$ASR = \frac{V_{cell} - V_{ocv}}{i} \qquad 23$$

Where V_{ocv} is the open circuit voltage, *i* is the current density (A/cm^2) and V_{cell} is the cell voltage measured at a set current density.

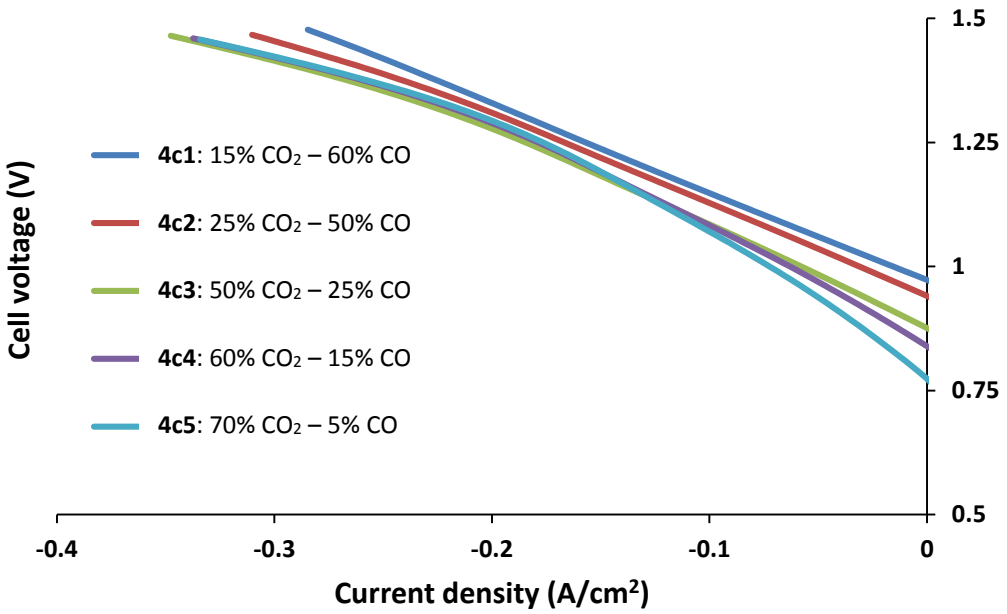

Figure 4–3: DC characterisation measurement at 850°C under different CO_2 partial pressures

Although not shown in Figure 4–3, it should be noted that no discontinuity was observed in the shift from fuel to electrolysis operation during DC characterisation. This confirms that these SOCs can indeed work under both galvanic and electrolytic modes. The fuel cell mode of operation is not shown in the *i*-V plot because this thesis solely investigates the performance of the cells under electrolytic conditions. From Figure 4–4, it can be seen that the measured ASR increases with increasing CO_2 composition in the CO_2/CO mixture. This trend is in coherence with information in literature. When operating with a Ni-YSZ supported cell (Ni-YSZ/YSZ/LSM-YSZ) at 850°C, Ebbesen and Mogensen (2009) calculated ASRs of 0.36 and 0.37 Ω cm^2 for reduction of CO_2 in CO_2/CO mixtures with a ratio of 50/50 and 70/30 respectively. From the shape of the *i*-V curve shown in Figure 4–3, the increasing ASR is thought to be related to the sluggish kinetics of the reactions taking place on the surface of the fuel electrode, therefore leading to an increase in cell resistance. The impedance spectra of Figure 4–5 show that the increase in ASR is predominantly associated with an increase in polarisation resistance across the fuel electrode.

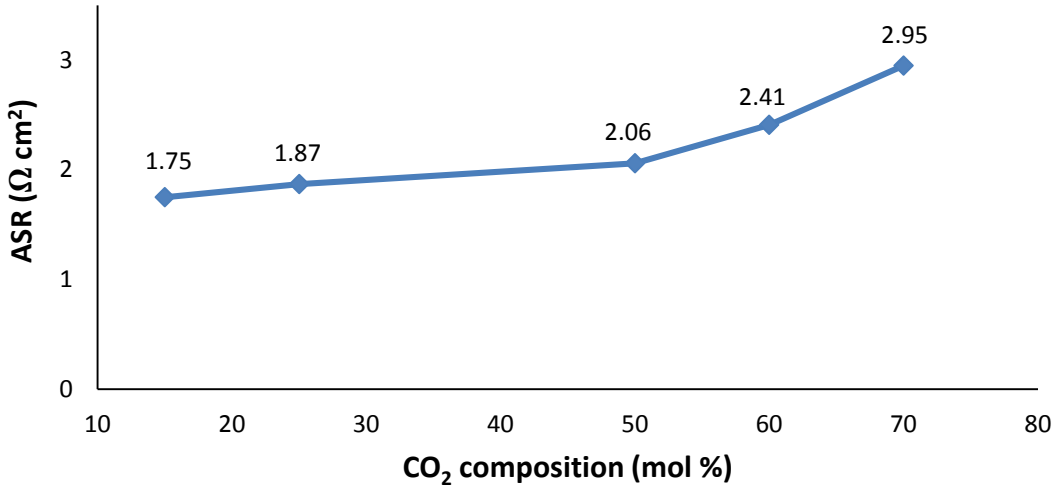

Figure 4–4: Area specific resistance with increasing CO_2 partial pressure

AC characterisation measurements at OCV was performed after recording the *i*-V plots and the results obtained at 850°C and varying CO_2 mixtures are shown in Figure 4–5. The analysis in this section discusses the impedance contributions of both electrodes to the varying compositions investigated.

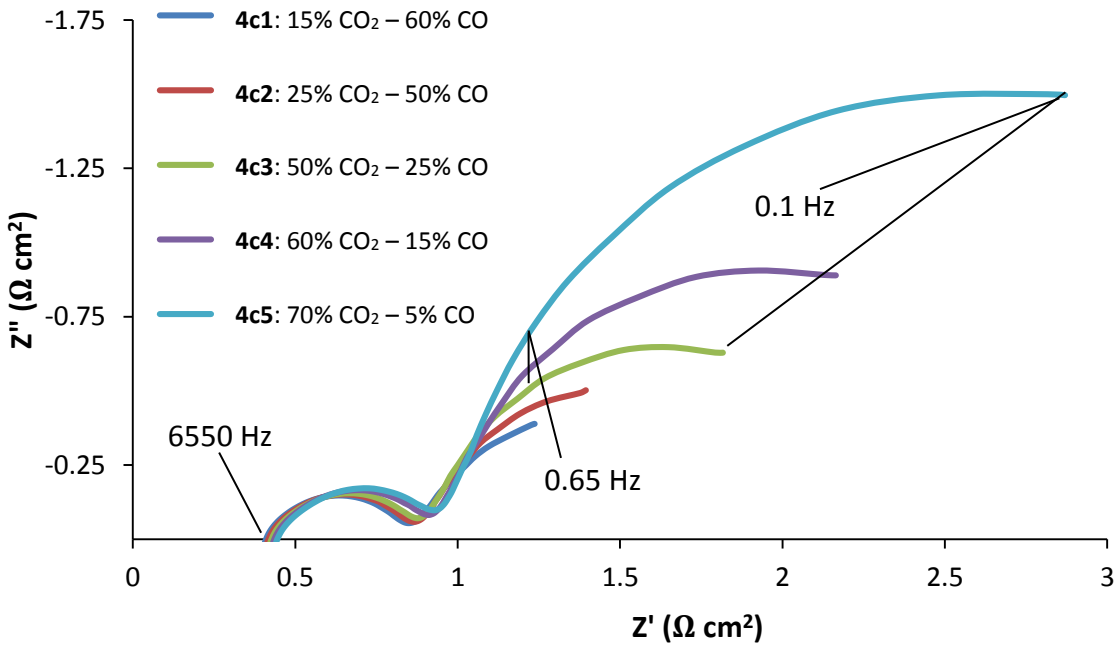

Figure 4–5: AC impedance spectra recorded at OCV under different CO_2 partial pressures

Table 4–4 shows the ohmic and polarisation resistances across the electrodes during CO_2 electrolysis at the oxygen and fuel electrodes as described in Section 3.9. The slight increase in ohmic resistance with increasing CO_2 concentration occurs as a consequence of variations in electrical contact between the electrode and current collector. The slight increase in ohmic resistance is a time dependent process and not caused by the increasing CO_2/CO ratio. This is verified in latter experiments carried out within a short period (i.e. 1 hour) in which the ohmic resistance remained constant at varying gas compositions.

Table 4–4: Ohmic and polarisation resistances during CO_2 electrolysis, obtained using equivalent circuit model from experimental Nyquist plot

	mol % of CO_2				
	15	**25**	**50**	**60**	**70**
Ohmic resistance ($\Omega.cm^2$) - R1	0.41	0.41	0.42	0.43	0.44
Oxygen electrode polarisation resistance ($\Omega.cm^2$) – R2	0.45	0.46	0.47	0.51	0.51
Fuel electrode polarisation resistance ($\Omega.cm^2$) – R3	1.1	1.41	1.60	2.09	3.55
Total polarisation resistance ($\Omega.cm^2$)	1.55	1.87	2.07	2.6	4.06
Total cell resistance ($\Omega.cm^2$)	1.96	2.28	2.49	3.03	4.50

The full impedance spectra for the data in the Table 4–4 and Figure 4–5 can be found in Appendices A – 3 to A – 7.

Analysis of the impedance spectra of Figure 4–5 shows a slight increase in polarisation resistance at the oxygen electrode with increasing CO_2/CO ratio as shown in Table 4–4. On the other hand at the fuel electrode, a significant increase in polarisation resistance with increasing CO_2/CO ratio is seen. This increase in polarisation resistance across the fuel electrode was also observed by Kim-Lohsoontorn and Bae (2010) and Ebbesen and Mogensen (2009) with increasing compositions of CO_2/CO mixtures. In this study as shown in Table 4–4, the polarisation resistance at the fuel electrode increased from 1.10 to 3.55 Ω cm^2 from 15% to 70% CO_2. It can therefore be concluded that processes occurring at the fuel electrode is primarily responsible for the increase in cell resistance with increasing CO_2/CO ratio. These processes as described in Section 3.9.3 include gas diffusion, gas conversion and gas-solid reaction at the TPB. DC characterisation shown as the *i*-V plot in Figure 4–3 indicates charge transfer processes are slower with increasing CO_2/CO compositions.

The majority of the information shown in literature has associated the polarisation resistance across the fuel electrode during CO_2 electrolysis with concentration polarisation due to diffusion and conversion (Ebbesen et al. 2012; Zhan et al. 2009). Zhan et al. (2009) explain that the higher molecular weight of CO_2 limits the diffusivity of the mixture at the fuel electrode. It could also be speculated from the information given in literature that the diffusion of the higher molecular weight CO_2 molecule through the porous electrode is primarily responsible for the significant increase in cell resistance in this study. However, detailed cell characterisation is still needed to ascribe the frequency ranges for these processes onto the impedance spectra.

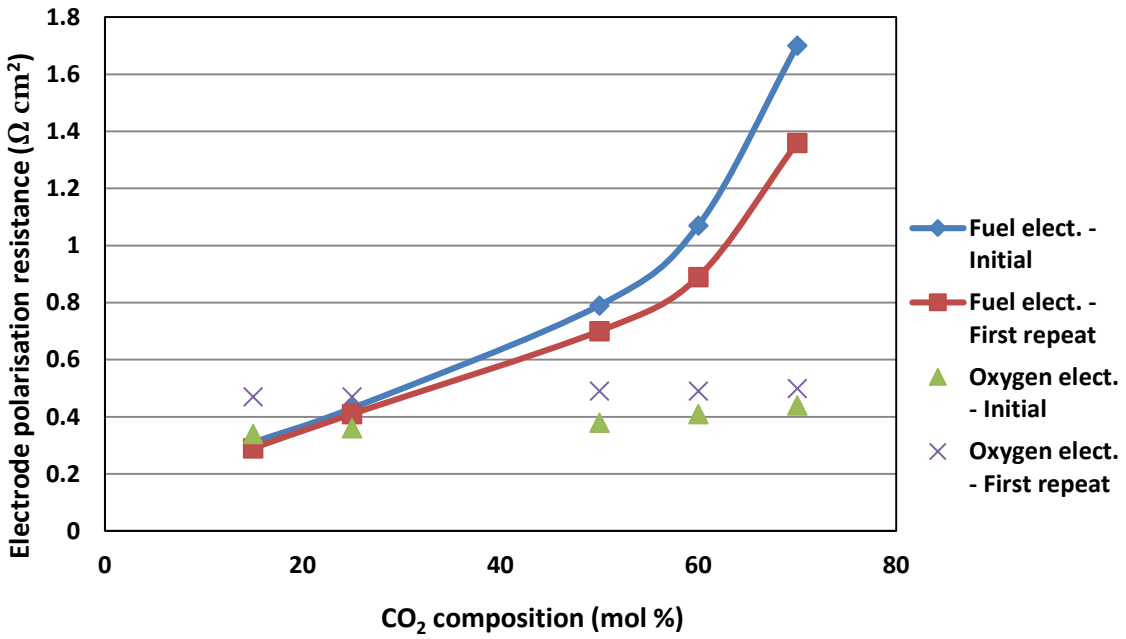

Figure 4–6: Polarisation resistance across the oxygen and fuel electrode at varying CO_2 compositions

Note: The polarisation resistances given in Figure 4–6 are based on the frequency ranges of 655 to 2.07 Hz at the oxygen electrode and 0.65 to 0.1 Hz at the fuel electrode described in Section 3.9.

It is important to note that upon repeating the CO_2 electrolysis experiments, the trend, and degree of increasing polarisation resistance with increasing CO_2/CO ratio, remained consistent at both electrodes. From Figure 4–6, a slight increase in polarisation resistance can be seen at the oxygen electrode when comparing the first repeat data with the initial

data. This indicates a time dependent degradation of the anode as the sweep gas remained unchanged throughout the duration of the experiment. At the fuel electrode, a decrease in polarisation resistance can be seen when comparing the initial data to the first repeat data. Activation of SOCs under electrolysis operation has been reported in literature in the first 100 hours of operation (Ebbesen et al. 2010; Ebbesen and Mogensen 2009). Therefore, it is likely that the decrease in polarisation resistance observed at the fuel electrode could be a time dependent activation process.

To summarise, it has been shown that the performance of the electrolysis cell operating under increasing CO_2/CO compositions is highly associated with the polarisation resistance across the fuel electrode. The increase in polarisation resistance seen in this study could be related to processes such as fuel electrode gas diffusion, slower charge transfer reaction rates for higher CO_2/CO mixtures and gas conversion.

4.2.5 Poisoning and Regeneration of NiO electrode during Electrolysis of Carbon dioxide

The aim of this study is to further understanding of the effect of the CO_2/CO mixtures on the fuel electrode of the electrolysis cell and analyse the regeneration of Ni catalyst. In this study, an aged cell from a previous test (CO_2/CO electrolysis cell used in Section 4.2.3) was compared with a new cell.

4.2.5.1 Experimental

CO_2/H_2 mixtures of compositions 60% H_2, 15% CO_2 & 25% N_2 were flowed to the fuel electrode after the CO_2 electrolysis investigations described in Section 4.2.3 had been carried out. The OCV was then monitored with synthetic air flowing to the oxygen electrode while operating at a cell temperature of 850^oC. Using a new cell, the OCV was also measured when operating at 850^oC and the same gas compositions.

The OCV of both data are compared to:

1. Determine the extent of performance loss in the fuel electrode after operation with CO_2/CO mixtures
2. Investigate the possibility of regeneration of cell performance with the removal of CO and addition of H_2.

During the CO_2 electrolysis investigation discussed in Section 4.2.3, the cell was operated for a total of 15 hours at an operating cell temperature of 850^oC under varying CO_2/CO compositions. Furthermore, only DC (i.e. *i*-V measurements) and AC characterisation (at OCV) were carried out on the cell during the CO_2 electrolysis. During DC characterisation, the current density was measured up to a maximum cell voltage of 1.46 V as shown in Figure 4–3.

Note: According to the gas manufacturers, the CO_2 and CO cylinders each have a 99.999% purity level (BOC; research grade). This implies that up to 10 ppm of impurities (which can include CH_4, H_2S, O_2, N_2, H_2 and moisture) are present in each cylinder.

4.2.5.2 Results and Discussion

Figure 4–7 and Figure 4–8 respectively are graphs showing the measured OCV against time of CO_2/H_2 mixtures with the aged and new cell. During this investigation, there was a 5 minute break in electrochemical measurement as seen in Figure 4–7 however CO_2/H_2 mixtures were still being flowed to the fuel electrode.

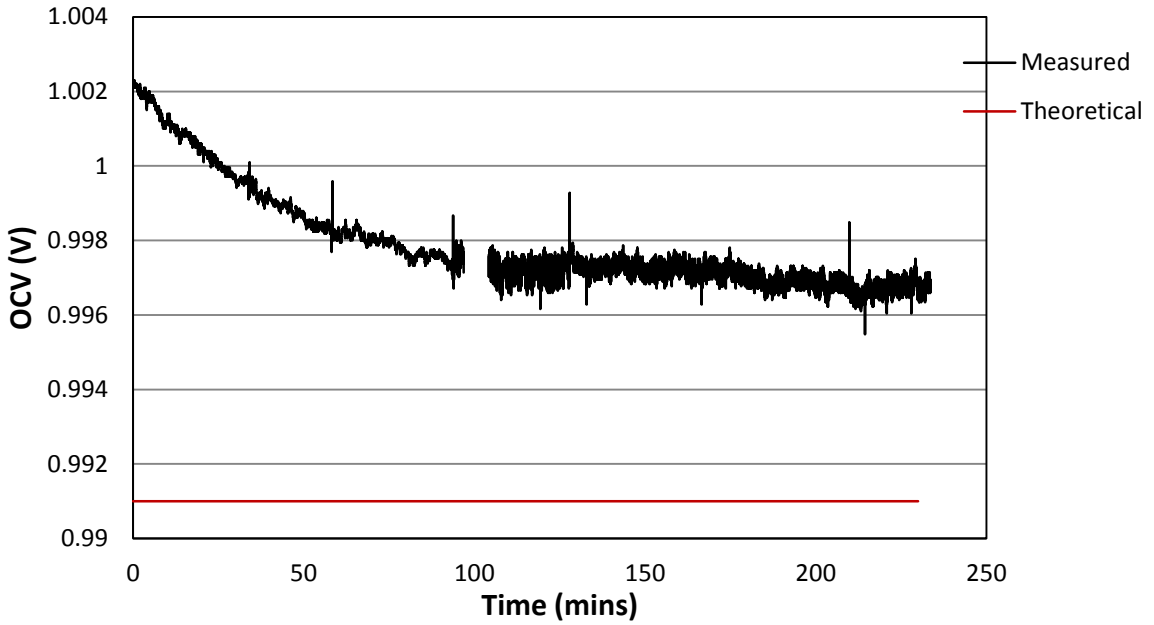

Figure 4–7: Open circuit voltage against time at 850°C with 15% CO_2, 60% H_2 and 25% N_2 supplied to the fuel electrode using the aged cell

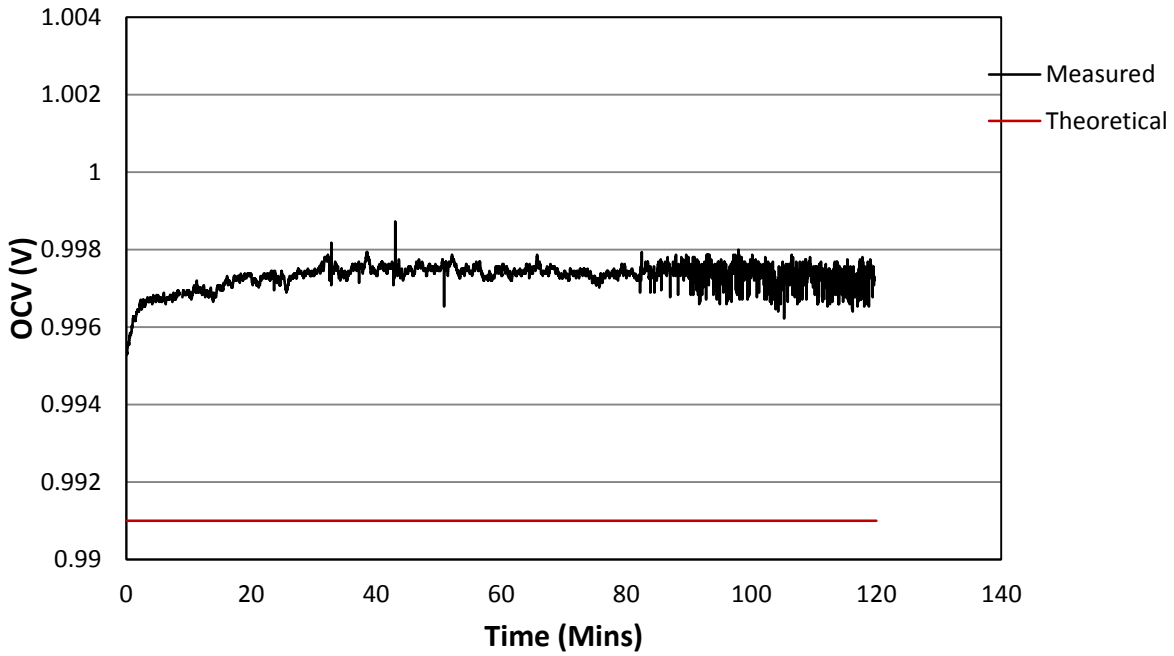

Figure 4–8: Open circuit voltage against time at 850°C with 15% CO_2, 60% H_2 and 25% N_2 supplied to the fuel electrode using a fresh cell

The reaction between CO_2 and H_2 is an equilibrium reaction catalysed by the Ni content present in the fuel electrode. The equilibrium of the rWGSR is close, but not fully reached when using a fresh electrolyte supported cell at the gas compositions indicated in Figure 4–

8. In a case whereby equilibrium of the rWGSR is reached and there are no gas leakages, the measured OCV should be within 2 mV of theoretical potential of 991 mV. Further details on the CO_2/H_2 co-electrolysis process including rWGSR equilibrium can be found in Chapter 5.

The ±2 mV error in the measured potential during CO_2/H_2O co-electrolysis originates from

- The 1.5% accuracy of the reading range for the MFC, equivalent to ±1 mV
- The Solatron electrochemical interface instrument has an error equivalent to a ±1 mV. This is due to the random error evident from the fluctuations in the instrument's readings

Comparing Figure 4–7 and Figure 4–8, it can be seen that in both cases the OCV plateaus at 997 ±1mV. The convergence to this value, however, occurs at different time periods. From Figure 4–7, an initial slow stage of up to 90 minutes can be seen during the reaction before convergence to the expected OCV of 997 mV.

Initially, the formation of carbon and re-oxidation of Ni in the fuel electrode of the aged cell are investigated and eliminated as possible causes for the initial slow process observed. According to thermodynamics, the formation of carbon is not favoured at the experimental conditions of the aged cell described in Section 4.2.5.1 (DC characterisation measurement of up to 1.46 V).

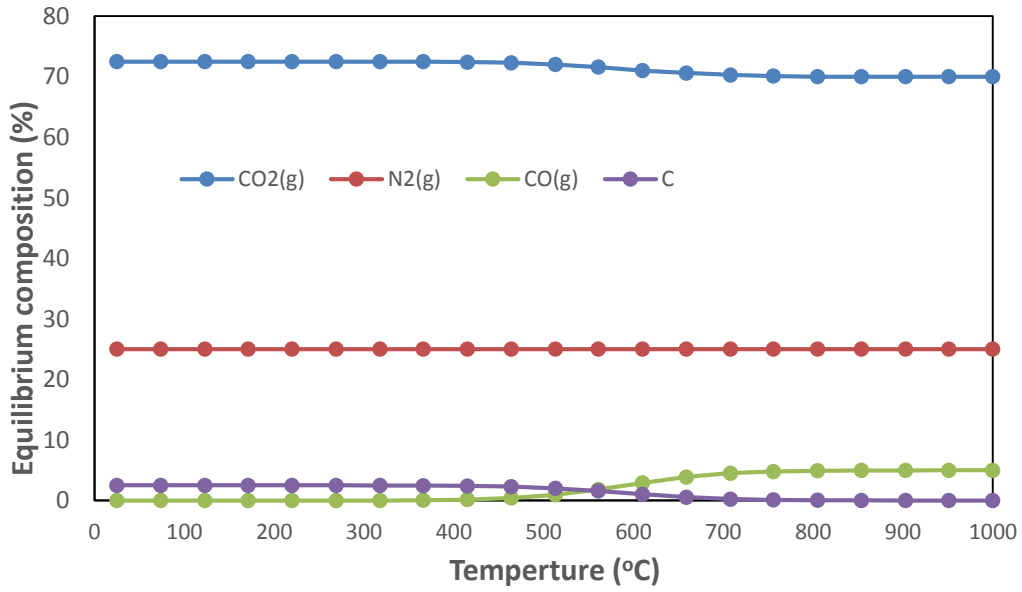

Figure 4–9: Thermodynamic analysis of the Boudouard reaction as a function of temperature operating at 70% CO_2, 5% CO and 25% N_2 flowed to the fuel electrode

At 850°C, carbon formation as calculated using thermodynamic properties from process simulation software HSC Chemistry 5.11 will occur at a cell voltage of 2.04 V as described in Section 2.6.2.2 via the reduction of CO. Furthermore, the equilibrium of the Boudouard reaction favours the reverse reaction producing CO despite the Ni catalyst at 850°C and under a reducing atmosphere of 5% CO, 70% CO_2 and 25% N_2. This is evident in the graphical illustration of Figure 4–9 which shows the thermodynamic analysis of the Boudouard reaction as a function of temperature at fuel electrode compositions of 5% CO, 70% CO_2 and 25% N_2. However as shown in Figure 4–10, carbon formation is likely to occur at high CO concentration, although, it is expected that the produced carbon would have been eliminated when operating at 5% CO, 70% CO_2 and 25% N_2 due to the reverse reaction.

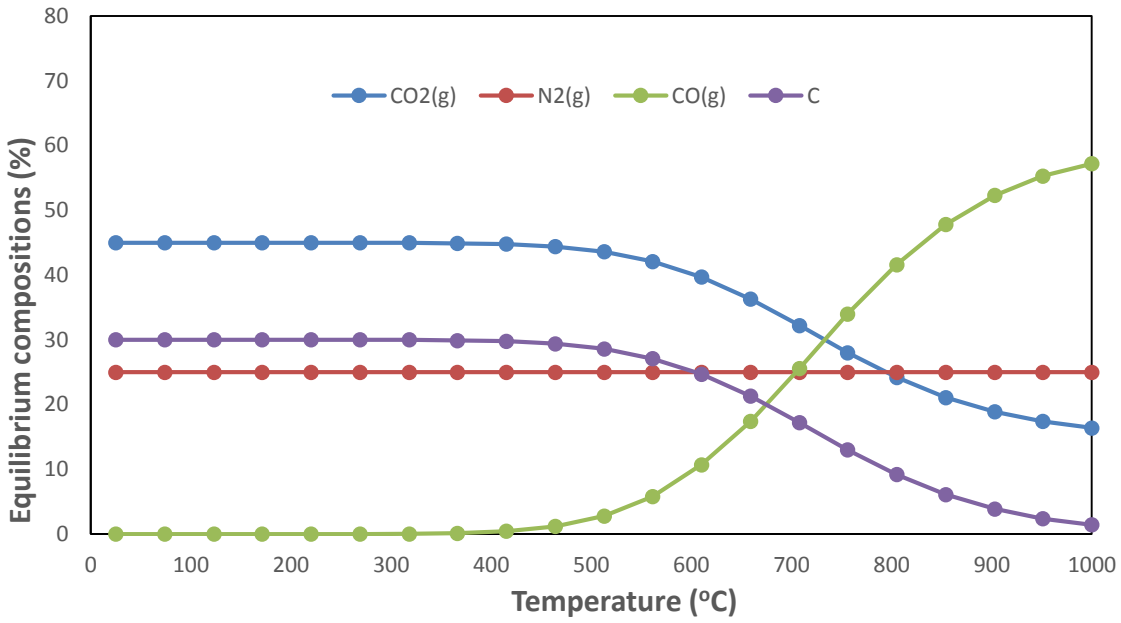

Figure 4–10: Thermodynamic analysis of the Boudouard reaction as a function of temperature operating at 15% CO_2, 60% CO and 25% N_2 flowed to the fuel electrode

Finally, the oxidation of Ni to NiO is not favoured at 850°C when operating under the reducing atmosphere according to the oxygen partial pressure chart of the Ellingham diagram (See Appendix B for operation point termed "B1" on Ellingham diagram). From this figure, the minimum ratio of CO to CO_2 at 850°C required to oxidise Ni to NiO is 0.01, a value higher on chart than the operation point of 0.07.

The initial 90 minute decay seen when using the aged cell (Figure 4–7) is thought to occur due to a process known as an induction period which indicates a process of transformation of the Ni catalyst in becoming active. In this study, it is thought that the presence of impurities (possibly H_2S in the CO cylinder) in nickel sites hinders the acceleration of the rWGSR. Oliphant et al. (1978) indicated, as fully described in Section 2.6.2.1, that poisoning of the Ni catalyst in the fuel electrode is caused by chemisorption of sulphur on the Ni surface as shown in Equation 19. Therefore, it is highly likely that sulphur became strongly adsorbed onto the Ni catalyst in the fuel electrode during prior experiments involving CO_2 electrolysis. Diffusion of the CO_2/H_2 gas mixtures is therefore hindered; due to blockage of the active catalytic sites. Hence, the chemical reaction becomes very slow in achieving equilibrium because of the reduced catalyst surface area. The addition of H_2 and removal of CO over a 90 minute period led to the regeneration of the cell. However, the extent of cell regeneration is still unclear and further work is still needed in this area. Other studies have also reported the regeneration of a cell upon the addition of H_2 and removal of CO or the impurity stream (Ebbesen et al. 2010; Zha et al. 2007)

Various mechanisms have been proposed for this process of nickel regeneration. First, the removal of CO will significantly decrease the concentration of H_2S present in the feed gas. In addition, according to thermodynamics, reaction 19 will be reversed when H_2 is introduced and the sulphide compound is not present. As a result, the sulphur absorbed to the Ni surface will be released leading to the formation of H_2S, which exits the electrode (Oliphant et al. 1978; Rasmussen and Hagen 2009; Sasaki et al. 2006; Zha et al. 2007). The effect of H_2S impurity on cell voltage has been largely described in literature and the findings from this study are discussed in Section 4.4.

To summarise, it has been shown that the addition of CO_2/CO mixtures to the fuel electrode leads to degradation of the cell. A 90 minute induction period was observed when a CO_2/H_2 mixture was introduced at the fuel electrode of a cell in which CO_2/CO electrolysis had occurred. This induction period, which is significantly larger than the 2 mins observed when using a fresh cell, indicates that impurities from the CO_2/CO gas stream (possibly H_2S in the CO stream) might have led to sulphur being adsorbed on some or all of the nickel sites subsequently blocking the active catalytic sites. The study shows that in such instances, the performance of the cell can be regenerated by the removal of CO and addition of H_2.

4.3 Electrochemical Performance of SOCs operating at varying Flow rates and Current densities during CO_2 electrolysis

4.3.1 Experimental

In this Section, the performance of the cell at current densities of -0.5 and -0.61 A/cm^2 is investigated under varying gas flow rates to the fuel electrode. The inlet gas compositions are kept constant and the gas conversion and current efficiency of the electrolyser are investigated. In each case, synthetic air was flowed to the oxygen electrode at a flow rate of 10 ml/min. Table 4–5 gives further information on the operating conditions for this investigation.

Table 4–5: Operating conditions for the electrolysis of CO_2 in a SOC

Cell temperature = 850^{o}C, Cell area = 1.227 cm^2				
Total flow rate (ml/min)	Fuel Electrode Composition (mol %)			Theoretical Nernst potential (mV)
	CO_2	CO	N_2	
20	50	25	25	887
40	50	25	25	887
80	50	25	25	887

4.3.2 Current Efficiency and Gas Conversion

Figure 4–11 and Figure 4–12 shows the quantity of CO produced when the cell was operated at current densities of -0.5 and -0.61 A/cm^2 respectively. Using the Faraday Equation (described in Section 1.3.2), the theoretical amount of CO produced at the current densities indicated were calculated. The exhaust composition of CO was measured using the GC and the amount produced was calculated using a mass balance based on the initial flow rate of CO_2 to the fuel electrode. See appendices C – 1 to C – 3 for GC data.

Note: As the same cell was used in all experiments in this section, the electrical conversion efficiency for the individual measurements could not be accurately quantified.

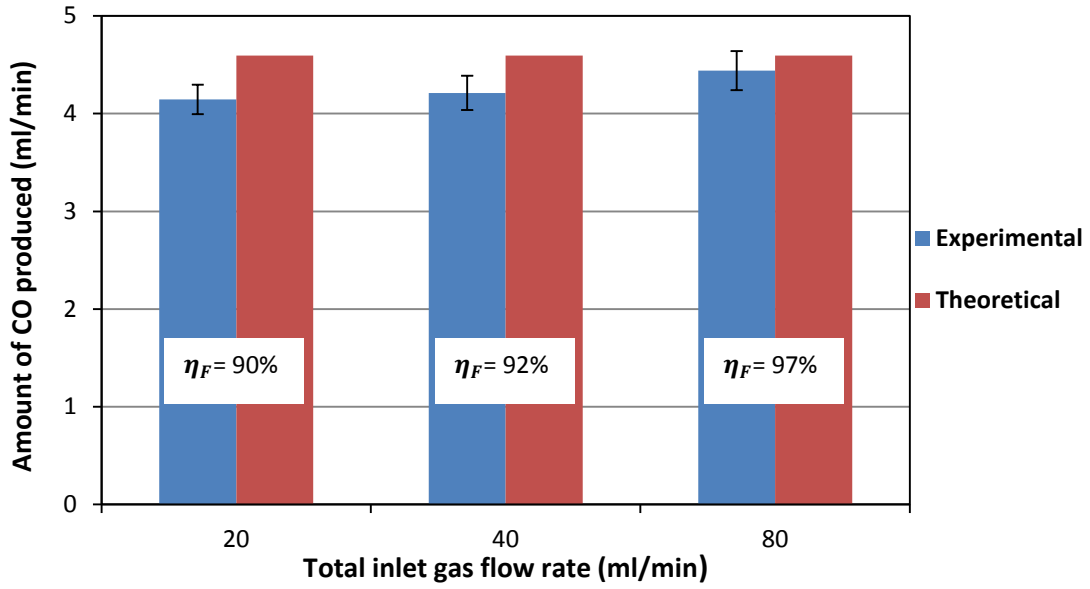

Figure 4–11: Current efficiency when operating at a current density of -0.5 A/cm^2

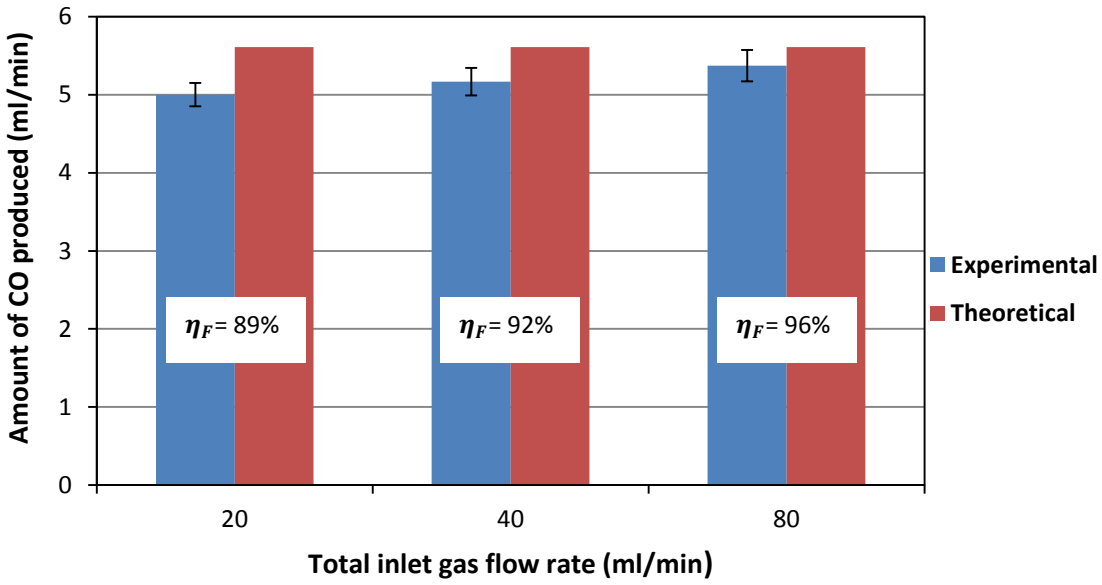

Figure 4–12: Current efficiency when operating at a current density of -0.61 A/cm^2

As seen in Figure 4–11 and Figure 4–12, a Faradaic efficiency of up to 97% was achieved when operating at a flow rate of 80 ml/min indicating a highly efficient operating cell. Furthermore, this is comparable with recent information in literature. In a study by Li et al. (2012), a Faradaic efficiency of 85% was achieved when operating with H_2O compositions to the fuel electrode, cell temperature of 700^{o}C and a current density of 80 mA/cm^2. Ursua et al. (2012) explains that one of the causes of a Faradaic efficiency lower than 100% is due to

the presence of parasitic currents that appear in the real electrolysis process and that do not contribute to the generation of useful fuel.

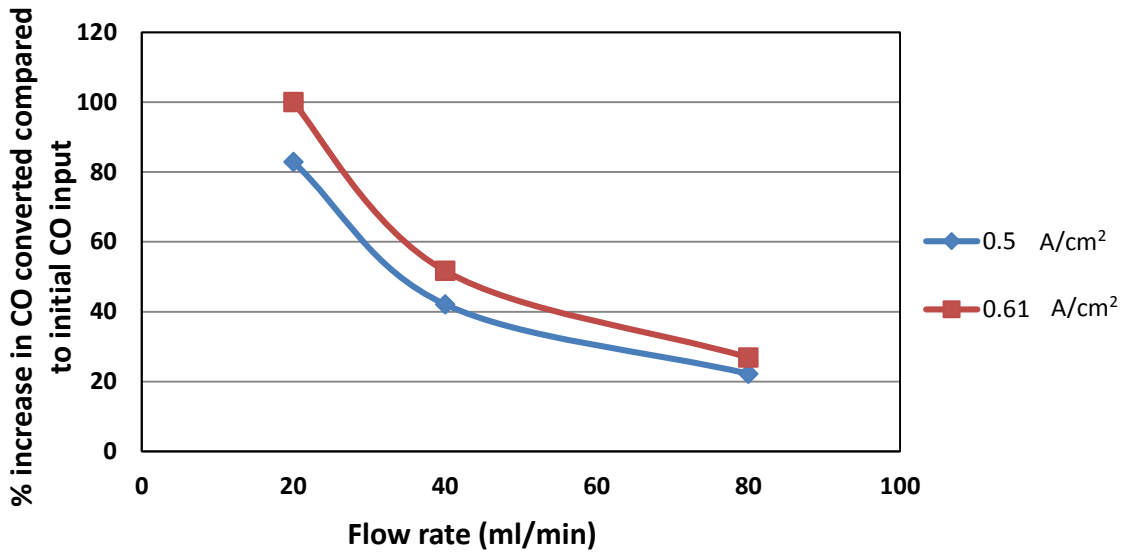

Figure 4–13: Gas conversion of carbon monoxide produced at -0.5 and -0.61 A/cm^2

Figure 4–13 shows the percentage increase in CO converted (calculated using Equation 24) when operating at fuel electrode compositions of 50% CO_2 - 25% CO, flow rates of 20, 40 and 80 ml/min and current densities of -0.5 and -0.61 A/cm^2. As the flow rate increases, the percentage increase in the conversion of CO decreases. Although it is important to note that the actual quantity of CO produced (in ml/min) remains fairly constant as shown in Figure 4–11 and Figure 4–12.

$$\frac{Total\ CO\ output - Initial\ CO\ input}{Initial\ CO\ input} \times 100 \qquad 24$$

In summary, it has been shown that the performance of an electrolysis cell during CO_2 electrolysis decreases slightly with increasing flow rates and a constant gas composition. Although the measured *i*-V curve showed a similar current density from OCV to 1.46 V for all three flow rates, AC impedance spectra showed a slight increase in polarisation resistance across the fuel electrode with increasing gas flow rate. Faradaic efficiencies up to 97% were achieved when operating at a flow rate of 80 ml/min and gas compositions 50% CO_2, 25% CO and 25% N_2 with the electrolyser being operated at -0.5 and -0.61 A/cm^2.

4.4 Durability of the SOCs during High Temperature Electrolysis of Carbon Dioxide

4.4.1 Experimental

The durability of the SOC was examined at 850^{o}C with 50% CO_2 – 25% CO – 25% N_2 supplied to the fuel electrode, synthetic air supplied to the oxygen electrode and a current density of -0.5 A/cm^2 applied to the cell. Using a fresh cell, this investigation was carried out following the reduction of NiO for 8 hours. During the durability study, the cell voltage was measured over 25 hours of operation. Electrochemical impedance spectra were recorded before and after the electrolysis test to determine the cause of degradation.

The aim of this study is to determine the performance of the electrolyser in the short term of operation and further understanding of the effect of the impurities on cell performance.

4.4.2 Effect on Cell Voltage

Figure 4–14 shows the change in cell voltage over the period of study. Furthermore, a breakdown of the passivation rates at various time scales can be seen in Table 4–6. Note that between 7.8 and 14 hours of operation, there was an interruption when the cell was subjected to zero current although the feed gasses were still being flowed to the fuel electrode. The measurement was stopped at the 8th hour when operating at a significantly higher cell voltage in order to avoid damaging the cell and also to determine the possible causes for phase 2 seen in Figure 4–14 through AC characterisation. During this period, DC (by recording *i*-V plots) and AC measurements were also carried out on the cell.

During the second measurement (run 2), the cell was left for a further 15 hours of operation at -0.5 A/cm^2. AC characterisation measurements at OCV were performed before and after the durability study and the results obtained are shown in Figure 4–16 and Figure 4–17.

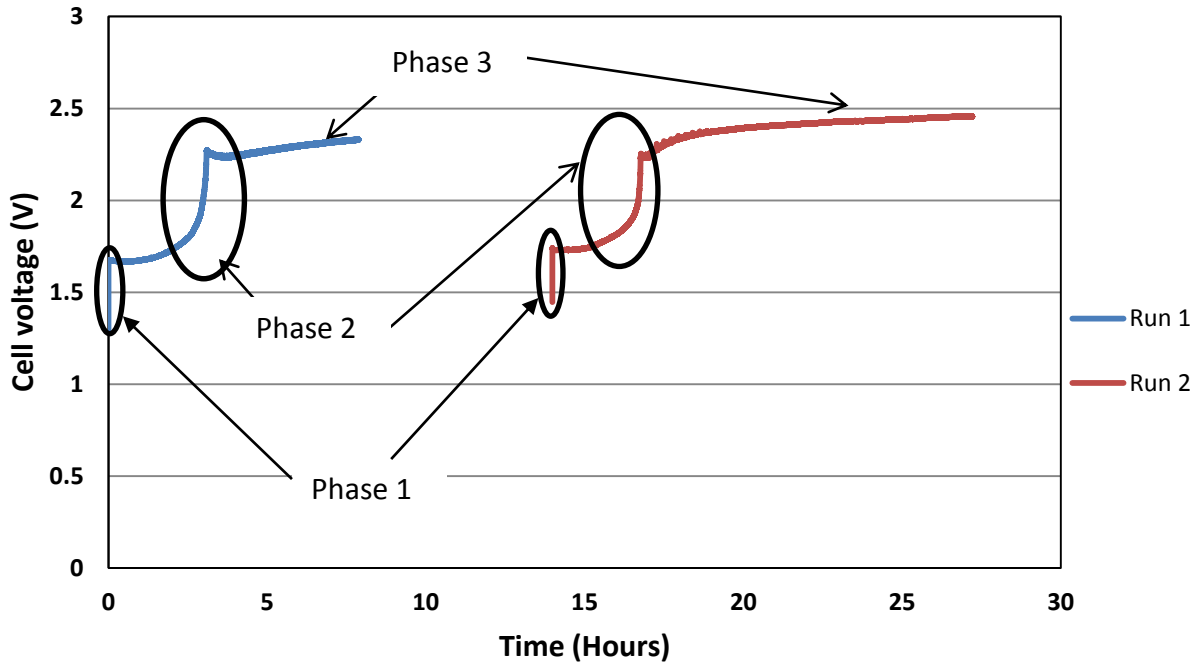

Figure 4–14: Cell voltage measured during CO_2 electrolysis with 50% CO_2 – 25% CO – 25% N_2 supplied to the fuel electrode, synthetic air supplied to the oxygen electrode at an operating temperature of 850°C and a current density of -0.5 A/cm^2

Note: The sharp increase in cell voltage observed in phase 1 is not a consequence of cell degradation but the type of electrochemical measuring instrument employed. The cell voltage increases to match its applied current density.

Table 4–6: Operating conditions, cell voltage and passivation during the CO_2 electrolysis durability tests (first and second measurement)

First measurement (run 1)		
Time (Hours)	Cell voltage (mV)	Degradation rate (mVh^{-1})
0.02 - 5	1670 - 2272	120
5 – 7.8	2272 – 2329	20.4
Second measurement (run 2)		
14 – 19	1730 - 2375	129
19 – 28	2375 – 2457	10.1

As shown in Figure 4–14, the overall degradation rate was 84.5 mV/h and 51.9 mV/h in the first and second measurements respectively. The degradation rates observed in this research are significantly higher than those given in literature. Ebbesen and Mogensen (2009) observed a degradation rate corresponding to 0.4299 mV/h over 50 hours when operating with a fuel electrode composition of 70% CO_2 and 30% CO at 850^oC and a current density of -0.5 A/cm^2. In another study, Ebbesen et al. (2010) observed a degradation rate corresponding to 0.217 mV/h over 50 hours when operating with a fuel electrode composition of 70% CO_2 and 30% CO at 850^oC and a lower current density of -0.25 A/cm^2. Furthermore, it was shown in these studies that cell degradation is eliminated at low current densities (<0.75 A/cm^2) after the inlet gas streamed had been cleaned of impurities.

During the first 5 hours of operation in this study as seen in Figure 4–14, an initial sharp increase in cell voltage can be observed resulting to a passivation rate of 120 mV/h. A similar increase in cell voltage can be seen in the second measurement (run 2) within 5 hours of operation resulting to a passivation rate of 129 mV/h. In both measurements, this was followed by a steady and continuous increase in cell voltage of 20 and 10 mV/h as shown in Table 4–6. A temporary activation period can be seen at the initial stages of "run 2" during which the initial value (phase 1) of its cell voltage starts from ~1.4 V despite a significant increase in cell voltage for "run 1". As previously indicated, the current applied to the cell was halted between "run 1 and 2" although the gasses (50% CO_2, 25% CO and 25% N_2) were still being flowed to the fuel electrode. Although this phenomenon is currently not understood, the cell voltage significantly increases at the same trend of "run 1" in ~5 hours of operation.

At first, it is important to eliminate the formation of carbon as a process contributing to this significant increase in cell voltage. As shown in Figure 4–15, carbon formation at equilibrium according to the Boudouard reaction is highly unlikely at 850^oC operating with 50% CO_2, 25% CO and 25% N_2 flowed to the fuel electrode. On the other hand, this trend of a sharp initial increase in cell voltage, followed by a steady increase is similar to those observed by other authors (Haga et al. 2008; Rasmussen and Hagen 2009; Sasaki et al. 2006; Yang et al. 2010; Zha et al. 2007) when investigating the effect of impurities (H_2S) on nickel based electrodes during fuel cell operation.

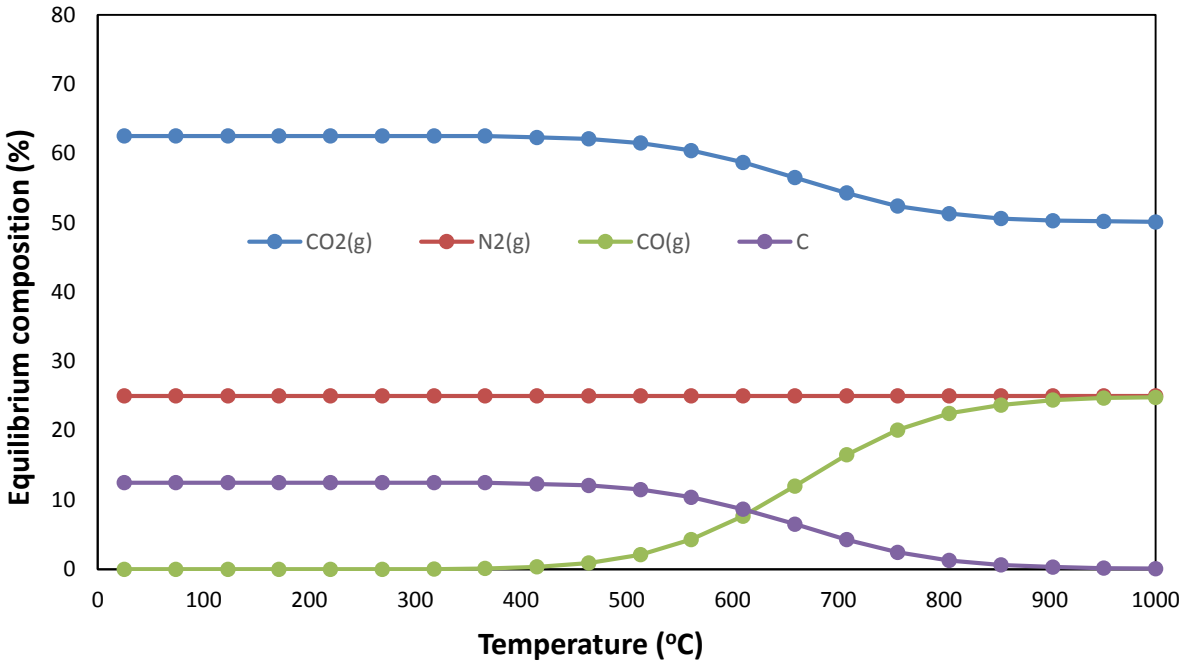

Figure 4–15: Thermodynamic analysis of the Boudouard reaction as a function of temperature operating at 50% CO_2, 25% CO and 25% N_2 flowed to the fuel electrode

Upon exposure to a fuel containing 50 ppm H_2S, Zha et al. (2007) observed a significant drop (-16.67%) in current density in the first 20 hours followed by a slow but continuous drop (-3.96%) in cell performance in the next 120 hours. The performance of the cell recovered in a two stage process (quick rebound followed by a gradual recovery) upon the removal of H_2S from the fuel. The same poisonous effect was also observed when operating with a fuel mixture containing 2 ppm of H_2S although the extent of degradation was much smaller at 12.67 %. Sasaki et al. (2006) also observed a similar sharp degradation although more severe upon operating a fuel cell with 5 ppm H_2S at the Ni anode and a current density of 200 mA/cm^2 within the first 5 mins. The cell voltage although remained stable over the next 60 mins. In both studies, upon removing the H_2S feed, the authors found that the cells recovered although the recovery kinetics was found to be slower than the poisoning kinetics in the latter case.

From Figure 4–14, it is thought that phase 2 occurs due to the sulphur being strongly adsorbed onto the surface of the Ni catalyst and therefore blocks the active sites. The chemical adsorption of sulphur to the Ni surface relates to the process occurring in phase 2 and is similar to the sulphur-Ni interaction mechanism explained in Section 2.6.2.1 and 4.2.5 in which the impurities block the active Ni sites for adsorption, dissociation and diffusion

along surfaces. This process is however reversible (Bartholomew et al. 1982). The second stage (phase 3) of sulphur poisoning is yet to be determined and further experiments are still needed to understand this issue. One possible explanation to phase three which shows a steady and slower degradation process as described by Zha et al. (2007) is that "after the surface adsorption of sulphur on Ni reaches an equilibrium, continued sulphur exposure leads to surface reconstruction of nickel". Furthermore, Oliphant et al. (1978) explains that at H_2S concentrations of 25 - 30 ppm, surface reconstruction of Ni is favoured for supported and unsupported Ni catalysts.

4.4.3AC characterisation – Effect on Impedance Spectra

In the previous Section, it was indicated that the effect of impurities on a SOEC was related to electrochemical changes at the fuel electrode. To further understand this increase in cell voltage (phase 2 and 3) and its effect on the SOEC, AC impedance measurements were performed before and after the durability studies as shown in Figure 4–16 and Figure 4–17. The data analysis carried out in this Section has focused predominantly on Figure 4–16. This is because this figure gives a true representation of the effect of the applied current whereas an *i*-V measurement was carried out before Figure 4–17.

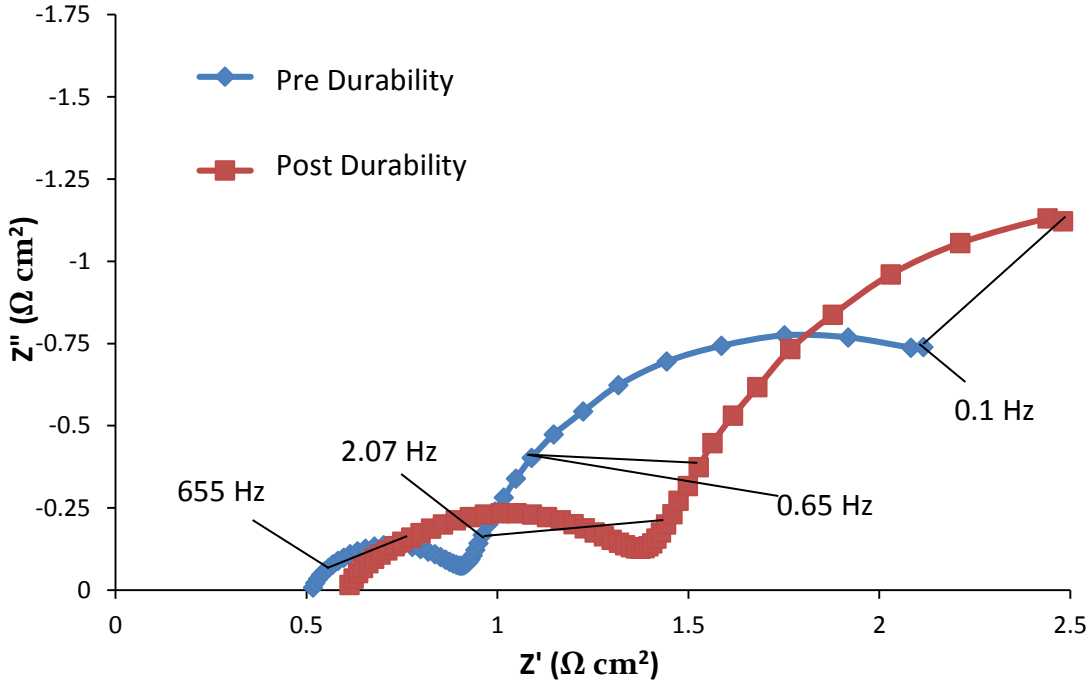

Figure 4–16: AC impedance spectra recorded at 850°C before and after durability study at -0.5 A/cm² (first measurement)

Table 4–7: Ohmic and polarisation resistances during durability studies for CO_2 electrolysis (first measurement), obtained using equivalent circuit model from experimental Nyquist plot

	Pre-durability	Post-durability
Ohmic resistance (Ωcm^2) - R1	0.51	0.60
Oxygen electrode polarisation resistance ($\Omega.cm^2$) – R2	0.41	0.83
Fuel electrode polarisation resistance ($\Omega.cm^2$) – R3	1.78	2.58
Total polarisation resistance ($\Omega.cm^2$)	2.19	3.41
Total cell resistance ($\Omega.cm^2$)	2.70	4.01

The full impedance spectra for the data in the Table 4–7 and Figure 4–16 is shown in Appendices A-8 and A-9.

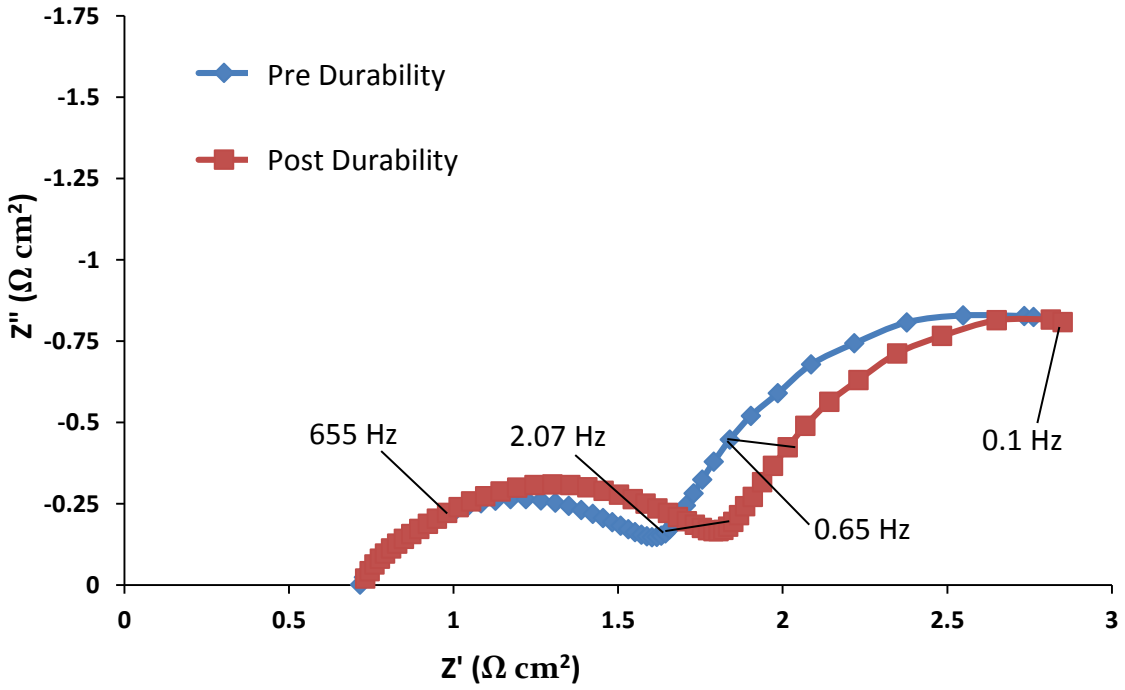

Figure 4–17: AC impedance spectra recorded at 850°C before and after durability study at -0.5 A/cm^2 (second measurement)

Table 4–8: Ohmic and polarisation resistances during durability studies for CO_2 electrolysis (second measurement), obtained using equivalent circuit model from experimental Nyquist plot

	Pre-durability	Post-durability
Ohmic resistance (Ωcm^2) - R1	0.71	0.71
Oxygen electrode polarisation resistance ($\Omega.cm^2$) – R2	0.98	1.17
Fuel electrode polarisation resistance ($\Omega.cm^2$) – R3	1.78	1.74
Total polarisation resistance ($\Omega.cm^2$)	2.76	2.91
Total cell resistance ($\Omega.cm^2$)	3.47	3.62

The full impedance spectra for the data in the Figure 4–17 and Table 4–8 is shown in Appendices A-10 and A-11.

Analysis of the impedance spectra of Figure 4–16 shows a significant increase in ohmic resistance over ~8 hours of operation. The ohmic resistance and polarisation resistances at the oxygen and fuel electrode are shown in Table 4–7. A significant increase in polarisation resistance can be seen in the oxygen electrode (up to ~80%). This region shows a significant increase in resistance, agreeing with the proposed degradation and increase in cell voltage mechanism described in Section 4.4.2.

It has been generally argued by Ebbesen et al. (2010) and Ebbesen et al. (2011) as discussed in Section 2.6.2.1 that degradation of SOECs at low current densities (<-0.75 A/cm^2) is heavily influenced by the presence of impurities at the inlet gasses and therefore by cleaning these gasses, this issue can be eliminated. Although this study shows a significant increase in polarisation resistance at the fuel electrode, detailed cell characterisation is still needed to ascribe the various electrochemical processes to frequency regions. Consequently, the deposition of impurities causing partial blockage of the TPB in the fuel electrode would be known.

A significant increase in ohmic resistance was observed in the first measurement during the first 8 hours of operation. On the other hand, the ohmic resistance of the second measurement, operated for ~14 hours, increased slightly. In this study, a time dependent degradation process relating to an increase in ohmic resistance has been reported and this could therefore correlate to the increase in ohmic resistance seen in the durability study. In

addition, Laguna-Bercero et al. (2011) observed a significant increase in ohmic resistance whereas the polarisation across the fuel and oxygen electrode remains unaltered upon degradation and consequently delamination of the oxygen electrode from the electrolyte. This study carried out at a current density of -1.75 A/cm^2, 895^{o}C and fuel electrode compositions of 70% H_2O and 30% H_2 showed a 63% increase in ohmic resistance after 10 minutes of operation. Therefore, it could also be speculated that the increase in ohmic resistance seen in this study is a result of this phenomenon. Further work including microstructural analysis of the cell is needed in order to determine the true cause of the increase in ohmic resistance observed.

At the oxygen electrode, a significant increase in polarisation resistance is also observed. The cause of this oxygen electrode degradation is currently unknown although it is highly unlikely this is a result of the sharp rise in cell voltage observed in phase 2 of Figure 4–14. This is because a similar increase in polarisation resistance at the oxygen electrode was observed during CO_2/H_2O co-electrolysis durability, however a sharp rise in cell voltage was not observed in the co-electrolysis study.

To summarise, it has been shown that although SOECs are capable of effectively reducing CO_2 to CO, stability of SOECs remains a critical issue (this is not the main topic of this work). Longer term experiments including SOEC optimisation, characterisation of electrochemical processes and microstructural analysis of the cells are still needed to further understanding of SOEC stability as described in Chapter 6.

Chapter 5

5. High Temperature Co-electrolysis of CO_2/H_2O in a Solid Oxide Cell

This chapter discusses the performance of an electrolysis cell operating under varying H_2O/CO_2 compositions. A durability study at -0.5 A/cm^2, 850^{o}C and fuel electrode compositions of 50% CO_2, 25% H_2 and 25% N_2 was carried out. The performance of the cell under varying compositions of CO_2/H_2O is compared to similar CO_2 electrolysis investigations discussed in Chapter 4.

5.1 Introduction

In recent years, there has been a significant increase in the number of investigations into the high temperature co-electrolysis of CO_2 and H_2O in a SOEC, as discussed in Chapter 2. This is due to the potential of the electrolyser to simultaneously reduce both feed stocks to produce synthetic gas, an intermediate in the production of synthetic fuels. The CO_2/H_2O co-electrolysis process, described in detail in Chapter 2 is, however, more complicated than individual steam and carbon dioxide electrolysis and the reaction mechanism for the production of syngas is not yet fully understood. A better understanding of the co-electrolysis reaction mechanism is important as this could provide vital information needed in the development of more efficient electrolysis cells.

This aim of this chapter is to gain further understanding into the co-electrolysis reaction mechanism by comparing the performances of SOEC for CO_2 electrolysis and CO_2/H_2O co-electrolysis.

Due to issues of condensation described in Section 3.5, H_2O was not used as an input gas during H_2O/CO_2 co-electrolysis as the gas composition could not be successfully controlled. Instead, cold inlet compositions of CO_2/H_2 mixtures were used and these mixtures were varied based on thermodynamic calculations such that the CO_2/H_2O equilibrium compositions (based on the rWGSR) at the fuel electrode are directly comparable to corresponding CO_2 electrolysis investigations.

5.2 Co-electrolysis of H_2O and CO_2

5.2.1 Experimental set-up

The test set-up and operation were described in detail in Chapter 3. Electrolyte supported cells were primarily used in this co-electrolysis experimental study; although the performance of the NiO electrode supported cell operating under CO_2/H_2O mixtures was also briefly investigated. Using both supported cell types, CO_2/H_2 mixtures shown in Table 5–1 were varied when operating at a cell temperature of 850^oC to investigate the performance of the electrolyser under co-electrolysis conditions. In each case, synthetic air (80% N_2 and 20% O_2) was flowed to the oxygen electrode at a flow rate of 10 ml/min.

In this study, two methods were employed to determine if the equilibrium of the rWGSR is reached in this reaction, as suggested by Ebbesen et al. (2012).

- The exhaust gas compositions at OCV must be close to the equilibrium composition, i.e. within 1% of the calculated values for the electrolyte supported cells and 2% for the electrode supported cells.
- The measured OCVs must be below or close to the theoretical potentials i.e. within 2 mV of the calculated value. In addition, a measured potential higher than its theoretical value is an indicating at the exhaust gas compositions are further away from the thermodynamic equilibrium compositions.

Table 5–1: Fuel electrode operating conditions for H_2O/CO_2 co-electrolysis process

Fuel electrode flow rate = 20 ml/min			
Cold Inlet composition (mol %)			
No	**CO_2**	**H_2**	**N_2**
4b1	15	60	25
4b2	25	50	25
4b3	50	25	25
4b4	60	15	25

Note that the above experiments were performed in the order shown in Table 5–1 (i.e. 4b1, 4b2, 4b3 and 4b4).

DC and AC characterisation measurements were recorded at the operating conditions shown in Table 5–1. During DC measurement, the *i*-V plot was recorded 3 times consecutively when operating at the same gas mixture to ensure accuracy. Unless otherwise stated, the *i*-V curves presented in this chapter are always the third of the measured set of data. AC characterisation measurements recording the impedance spectra were carried out after DC measurements. All investigations presented in this chapter were repeated to estimate any errors.

5.2.2 Initial Cell Characterisation

5.2.2.1 Electrolyte supported cell

Due to the possibility of variation in performance of the purchased cells, initial cell characterisation under NiO reducing conditions is important in order to ensure consistency and a base comparison with the processes of CO_2 electrolysis described in Chapter 4. Prior to the CO_2/H_2O co-electrolysis investigations, the operating electrolyte supported SOC was characterised by AC impedance spectroscopy to determine the initial performance of the cell. The measured OCV under NiO reducing conditions of 49% N_2, 49% H_2 and ~2% H_2O at 850°C was determined to be 1060 ±4mV as shown in Table 5–2.

Table 5–2: Measured OCV of electrolyte supported cells at 850°C under NiO reducing conditions

Cold inlet gas composition (%)			Theoretical Nernst Potential (mV)	Experimental OCV (mV)	
N_2	H_2	H_2O		$Cell_{CO2}$	$Cell_{CO2/H2O}$
49.1	49.1	1.8 (±0.2)	1086 (±3)	1065 (±4)	1060 (±4)

Note: $Cell_{CO2}$ and $Cell_{CO2/H2O}$ are the cells used during CO_2 electrolysis and CO_2/H_2O co-electrolysis respectively.

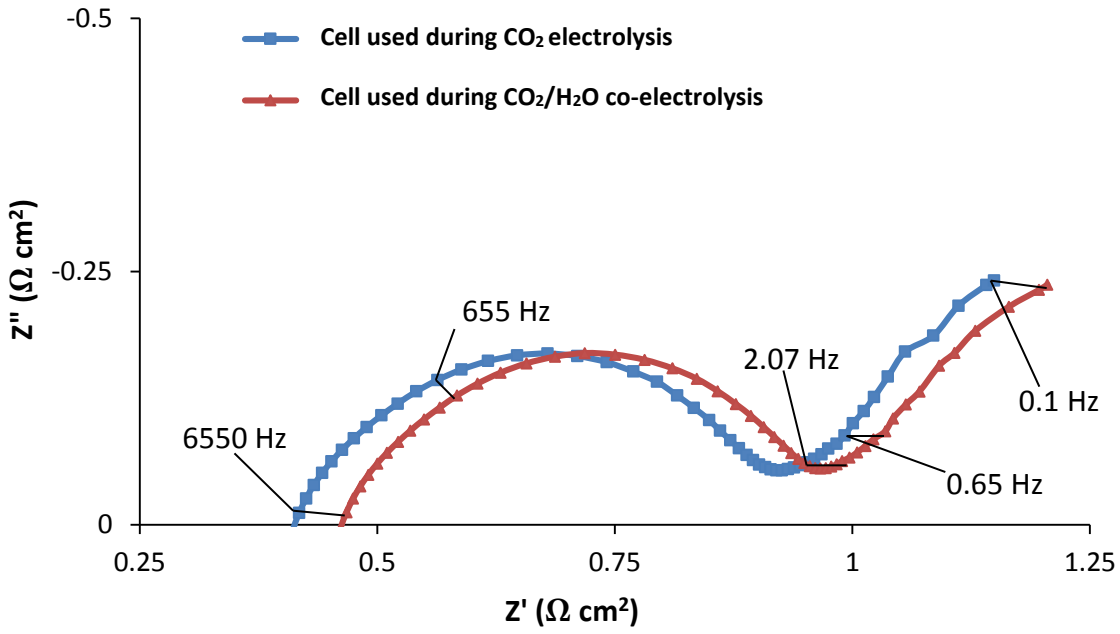

Figure 5–1: AC impedance spectra recorded at OCV, 850°C, fuel electrode gas compositions of 49% N_2, 49% H_2 and ~2% H_2O and synthetic air to the oxygen electrode

The AC impedance measurement shown in Figure 5–1 indicates a similar polarisation resistance of 1.53 and 1.55 Ωcm^2 for $cell_{co\text{-}elec.}$ and $cell_{CO2\ elec.}$. Table 5–3 shows the ohmic resistance of both cells and a breakdown of the polarisation resistances across both electrodes. The slight difference in the initial ohmic resistance shown in Figure 5–1 is caused by poor contact between the platinum electrical mesh and the fuel electrode side of the SOEC upon loading of the cell.

Overall, a similar performance can be seen across the fuel and oxygen electrodes. This implies little variation in the performance of the cells and therefore subsequent electrolysis investigations can be carried out and the results compared. The measured cell voltage at open circuit, which gives an indication of gas leakages across the cell, is similar to the cell used for CO_2 electrolysis indicating a consistent overall operating system. Furthermore, this shows the cell is sealed satisfactorily.

Table 5–3: Ohmic and polarisation resistances of both cells under NiO reducing conditions, obtained using equivalent circuit model from experimental Nyquist plot

	Cell $_{CO2elec}$	Cell $_{Co\text{-}elec}$
Ohmic resistance (Ωcm^2) - R1	0.41	0.46
Oxygen electrode polarisation resistance ($\Omega.cm^2$) – R2	0.53	0.52
Fuel electrode polarisation resistance ($\Omega.cm^2$) – R3	1.02	1.01
Total polarisation resistance ($\Omega.cm^2$)	1.55	1.53
Total cell resistance ($\Omega.cm^2$)	1.96	1.99

The full impedance spectra for the data in the Table 5–3 and Figure 5–1 is shown in Appendices A-1 and A-2.

To summarise, a comparable initial performance was observed for both electrolyte supported cells used for CO_2 electrolysis and CO_2/H_2O co-electrolysis investigations indicating little variation in the performance of the produced cells. Therefore subsequent electrolysis investigations can be carried out and the results compared.

5.2.2.2 Electrode supported SOEC

It was shown in Chapter 3 that the contact resistance is significantly reduced by applying Pt ink to the fuel electrode. In this chapter, the performance of the cell under CO_2/H_2O co-electrolysis mixtures is presented in two Sections: 1) Using the electrode supported cell with Pt ink added to the fuel electrode and 2) electrode supported cell without Pt ink. The co-electrolysis investigations described in this chapter using the electrode supported cells were carried out after all electrolyte supported cell investigations had been completed.

5.2.3 Equilibrium of the rWGSR

5.2.3.1 Thermodynamic Equilibrium and Exhaust Gas Compositions

The compositions of CO_2 and H_2O to be investigated were calculated such that a comparison could be drawn with the CO_2 electrolysis compositions described in Chapter 4. This implies that, the sum of the co-electrolysis compositions (CO_2+H_2O) at the fuel electrode should always equal that of the CO_2 electrolysis compositions (CO_2).

The exhaust gas compositions are compared to the thermodynamic equilibrium compositions to determine if the equilibrium of the rWGSR is reached. The thermodynamic equilibrium composition was calculated using thermodynamic properties from process simulation software HSC Chemistry 5.11. The co-electrolysis compositions were determined using the gas compositions measured via the GC and a mass balance around the cell rig was carried out as shown in Figure 5–2. A mass balance is needed as the GC does not measure the steam composition from the cell rig.

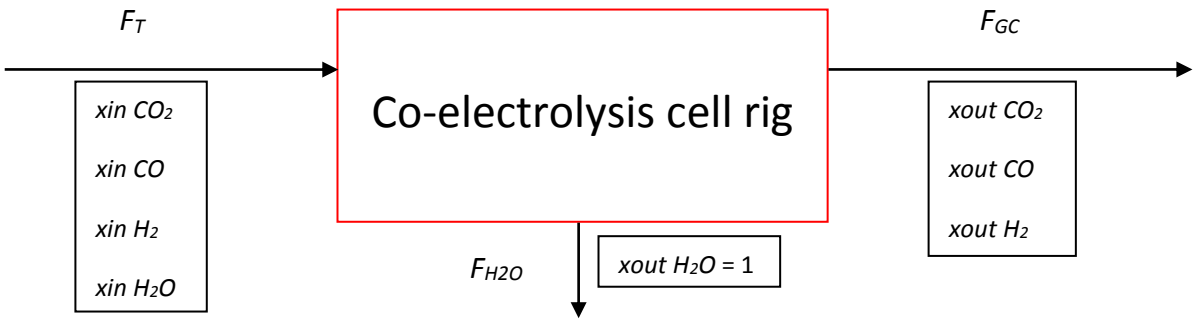

Figure 5–2: Schematic diagram showing a mass balance around the cell rig during the high temperature CO_2/H_2O co-electrolysis process

Where F_T is the total flow rate (ml/min) to the fuel electrode, F_{GC} is the flow rate to the GC after steam has been removed and F_{H20} is the flow rate of steam condensed. *xin* and *xout* are compositions of individual gasses in and out of the fuel electrode respectively.

The mass balance on the cell rig shown in Figure 5–2 is given in Equation 19:

$$F_T = F_{H2O} + F_{GC} \quad 25$$

A mass balance on carbon is given in Equation 20:

$$F_T(xin\ CO_2 + xin\ CO) = F_{GC}\ (xout\ CO_2 + xout\ CO) \quad 26$$

From the above Equation, the GC flow rate can then be calculated as the compositions of CO_2 and CO can be obtained from the GC.

A mass balance on hydrogen is given in Equation 21:

$$F_T(xin\ H_2O + xin\ H_2) = F_{H2O} + F_{GC}\ (xout\ H_2) \quad 27$$

With this information, the gas compositions exiting the cell rig can be fully monitored.

Table 5–4, Table 5–5 and Table 5–6 all show the co-electrolysis exhaust gas compositions of Table 5–1 using an electrolyte supported cell, electrode supported cell without Pt ink and an electrode supported cell with Pt paste added to the fuel side electrode respectively.

Table 5–4: Thermodynamic equilibrium and exhaust gas composition at 850°C using the electrolyte supported cell

	Cold Inlet composition (%)			Thermodynamic equilibrium (mol %)					Exhaust gas composition (mol %)				
No	**CO_2**	**H_2**	**N_2**	**H_2O**	**CO_2**	**H_2**	**CO**	**N_2**	**H_2O**	**CO_2**	**H_2**	**CO**	**N_2**
4b1	15	60	25	12.2	2.8	47.8	12.2	25	11	2.8	49	12.2	25
4b2	25	50	25	17.1	7.95	33	17.1	25	15.1	8.7	34.9	16.3	25
4b3	50	25	25	17.1	33	7.95	17.1	25	15.3	32.7	9.7	17.3	25
4b4	60	15	25	12.2	47.8	2.8	12.2	25	12.3	46	2.7	13.8	25

Note: The exhaust gas compositions using the electrolyte supported cell has an error of ~±1%

Table 5–5: Thermodynamic equilibrium and exhaust gas composition at 850°C using the electrode supported cell (without Pt ink added to the fuel electrode)

	Cold Inlet composition (%)			Thermodynamic equilibrium (mol %)					Exhaust gas composition (mol %)				
No	**CO_2**	**H_2**	**N_2**	**H_2O**	**CO_2**	**H_2**	**CO**	**N_2**	**H_2O**	**CO_2**	**H_2**	**CO**	**N_2**
4b2	25	50	25	17.1	7.95	33	17.1	25	18.3	7.8	31.7	17.2	25
4b3	50	25	25	17.1	33	7.95	17.1	25	17.3	31.9	7.7	18.1	25

Note: The exhaust gas compositions using the electrode supported cell has an error of ~±2%

Table 5–6: Thermodynamic equilibrium and exhaust gas composition at 850°C using the electrode supported cell (with Pt ink added to the fuel electrode)

	Cold Inlet composition (%)			Thermodynamic equilibrium (mol %)					Exhaust gas composition (mol %)				
No	**CO_2**	**H_2**	**N_2**	**H_2O**	**CO_2**	**H_2**	**CO**	**N_2**	**H_2O**	**CO_2**	**H_2**	**CO**	**N_2**
4b2	25	50	25	17.1	7.95	33	17.1	25	9.4	16.2	40.6	8.8	25
4b3	50	25	25	17.1	33	7.95	17.1	25	12.1	39.3	12.9	10.7	25

Error Analysis

The ±1% error in the exhaust gas compositions given for the electrolyte supported cell originates from the GC (i.e. calibration, integration, etc.) as described in Section 3.7.2. The additional ±1% for the electrode supported cell is a result of larger gas leakages around the cell compared to the electrolyte supported cell as described in Section 3.8.2.

Appendices C–4, C–5 and C–6 shows the GC data obtained in order to calculate the above exhaust gas compositions in Table 5–4, Table 5–5 and Table 5–6 respectively.

Comparing Table 5–4 and Table 5–5, it can be seen that the exhaust gas compositions are both close to the thermodynamic equilibrium compositions. However, the equilibrium of the rWGSR is only fully reached when using the electrode supported cell as the gas compositions are within the stated error range and closer to the thermodynamic equilibrium compositions. On the other hand, the exhaust gas compositions are not within 1% of the equilibrium compositions when using an electrolyte supported cell. The equilibrium of the rWGSR is not fully reached in this case due to the lower Ni catalyst content (i.e. lower surface area of catalyst) present within the 50 µm thick fuel side electrode; 80% lower than the 250µm thick fuel electrode of the NiO fuel electrode supported cell. This implies a lower gas conversion for CO production when using the electrolyte supported cells at OCV.

From Table 5–6, it can be seen that the equilibrium of the rWGSR is not reached when using an electrode supported cell with pure Pt ink added to the fuel electrode. The exhaust gas composition in each experiment is further away from the equilibrium composition. At first, it is important to note that the platinum paste applied to the fuel electrode contained frit, a glassy ceramic compound. It is highly likely that the presence of glassy ceramic compound could have accumulated at the surface of nickel in the fuel electrode. Ultimately, this would reduce the active surface area of the catalyst and hence explain why equilibrium of the rWGSR is not reached.

5.2.3.2 Open Circuit Voltage

In this section, the measured OCVs are compared to calculated potentials. The theoretical potentials shown in Figure 5–3, Figure 5–4 and Figure 5–5 were calculated using the Nernst Equation (Equation 6) and the thermodynamic equilibrium compositions given in Table 5–4, Table 5–5 and Table 5–6 respectively. Furthermore, the theoretical GC voltages for H_2O/H_2 and CO_2/CO mixtures (calculated using the Nernst potential and the exhaust compositions) are compared to the measured OCV. The closeness of the measured potential to the theoretical values can aid in determining if equilibrium of the rWGSR is reached.

Note: The measured potentials each have an error of ±2 mV originating from; 1.5% reading accuracy of the MFC equivalent to ±1 mV and a reading error of the electrochemical

interface instrument used when monitoring the OCV during CO_2/H_2O co-electrolysis equivalent to ±1 mV.

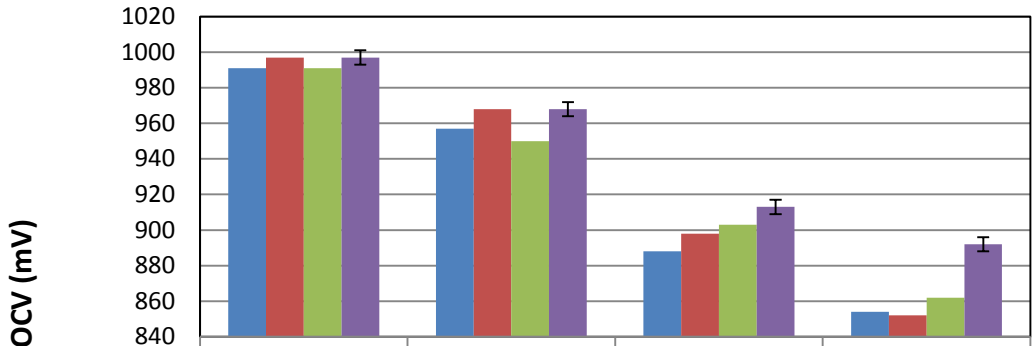

	4b1: 15% CO2 - 60% H2	4b2: 25% CO2 - 50% H2	4b3: 50% CO2 - 25% H2	4b4: 60% CO2 - 15% H2
Theoretical	991	957	888	854
Theo GC (H2O/H2)	997	968	898	852
Theo GC (CO2/CO)	991	950	903	862
Measured	997	968	913	892

Figure 5–3: Open circuit voltage measured of varying CO_2/H_2O compositions at 850°C when using an electrolyte supported cell

Note: The theoretical GC voltage is the calculated Nernst potential based on the exhaust compositions.

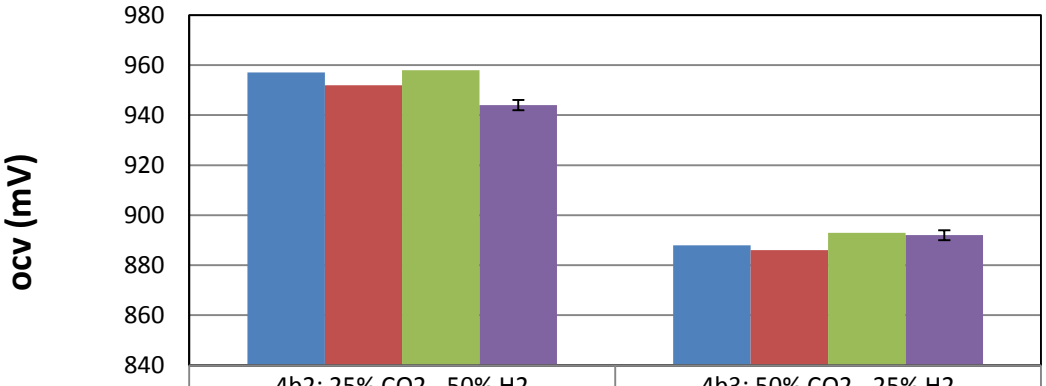

	4b2: 25% CO2 - 50% H2	4b3: 50% CO2 - 25% H2
Theoretical	957	888
Theo GC (H2O/H2)	952	886
Theo GC (CO2/CO)	958	893
Measured	944	892

Figure 5–4: Open circuit voltage measured of varying CO_2/H_2O compositions at 850°C when using an electrode supported cell

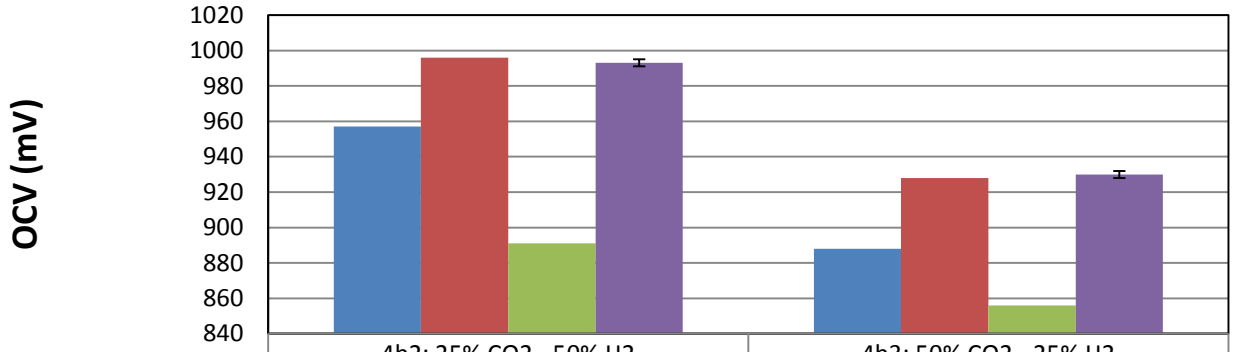

	4b2: 25% CO2 - 50% H2	4b3: 50% CO2 - 25% H2
Theoretical	957	888
Theo GC (H2O/H2)	996	928
Theo GC (CO2/CO)	891	856
Measured	993	930

Figure 5–5: Open circuit voltage measured of varying CO_2/H_2O compositions at 850°C when using an electrode supported cell with platinum paste added to the fuel electrode

Comparing Figure 5–3, Figure 5–4 and Figure 5–5, it can be seen that the measured OCVs in all cases are closest to the theoretical potentials only when using a NiO electrode supported without Pt ink. The larger differences between measured and theoretical potentials shown in Figure 5–3 and Figure 5–5 indicates that these compositions are further away from equilibrium, confirming the initial results in Section 5.2.3.1. Additionally, it can be seen in Figure 5–3 and Figure 5–5 that the measured potentials are significantly higher than the theoretical values whereas in Figure 5–4, the measured potentials are either below or within 4 mV of the calculated potentials.

Measured OCVs higher than corresponding theoretical values are usually stated in literature although less widely discussed during CO_2/H_2O co-electrolysis. This is due to the complexity of gas leakages and gas conversion during the equilibrium chemical reaction. In a study by Zhan and Zhao (2010), the measured OCV was recorded to be 20 mV above the theoretical values when operating at 800°C with fuel electrode compositions of 25% H_2 and 75% CO_2 using a Ni-YSZ electrode supported cell (Ni-YSZ/YSZ/GDC-LSCF). Zhan et al. (2009) also observed a measured OCV to be 10 mV above the theoretical values when operating at a temperature of 800°C with fuel electrode compositions of 25% H_2, 25% CO_2 and 50% H_2O. Ebbesen et al. (2012) however measured an OCV value 13 mV below the theoretical value

when operating at 850°C with 50% CO_2 – H_2% CO – 25% Ar to the fuel electrode and pure oxygen to the oxygen electrode and using a Ni-YSZ/YSZ/LSM-YSZ cathode supported cell. Although some leakages were identified, the exhaust gas compositions were within 1 mol % of the thermodynamic equilibrium compositions.

In this study, the very small differences between the Nernst potential and the OCV indicate that the rWGSR is closest to equilibrium when using a NiO electrode supported without Pt ink.

To summarise, it has been shown that comparing the CO_2/H_2O exhaust compositions and measured OCV to respective thermodynamic equilibrium compositions and theoretical OCV can aid in determining if equilibrium of the rWGSR is reached. When using a NiO fuel electrode supported cell, the equilibrium of the rWGSR is reached. On the other hand, the equilibrium of the rWGSR is close, but not fully reached when using an electrolyte supported cell due to the lower Ni catalyst content present within the fuel electrode of the cell.

5.3 Electrochemical Measurements

5.3.1 DC Characterisation

In this section, the performance of the electrolyte supported cell under varying CO_2/H_2O mixtures is discussed. In addition, these performances are compared with the CO_2 electrolysis investigations described in Chapter 4. The initial performance of the cell was measured by recording *i*-V curves at varying fuel electrode compositions and the results of the initial DC characterisation measurements are shown in Figure 5–6. The *i*-V curves were recorded at 850°C with synthetic air being flowed to the oxygen electrode. Although not shown, no discontinuity was observed in the *i*-V plot when operating from fuel to electrolysis mode similar to that observed during CO_2 electrolysis.

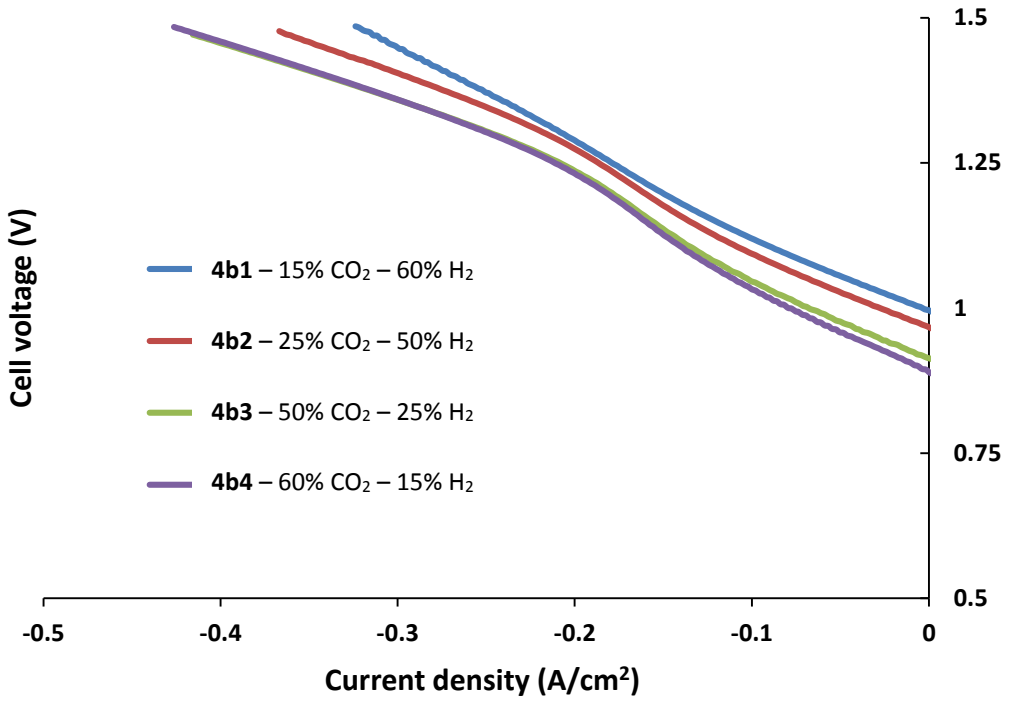

Figure 5–6: DC characterisation measurement at 850°C under varying mixtures of CO_2/H_2

Table 5–7: Measured current densities of similar CO_2 and CO_2/H_2O compositions at 1.46 V and 850°C cell temperature

	4c1	4b1	4c2	4b2	4c3	4b3	4c4	4b4
	15% CO_2 60% CO	15% CO_2 60% H_2	25% CO_2 50% CO	25% CO_2 50% H_2	50% CO_2 25% CO	50% CO_2 25% H_2	60% CO_2 15% CO	60% CO_2 15% H_2
Current density (A/cm^2)	0.27	↑ 0.31	0.30	↑ 0.35	0.33	↑ 0.40	0.33	↑ 0.40

From Figure 5–6, it can be seen that the current density values at a given cell voltage generally increases with increasing CO_2 and H_2O mixtures. At higher feed concentrations (50% CO_2 - 25% H_2 and 60% CO_2 - 15% H_2); a plateau in the current density can be seen above ~1.25 V. This trend is similar to that observed during CO_2 electrolysis (see Section 4.2.4) in which the *i*-V curve indicated a maximum in activation losses at higher feed concentrations of 50%, 60% and 70% CO_2.

A comparison of the performance of the electrolysis cell during CO_2 electrolysis and CO_2/H_2O co-electrolysis showed that at a given cell voltage, the current density is higher in the co-electrolysis mixtures as shown in Table 5–7. The presence of steam at the fuel electrode during CO_2 electrolysis increases the performance of the cell by up to 21%.

From Figure 5–6, a slight shift can be seen in the *i*-V plots in which the graph line becomes steeper and moves away from its original shape. Between -0.1 and -0.4 A/cm^2, an increase in cell resistance is observed as evident from the "S" – shaped *i*-V plot. It is important to note that during CO_2 electrolysis, the "S"- shaped *i*-V plot was not observed. To further understand the origin of this process, DC characterisation measurements were carried out on a new cell at fuel electrode compositions of 50% CO_2, 25% H_2 and 25% N_2 (experiment 4b3) and the data was compared to the *i*-V plot of Figure 5–6 when using an aged cell.

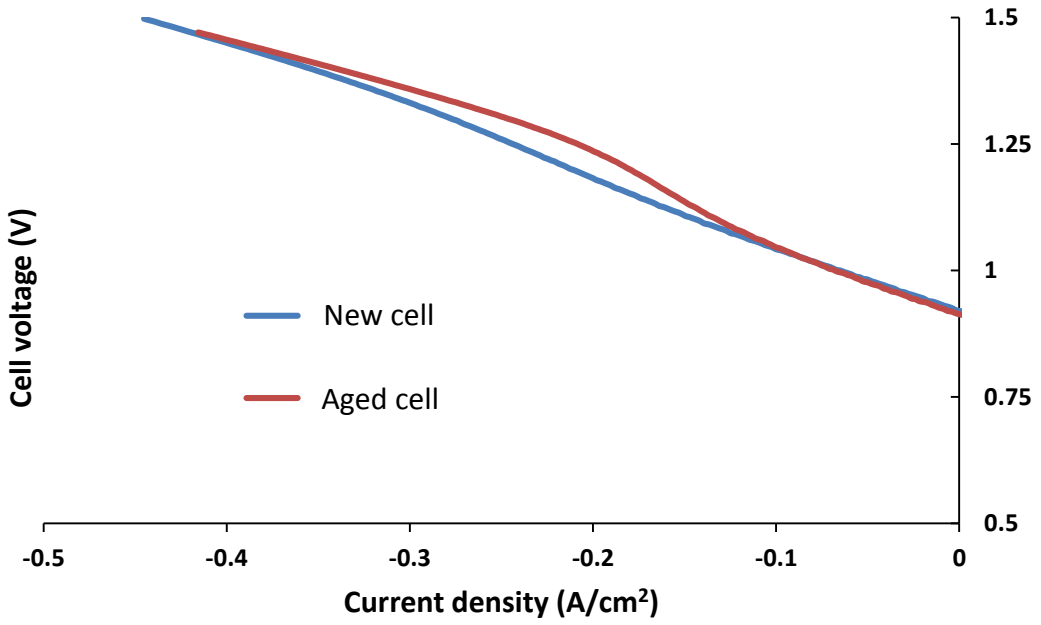

Figure 5–7: DC characterisation measurement at 850°C and 50% CO_2, 25% H_2 and 25% N_2 (4b3) when using a new and aged cell

Figure 5–7 is an *i*-V plot which compares DC characterisation measurements at 850°C and 50% CO_2, 25% H_2 and 25% N_2 fuel electrode compositions using a new cell and an aged cell (i.e. the same cell used for all gas mixtures during the initial co-electrolysis investigation as shown in Figure 5–6). Although the performance of the cell remains the same evident by a similar current density at cell voltages beyond ~1.4 V, the shapes of the *i*-V plots differs. The increase in cell resistance between -0.1 and -0.4 A/cm^2 is more evident in Figure 5–7.

This information shows that the increasing CO_2/H_2O co-electrolysis gas compositions at the fuel electrode are not a cause for the "S" – shaped *i*-V plot.

As explained in the experimental Section 5.2.1, the *i*-V plot was recorded 3 times in a row (run 1, run 2 and run 3) when operating at a set gas mixture. Figure 5–8 is an *i*-V curve showing all three measurements when recording an *i*-V curve. An increase in resistance can be seen at low current densities between -0.2 and -0.4 A/cm^2 with increasing DC measurements. The evidence presented suggests that this increase in cell resistance at low current densities is associated with an increase in DC measurements only during CO_2/H_2O co-electrolysis. The electrochemical process contributing to the resistance in the formation of the "S" – shaped *i*-V curve is currently unknown.

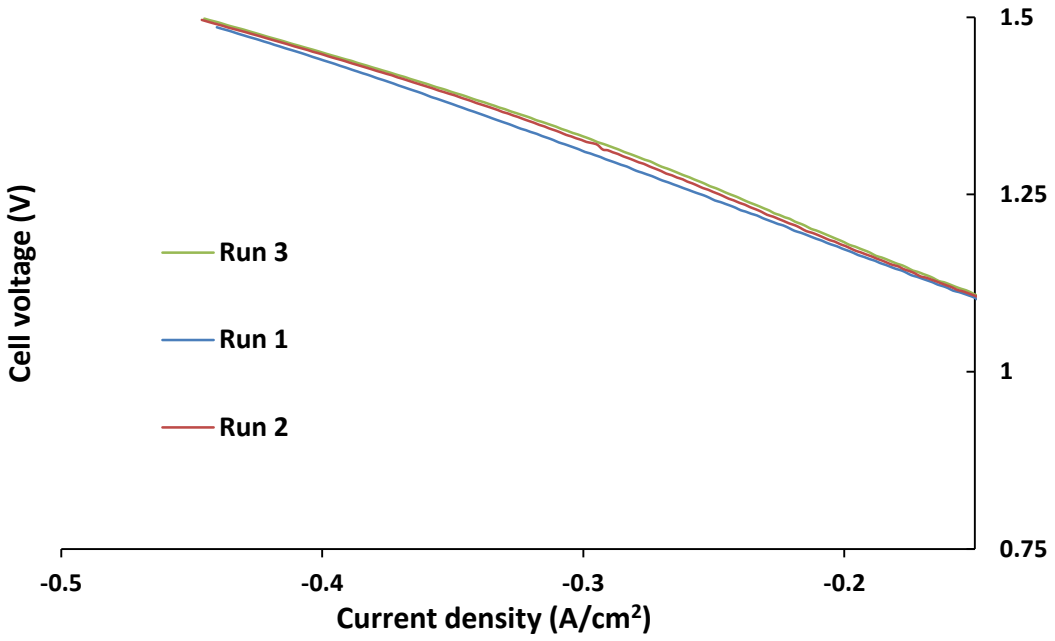

Figure 5–8: Simultaneous DC measurements at 850^{o}C and fuel electrode compositions of 50% CO_2, 25% H_2 and 25% N_2 (4b3) when using a new cell

5.3.2 Area Specific Resistance during CO_2/H_2O co-electrolysis

The cell ASRs under varying gas mixtures outlined in Table 5–1 were calculated from the *i*-V plot of Figure 5–6 as the line from the OCV to the cell voltage measured at a current density of -0.1 A/cm^2. The measured ASR is seen to increase with increasing CO_2/H_2O mixtures as shown in Figure 5–9. The CO_2/H_2O co-electrolysis ASRs were also compared to equivalent CO_2 electrolysis mixtures.

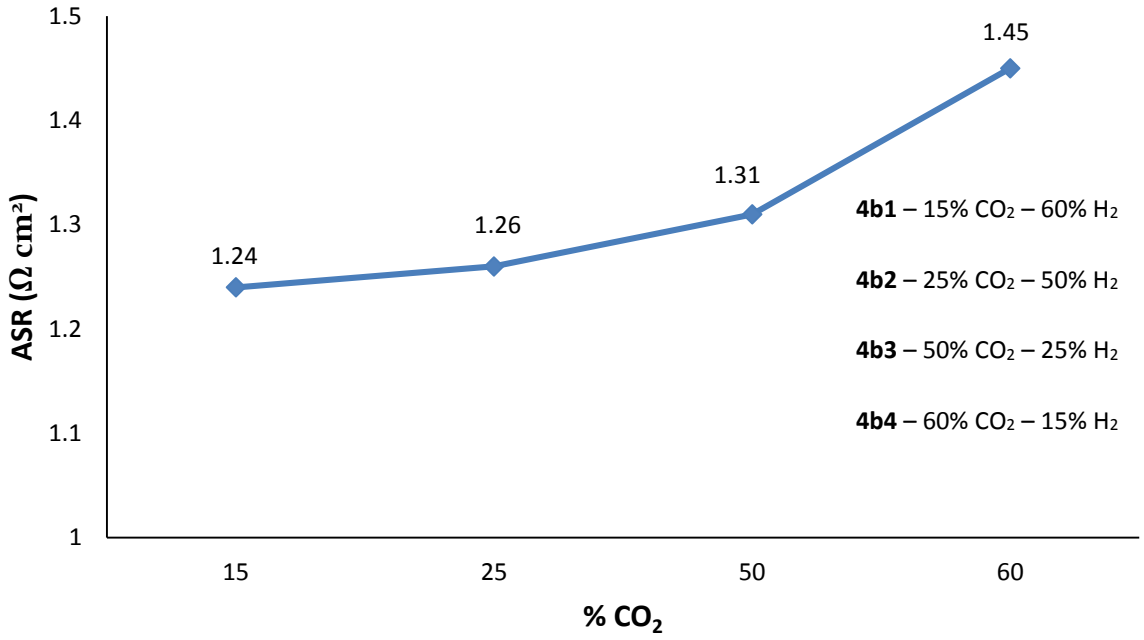

Figure 5–9: Area specific resistance with increasing CO_2/H_2O compositions

Table 5–8: Measured ASR of equivalent CO_2 and CO_2/H_2O mixtures at -0.1A/cm²

	4c1 15% CO_2 60% CO	**4b1** 15% CO_2 60% H_2	**4c2** 25% CO_2 50% CO	**4b2** 25% CO_2 50% H_2	**4c3** 50% CO_2 25% CO	**4b3** 50% CO_2 25% H_2	**4c4** 60% CO_2 15% CO	**4b4** 60% CO_2 15% H_2
CO_2 (Ω cm²)	1.75	↑	1.87	↑	2.06	↑	2.41	↑
CO_2/H_2O (Ω cm²)		1.24		1.26		1.31		1.45

Where b and c represents the cold inlet compositions for CO_2/H_2O co-electrolysis and CO_2 electrolysis respectively

As shown in Table 5–8, the cell ASR for the co-electrolysis process is 40% lower than corresponding carbon dioxide electrolysis processes. AC impedance characterisation of both mixtures is compared to gain further understanding of the origin of these resistances.

5.3.3 AC Characterisation

AC characterisation at OCV was performed after recording the *i*-V plots and the results obtained at 850°C and varying CO_2/H_2O mixtures are shown in Figure 5–10.

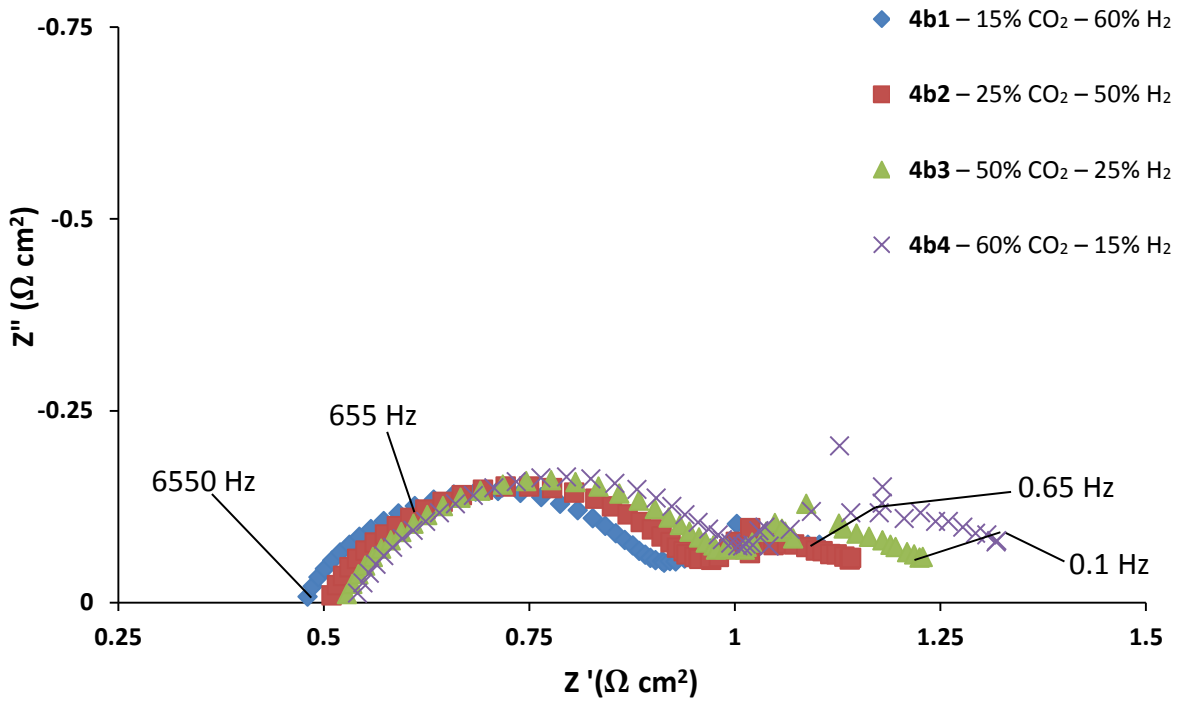

Figure 5–10: AC impedance measurement recorded at OCV under different CO_2/H_2 compositions

From Table 5–9, a slight increase in the total polarisation resistance can be seen with increasing CO_2 and H_2O compositions. This trend of an increase in resistance corresponds to the ASRs calculated from the *i*-V curve as shown in Figure 5–9. A breakdown of the cell resistances as shown in Table 5–9 shows a slight increase in ohmic resistance increases with time. Similar to electrical contact issues discussed in Section 4.2.4, the change in the ohmic resistance was mainly a consequence of variations in the contact between the current collector and the cell. The increasing CO_2/H_2O mixture is not a cause for the observed increase in ohmic resistance. Furthermore, it was observed in latter experiments that the ohmic resistance remained the same for varying gas compositions when carried out within a short period (i.e. 1 hour).

Table 5–9: Ohmic and polarisation resistances during CO_2/H_2O co-electrolysis, obtained using equivalent circuit model from experimental Nyquist plot

	4b1 15% CO_2 60% H_2	4b2 25% CO_2 50% H_2	4b3 50% CO_2 25% H_2	4b4 60% CO_2 15% H_2
Ohmic resistance ($\Omega.cm^2$) - R1	0.48	0.50	0.53	0.54
Oxygen electrode polarisation resistance ($\Omega.cm^2$) – R2	0.44	0.47	0.47	0.48
Fuel electrode polarisation resistance ($\Omega.cm^2$) – R3	0.26	0.22	0.26	0.34
Total polarisation resistance ($\Omega.cm^2$)	0.7	0.69	0.73	0.82
Total cell resistance ($\Omega.cm^2$)	1.18	1.19	1.26	1.36

The full impedance spectra for the data in the Figure 5–10 and Table 5–9 can be found in Appendices A–12 to A–15.

At the oxygen electrode, the polarisation resistance remained fairly constant. At the fuel electrode, a slight increase in polarisation resistance is observed between 25% CO_2 – 50% H_2 and 60% CO_2 – 15% H_2 of experiments 4b2 to 4b4. Fuel electrode polarisation resistance due to charge transfer reactions, gas diffusion and gas conversion are electrochemical processes known to occur at the fuel electrode which could be contributing to the changing cell resistances. However, further characterisation work is still needed to ascribe these electrochemical processes to specific frequencies in the impedance spectra.

Comparing CO_2 electrolysis to CO_2/H_2O co-electrolysis, it can be seen that the presence of steam at the fuel electrode significantly increases the performance of the electrolyser as shown in Figure 5–11.

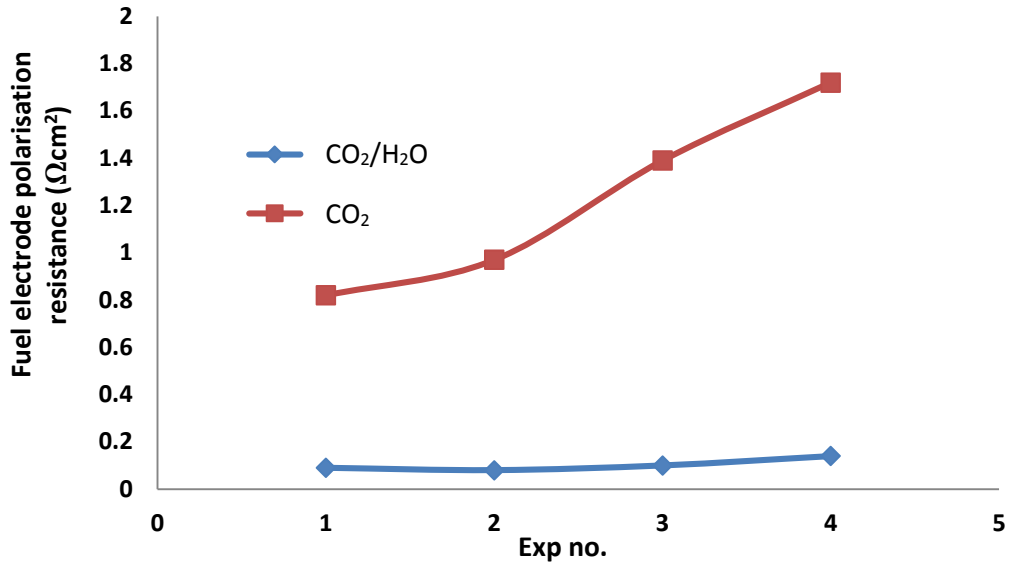

Figure 5–11: Polarisation resistance at the fuel electrode during CO_2 electrolysis and CO_2/H_2O co-electrolysis between 0.65 and 0.1 Hz

To summarise, it has been shown that the slight increase in polarisation resistance with increasing H_2O and CO_2 compositions is predominantly associated with processes across the fuel electrode. A comparison of the CO_2/H_2O co-electrolysis with the CO_2 electrolysis process has shown that by substituting some CO_2 with H_2O, the performance of the electrolyser significantly increases by up to 21%. A detailed breakdown of the other electrochemical processes that contribute to these resistances in the impedance spectra is still needed.

5.4 Durability of SOCs during High Temperature Co-electrolysis of Carbon dioxide and Steam

5.4.1 Experimental

The durability of the SOC was examined at 850°C with 50% CO_2 – 25% H_2 – 25% N_2 supplied to the fuel electrode, synthetic air supplied to the oxygen electrode and a current density of -0.5 A/cm^2 applied to a fresh cell. The study was carried out over a short period (~45 hours) in which the cell voltage was continuously monitored. Electrochemical impedance spectra were recorded before and after the electrolysis test to determine the cause of degradation.

5.4.2 Cell Voltage and AC Characterisation

Figure 5–12 shows the change in cell voltage over the period of study. AC characterisation measurements at OCV were performed before and after the durability study and the results obtained are shown in Figure 5–13. Furthermore, a breakdown of the passivation rates at various time scales can be seen in Table 5–10.

.

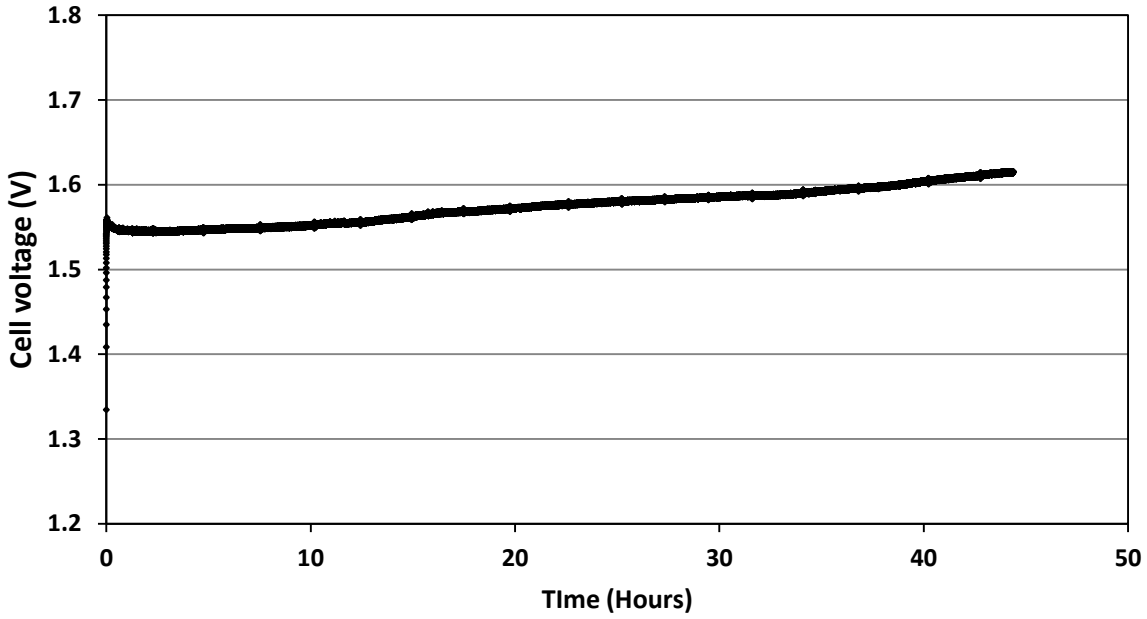

Figure 5–12: Cell voltage measured during CO_2/H_2O co-electrolysis at -0.5 A/cm^2 and 850^{o}C

Table 5–10: Operating conditions, cell voltage and degradation during the CO_2/H_2O co-electrolysis durability tests

Time (Hours)	Cell voltage (mV)	Degradation (mV/h)
0.02 - 5	1558 - 1550	-1.6
5 – 30	1550 – 1586	1.44
30 – 44.4	1586 - 1615	2.01

As shown in Table 5–10, the cell voltage decreased slightly during the initial electrolysis period of 5 hours corresponding to an activation rate of 1.6 mV/h. Activation of SOCs is not new and has been shown in a previous longer term study by Ebbesen et al. (2010). However, the authors observed activation rates after long hours of operation between 400 and 600th hour and 700 and 900th hour of operation. Over the next 39 hours of operation in this study, the cell voltage increased from 1550 to 1615 mV corresponding to a passivation rate of 1.65 mV/h.

As previously indicated in Section 2.6.2.1, Zhan et al. (2009) observed a degradation rate corresponding to 0.26 mV/h over 100 hours of operation when operating with a fuel electrode composition of 25% H_2, 25% CO_2 and 50% H_2O at 850^oC and a current density of -1.05 A/cm^2. Ebbesen et al. (2010) also reported a degradation rate of 0.377 mV/h in the first 50 hours of operation during CO_2/H_2O co-electrolysis when operating at a current density of -0.25 A/cm^2. Although, this value significantly decreased up to 0.003 mV/h over 1000 hours of operation. The overall passivation rate of 1.3 mV/h observed in this study over 44 hours of operation is significantly higher than those presented in literature. The key factors which affect this increase in cell voltage include increasing ohmic resistance with time (arising from cell and electrical mesh contact), presence of impurities in the fuel electrode, lower performing materials, etc. AC impedance spectroscopy measurements have been carried out to further understanding of the resistances contributing to the increase in cell voltage.

A comparison of the changes in cell voltages in this study to that presented in Section 4.4 during the durability of SOC during CO_2 electrolysis shows a significant increase in cell performance. An overall passivation rate of 1.3 mV/h was observed in this study whereas a passivation rate of 36.1 mV/h was observed during the durability of SOC during CO_2 electrolysis. It was argued previously in Section 4.4.2 that the presence of impurities (possibly sulphur from H_2S), thought to have originated mostly from the CO gas content, deposited on the active nickel sites causing a significant increase in cell voltage. Furthermore, when investigating the effect of impurities and regeneration of the NiO electrode in a SOC as shown in Section 4.2.5, it was shown that the addition of H_2 and removal of CO (thus reducing the impurity content) significantly increases the performance of the cell because the presence of sulphur in the electrode is mostly eliminated.

AC impedance measurements were also performed before and after the durability study.

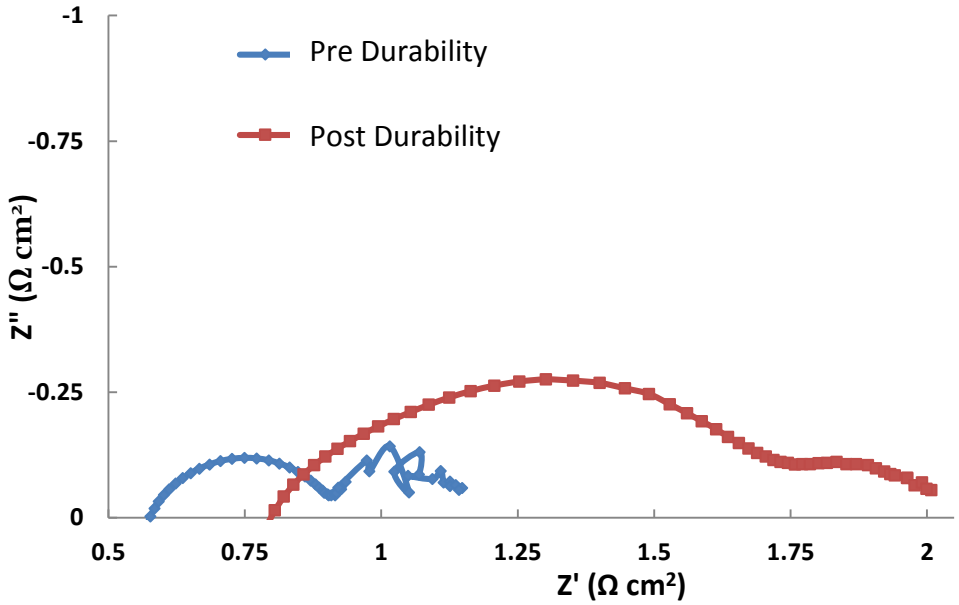

Figure 5–13: AC impedance spectra at 850°C before and after durability study at -0.5 A/cm^2

Table 5–11: Ohmic and polarisation resistances during durability studies for CO_2/H_2O co-electrolysis, obtained using equivalent circuit model from experimental Nyquist plot

	Pre-durability	Post-durability
Ohmic resistance (Ω.cm^2) - R1	0.58	0.79
Oxygen electrode polarisation resistance (Ω.cm^2) – R2	0.33	0.97
Fuel electrode polarisation resistance (Ω.cm^2) – R3	0.27	0.3
Total polarisation resistance (Ω.cm^2)	0.6	1.27
Total cell resistance (Ω.cm^2)	1.18	2.06

The full impedance spectra for the data in the Table 5–11 and Figure 5–13 is shown in Appendices A-16 and A-17.

Similar to the information presented in Table 4–7 during investigations into the durability of SOCs under carbon dioxide electrolysis, analysis of Figure 5–13 shows a significant increase in ohmic resistance and polarisation resistance across the oxygen electrode. Over the 44 hours of operation, a 36% (0.58 to 0.79 Ω cm^2) increase in ohmic resistance is observed during CO_2/H_2O co-electrolysis, a value much higher than the 18% (0.51 to 0.60 Ω cm^2) observed during CO_2 electrolysis although the cell was operated for a shorter period of 8 hours in the latter case. Additionally, 194% (0.33 to 0.97 Ω cm^2) increase polarisation

resistance at the oxygen electrode was observed, a value significantly higher than the 102% (0.41 to 0.83 Ω cm^2) observed during CO_2 electrolysis. The electrochemical process associated with the increase in ohmic and polarisation resistance at the oxygen electrode which affects cell degradation during CO_2/H_2O co-electrolysis are similar to those described during CO_2 electrolysis as shown in Section 4.4.3.

Despite a significantly larger operating time, a lower fuel electrode polarisation resistance is observed during CO_2/H_2O co-electrolysis (0.27 to 0.3 Ω cm^2) compared to the 1.78 to 2.58 Ω cm^2 observed during CO_2 electrolysis. In Section 4.4, it was hypothesised that the significant increase in cell voltage is related to electrochemical changes at the fuel electrode predominantly caused by the deposition of impurities at the active sites and arising primarily from the CO stream. In this Section, the effect of impurities is significantly reduced as CO is not included in the inlet gas stream and H_2 is introduced. However, the effect of impurities from the CO_2 stream is not eliminated as a possible cause for the increase in resistance. Furthermore, Ebbesen et al. (2010) has shown that when operating at low current densities, impurities at the fuel electrode is the major contributing factor to an increase in cell resistance.

Overall, it has been shown that by substituting CO with H_2, the sharp rise in cell voltage seen during CO_2 electrolysis can be eliminated. A period of cell activation corresponding to a rate of 1.6 mV/h is observed during CO_2/H_2O co-electrolysis in the first 5 hours of operation. However, the cell degraded at a rate of 1.65 mV/h over the next 39 hours of operation. AC impedance spectroscopy measurements have shown a significant increase in ohmic and polarisation resistance at the oxygen electrode whereas the polarisation resistance at the fuel electrode increase slightly before and after durability studies. Further work is needed in this study to decouple the electrochemical processes within the impedance spectra that contribute to SOC degradation particularly at the oxygen electrode.

5.5 Current Efficiency and Syngas Production at varying Current Densities

In this Section, the exhaust gas compositions is analysed when operating at open circuit voltage and varying current densities. This is important in order to quantify the amounts of feed (CO_2 and H_2O) converted during CO_2/H_2O co-electrolysis with an aim to further the understanding of the co-electrolysis reaction. During CO_2 electrolysis, a current efficiency of 90% (equivalent to 4.14 ml/min of CO produced) was reported when operating at -0.5 A/cm^2 with 50% CO_2, 25% CO & 25% N_2 flowed to the fuel electrode at 20 ml/min.

Table 5–12: Exhaust gas compositions measured at open circuit voltage and -0.5 A/cm^2 when operating at 850^{o}C and inlet gas compositions of 50% CO_2 – 25% H_2 – 25% N_2 at 20 ml/min

	Cold Inlet composition (%)			Exhaust gas composition at 0 A/cm^2 (mol %)					Exhaust gas composition at -0.5 A/cm^2 (mol %)				
No	**CO_2**	**H_2**	**N_2**	**H_2O**	**CO_2**	**H_2**	**CO**	**N_2**	**H_2O**	**CO_2**	**H_2**	**CO**	**N_2**
4b3	50	25	25	15.3	32.7	9.7	17.3	25	6.9	20.6	18.1	29.4	25

From Table 5–12, the total amount of syngas (H_2 + CO) produced at -0.5 A/cm^2 is calculated to be 4.1 ml/min, similar to the amount of CO produced (4.14 ml/min) during CO_2 electrolysis when operating with fuel electrode compositions of 50% CO_2, 25% CO & 25% N_2. As discussed in Section 1.3.2.1, determining the Faradaic efficiency for co-electrolysis is more complicated than individual steam and carbon dioxide electrolysis. The Faradaic efficiency in this instance was therefore calculated on the assumption of the basis for theoretical individual CO_2 and H_2O electrolysis for CO and H_2 production respectively.

The current density was varied between -0.25, -0.4 and -0.5 A/cm^2 at 850^{o}C and fuel electrode compositions of 50% CO_2, 25% H_2 & 25% N_2 at a flow rate of 20ml/min. From Figure 5–14, the molar composition of syngas produced can be seen to increase with increasing current density. The current efficiency (see Section 1.3.2.1) was calculated using the theoretical amount of CO and H_2 production as seen in Table 5–13 indicates overall a

highly efficient electrolyser for co-electrolysis. Appendix C–7 shows the GC data obtained in order to calculate the exhaust gas compositions at the varying current densities shown in Table 5–13.

Table 5–13: Current efficiency of syngas produced at varying current densities

Current density (A/cm^2)	Current efficiency (%)	
	CO produced	H_2 produced
- 0.5	89	96
- 0.4	89	96
- 0.25	91	97

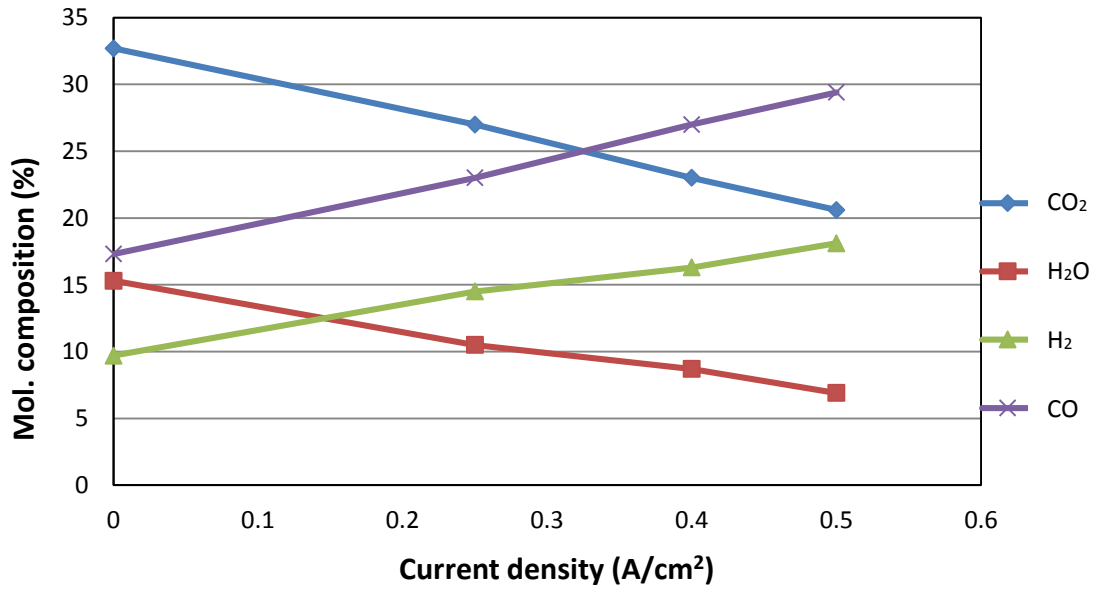

Figure 5–14: Graph showing the mol. composition of syngas produced at OCV, -0.25, -0.4 and -0.5 A/cm^2

Co-electrolysis reaction mechanism

This Section provides a method and possible explanation of the co-electrolysis reaction mechanism using experimental data shown in Figure 5–14 and process simulation data from HSC Chemistry 5.11. To do so, the measured exhaust gas compositions at -0.25 A/cm^2 shown in Figure 5–14 will be compared to the predicted gas compositions calculated on the assumption that pure steam electrolysis and the rWGSR are the only two reactions to occur within this process as suggested by (Stoots et al. 2008).

The predicted gas compositions at 850°C, -0.25 A/cm^2 and inlet fuel electrode compositions of 50% CO_2, 25% H_2 & 25% N_2 are calculated on the assumption that:

- The majority of the electrochemical reactions occur closest to the electrolyte as discussed in Section 1.2.3 and shown in Figure 2–5 by (Ni 2011), whereas the majority of the chemical reaction occurs in the bulk of the electrode.

This implies that:

1. At OCV, the hot inlet compositions would differ to the inlet fuel electrode compositions due to the rWGSR (given in Table 5–12).
2. At -0.25 A/cm^2 and following the reduction of H_2O to H_2, the gas compositions at the fuel side electrode/electrolyte region (where the electrochemical reaction occurs) after the applied current density would differ to the exhaust gas compositions due to the rWGSR.

In the case of no. 2, it is assumed that equilibrium of the rWGSR is reached following the reduction of H_2O to H_2. The predicted gas compositions are therefore calculated using HSC Chemistry process simulation.

Table 5–14: Predicted and measured exhaust gas compositions at OCV and -0.25 A/cm^2 when operating at 850°C and inlet gas compositions of 50% CO_2, 25% H_2 & 25% N_2 at 20 ml/min

Current density (A/cm^2)	CO_2 (mol %)	H_2O (mol %)	CO (mol %)	H_2 (mol %)	N_2 (mol %)
0	32.7	15.3	17.3	9.7	25
-0.25 (Measured data)	27	10.5	23	14.5	25
*Theoretical data (predicted compositions)	25.5	13	24.5	12	25

*The theoretical data is calculated on the assumption of 97 % current efficiency at -0.25 A/cm^2 if only steam electrolysis occurred. Following this, the predicted gas compositions are then calculated on the assumption that equilibrium of the rWGSR is reached.

The data from Table 5–14 shows that the measured data are not close enough to the gas compositions. It could therefore be speculated that steam electrolysis is not the only electrochemical reaction occurring during the high temperature co-electrolysis of CO_2 and

H_2O in a SOEC. However, in order for this study to be fully validated, the exhaust compositions at -0.25 A/cm^2 has to be carried out using an electrode supported cell as equilibrium of the rWGSR has been shown to be reached in this case. Consequently, an accurate comparison and analysis of the measured and predicted data can be obtained. Additionally, further work is still needed in this study to determine the effect of temperature and inlet gas compositions at varying current densities.

Chapter 6

6. Conclusion and Future Work

The main conclusions drawn from Chapters 1 to 5 are presented in this Chapter. This study has successfully accomplished one of its goals in furthering the understanding of the performance of a SOC during CO_2 electrolysis and CO_2/H_2O co-electrolysis. Furthermore, the increase in cell performance observed during CO_2/H_2O co-electrolysis has been quantified compared to CO_2 electrolysis. However, this study is yet to fully determine the co-electrolysis reaction mechanism as part of the second aim of this PhD project.

Further work is still needed to fully determine all electrochemical processes on the impedance spectra that contribute to cell resistance during CO_2 electrolysis and CO_2/H_2O co-electrolysis. The key areas of improvement within this research that could successfully aid in gaining a better understanding of the co-electrolysis reaction mechanisms and SOEC failure at high current densities are also outlined.

6.1 Conclusion

Chapter 1:

- Synthetic fuel production via the high temperature co-electrolysis of CO_2 and H_2O in a SOC, coupled with the FTS, is a promising pathway for CO_2 utilisation.
- Conventional solid oxide cells used during steam electrolysis and consisting of Ni-YSZ as the fuel electrode, YSZ as the electrolyte and LSM-YSZ as the oxygen electrode, can be directly applied for CO_2/H_2O co-electrolysis in the production of syngas and electrolysis of CO_2 for CO production.
- Steam electrolysis, carbon dioxide electrolysis and the reverse water gas shift reaction (rWGSR) are the three reactions that could take place during the high temperature co-electrolysis of CO_2 and H_2O in a SOEC.
- The proportions of each reaction in the contribution to H_2/CO production will depend on the cell materials, cell morphology, operating temperature, inlet gas compositions and operating voltages.
- There is however lack of understanding of the co-electrolysis reaction mechanisms as it is still unclear which reaction contributes to the production of CO and this thesis aims to gain further understanding of the type of reactions that occur in the production of H_2 and CO.
- Finally, economic analysis of fuel production with the GHG originating from air capture showed that SOECs must be able to operate at current densities of ~–2 A/cm^2 with little (0.0018 mΩ cm^2/h) or no degradation over a 5 year period for the commercialisation of this technology.

Chapter 2:

- In understanding the co-electrolysis reaction mechanism, it has been argued that steam electrolysis and the rWGSR are the only two reactions that occur within this process with the H_2 produced from steam electrolysis used in the chemical reaction to produce CO. Contradicting this report, it has also been argued in other studies that all three reactions occur in the production of H_2 and CO. A better understanding of the co-electrolysis process is vital as this could provide further knowledge in the development of materials for more efficient SOECs.

- The performance of a cell under H_2O electrolysis is greater than CO_2/H_2O co-electrolysis and significantly greater than CO_2 electrolysis. A comparison of the cell's ASR under these operating conditions showed a slight increase in resistance for CO_2/H_2O mixtures compared to H_2O. In addition, a significantly higher ASR has been observed for CO_2 electrolysis.
- Although SOCs were initially developed and optimised for fuel cell mode operation, differences in operating conditions (such as high steam content environment in the bulk of the fuel electrode, thus accelerating the agglomeration of Ni particles present in the fuel electrode) for electrolysis purposes means there is a great interest in the optimisation of conventional materials and development of newer SOE materials.
- At the fuel electrode, the use of perovskite structured materials such as LSCrM/GDC and LST have gained significant interest because they do not require a continuous flow of reducing gas (such as H_2) to avoid Ni oxidation. At the oxygen electrode, MIEC materials such as BSCF, LSCF and BCFN have gained significant interest due to their ability to extend the reaction sites across the full depth of the electrode.
- A review of the status of the high temperature co-electrolysis of carbon dioxide and steam in a solid oxide cell showed that operation at high current densities (>–0.75 A/cm^2) is a technological barrier that needs to be addressed.
- At low current densities (<–0.75 A/cm^2), it has been shown that SOECs are capable of operating with little or no degradation when impurities present within the gas stream are removed. At high current densities (>–0.75 A/cm^2), degradation of the oxygen electrode occurs due to the high oxygen partial pressures at the oxygen electrode/electrolyte interface. In most cases, this degradation typically leads to the delamination of the oxygen electrode from the electrolyte.
- The optimisation of conventional SOC materials and the development of novel materials is currently a major part of the research in eliminating issues of cell failure at high current densities.

Chapter 3:

- The experimental design, methods and commissioning for the new equipment used during this project along with many issues overcame were discussed.
- Glass was shown to be more effective than mica in cell sealing, resulting in lower gas leakages.
- The use of a temperature controlled water bath and a carrier gas (N_2) has been shown to be effective in producing highly stable and large amounts of steam (concentrations up to 900, 000 ppm). However, issues of condensation downstream of the water bath ought to be eliminated before steam electrolysis can be effectively carried out.
- In this research, electrolyte supported cells were shown to be preferable to NiO electrode supported cells due to lower gas leakages upon loading and lower degree of ohmic resistance variation when tested over 50 hours of operation under varying $H_2O/H_2/N_2$ compositions. This issue of contact resistance was however eliminated when platinum ink was applied to the fuel side electrode.
- Electrolyte supported cell characterisation through electrochemical impedance spectroscopy and analysis of the impedance spectra carried out at with the cell operating at OCV showed that the high frequency arc was related primarily to processes occurring at the oxygen electrode while the low frequency arc was related primarily to processes occurring at the fuel electrode.

Chapter 4:

- During CO_2 electrolysis, the experimental OCV of varying gas compositions were 3 – 6 ±2 mV below the theoretical value indicating the cell was sealed satisfactorily.
- An increasing ASR, calculated from the *i*-V plot as the line from the OCV to the cell voltage measured at a current density of -0.1 A/cm^2, was observed with increasing CO_2/CO ratio.
- AC impedance measurements showed the ohmic and polarisation resistance at the oxygen electrode remained fairly constant while polarisation resistance at the fuel electrode significantly increased.

- Poisoning of the fuel electrode during electrolysis of CO_2 was also observed. The presence of impurities in the CO_2/CO stream reduces the surface area of the active catalysts. It was shown that the addition of H_2 and removal of CO led to the regeneration of the cell, indicating the possible presence of impurities in the CO gas stream.
- Short term durability studies, carried out on the cell during CO_2 electrolysis indicated two key phases of cell degradation. An initial sharp increase in cell voltage, equivalent to a degradation rate of ~120 mV/h in the first 5 hours followed by a slow and continuous increase in cell voltage equivalent to ~10 mV/h over a 2 hour period. The initial increase in cell voltage is caused by deposition of sulphur to the nickel surface thus blocking the active nickel sites for adsorption, dissociation and diffusion along surfaces. Further work is still needed to understand the cause of the second phase of degradation.
- A Faraday efficiency of 90%, indicating a highly efficient electrolysis cell, was achieved during CO_2 electrolysis when operating at fuel electrode compositions of 50% CO_2 and 25% CO, flow rates of 20 ml/min and current density -0.5 A/cm^2.

Chapter 5:

- The rWGSR was close to equilibrium during the high temperature (850^{o}C) co-electrolysis of CO_2 and H_2O when using an electrolyte supported cell and operating at OCV. Exhaust gas composition measurements were ±2 mol% of the thermodynamic equilibrium composition.
- On the other hand, equilibrium of the rWGSR is reached when using a NiO electrode supported cell.
- DC measurements showed up to a 21% increase in cell performance during CO_2/H_2O co-electrolysis compared to CO_2 electrolysis.
- An increasing ASR was observed with increasing CO_2/H_2O compositions. Furthermore, the cell ASR during CO_2/H_2O co-electrolysis was 40% lower than the ASR during CO_2 electrolysis.
- AC impedance measurements showed the ohmic resistance and polarisation resistance at the oxygen electrode remained fairly constant while polarisation resistance at the fuel electrode increased slightly. Activation and concentration

polarisation due to gas diffusion and conversion are possible causes for this increase in resistance.

- A comparison of the electrochemical impedance spectra showed up to a 55% decrease in polarisation resistance at the oxygen and fuel electrode during CO_2/H_2O co-electrolysis than CO_2 electrolysis.
- Short term durability studies showed a passivation rate corresponding to 1.3 mV/h over 44 hours of operation, a value significantly lower than that reported for CO_2 electrolysis. AC impedance spectra showed an increase in ohmic and polarisation resistances at the oxygen and fuel electrode.
- A Faraday efficiency of 89 % was achieved during CO_2/ H_2O co-electrolysis when operating at fuel electrode compositions of 50% CO_2 and 25% H_2, flow rates of 20 ml/min and current density -0.5 A/cm^2. The calculated current efficiency is similar to that observed during CO_2 electrolysis indicating a highly efficient electrolysis cell for syngas production.

6.2 Future Work

The commercialisation of SOEC technology for synthetic gas production via the high temperature co-reduction of CO_2 and H_2O is highly dependent on eliminating all issues of degradation at high current densities (>-0.75 A/cm^2) as discussed in Section 1.4. The majority of the work in the high temperature co-electrolysis of CO_2 and H_2O in a SOEC is therefore geared towards the development and testing of newer SOEC materials, as well as the optimisation of conventional materials (see Section 2.6.2.2).

This project has focused primarily on the testing of SOCs under varying compositions of CO_2 and CO_2/H_2O with an aim to improve the performance of the electrolyser for syngas production. However, further work is needed in the following areas:

- Eliminating all issues of steam condensation downstream of the water bath
- Investigating, and subsequently eliminating the presence of sulphur in the carbon monoxide gas stream
- Optimisation of electrode supported cells for electrolysis testing
- Detailed cell characterisation to determine the processes during CO_2/H_2O co-electrolysis and quantitatively obtain their equivalent cell resistances

In addition to the above points, continuous optimisation of the current procedure of testing and data analysis is needed.

6.2.1 Eliminating Issues of Steam Condensation

The use of a carrier gas coupled with a temperature controlled heated water bath has been shown to be a feasible and effective process in the production of steam stable up to 900,000 ppm as discussed in Section 3.5. However, issues of condensation downstream of the water bath (before steam arrives at the inlet of the fuel electrode) need to be eliminated before this system can be implemented for electrolysis operation. Due to this issue, H_2O was not used as an input gas during H_2O/CO_2 co-electrolysis as the gas composition could not be successfully controlled. Instead, cold inlet compositions of CO_2/H_2 mixtures were used and the resulting fuel electrode compositions (H_2O, H_2, CO and CO_2 due to the rWGSR) were measured using a gas chromatograph.

The development of a new test facility or optimisation of the current system in which the water bath is closer to the operating cell in the furnace is very important. Potential solutions include:

- Reduction of the stainless steel tube length between the outlet of the water bath and the inlet of the base unit of the cell rig.
- Construction of a new, shorter length cell rig fitted to the 300 mm height furnace used in this research. Alternatively, a furnace which covers the entire length of the ProboStat could be utilised.
- Improved heat insulation downstream of the water bath such that the heat traced line is maintained at a high enough temperature to avoid condensation before entering the base unit of the ProboStat.

6.2.2 Sulphur Poisoning

In Section 4.2.5, it was hypothesised that the presence of H_2S in the CO stream reduces the surface area of the active catalytic sites in the fuel electrode during CO_2 electrolysis. To confirm that H_2S is indeed the active impurity contributing to cell degradation, the following experiments can be carried out:

- Post-Morton analysis - Following the CO_2 electrolysis experiment involving CO_2 and CO gas streams, EDX analysis should be carried out on the cell to detect any impurities
- In addition, mass spectrometry analysis of the CO gas stream can also be investigated for the detection of sulphur.

Based on the hypothesis of the presence of H_2S in the gas streams, higher purity gasses (>99.999%) should be employed in future experiments to minimise the presence of impurities on the cell. The use of a filter bed is also important in minimising the presence of impurities. This technique is currently being employed at Riso (Ebbesen et al. 2010).

6.2.3 Optimisation of the Electrode Supported Cells

In this project, electrolyte supported cells have been predominantly investigated for CO_2 electrolysis and CO_2/H_2O co-electrolysis. Cathode supported SOECs are however generally preferable during SOEC operation and consequently used predominantly in SOEC investigations. This is mainly due to their thin electrolyte, therefore leading to lower ohmic resistance as described in Section 2.1.1. It is therefore important that these cells are prioritised, operated and tested as they lead to a lower overall cell resistance.

One of the key challenges encountered with the use of electrode supported cells here was a large contact resistance between the fuel electrode and current collector described in Section 3.8.3. The addition of Pt ink to the surface of the fuel electrode was later shown to eliminate this issue described in Section 3.8.4. However, in Section 5.2.3.1, it was shown that the addition of pure Pt ink reduced the surface area of the active catalytic sites for the reduction of CO_2 and H_2O. Consequently, this cell needs to be optimised through the use of a frit free Pt ink and/or the use of a Pt ink (frit free) and organic solvent mixture.

AC impedance characterisation of the cell ought to be carried out to ensure the addition of the Pt ink doesn't have a detrimental effect on the performance of the cell. This can be done by comparing the polarisation resistance of the cell before and after Pt ink has been applied.

6.2.4 Detailed Electrochemical Characterisation of Electrode supported cells

In this study, two-electrode cell measurements have been performed during EIS in determining the resistance of the whole cell. As a result, a better understanding of the contribution of the electrolyte, oxygen and fuel electrode processes as a whole has been obtained. However, further work is still needed to understand the individual processes across the whole cell contributing particularly to the anode and cathode resistances.

The information below details specific experiments that ought to be carried out to achieve a better understanding of cell processes:

- Quantitatively determine the electrode processes - At the fuel electrode, it is important to quantify the contribution of the all processes (gas diffusion, charge transfer reactions and gas conversion) on the impedance spectra. Similarly, at the oxygen electrode, the processes contributing to cell resistance as shown on the impedance spectra should be thoroughly investigated. This would involve careful design of experiments in which conditions are systematically varied. These conditions include gas partial pressure, temperature, etc. Furthermore, obtaining impedance spectra both at OCV and higher cell voltages is vital as discussed in Section 2.1.1.
- Introduction of three-electrode cell measurements - The advantage of three-electrode measurements is that it enables a more detailed understanding of only one half of the cell. Consequently, a better understanding of the chemical and electrochemical reactions at, for example the fuel electrode can be obtained
- Development of a suitable equivalent circuit model – Following on from the above points, it is important to develop a suitable circuit model for these processes. Zview is a numerical analysis software tool extremely useful in the combination of commonly used SOEC elements such as resistors, constant phase elements and the Warburg diffusion element as detailed in Section 2.2.2.3.

7. References

ÅŽAHIN, A. D. 2004. Progress and recent trends in wind energy. *Progress in Energy and Combustion Science,* 30**,** 501-543.

BADWAL, S. P. S., CIACCHI, F. T. & MILOSEVIC, D. 2000. Scandia–zirconia electrolytes for intermediate temperature solid oxide fuel cell operation. *Solid State Ionics,* 136–137**,** 91-99.

BADWALL, S. P. S. 2001. Stability of solid oxide fuel cell components. *Solid State Ionics,* 143**,** 39-46.

BARFORD, R., MOGENS, M., KLEMENSO, T., HAGEN, A., LIU, Y.-L. & VANG, P. 2007. Detailed Characterisation of Anode-Supported SOFCs by Impedance Spectroscopy. *Journal of Electrochemical Society,* 154**,** B371 - B378.

BARTHOLOMEW, C. H., AGRAWAL, P. K. & KATZER, J. R. 1982. Sulfur Poisoning of Metals. *In:* D.D. ELEY, H. P. & PAUL, B. W. (eds.) *Advances in Catalysis.* Academic Press.

BO, Y., WENQIANG, Z., JINGMING, X. & JING, C. 2008. Microstructural characterization and electrochemical properties of $Ba_{0.5}Sr_{0.5}Co_{0.8}Fe_{0.2}O_{3-\delta}$ and its application for anode of SOEC. *International journal of hydrogen energy,* 33**,** 6873-6877.

BROWN, M., PRIMDAHL, S. & MOGENSEN, M. 2000. Structure/Performance Relations for Ni/Yttria-Stabilized Zirconia Anodes for Solid Oxide Fuel Cells. *Journal of Electrochemical Society,* 147**,** 475-485.

BUTLER, J. & MONTZKA, S. 2013. THE NOAA ANNUAL GREENHOUSE GAS INDEX (AGGI). *In:* U.S DEPARTMENT OF COMMERCE | NATIONAL OCEANIC & ATMOSPHERIC ADMINISTRATION | NOAA RESEARCH (ed.). Colorado.

CHAMORRO, C. R., MONDEJAR, M. E., RAMOS, R., SEGOVIA, J. J., MARTIN, M. C. & VILLAMANAN, M. A. 2012. World geothermal power production status: Energy, environmental and economic study of high enthalpy technologies. *Energy,* 42**,** 10-18.

CHEN, K., AI, N. & JIANG, S. P. 2010. Development of (Gd,Ce) O_2 -impregnated (La,Sr) MnO_3 anodes of high temperature solid oxide electrolysis cells. *Journal of the Electrochemical Society,* 157**,** P89-P94.

CHEN, K. & JIANG, S. P. 2011. Failure mechanism of (La,Sr)MnO_3 oxygen electrodes of solid oxide electrolysis cells. *International Journal of Hydrogen Energy,* 36**,** 10541-10549.

CHENG, Z., ZHA, S. & LIU, M. 2006. Stability of Materials as Candidates for Sulfur-Resistant Anodes of Solid Oxide Fuel Cells. *Journal of Electrochemical Society,* 153**,** A1302 - A1309.

CHENG, Z., ZHA, S. & LIU, M. 2007. Influence of cell voltage and current on sulfur poisoning behavior of solid oxide fuel cells. *Journal of Power Sources,* 172**,** 688-693.

CIACCHI, F. T. & BADWAL, S. P. S. 1991. The system Y_2O_3-Sc_2O_3-ZrO_2: Phase stability and ionic conductivity studies. *Journal of the European Ceramic Society,* 7**,** 197-206.

DAVEY, E. 2012. CCS Roadmap - Supporting deployment of Carbon Capture and Storage in the UK. *In:* DEPARTMENT OF ENERGY AND CLIMATE CHANGE (ed.). London: Crown Copyright.

DECC. 2014. *Peterhead Carbon Capture and Storage Project* [Webpage]. London, United Kingdom. [Accessed 24-04-2014 2014].

DEMIBRAS, A. 2009. Biofuels securing the planet's future energy needs. *Energy Conversion and Management,* 50**,** 2239-2249.

DIGIUSEPPE, G. & SUN, L. 2011. Electrochemical performance of a solid oxide fuel cell with an LSCF cathode under different oxygen concentrations. *International journal of hydrogen energy,* 36**,** 5076-5087.

DONG, J., CHENG, Z., ZHA, S. & LIU, M. 2006. Identification of nickel sulfides on Ni–YSZ cermet exposed to H2 fuel containing H2S using Raman spectroscopy. *Journal of Power Sources,* 156**,** 461-465.

DÖNITZ, W. & ERDLE, E. 1985. High-temperature electrolysis of water vapor-status of development and perspectives for application. *International Journal of Hydrogen Energy,* 10**,** 291-295.

DONITZ, W., SCHMIDBERGER, R., STEINHEIL, E. & STREICHER, R. 1980. Hydrogen production by high temperature electrolysis of water vapour. *International journal of hydrogen energy,* 5**,** 55-63.

DURAN, S. 2014. *Technical Information - Product Specific Section* [Webpage]. Available: http://www.schott.com/uk/english/download/09_technical_information.pdf [Accessed 02-05-2014].

EBBESEN, S., GRAVES, C., HAUCH, A., JENSEN, S. H. & MOGENSEN, M. 2010. Poisoning of Solid Oxide Elctrolysis Cells by Impurities. *Journal of The Electrochemical Society,* 157**,** B1419 - B1429.

EBBESEN, S., GRAVES, C. & MOGENSEN, M. 2009. Production of synthetic fuels by co-electrolysis of steam and carbon dioxide. *Int. J. Green Energy,* 6**,** 646-660.

EBBESEN, S., HOGH, J., NEILSEN, K. A., NIELSEN, J. U. & MOGENSEN, M. 2011. Durable SOC stacks for production of hydrogen and synthesis gas by high temperature electrolysis. *International Journal of Hydrogen Energy* 1-11.

EBBESEN, S., KNIBBE R & MOGENSEN M 2012. Co-Electrolysis of Steam and Carbon dioxide in Solid Oxide Cells. *Journal of The Electrochemical Society,* 159**,** F482-F489.

EBBESEN, S. & MOGENSEN, M. 2009. Electrolysis of carbon dioxide in Solid Oxide Electrolysis Cells. *Journal of Power Sources,* 193**,** 349 - 358.

EGUCHI, K., HATAGISHI, T. & ARAI, H. 1996. Power generation and steam electrolysis characteristics of an electrochemical cell with a zirconia- or ceria-based electrolyte. *Solid State Ionics,* 86–88, Part 2**,** 1245-1249.

EGUCHI, K., KUNISA, Y., ADACHI, K., KAYANO, M., SKIZAWARD, K. & ARAI, H. 1995. *Chem. Lett.,* 24**,** 963 - 964.

ELIKAN, L. & MORRIS, J. P. 1969. Solid electrolyte system for oxygen regeneration. *In:* NATIONAL AERONAUTICS AND SPACE ADMINISTRATION (ed.). Washington, DC.

ELIKAN, L., MORRIS, J. P. & WU, C. K. 1972. Development of a solid electrolyte carbon dioxide and water reduction system for oxygen recovery. *In:* NATIONAL AERONAUTICS AND SPACE ADMINISTRATION (ed.). Washington, DC.

FORSBERG, C. W. 2009. Sustainability by combining nuclear, fossil, and renewable energy sources. *Progress in Nuclear Energy,* 51**,** 192-200.

FUELCELLMATERIALS. 2013. *NEXTCELL-2.0* [Webpage]. USA.

GOODENOUGH, J. B. & HUANG, Y.-H. 2007. Alternative anode materials for solid oxide fuel cells. *Journal of Power Sources,* 173**,** 1-10.

GORTE, R. J. & VOHS, J. M. 2003. Novel SOFC anodes for the direct electrochemical oxidation of hydrocarbons. *Journal of Catalysis,* 216**,** 477-486.

GRAVES, C., EBBESEN, S. D. & MOGENSEN, M. 2011. Co-electrolysis of CO_2 and H_2O in solid oxide cells: Performance and durability. *Solid State Ionics***,** 1-6.

GRAVES, C., EBBESEN, S. D., MOGENSEN, M. & LACKNER, S. K. 2010. Sustainable hydrocarbon fuels by recycling CO_2 and H_2O with renewable or nuclear energy. *Renewable and Sustainable Energy Reviews,* 15**,** 1-23.

HAGA, K., ADACHI, S., SHIRATORI, Y., ITOH, K. & SASAKI, K. 2008. Poisoning of SOFC anodes by various fuel impurities. *Solid State Ionics,* 179**,** 1427-1431.

HUBER, J. 2004. *New Technologies and Environmental Innovation,* Halle, Germany, Edward Elgar Publishing Limited.

IEA. 2013. *Key World Energy Statistcs* [Webpage]. Paris, France. [Accessed 23-11-2013 2013].

INTERNATIONAL ENERGY AGENCY 2010. Carbon Capture and Storage - Progress and Next Steps. Paris.

IPCC 2007. Climate Change 2007: Mitigation of Climate Change. Cambridge University Press, Cambridge, United Kingdom and New York, NY, USA.

IPCC 2013. Climate Change 2013 - The Physical Science Basis. *Fifth Assesment Report.*

JAY, S. 2011. Mobilising for marine wind energy in the United Kingdom. *Energy Policy,* 39**,** 4125-4133.

JENSEN, S. H., ANNE HAUCH, PETER VANG HENDRIKSEN, MOGENS MOGENSEN, AND, N. B. & JACOBSENB, T. 2007b. A Method to Separate Process Contributions in Impedance Spectra by Variation of Test Conditions. *Journal of The Electrochemical Society,* 154**,** B1325 - B1330.

JENSEN, S. H., LARSEN, P. H. & MOGENSEN, M. 2007a. Hydrogen and synthetic fuel production from renewable energy sources. *International Journal of Hydrogen Energy,* 32**,** 3253-3257.

JENSEN, S. H., SUN, X., EBBESEN, S. D., KNIBBE, R. & MOGENSEN, M. 2010. Hydrogen and synthetic fuel production using pressurized solid oxide electrolysis cells. *International Journal of Hydrogen Energy,* 35**,** 9544 - 9549.

JIN, C., YANG, C., ZHAO, F., CUI, D. & CHEN, F. 2011. $La_{0.75}Sr_{0.25}Cr_{0.5}Mn_{0.5}O_3$ as hydrogen electrode for solid oxide electrolysis cells. *International journal of hydrogen energy,* 36**,** 3340-3346.

KERAFOL. 2014. *Glass Sealing Tape* [Webpage]. [Accessed 26-04-2014 2014].

KIM-LOHSOONTORN, P. & BAE, J. 2010. Electrochemical performance of solid oxide electrolysis cell electrodes under high-temperature coelectrolysis of steam and carbon dioxide. *Journal of Power Sources***,** 1-8.

KIM-LOHSOONTORN, P., BRETT, D. J. L., LAOSIRIPOJANA, N., KIM, Y. M. & BAE, J. M. 2010. Performance of solid oxide electrolysis cells based on composite $La_{0.8}Sr_{0.2}MnO_{3-\delta}$ – yttria stabilized zirconia and $Ba_{0.5}Sr_{0.5}Co_{0.8}Fe_{0.2}O_{3-\delta}$ oxygen electrodes. *International Journal of Hydrogen Energy,* 35**,** 3958-3966.

KIM-LOHSOONTORN, P., LAOSIRIPOJANA, N. & BAE, J. 2011. Performance of solid oxide electrolysis cell having bi-layered electrolyte during steam electrolysis and carbon dioxide electrolysis. *Current Applied Physics,* 11**,** S223 - S228.

KIM, H. Y., JUN, K. W., HAN, C. & SONG, I. K. 2009. A simulation study on gas-to-liquid (natural gas to Fischer-Tropsch synthetic fuel) process optimisation. *Chemical Engineering Journal,* 155**,** 427 - 432.

KNIBBE, R., TRAULSEN, M. L., HAUCH, A., EBBESEN, S. D. & MOGENSEN, M. 2010. Solid oxide electrolysis cell: Degradation at high current densities. *Journal of The Electrochemical Society,* 157**,** B1209-B1217

KUHN, E. R. 2002. Water Injections In GC – How Wet Can You Get? . *LCGC ASIA PACIFIC,* 5**,** 30 - 32.

LAGUNA-BERCERO, M. A. 2012. Recent advances in high temperature electrolysis using colid oxide fuel cells: A review. *Journal of Power Sources***,** 4 - 16.

LAGUNA-BERCERO, M. A., CAMPANA, R., LARREREA, A., KILNER, J. A. & ORERA, V. M. 2011. Electrolyte degradation in anode supported microtubular yttria stabilized zirconia-based solid oxide steam electrolysis cells at high voltages of operation. *Journal of Power Sources*, 1 - 6.

LEAH, R., BONE, A., SELCUK, A., CORCORAN, D., LANKIN, M., DEHANEY-STEVEN, Z., SELBY, M. & WHALEN, P. 2011. *Development of Highly Robust, Volumne-Manufacturable, Metal-Supported SOFC for Operation Below 600°C*, Electrochemical Society.

LEE, S., SONG, H. S., HYUN, S. H., KIM, J. & MOON, J. 2009. Interlayer-free nanostructured $La_{0.58}Sr_{0.4}Co_{0.2}Fe_{0.8}O_{3-\delta}$ cathode on scandium stabilized zirconia electrolyte for intermediate-temperature solid oxide fuel cells. *Journal of Power Sources,* 187, 74-79.

LEE, S., SONG, H. S., HYUN, S. H., KIM, J. & MOON, J. 2010. LSCF–SDC core–shell high-performance durable composite cathode. *Journal of Power Sources,* 195, 118-123.

LEUNG, D. Y. C., CARAMANNA, G. & MAROTO-VALER, M. M. 2014. An overview of current status of carbon dioxide capture and storage technologies. *Renewable and Sustainable Energy Reviews,* 39, 426-443.

LI, S., LI, Y., GAN, Y., XIE, K. & MENG, G. 2012. Electrolysis of H_2O and CO_2 in an oxygen-ion conducting solid oxide electrolyzer with a $La_{0.2}Sr_{0.8}TiO_{3+\delta}$ composite cathode. *Journal of Power Sources,* 218, 244-249.

LIN, L., CUNSHAN, Z., VITTAYAPADUNG, S., XIANGQIAN, S. & MINGDONG, D. 2011. Opportunities and challenges for biodiesel fuel. *Applied Energy,* 88, 1020-1031.

LIU, M., DING, D., BLINN, K., LI, X., NIE, L. & LIU, M. 2012. Enhanced performance of LSCF cathode through surface modification. *International journal of hydrogen energy,* 37, 8613-8620.

LUSSIER, A., SOFIE, S., DVORAK, J. & IDZERDA, Y. U. 2008. Mechanism for SOFC anode degradation from hydrogen sulfide exposure. *International Journal of Hydrogen Energy,* 33, 3945-3951.

LVOVICH, V. F. 2012. Examples of Ideal Equivalent Circuit Models. *Impedance Spectroscopy: Applications to Electrochemical and Dielectrical Phenomena.* USA: John Wiley & Sons, Inc.

MACDONALD, J. R. 1992. Impedance spectroscopy. *Annals of Biomedical Engineering,* 20, 289-305.

MARINA, O. A., PEDERSON, L. R., WILLIAMS, M. C., COFFEY, G. W., MEINHARDT, K. D., NGUYEN, C. D. & THOMSEN, E. C. 2007. Electrode Performance in Reversible Solid Oxide Fuel Cells. *Journal of Electrochemical society,* 154, B452 - B459.

MATSUZAKI, Y. & YASUDA, I. 2000. The poisoning effect of sulfur-containing impurity gas on a SOFC anode: Part I. Dependence on temperature, time, and impurity concentration. *Solid State Ionics,* 132, 261-269.

MCINTOSH, S. & GORTE, R. J. 2004. Direct Hydrocarbon Solid Oxide Fuel Cells. *Chem.Rev.,* 104, 4845 - 4865.

MCKELLAR, M. G., SOHAL, M. S., STOOTS, C. M., MULLOTH, M., LUNA, B. & ABNEY, M. B. 2010. Mathematical Analysis of High-Temperature Co-Electrolysis of CO_2 and O_2 Production in a Closed-Loop Atmosphere Revitalization System. Idaho: Idaho National Laboratory.

MEKHILEF, S., SAIDUR, R. & SAFARI, A. 2011. A review on solar energy use in industries. *Renewable and Sustainable Energy Reviews,* 15, 1777-1790.

METAL-PAGES.COM 2015. http://www.metal-pages.com/metalprices.

MILLER, S. P., DUNLAP, B. I. & FLEISCHER, A. S. 2013. Effects of dopant clustering in cubic zirconia stabilized by yttria and scandia from molecular dynamics. *Solid State Ionics,* 253**,** 130-136.

MINH, N. Q. 2004. Review - Solid oxide fuel cell technology—features and applications. *Solid State Ionics,* 174**,** 271-277.

MIT. 2009. *Ellingham diagrams* [Webpage]. USA: Massachusetts Institute of Technology. [Accessed 29-09-2014 2014].

MIZUTANI, Y., TAMURA, M., KAWAI, M. & YAMAMOTO, O. 1994. Development of high-performance electrolyte in SOFC. *Solid State Ionics,* 72, Part 2**,** 271-275.

MOGENSEN, M. & HENDRIKSEN, P. 2003. *Testing of Electrodes, Cells and Short stacks* London, Elsevier.

NAMIES´NIK, J. 1984. Generation of standard gaseous mixtures. *Journal of Chromatography A,* 300**,** 79-108.

NECHACHE, A., CASSIR, M. & RINGUEDÉ, A. 2014. Solid oxide electrolysis cell analysis by means of electrochemical impedance spectroscopy: A review. *Journal of Power Sources,* 258**,** 164-181.

NI, M. 2011. An electrochemical model for syngas production by co-electrolysis of H_2O and CO_2. *Journal of Power Sources,* 202**,** 209-216.

NI, M., LEUNG, M. K. H. & LEUNG, D. Y. 2008. Technological development of hydrogen production by solid oxide electrolyzer cell (SOEC). *International Journal of Hydrogen Energy,* 33**,** 2337-2354.

NOAA. 2013. *Global Climate Change Indicators* [Webpage]. USA: National Oceanic and Atmospheric Administration. [Accessed 26-12-2013.

NOAA. 2014. *Trends in Atmospheric Carbon dioxide* [Webpage]. USA: National Oceanic and Atmospheric Administration. [Accessed 23-07-2014.

NORECS. 2014. *http://www.norecs.com/index.php?page=ProboStat* [Webpage]. Norway: NorECs - Norwegian Electro Ceramic AS. [Accessed 09-03-2014 2014].

NRC. 2010. Advancing the Science of Climate Change. *In:* NATIONALRESEARCHCOUNCIL (ed.) *America's Climate Choices: Panel on Advancing the Science of Climate Change.* The National Academies Press.

O'BRIEN, J. E., MCKELLAR, M. G., STOOTS, C. M., HERRING, J. S. & HAWKES, G. L. 2009. Parametric study of large-scale production of syngas via high-temperature co-electrolysis. *International Journal of Hydrogen Energy,* 34**,** 4216-4226.

OLIPHANT, J. L., FOWLER, R. W., PANNELL, R. B. & BARTHOLOMEW, C. H. 1978. Chemisorption of hydrogen sulfide on nickel and ruthenium catalysts: I. Desorption isotherms. *Journal of Catalysis,* 51**,** 229-242.

ORAZEM, M. E. & TRIBOLLET, B. 2008. *Electrochemical Impedance Spectroscopy,* New Jersey, USA, John Wiley and Sons,.

PIRES, J. C. M., MARTINS, F. G., ALVIM-FERRAZ, M. C. M. & SIMÃµES, M. 2011. Recent developments on carbon capture and storage: An overview. *Chemical Engineering Research and Design,* 89**,** 1446-1460.

PLASSERAUD, L. 2010. Carbon Dioxide as Chemical Feedstock. Edited by Michele Aresta. *ChemSusChem,* 3**,** 631-632.

PRIMDAHL, S. & MOGENSEN, M. B. 1998. Gas conversion impedance: A test geometry effect in characterisation of solid oxide fuel cell anodes. *Journal of Electrochemical Society,* 145**,** 2431-2438.

QI, Z. 2008. *Electrochemical Methods for Catalyst Activity,* London, Springer.

QUADRELLI, E. A., CENTI, G., DUPLAN, J.-L. & PERATHONER, S. 2011. Carbon Dioxide Recycling: Emerging Large-Scale Technologies with Industrial Potential. *ChemSusChem,* 4**,** 1194-1215.

RAI, V., VICTOR, D. G. & THURBER, M. C. 2010. Carbon capture and storage at scale: Lessons from the growth of analogous energy technologies. *Energy Policy,* 38**,** 4089-4098.

RAIKOVA, G., CARPANESE, P., STOYNOV, Z., VLADIKOVA, D., VIVIANI, M. & BARBUCCI, A. 2009. Inductance correction in impedance studies of solid oxide fuel cells *Bulgarian Chemical Communications,* 41**,** 199 - 206.

RASMUSSEN, J. F. B. & HAGEN, A. 2009. The effect of H2S on the performance of Ni–YSZ anodes in solid oxide fuel cells. *Journal of Power Sources,* 191**,** 534-541.

SASAKI, K., SUSUKI, K., IYOSHI, A., UCHIMURA, M., IMAMURA, N., KUSABA, H., TERAOKA, Y., FUCHINO, H., TSUJIMOTO, K., UCHIDA, Y. & JINGO, N. 2006. H_2S poisoning of Solid Oxide Fuel Cells. *Journal of Electrochemical Society,* 153**,** A2023 - A2029.

SCHICHLEIN, H., MÜLLER, A. C., VOIGTS, M., KRÜGEL, A. & IVERS-TIFFÉE, E. 2002. Deconvolution of electrochemical impedance spectra for the identification of electrode reaction mechanisms in solid oxide fuel cells. *Journal of Applied Electrochemistry,* 32**,** 875-882.

SCHILLER, G., ANSAR, A., LANG, M. & PATZ, O. 2009. High temperature water electrolysis using metal supported solid oxide electrolyser cells (SOEC). *Journal of Applied Electrochemistry,* 39**,** 293-301.

SEHESTED, J. 2006. Four challenges for nickel steam-reforming catalysts. *Catalysis Today,* 111**,** 103-110.

SIMNER, S. P., BONNETT, J. F., CANFIELD, N. L., MEINHARDT, K. D., SHELTON, J. P., SPRENKLE, V. L. & STEVENSON, J. W. 2003. Development of lanthanum ferrite SOFC cathodes. *Journal of Power Sources,* 113**,** 1-10.

SPIRIN, A., IVANOV, V., NIKONOV, A., LIPILIN, A., PARANIN, S., KHRUSTOV, V. & SPIRINA, A. 2012. Scandia-stabilized zirconia doped with yttria: Synthesis, properties, and ageing behavior. *Solid State Ionics,* 225**,** 448-452.

STEELE, B. C. H. 2000. Appraisal of Ce1−yGdyO2−y/2 electrolytes for IT-SOFC operation at 500°C. *Solid State Ionics,* 129**,** 95-110.

STOOTS, C. M., O'BRIEN, J. E. & HARTVIGSEN, J. Carbon Neutral Production of Syngas Via High Temperature Electrolytic Reduction of Steam and CO_2. International Mechanical Engineering Congress and Exposition, 2007 Seattle, Washington, USA. 1-10.

STOOTS, C. M., O'BRIEN, J. E., HERRING, J. S. & HARTVIGSEN, J. J. 2008. Syngas Production via High-Temperature Coelectrolysis of Steam and Carbon Dioxide. *Journal of Fuel Cell Science and Technology,* 6**,** 011014/1-011014/12.

STOYNOV, Z. B. & VLADIKOVA, D. E. 2009. MEASUREMENT METHODS | Electrochemical: Impedance Spectroscopy. *In:* GARCHE, J. (ed.) *Encyclopedia of Electrochemical Power Sources.* Amsterdam: Elsevier.

STYRING, P., JENSEN, D., CONINCK, H., REITH, H. & ARMSTRONG, K. 2011. Carbon Capture and Utilisation in the green economy. *Using CO_2 to manufacture fuel, chemicals and materials.* York: Energy Research Centre of the Netherlands (ECN) and the University of Sheffield.

SUN, C. & STIMMING, U. 2007. Recent anode advances in solid oxide fuel cells. *Journal of Power Sources,* 171**,** 247-260.

TANASINI, P., CANNAROZZO, M., COSTAMAGNA, P., FAES, A., VAN HERLE, J., HESSLER-WYSER, A. & COMNINELLIS, C. 2009. Experimental and theoretical investigation of degradation mechanisms by particle coarsening in sofc electrodes. *Fuel Cells,* 9**,** 740-752.

TAO, Y., EBBESEN, S. D. & MOGENSEN, M. B. 2014. Carbon deposition in Solid Oxide Cells during Co-Electrolysis of H_2O and CO_2. *Journal of Electrochemical Society,* 161**,** F337 - F343.

URSUA, A., GANDIA, L. & SANCHIS, P. 2012. Hydrogen production from water electrolysis: Current status and future trends. *Proceedings of the IEE,* 100**,** 410-423.

VAISALA. 2014. *Vaisala Humidity Caculator* [Webpage]. Finland. [Accessed 08-07-2014 2014].

VIRKAR, A. V. 2010. Mechanism of oxygen electrode delamination in solid oxide electrolyzer cells. *International Journal of Hydrogen Energy,* 35**,** 9527-9543.

VLADIKOVA, D., RAIKOVA, G., STOYNOV, Z., TAKENOUTI, H., KILNER, J. & SKINNER, S. 2005. Differential impedance analysis of solid oxide materials. *Solid State Ionics,* 176**,** 2005-2009.

WANG, S., JIANG, Y., ZHANG, Y., LI, W., YAN, J. & LU, Z. 1999. Electrochemical performance of mixed ionic–electronic conducting oxides as anodes for solid oxide fuel cell. *Solid State Ionics,* 120**,** 75-84.

WEISSBART, J. & SMART, W. H. 1967. Study of electrolytic dissociation of CO_2–H_2O using a solid oxide electrolyte. *National Aeronautics and Space Administration.* USA.

WINCEWICZ, K. C. & COOPER, J. S. 2005. Taxonomies of SOFC material and manufacturing alternatives. *Journal of Power Sources,* 140**,** 280-296.

YAMAJI, K., KISHIMOTO, H., BRITO, M. E., HORITA, T., YOKOKAWA, H., SHIMAZU, M., YASHIRO, K., KAWADA, T. & MIZUSAKI, J. 2013. Effect of Mn-doping on stability of Scandia stabilized zirconia electrolyte under dual atmosphere of solid oxide fuel cells. *Solid State Ionics,* 247–248**,** 102-107.

YAMAMOTO, O. 2000. Solid oxide fuel cells: fundamental aspects and prospects. *Electrochimica Acta,* 45**,** 2423-2435.

YAMAURA, H., IKUTA, T., YAHIRO, H. & OKADA, G. 2005. Cathodic polarization of strontium-doped lanthanum ferrite in proton-conducting solid oxide fuel cell. *Solid State Ionics,* 176**,** 269-274.

YAN, W. J., LU, G. Z., JIANG, Y., DONG, L., YU, Y. C. & LI, W. Z. 2002. Fabrication and Testing of a Doped Lanthanum Gallate Electrolyte Thin-Film Solid Oxide Fuel Cell. *Journal of Electrochemical Society,* 149**,** A1132 - A1135.

YANG, L., CHENG, Z., LIU, M. & WILSON, L. 2010. New insights into sulfur poisoning behavior of Ni-YSZ anode from long-term operation of anode-supported SOFCs. *Energy & Environmental Science,* 3**,** 1804-1809.

YANG, X. & IRVINE, J. T. S. 2008. $(La_{0.75}Sr_{0.25})_{0.95}Mn_{0.5}Cr_{0.5}O_3$ as the cathode of solid oxide electrolysis cells for high temperature hydrogen production from steam. *Journal of Materials Chemistry,* 18**,** 2349-2354.

YANG, Z., JIN, C., YANG, C., HAN, M. & CHEN, F. 2011. $Ba_{0.9}Co_{0.5}Fe_{0.4}Nb_{0.1}O_{3-\delta}$ as novel oxygen electrode for solid oxide electrolysis cells. *International Journal of Hydrogen Energy,* 36**,** 11572-11577.

YOKOKAWA, H. & HORITA, T. 2003. Chapter 5 - Cathodes. *In:* SINGHAL, S. C. & KENDAL, K. (eds.) *High Temperature and Solid Oxide Fuel Cells.* Amsterdam: Elsevier Science.

YOON, K. J., ZINK, P., GOPALAN, S. & PAL, B. U. 2007. Polarization measurments on single-step co-fired solid oxide fuel cells (SOFCs). *Journal of Power Sources,* 172**,** 39 - 49.

YUAN, Z.-Z., SONG, C., WANG, H. & ZHANG, J. 2010. *Electrochemical Impedance Spectroscopy in PEM Fuel Cells - Fundamentals and Applications*, Springer.

YUE, X. & IRVINE, J. T. S. 2012. (La,Sr)(Cr,Mn)O_3/GDC cathode for high temperature steam electrolysis and steam-carbon dioxide co-electrolysis. *Solid State Ionics*.

ZHA, S., CHENG, Z. & LIU, M. 2007. Sulfur Poisoning and Regeneration of Ni-Nased Anodes in Solid Oxide Fuel Cells. *Journal of Electrochemical Society,* 154**,** B201 - B206.

ZHAN, Z., KOBSIRIPHAT, W., WILSON, J. R., PILLAI, M., KIM, I. & BARNETT, S. A. 2009. Syngas Production By co-electrolysis of CO_2/H_2O: The Basis for a Renewable Energy Cycle. *Energy and Fuels,* 23**,** 3089 - 3096.

ZHAN, Z. & ZHAO, L. 2010. Electrochemical reduction of CO_2 in solid oxide electrolysis cells. *Journal of Power Sources,* 195**,** 7250-7254.

8. Appendices

Appendix A

As discussed in Section 3.9.4, a resistor (R1) in series with two parallel connections of CPE (CPE1 and CPE2) and resistor (R2 and R3) are fitted to the high and low frequency impedance arcs of the Nyquist plots presented in Chapters 4 and 5 in order to estimate the total polarisation resistance. Appendix A presents these data.

The red dotted line on the graph shows the experimental data (including induction) while the green line shows the modelled data. The modelled data is not as visible in the high frequency arc as it is located beneath the depressed semi-circle. The resistances shown in Appendices A-1 to A-16 are given in ohms.

Appendix A – 1: Initial Cell Characterisation (Cell used for CO_2 electrolysis)

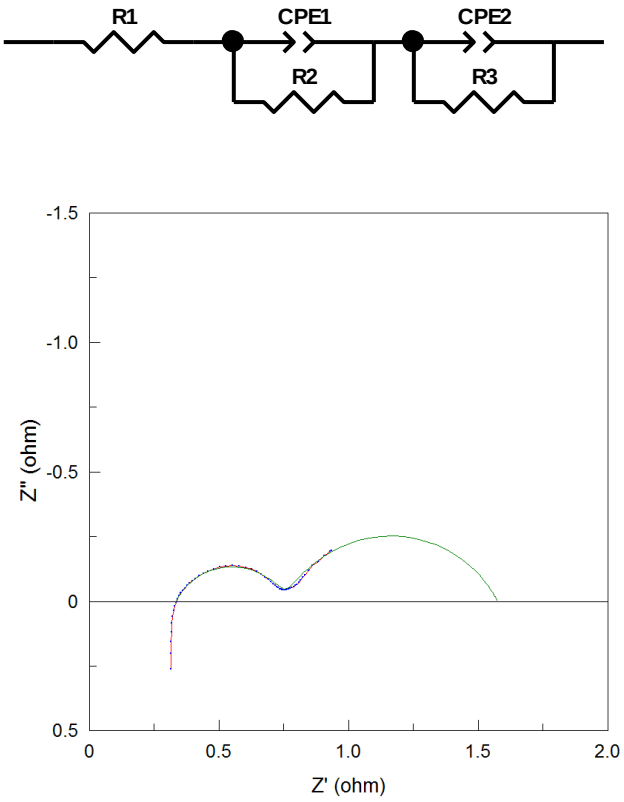

Figure A-1: Nyquist plot of modelled and experimental data recorded at OCV under NiO reducing conditions for the cell used during CO_2 electrolysis (Section 4.2.2)

Appendix A – 2: Initial Cell Characterisation (Cell used for CO_2/H_2O co-electrolysis)

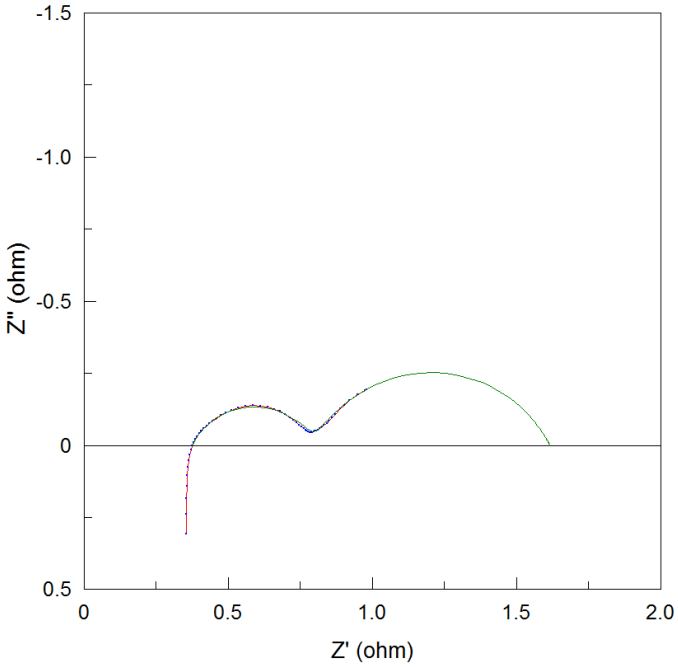

Figure A-2: Nyquist plot of modelled and experimental data recorded at OCV under NiO reducing conditions for the cell used during CO_2 electrolysis (Section 5.2.2)

Appendix A – 3: Electrolysis of CO_2 (15% CO_2 - 60% CO)

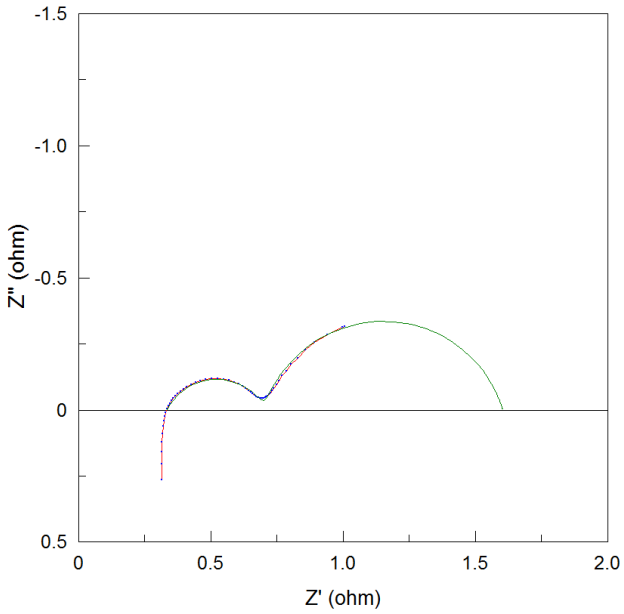

Figure A-3: Nyquist plot of modelled and experimental data recorded 850°C and with fuel electrode compositions of 15% CO_2 - 60% CO (4c1) while synthetic air is flowed to the oxygen electrode (See Section 4.2.4)

Appendix A – 4: Electrolysis of CO_2 (25% CO_2 - 50% CO)

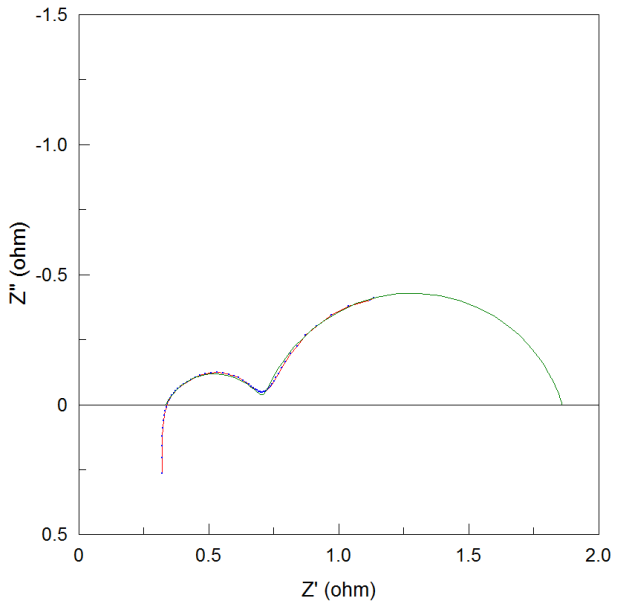

Figure A-4: Nyquist plot of modelled and experimental data recorded 850°C and with fuel electrode compositions of 25% CO_2 - 50% CO (4c2) while synthetic air is flowed to the oxygen electrode (See Section 4.2.4)

Appendix A – 5: Electrolysis of CO_2 (50% CO_2 - 25% CO)

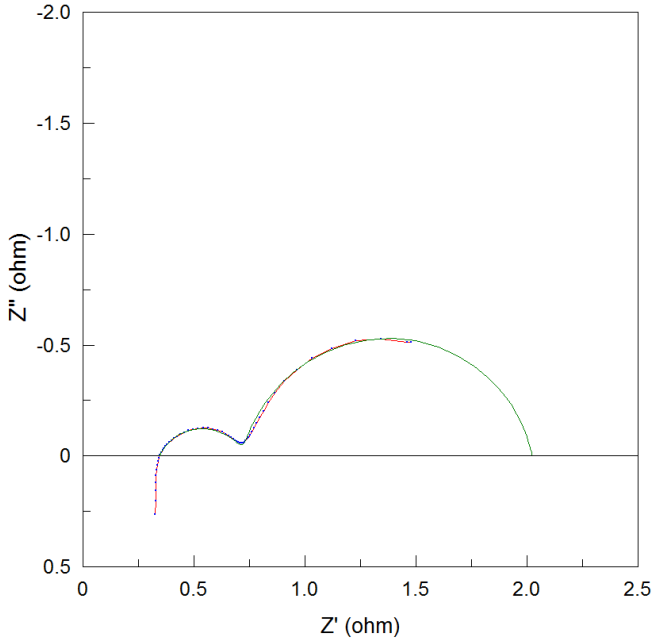

Figure A-5: Nyquist plot of modelled and experimental data recorded 850°C and with fuel electrode compositions of 50% CO_2 - 25% CO (4c3) while synthetic air is flowed to the oxygen electrode (See Section 4.2.4)

Appendix A – 6: Electrolysis of CO_2 (60% CO_2 - 15% CO)

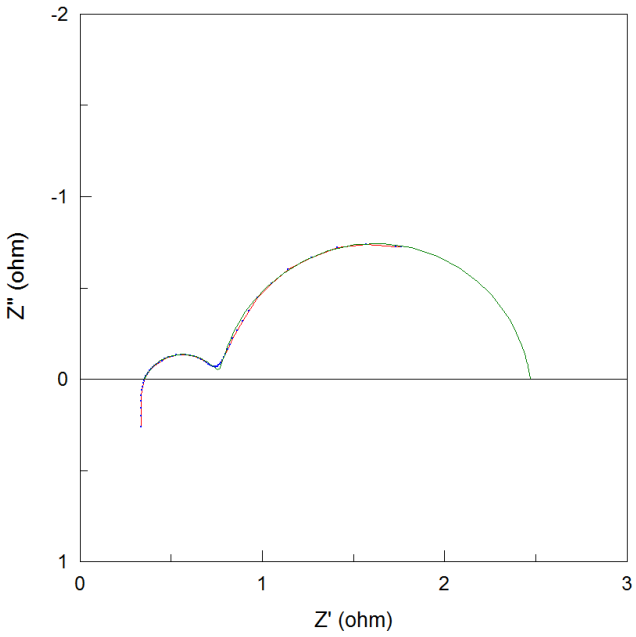

Figure A-6: Nyquist plot of modelled and experimental data recorded 850°C and with fuel electrode compositions of 60% CO_2 - 15% CO (4c4) while synthetic air is flowed to the oxygen electrode (See Section 4.2.4)

Appendix A – 7: Electrolysis of CO_2 (70% CO_2 - 5% CO)

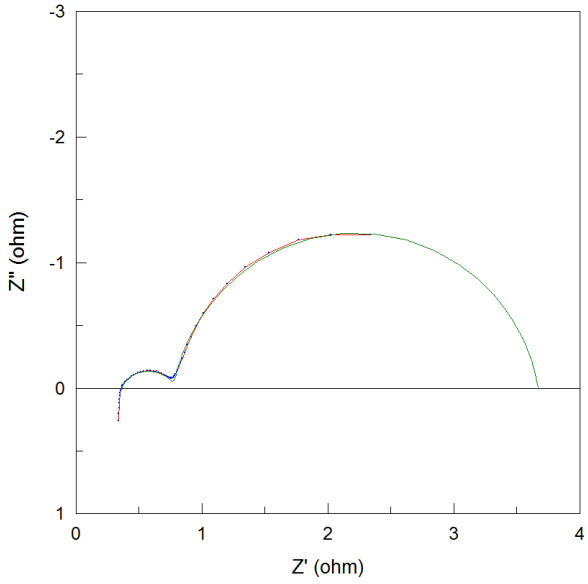

Figure A-7: Nyquist plot of modelled and experimental data recorded 850°C and with fuel electrode compositions of 70% CO_2 - 5% CO (4c5) while synthetic air is flowed to the oxygen electrode (See Section 4.2.4)

Appendix A – 8: Durability of SOCs during CO_2 electrolysis (before -0.5A/cm^2 was applied)

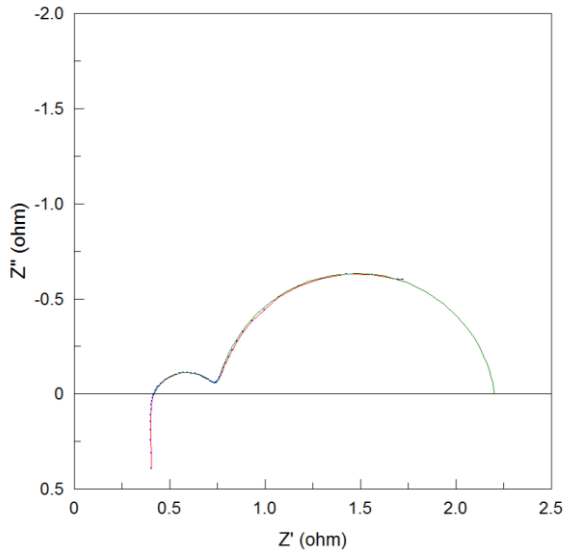

Figure A-8: Nyquist plot of modelled and experimental data (First measurement before durability study at -0.5 A/cm^2) recorded at OCV, 850^{o}C and with fuel electrode compositions of 50% CO_2 - 25% CO while synthetic air is flowed to the oxygen electrode (See Section 4.4.3)

Appendix A – 9: Durability of SOCs during CO_2 electrolysis (after -0.5A/cm^2 was applied)

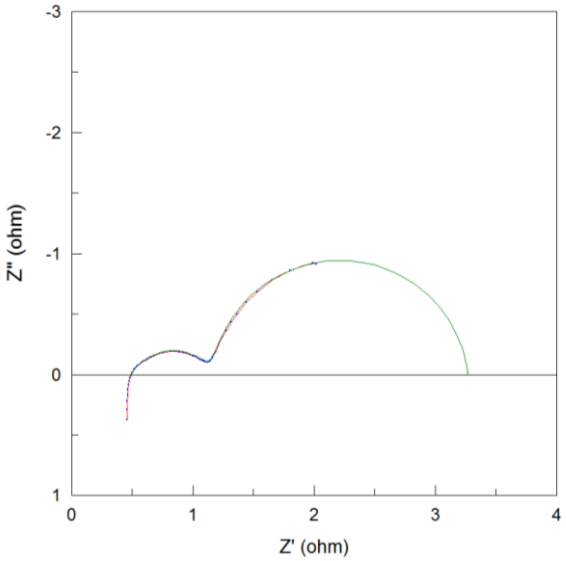

Figure A-9: Nyquist plot of modelled and experimental data (First measurement after durability study at -0.5 A/cm^2) recorded at OCV, 850^{o}C and with fuel electrode compositions of 50% CO_2 - 25% CO while synthetic air is flowed to the oxygen electrode (See Section 4.4.3)

Appendix A – 10: Durability of SOCs during CO_2 electrolysis (before -0.5A/cm^2 was applied)

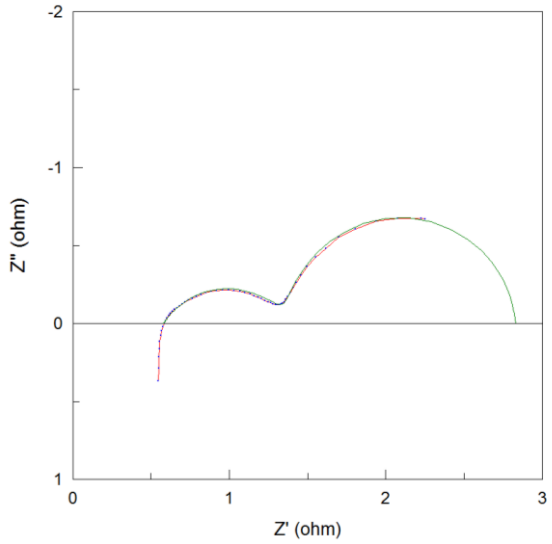

Figure A-10: Nyquist plot of modelled and experimental data (Second measurement before durability study at -0.5 A/cm^2) recorded at OCV, 850^{o}C and with fuel electrode compositions of 50% CO_2 - 25% CO while synthetic air is flowed to the oxygen electrode (See Section 4.4.3)

Appendix A – 11: Durability of SOCs during CO_2 electrolysis (after -0.5A/cm^2 was applied)

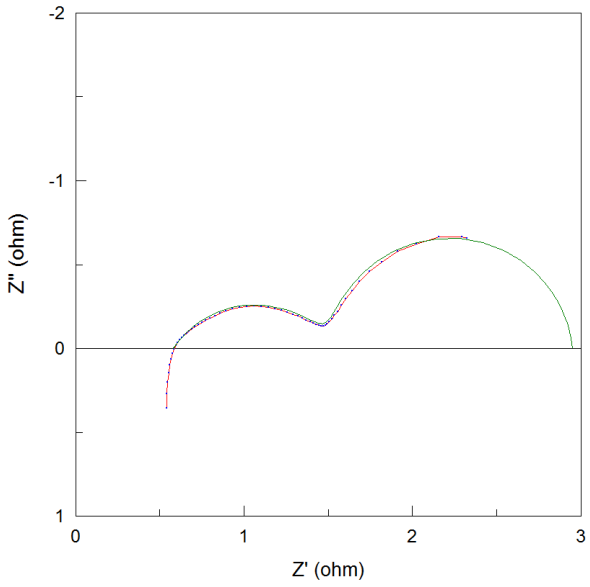

Figure A-11: Nyquist plot of modelled and experimental data (Second measurement after durability study at -0.5 A/cm^2) recorded at OCV, 850^{o}C and with fuel electrode compositions of 50% CO_2 - 25% CO while synthetic air is flowed to the oxygen electrode (See Section 4.4.3)

Appendix A – 12: Co-electrolysis of CO_2 and H_2O (15% CO_2 - 60% H_2)

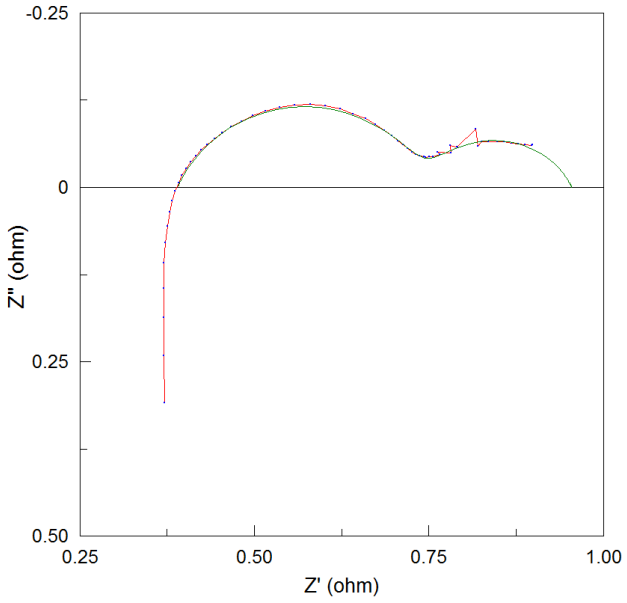

Figure A-12: Nyquist plot of modelled and experimental data recorded 850°C and with fuel electrode compositions of 15% CO_2 - 60% H_2 (4b1) while synthetic air is flowed to the oxygen electrode (See Section 5.3.3)

Appendix A – 13: Co-electrolysis of CO_2 and H_2O (25% CO_2 - 50% H_2)

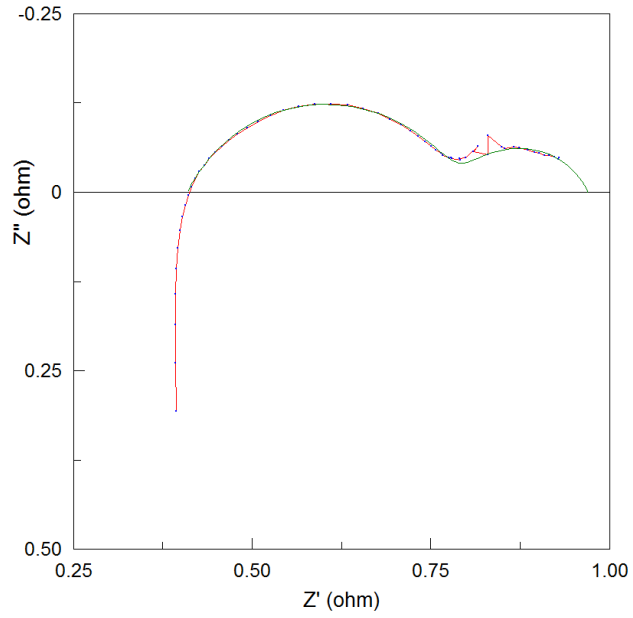

Figure A-13: Nyquist plot of modelled and experimental data recorded 850°C and with fuel electrode compositions of 25% CO_2 - 50% H_2 (4b2) while synthetic air is flowed to the oxygen electrode (See Section 5.3.3)

Appendix A – 14: Co-electrolysis of CO_2 and H_2O (50% CO_2 - 25% H_2)

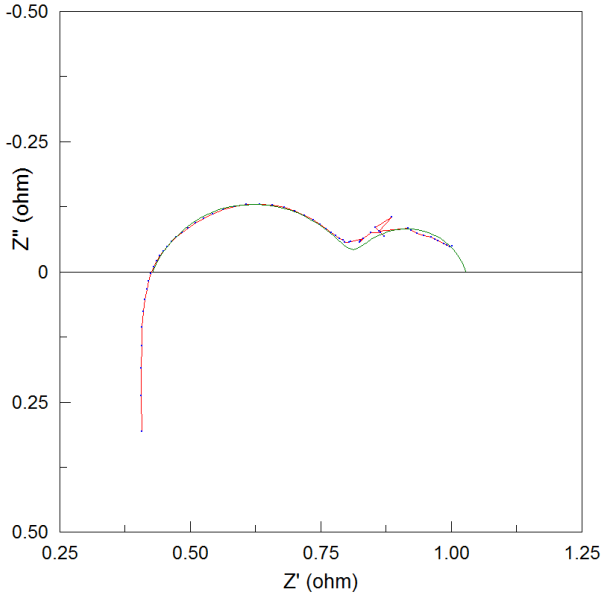

Figure A-14: Nyquist plot of modelled and experimental data recorded 850°C and with fuel electrode compositions of 50% CO_2 - 25% H_2 (4b3) while synthetic air is flowed to the oxygen electrode (See Section 5.3.3)

Appendix A – 15: Co-electrolysis of CO_2 and H_2O (60% CO_2 - 15% H_2)

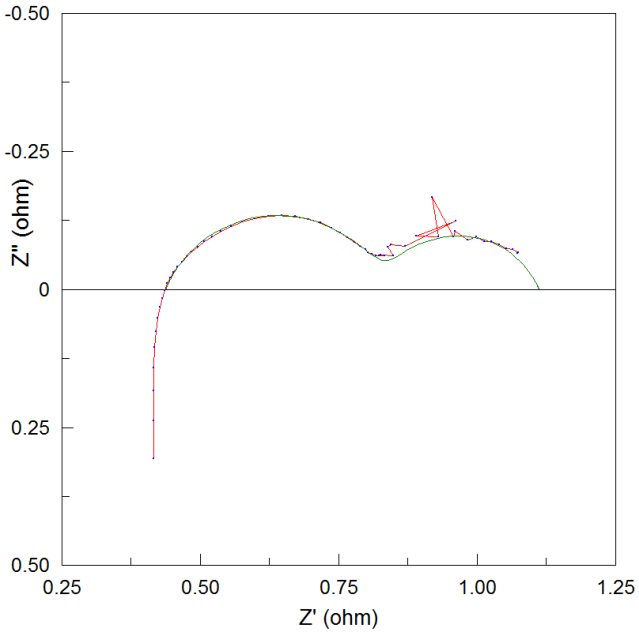

Figure A-15: Nyquist plot of modelled and experimental data recorded 850°C and with fuel electrode compositions of 60% CO_2 - 15% H_2 (4b4) while synthetic air is flowed to the oxygen electrode (See Section 5.3.3)

Appendix A – 16: Durability of SOCs during CO_2/H_2O co-electrolysis (before -0.5A/cm^2 was applied)

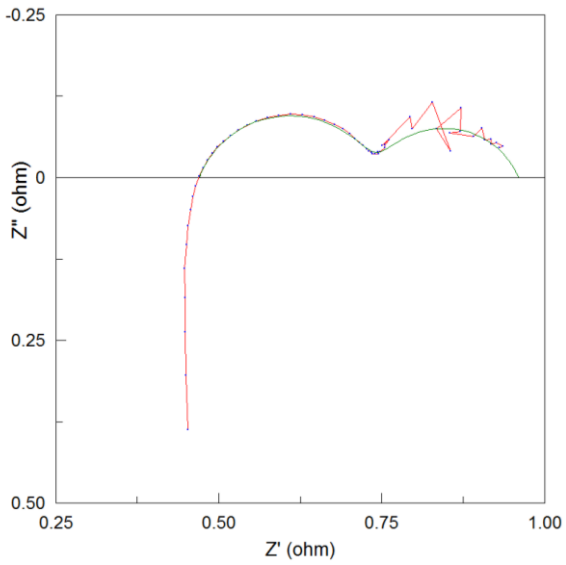

Figure A-16: Nyquist plot of modelled and experimental data recorded at OCV, 850^{o}C and with fuel electrode compositions of 50% CO_2 - 25% H_2 while synthetic air is flowed to the oxygen electrode (See Section 5.4.2)

Appendix A – 17: Durability of SOCs during CO_2/H_2O co-electrolysis (after -0.5A/cm^2 was applied)

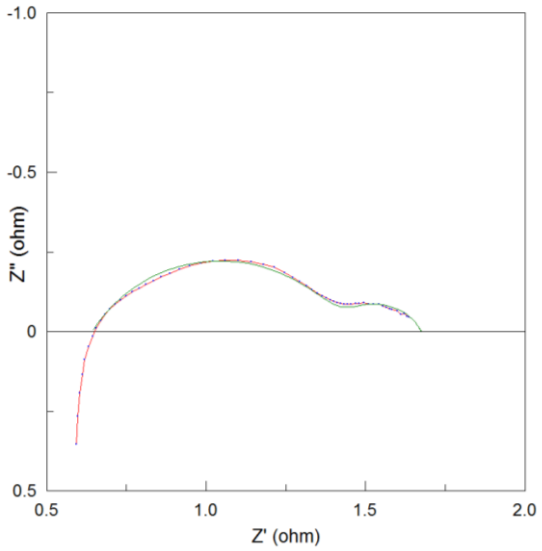

Figure A-17: Nyquist plot of modelled and experimental data recorded at OCV, 850^{o}C and with fuel electrode compositions of 50% CO_2 - 25% H_2 while synthetic air is flowed to the oxygen electrode (See Section 5.4.2)

Appendix B – Ellingham diagram

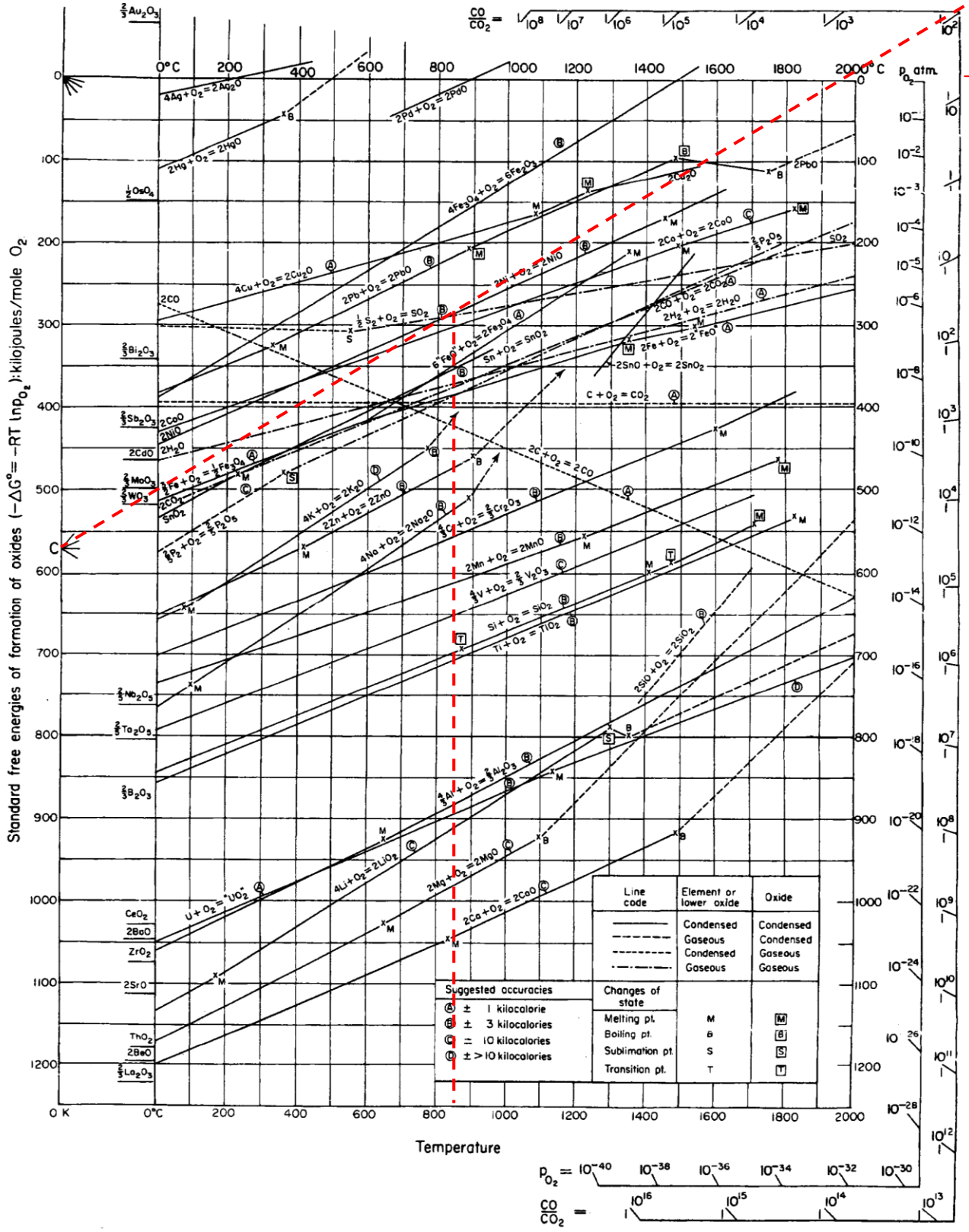

Appendix B -1: Ellingham diagram showing the operating point and the ratio of CO/CO_2 that will be required in order to oxidise Ni at 850°C (MIT 2009)

Appendix C – Gas Chromatograph results

In this Section, the data from the gas chromatograph are presented.

Appendices C – 1 to C - 3: Exhaust gas compositions at OCV and at varying current densities during CO_2 electrolysis

The GC data used in calculating the faraday efficiency for CO_2 electrolysis at varying flow rates and current densities shown in Section 4.3.2 are presented. In calculating the current, the active electrode cell area is 1.227 cm^2.

Table C – 1: GC data obtained during CO_2 electrolysis at 20 ml/min

Active gasses to the fuel electrode	OCV	Current density (A/cm^2)	
		-0.5	-0.61
CO_2 (mol %)	49.4	29.6	25.6
CO (mol %)	24.8	46	50.6

Table C – 2: GC data obtained during CO_2 electrolysis at 40 ml/min

Active gasses to the fuel electrode	OCV	Current density (A/cm^2)	
		-0.5	-0.61
CO_2 (mol %)	49.4	39.6	38.2
CO (mol %)	24.8	35.6	38.6

Table C – 3: GC data obtained during CO_2 electrolysis at 80 ml/min

Active gasses to the fuel electrode	OCV	Current density (A/cm^2)	
		-0.5	-0.61
CO_2 (mol %)	49.4	45.7	45.4
CO (mol %)	24.8	31.1	32.7

Appendices C – 3 to C - 7: Exhaust gas compositions at OCV and at varying current densities during CO_2/H_2O co-electrolysis

The GC data used in calculating the exhaust gas compositions during CO_2/H_2O co-electrolysis shown in Section 5.2.3.1 are presented.

Table C – 4: GC data obtained during CO_2/H_2O co-electrolysis when using an electrolyte supported cell (see Table 5–4)

	4b1	4b2	4b3	4b4
CO_2 (mol %)	3	9.8	40.4	50.4
CO (mol %)	13.1	18.4	21.3	15.1
H_2 (mol %)	52.7	39.4	12	3

Table C – 5: GC data obtained during CO_2/H_2O co-electrolysis when using a fresh electrode supported cell (see Table 5–5)

	4b2	4b3
CO_2 (mol %)	9.9	39.7
CO (mol %)	21.7	22.5
H_2 (mol %)	40.1	9.6

Table C – 6: GC data obtained during CO_2/H_2O co-electrolysis when using an electrode supported cell with Pt paste added to the fuel electrode (see Table 5–6)

	4b2	4b3
CO_2 (mol %)	17.9	44.5
CO (mol %)	9.8	12.1
H_2 (mol %)	45	14.6

Table C – 7: GC data obtained during CO_2/H_2O co-electrolysis when using an electrolyte supported cell at varying current densities (see Section 5.5 for inlet gas compositions and temperature)

	Current density (A/cm^2)		
	-0.25	-0.4	-0.5
CO_2 (mol %)	30.4	25.8	22.8
CO (mol %)	26.5	30.3	32.5
H_2 (mol %)	16.4	18.3	20